Alma Mater Studiorum – Università di Bologna

DOTTORATO DI RICERCA IN

Meccanica e Scienze Avanzate dell'Ingegneria

Ciclo XXXIII

Settore Concorsuale: 09/A3

Settore Scientifico Disciplinare: ING-IND/21

ADDITIVE MANUFACTURING BY LPBF AND WAAM OF METALS: CORRELATION BETWEEN PRODUCTION PROCESS, MICROSTRUCTURE AND MECHANICAL PROPERTIES

Presentata da:

Lavinia Tonelli

Coordinatore Dottorato

Prof. Marco Carricato

Supervisore

Prof.ssa Lorella Ceschini

Esame finale anno 2021

Abstract

In the most recent years, Additive Manufacturing (AM) has drawn the attention of both academic research and industry, as it might deeply change and improve several industrial sectors. From the material point of view, AM results in a peculiar microstructure that strictly depends on the conditions of the additive process and directly affects mechanical properties.

The present PhD research project aimed at investigating the process-microstructure-properties relationship of additively manufactured metal components. Two technologies belonging to the AM family were considered: Laser-based Powder Bed Fusion (LPBF) and Wire-and-Arc Additive Manufacturing (WAAM). The experimental activity was carried out on different metals of industrial interest: a CoCrMo biomedical alloy and an AlSi7Mg0.6 alloy processed by LPBF, an AlMg4.5Mn alloy and an AISI 304L austenitic stainless steel processed by WAAM.

In case of LPBF, great attention was paid to the influence that feedstock material and process parameters exert on hardness, morphological and microstructural features of the produced samples. The analyses, targeted at minimizing microstructural defects, lead to process optimization. For heat-treatable LPBF alloys, innovative post-process heat treatments, tailored on the peculiar hierarchical microstructure induced by LPBF, were developed and deeply investigated. Main mechanical properties of as-built and heat-treated alloys were assessed and they were well-correlated to the specific LPBF microstructure. Results showed that, if properly optimized, samples exhibit a good trade-off between strength and ductility yet in the as-built condition. However, tailored heat treatments succeeded in improving the overall performance of the LPBF alloys.

Characterization of WAAM alloys, instead, evidenced the microstructural and mechanical anisotropy typical of AM metals. Experiments revealed also an outstanding anisotropy in the elastic modulus of the austenitic stainless-steel that, along with other mechanical properties, was explained on the basis of microstructural analyses.

List of symbols and abbreviations

A	Austenite solidification mode
A%	Elongation
AF	Austenite-Ferrite solidification mode
AM	Additive Manufacturing
area%	Area percentage
at.%	Atomic percentage
bcc	body-centered cubic crystal structure
bct	body-centered tetragonal crystal structure
BMI	Bernard Marangoni Surface Instability
BSE	Back Scattered Electrons
CET	Columnar to equiaxed transition
CMT	Cold Metal Transfer
COF	Coefficient of Friction
Cr_{eq}	Cr equivalency
d	Layer thickness
DED	Direct Energy Deposition
DMLS	Direct Metal Laser Deposition
DTA	Differential Thermal Analysis
E	Elastic modulus
EBSD	Electron Back Scattered Diffraction
EDS	Energy Dispersive Spectroscopy
F	Ferrite solidification mode
FA	Ferrite-Austenite solidification mode
fcc	Face-centered cubic crystal structure

FEG-SEM	Field Emission Gun - Scanning Electron Microscope
G	Temperature gradient
GA	Gas atomization
GD-OES	Glow Discharge Optical Emission Spectroscopy
GMAW	Gas Metal Arc Welding
GTAW	Gas Tungsten Arc Welding
h	Hatch distance
HB	Brinell Hardness
hcp	Hexagonal-closed package crystal structure
HIP	Hot Isostatic Pressing
HRC	Rockwell Hardness
HV	Vickers Hardness
LBM	Laser Beam Melting
LED	Laser Energy Density
LPBF	Laser-based Powder Bed Fusion
MIM	Metal Injection Molding
Ni_{eq}	Ni equivalency
OM	Optical Microscope
P	Laser power
PAS	Particle Accumulated Structure mechanism
PAW	Plasma Arc Welding
PBF	Powder Bed Fusion
PBS	Phosphate-Buffered Saline solution
PREP	plasma rotating electrode process
R_m	Ultimate Tensile Strength
Rp	Polarization Resistance
$R_{p0.2}$	Proof stress
SDAS	Secondary Dendrite Arm Spacing
SE	Secondary Electrons
SEM	Scanning Electron Microscope
SLM	Selective Laser Melting

SLM	Selective Laser Melting
UTS	Ultimate Tensile Strength
v	Scanning velocity
vol.%	Volume percentage
WAAM	Wire-and-Arc Additive Manufacturing
wt.%	Weight percentage
XPS	X-ray Photoelectron Spectroscopy
XRD	X-ray diffraction
Ys	Yield strength
λ_1	Primary spacing of dendrites/cells

Index

Introduction

In the most recent years, Additive Manufacturing (AM) has drawn the attention of both scientific research and industry. The attractivity of these innovative technologies relies in the possibility of realizing three-dimensional near-net shape components by the consecutive joining of layers of materials, thus allowing a minimum waste and limiting successive processing [1,2]. AM can be applied to a wide range of materials (i.e. polymers, metals and ceramics) and can be exploited for the fabrication of very different three-dimensional parts in terms of size and shape, such as cardiovascular stents [3] and buildings [4].

In case of metallic materials, AM is highly valued especially in the biomedical, aerospace and automotive sectors for the realization of customized components with a high level of geometric complexity [5], like orthopedic implants, engine parts with conformal cooling channels and innovative architectural structures. In fact, AM innovative technologies might deeply change and improve several industrial sectors by shortening the manufacturing route and by enabling new site-specific design possibilities or new alloy compositions [6]. However, the arising interest in metals additive manufacturing technologies should be associated with a proper knowledge of the process-microstructure-properties relationship. AM technologies are as innovative as they are complex, since they are driven by a large number of process parameters and directly rely on the feedstock quality and processing conditions [7–9]. In order to fully exploit AM potential, a comprehensive and thorough study of peculiar microstructural features resulting

from additive processes (i.e. the metastable supersaturated solid solution, anisotropy, residual stress, etc…) has to be conducted.

In this view, the PhD research project discussed in the present dissertation focused on the investigation of the relationship between process-microstructure-properties of AM metal components. For this purpose, among the AM processes currently available, the most widespread and industrially developed Powder Bed Fusion (PBF) and Direct Energy Deposition (DED) technologies were considered. They are fusion-based AM processes and the core of both PBF and DED is a computer-guided thermal source that joins the material by following a given path in order to reproduce the desired geometry. In PBF layers of fine metallic powder are subsequently and selectively melted, while in DED molten material is deposited layer-by-layer. More specifically, in the present project the Laser-based Powder Bed Fusion (LPBF) and the Wire-and-Arc Additive Manufacturing (WAAM) processes were examined, belonging to PBF and DED respectively. A total of four different metal alloys were processed and studied: an aluminum alloy (AlSi7Mg0.6) and a Co-based alloy (Co28Cr6Mo) for LPBF, an austenitic stainless steel (AISI 304L) and an aluminum alloy (AlMg4.5Mn) for WAAM.

As regards LPBF alloys, the experimental work covered the whole manufacturing process, starting from the characterization of the powder feedstock, moving to the process optimization and finally to the optimization of the post-process heat treatment and assessment of final mechanical properties. At every step, extensive microstructural analyses were conducted in order to study microstructural features, highlight the process-related aspects, investigate type of defects and also to correlate the mechanical response to the final microstructure. In case of WAAM alloys, instead, the experimental analyses focused on the mechanical and microstructural characterization of deposited plates with the aim to investigate the anisotropy induced by the additive process.

Accordingly, the present dissertation is organized in two mains parts, named part A and B, devoted respectively to the LPBF and WAAM activities. Parts A and B are preceded by a summary of the theoretical background mainly regarding microstructural features of additively manufactured metal parts (Chapter 1). Part A is arranged in literature review and experimental activities of LPBF Co28Cr6Mo (Chapters 2 and 3) and LPBF AlSi7Mg0.6 (Chapters 4 and 5) alloys, respectively. Likewise, Part B is organized in literature review and experimental activities of WAAM AISI 304L (Chapters 6 and 7) and WAAM AlMg4.5Mn alloy (Chapters 8 and 9). Experimental sections contain selected parts of the scientific papers for which I was the principal investigator and, for the most part, first and corresponding author.

Research activities were conducted at the Department of Industrial Engineering at the University of Bologna under the supervision of Prof. Lorella Ceschini. The experimental work here discussed is the result of fruitful collaborations established with several research groups: the Laser Group at the University of Bologna, headed by Prof. Alessandro Fortunato, for LPBF activities; the Structural Engineering Group at the University of Bologna, headed by Prof. Tomaso Trombetti, for WAAM activities; the Corrosion and Metallurgy Study Centre "Aldo Daccò", headed by Prof. Cecilia Monticelli, for corrosion tests on the Co-based LPBF alloy.

References

[1] T.D. Ngo, A. Kashani, G. Imbalzano, K.T.Q. Nguyen, D. Hui, Additive manufacturing (3D printing): A review of materials, methods, applications and challenges, Compos. Part B Eng. 143 (2018) 172–196. doi:10.1016/j.compositesb.2018.02.012.

[2] S.A.M. Tofail, E.P. Koumoulos, A. Bandyopadhyay, S. Bose, L. O'Donoghue, C. Charitidis, Additive manufacturing: scientific and technological challenges, market uptake and opportunities, Mater. Today. 21 (2018) 22–37. doi:10.1016/j.mattod.2017.07.001.

[3] S. Bose, D. Ke, H. Sahasrabudhe, A. Bandyopadhyay, Additive manufacturing of biomaterials, Prog. Mater. Sci. 93 (2018) 45–111. doi:10.1016/j.pmatsci.2017.08.003.

[4] C. Buchanan, L. Gardner, Metal 3D printing in construction: A review of methods, research, applications, opportunities and challenges, Eng. Struct. 180 (2019) 332–348. doi:10.1016/j.engstruct.2018.11.045.

[5] T. DebRoy, H.L. Wei, J.S. Zuback, T. Mukherjee, J.W. Elmer, J.O. Milewski, A.M. Beese, A. Wilson-Heid, A. De, W. Zhang, Additive manufacturing of metallic components – Process, structure and properties, Prog. Mater. Sci. 92 (2018) 112–224. doi:10.1016/j.pmatsci.2017.10.001.

[6] S. Tammas-Williams, I. Todd, Design for additive manufacturing with site-specific properties in metals and alloys, Scr. Mater. 135 (2017) 105–110. doi:10.1016/j.scriptamat.2016.10.030.

[7] R.J. Hebert, Viewpoint: metallurgical aspects of powder bed metal additive manufacturing, J. Mater. Sci. 51 (2016) 1165–1175. doi:10.1007/s10853-015-9479-x.

[8] W.J. Sames, F.A. List, S. Pannala, R.R. Dehoff, S.S. Babu, The metallurgy and processing science of metal additive manufacturing, Int. Mater. Rev. 6608 (2016) 1–46. doi:10.1080/09506608.2015.1116649.

[9] P.C. Collins, D.A. Brice, P. Samimi, I. Ghamarian, H.L. Fraser, Microstructural Control of Additively Manufactured Metallic Materials, Annu. Rev. Mater. Res. 46 (2016) 63–91. doi:10.1146/annurev-matsci-070115-031816.

Chapter 1

METALLURGICAL FEATURES OF ADDITIVELY MANUFACTURED METAL PARTS

THEORETICAL BACKGROUND

1.1 Overview of Metal Additive Manufacturing processes

Additive Manufacturing (AM) is defined as: "*the process of joining materials to make objects from 3D model data, usually layer upon layer, as opposed to subtractive manufacturing methodologies*", as reported in the EN ISO/ASTM 52900 standard [1]. Therefore, AM technologies enable the fabrication of near-net-shape three-dimensional components, even with complex design, with a minimum consumption and waste of feedstock material. AM technologies benefit of great interest from both academia and industry, as demonstrated by the increasing trend in the published researches regarding "additive manufacturing of metals" indexed by Scopus® from 1980, when AM starts to gradually spreading, to 2020 (Figure 1.1).

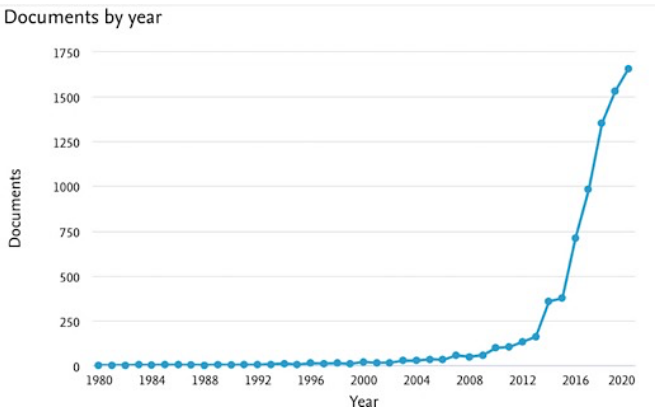

Figure 1.1: Published researches on AM of metals indexed by Scopus® (accessed on October 12, 2020)

The family of AM, as defined by the aforementioned standard, include processes for all class of materials (polymers, ceramic, metals and composite). By focusing on the AM technologies for metallic materials, the classification reported in Figure 1.2 can be adopted and processes can be divided into fusion-based ones and solid-state ones. Currently, fusion-based one, in which the feedstock material undergoes melting and rapidly solidifies, are the most industrially and academically investigated. Fusion-based AM processes are divided in Direct Energy Deposition (DED) and Powder Bed Fusion (PBF). In DED, the final component is additively manufactured by consequent deposition of molten material, while in PBF it is fabricated via selective melting of subsequent layers of powder. DED and PBF processes are classified according to the thermal source and, in the present dissertation, the Laser-Based Powder Bed Fusion (LPBF), belonging to PBF, and the Wire-and-Arc Additive Manufacturing (WAAM), belonging to DED, have been considered.

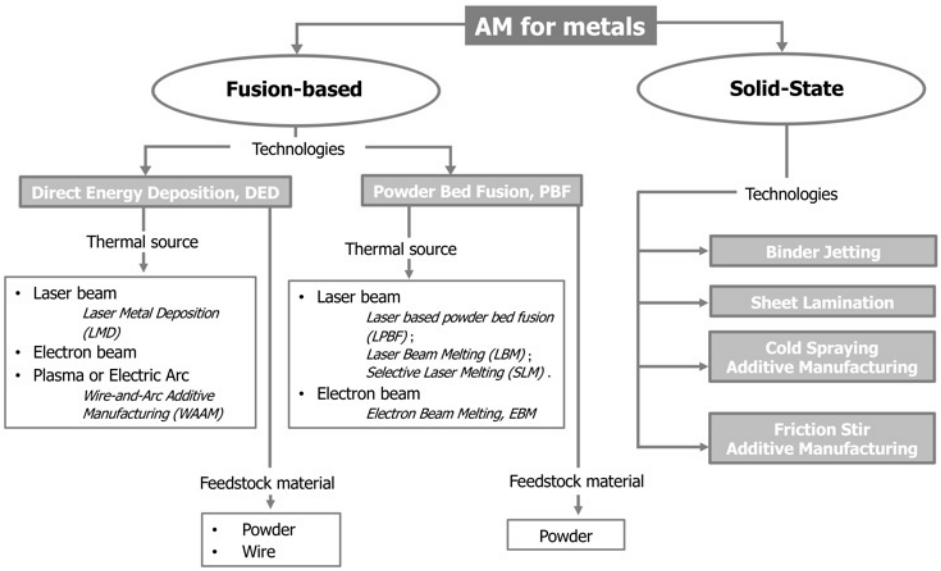

Figure 1.2: Classification of additive manufacturing technologies for metals (adapted from [1]).

One of the main criteria for the selection of the AM process results from the trade-off between part complexity and dimensions, as shown by the graphs in Figure 1.3. LPBF is usually adopted for the production of relatively small and very complex components that can afford intricated lattice structures and inner cavities maintaining an elevated accuracy. WAAM, instead, is essentially devoted to the

manufacture of large components, with a lower level of complexity and accuracy, and therefore can be also employed for civil engineering applications [2,3].

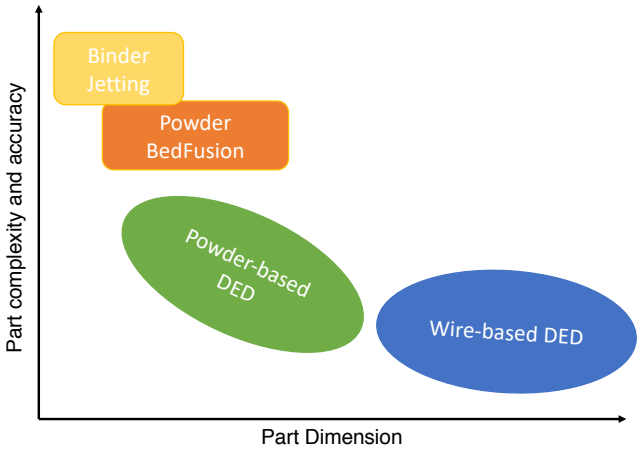

Figure 1.3: Classification of AM processes for metals as a function of part complexity and dimension

1.1.1 Laser based Powder bed fusion

Laser-Based Powder Bed Fusion (LPBF) relies on the selective melting of a layer of fine metallic powder by means of a laser beam. This technology is also known as Selective Laser Melting (SLM), Laser Beam Melting (LBM), Direct Metal Laser Sintering (DMLS). As illustrated in Figure 1.4a, the process is conducted inside a closed chamber whose atmosphere is carefully controlled: the oxygen content is limited and a flow of an inert shielding gas (N_2 or Ar) is ensured on the powder bed. Three main area can be identified: a powder supply chamber containing the feedstock powder, a working platform, and an overflow container in which the powder surplus is collected. For each layer, the proper amount of powder is distributed on the working platform by a recoater (usually in form of blade or roller) and then processed by a computer-guided laser that replicates the geometry based on the 3D CAD model of the components [2,4]. These steps are continuously repeated for the whole process and the components is built, layer after layer, inside the powder bed.

LPBF is the most widespread AM technology and yet one of the most complicated, driven by more than 100 process parameters [5], that can be divided in four main groups:

- *Laser and scanning parameters*: laser power (average and peak), mode (continuous or pulsed laser), wavelength, spot size, scanning velocity, scanning pattern or strategy, hatch spacing, etc…
- *Powder material properties:* particle size distribution, surface roughness, flowability, density, thermal conductivity, heat capacity, latent heat of fusion, melting temperature, boiling temperature, melt pool viscosity, vapour pressure, absorptivity, etc…
- *Powder bed properties and recoat parameters*: apparent density of the layer of powder, layer thickness, powder bed temperature, thermal conductivity, heat capacity, absorptivity, emissivity, recoater velocity, recoater type, recoater pressure.
- *Build environment parameters*: type of shielding gas (nitrogen or argon) and its molecular weight, thermal conductivity, viscosity heat capacity, pressure, flow rate, content of oxygen, etc…

Powder material properties will be discussed in the following sections, while the main process parameters related to laser, scanning and powder bed conditions are schematically shown in Figure 1.4b.

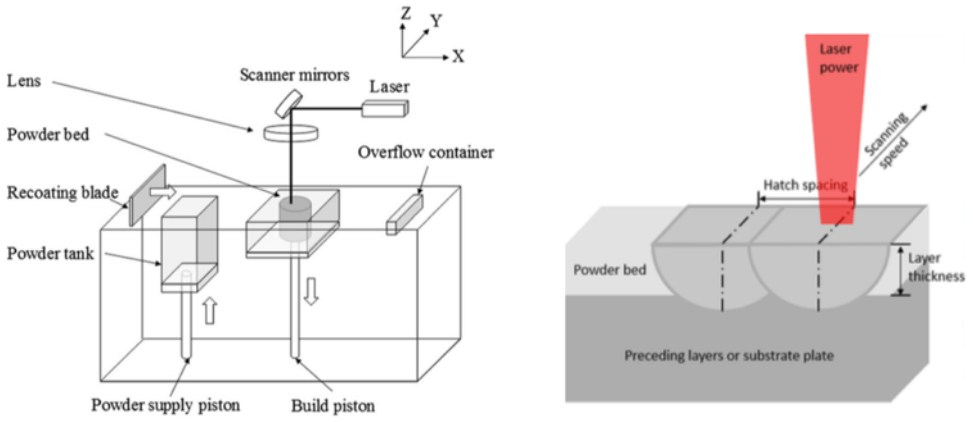

a b

Figure 1.4: Schematic representation of LPBF process (a), detail of process parameters (b) [2,6]

The layer thickness for LPBF is usually in the range 20-40 μm and this aspect contributes to determine the high accuracy and the relative low production rate that characterize LPBF. Scanning speed can be up to 1200-1500 mm s^{-1} while laser power can reach 1 kW [4]. Another scanning-related important parameter is represented by the scanning strategy, that represents the path adopted to process the powder layer (Figure 1.5). Scanning strategy directly influences thermal cycles of the building, thus residual stress, porosity content and microstructure, as will be later discussed [7,8].

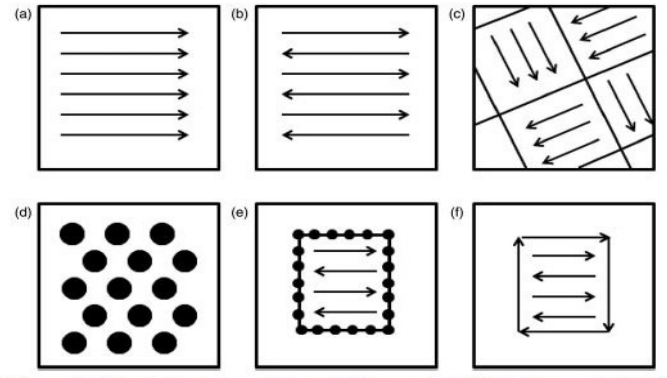

Figure 1.5: Scanning strategy: a) unidirectional or concurrent fill, b) bi-directional, snaking or countercurrent fill, c) island or chessboard scanning, d) spot melting, e) spot melting contours with snaking fill, f) line melting contours with snaking fill [7]

Many of the aforementioned parameters are strongly influenced by the architecture of each printing machine and can vary significantly among different brands.

1.1.2 Wire and Arc Additive Manufacturing

The Wire-and-Arc Additive Manufacturing (WAAM) is based on automated welding processes like: arc welding (GMAW), plasma arc welding (PAW), and gas tungsten arc welding (GTAW) [9–11]. Among WAAM processes, GMAW is the most widely used and it is based on the deposition of molten material from the feedstock wire by means of an electric arc generated between the wire itself and the workpiece (Figure 1.6), in which a six-axis robot guides the torch. It is also

known as metal inert gas (MIG) or metal active gas (MAG) process. Conversely to PBF systems, WAAM does not require a closed chamber to operate, thus the size of the metallic parts is only determined by the limitations given by manipulators. Deposition rates for this specific technology range between 15-160 g min^{-1} [10] and layer thickness can be up to 2 mm, making this technology suitable for the production of large metallic parts, also in the construction field [3,12].

As for other fusion-based AM technologies like LPBF, main process parameters of WAAM regard the control of the thermal source and deposition of materials and can be synthetized as follows:

- current and arc voltage;
- angle between electrode and layer;
- welding speed;
- wire feed rate;
- layer thickness;
- type and dimension of feeding wire;
- type and flow rate of the shielding gas.

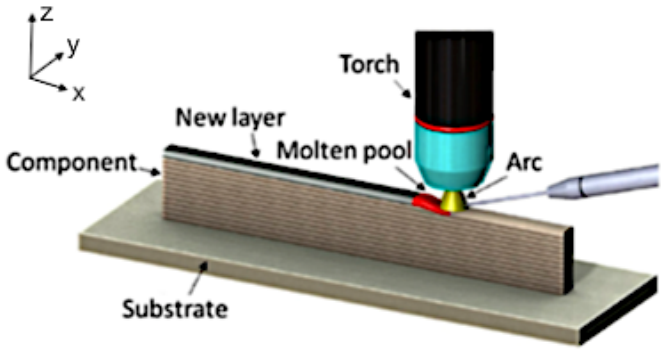

Figure 1.6: Schematic representation of the WAAM process (adapted from [10]).

Besides post-process heat treatments, two main post-deposition processes can improve the quality of the final part: interlayer rolling and interpass cooling [10,13]. The interlayer rolling is a cold-working process that induces plastic deformation and recrystallization of the deposited layer, before the deposition of the successive

one. Interlayer rolling can result in the reduction of porosity, an increase of mechanical strength and reduction of residual stress. It should be noticed that rollers have to be customized on the specific design of the building components and it may not be very convenient for complex geometries. The interpass cooling consists in the forced or assisted cooling of the newly deposited layer, with the aim to control the thermal cycle in order to reduce residual stress or limit the idle time between consequent depositions.

WAAM uses as feedstock material commercially available filling wire developed for conventional welding technologies. As a consequence, a wide range of materials can be proficiently processed with this technology and, with respect to typical feedstock materials used for PBF technologies, costs for feedstock supply are considerably lower [11].

1.2 Microstructural features of AM of metals

Additive manufacturing technologies benefit of great interest from several industrial fields mainly in the reason of the complex designs that can be obtained. However, from the material point of view, due to the non-equilibrium solidification conditions, AM leads to peculiar microstructural features substantially different from those obtained with conventional manufacturing processes. Indeed, additively manufactured metal parts, both LPBF and WAAM, are characterized by a hierarchical microstructure that relies on the specific melting and solidification conditions that will be described in the following sections. The schematic representation of the hierarchical microstructure of metals produced by AM is reported in Figure 1.7 in which it can be recognized: a) layered structure consequent to the layer-by-layer approach; b) solidified melt pools due to the localized melting of the feedstock material, or to the local deposition of molten material, related to the complex scanning or deposition strategy; c) epitaxial grains crossing-over layers due to the peculiar solidification conditions in which the material solidifies above itself; d) fine sub-structure (i.e. cellular or columnar) formed within grains inside the melt pool.

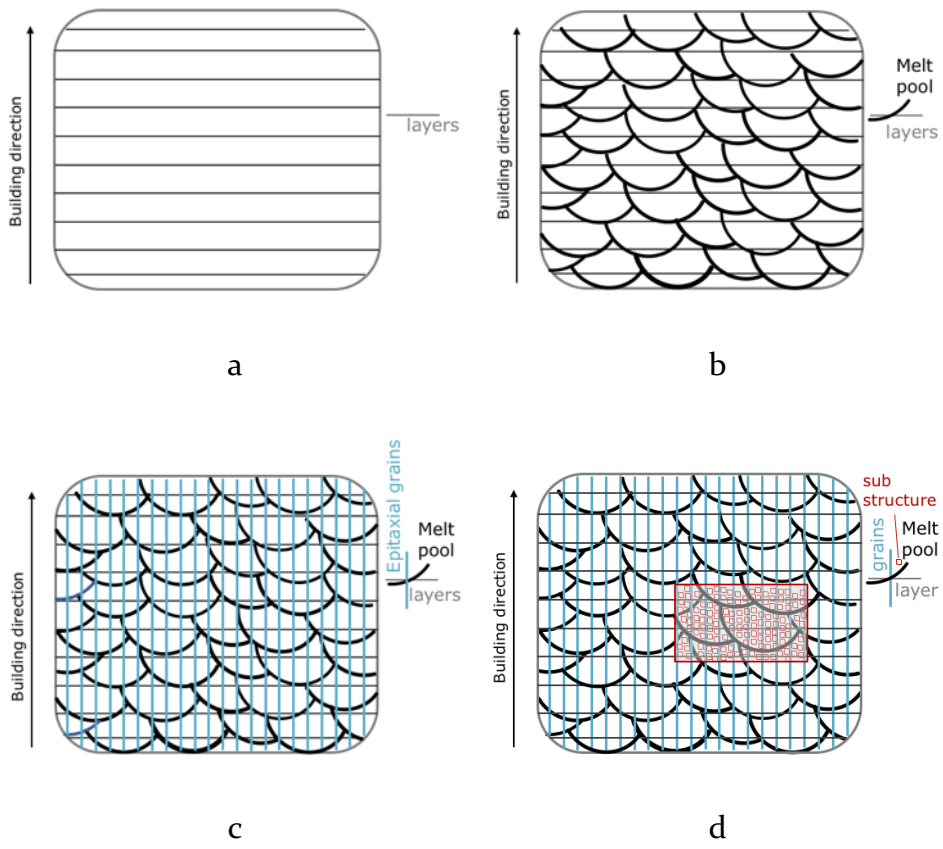

Figure 1.7: Schematic representation of the hierarchical microstructure of additively manufactured parts: a) layers, b) melt pools, c) epitaxial grains, d) fine sub-structure.

1.2.1 Melt pool formation

In fusion-based metal additive manufacturing technology small portions of feedstock material are continuously melted and rapidly solidified. In direct deposition processes, as WAAM, feedstock material is melted and then deposited. In powder bed fusion processes, instead, the feedstock powder is locally melted by the thermal source. Either way, an almost semicircular fusion zone, typically referred to as melt or molten pool, is formed, as schematically represented in Figure 1.8 for PBF. By reason of heat conduction, the melt pool is only partially directly irradiated by the thermal source that, ideally, involve the center of the fusion zone thus generating a temperature gradient between the center and peripheric area in direct contact with the cold metal. Furthermore, due to heat

conduction, also the upper part of the previously deposited layer is heat-affected and/or partly re-melted.

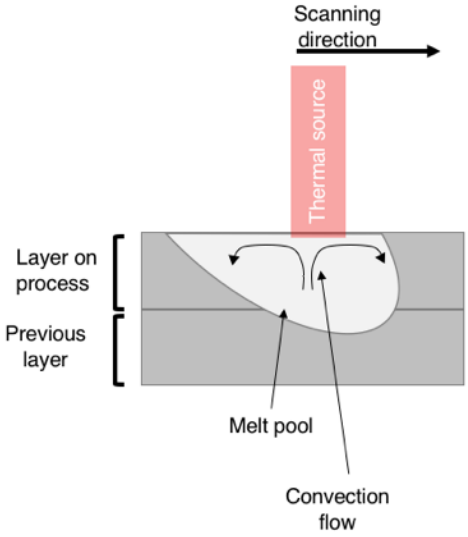

Figure 1.8: Schematic representation of semicircular fusion zone (melt pool) formed in additive manufacturing technologies

As already found in case of conventional welding [14], inside melt pool the convection flow of liquid metal is driven by several forces, as represented in Figure 1.9. Driving forces are: buoyancy (or gravitational), Lorentz, surface tension (Marangoni) and shear stress induced by plasma force. Among these forces, buoyancy and especially surface tension ones dominate the fluid flow in additive manufacturing, while Lorentz and shear stress forces are mostly related to welding processes based on electric arc and plasma jet respectively [15–17]. Buoyancy or gravitational flow is related to the density (ρ) of the liquid metal that decreases with increasing temperature. As a consequence, liquid metal in zones *b* in Figure 1.9a is heavier than the liquid in the center of the melt pool (zone *a* in the same Figure), Hence, in account of gravitational force, the heavier liquid falls along pool boundaries and arise along the pool axis when temperature increases, generating the centrifugal flow in Figure 1.9b. Marangoni flow is instead related to the surface tension (γ) of the liquid that still decreases with increasing temperature. Hence, the liquid in zone *a* of Figure 1.9e has a lower surface tension than liquid in zone *b* and it is pulled towards the melt pool border as a consequence of the shear stress induced by the surface tension gradient, generating the flow in Figure 1.9f. This phenomenon is also called thermocapillary convection flow.

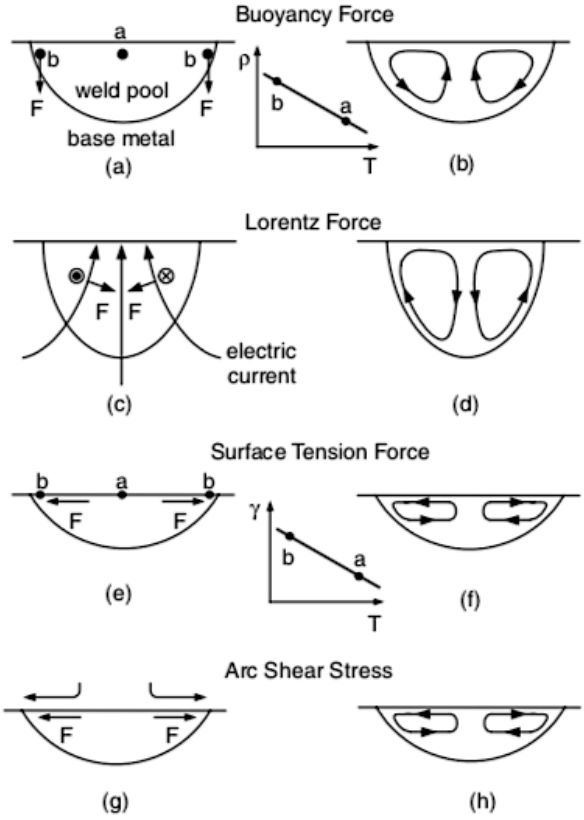

Figure 1.9: Driving forces of convection flow (a,c,e,g); relative flow inside melt pools (b, d, f, h) [14].

However, as represented in Figure 1.10, the centrifugal Marangoni flow can be reversed, becoming a centripetal flow. This occurs when a small amount of surface-active agent is present. Surface-active agents are usually consequent to contamination of the pool, frequently due to oxygen, that invert the surface tension gradient. A centripetal flow is detrimental for the proper wetting and spreading of the liquid metal that ensures overlap with surrounding solidified tracks, promoting the formation of a sound component. The inversion of the flow can even lead to arising of liquid metal from the pool that eventually solidifies in globular particles, inducing the so-called balling phenomenon [14,18]. Consequently, an adequate protection from oxidation and contaminations of the fusion zone has to be assured by shielding gas and control of feedstock material quality.

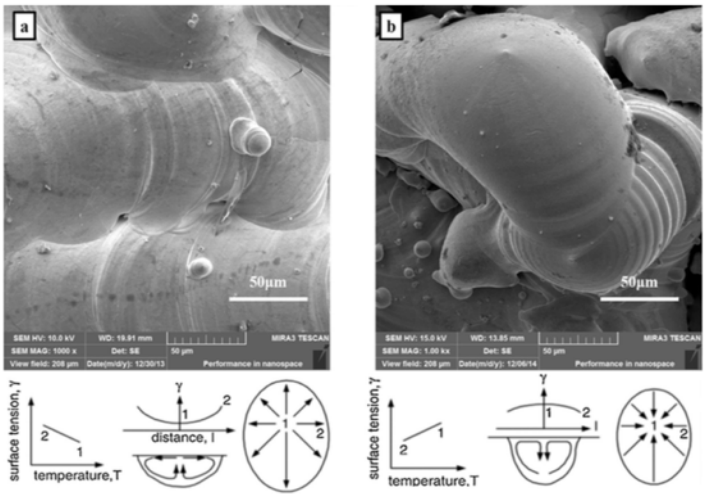

Figure 1.10: Surface tension (Marangoni) flow: a) regular centrifugal flow enhancing wetting and spreading; b) reversed flow to oxidation generating balling [18].

By reason of the elevated cooling rates (up to 10^5-10^6 K s^{-1}), the solidification of liquid metal inside melt pools develops very rapidly [4,7]. Indeed, melt pool is surrounded by colder and solid metal, being previously solidified metal layers or unprocessed powder in case of powder bed fusion processes. Thus, elevated heat gradient is developed between the superheated liquid metal inside melt pool and the cold melt pool border. Consequently, solidification of the metal starts from cold melt pool border and develop towards the melt pool core. As will be discussed, these peculiar conditions determine an epitaxial grain growth as well as size and morphology of the sub-structure that compose the typical hierarchical microstructure of additively manufactured metal parts.

1.2.2 Epitaxial grains

The epitaxial growth is developed when a solid grain nucleates from liquid metal in direct contact with a solid substrate with its same chemical composition, as for the melt pool. The literature refers to this phenomenon either as epitaxial growth or epitaxial nucleation [19–22]. However, as it will be reported below, it is commonly discussed as a particular case of heterogenous nucleation in which it is demonstrated that nucleation of new grains does not occur. Heterogenous

nucleation is governed by the balance of interfacial free energies of the liquid, the solid, and the nucleus, described by the following equation [20]:

$$\gamma_{ML} = \gamma_{SM} + \gamma_{SL} \cos \phi \quad (1)$$

Where, as schematically represented in Figure 1.11:

γ_{ML} is the interface free energy between solid metal substrate and liquid metal

γ_{SM} is the interface free energy between solid nucleus and solid metal substrate

γ_{SL} is the interface free energy between solid nucleus and liquid metal

ϕ is the contact angle

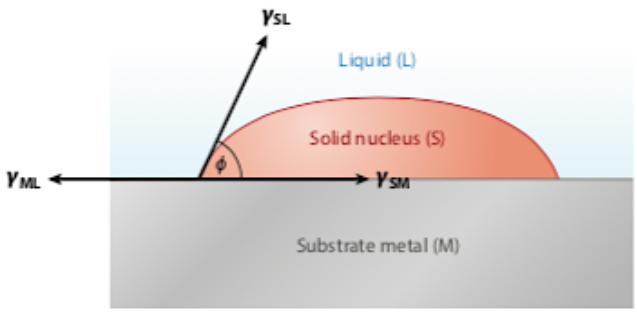

Figure 1.11: Schematic representation of the solid nucleus in contact with solid substrate and liquid metal [20]

In Equation 1, since the chemical composition of solid and liquid is the same, the term γ_{SM} is negligible and it can be considered $\gamma_{SL} \simeq \gamma_{ML}$ [20,22]. Hence, Equation 1 can be simplified as follows:

$$\gamma_{ML} = \gamma_{SL} \cos \phi$$
$$\text{and } \gamma_{SL} \simeq \gamma_{ML} \quad (2)$$
$$\text{thus } \cos(\phi) \simeq 1 \rightarrow \phi \simeq 0$$

As result from Equation 2, the contact angle ϕ is zero, therefore the liquid wets completely the metal substrate. For heterogeneous nucleation on an existing wall, the change in the free energy needed to nucleate a solid grain, is given by the formula [22]:

$$\Delta G_{Het} = -V_S \Delta G_V + A_{SL}\gamma_{SL} + A_{SM}(\gamma_{SM} - \gamma_{LM}) \quad (3)$$

Where, in Equations 3:

ΔG_v is the change in the free energy per unit volume associated to the formation of a new nucleus

V_s is the volume of the nucleus

A_{SL} is the surface area of the interface created by the liquid and the nucleus

A_{SM} is the surface area of the interface created by the metal substrate and the nucleus

Assuming that the nucleus forms as a spherical cap, it can be assumed:

$$A_{SL} = 2\pi r^2 (1 - \cos\phi)$$

$$A_{SM} = \pi r^2 \sin^2\phi \quad (4)$$

$$V_S = \pi r^3 (2 + \cos\phi)\frac{(1-\cos\phi)^2}{3}$$

By combining Equations 1, 3 and 4, ΔG_{Het} can be written as:

$$\Delta G_{Het} = S(\phi)[\frac{4\pi}{3} r^3 \Delta G_V + 4\pi r^2 \gamma_{SL}] \quad (5)$$

where $S(\phi) = (2 + \cos\phi)\frac{(1-\cos\phi)^2}{4}$ is the shape factor

As previously demonstrated (Equation 2), in case of liquid metal in direct solidifying on a solid substrate with its same chemical composition the contact

angle ϕ is zero, or almost zero. Consequently, the change in free energy required for the formation of a new nucleus (ΔG_{Het}) in the epitaxial growth is approximately zero. Thus, a solid grain can nucleate without the need to overcome an energy barrier as the solid metal substrate presents a perfect crystallographic match for growth of the solid nucleus. However, it is commonly assumed that growth occurs directly from the preexisting solid without the need for nucleation [22] and this phenomenon is known as epitaxial growth, schematically represented in Figure 1.12a.

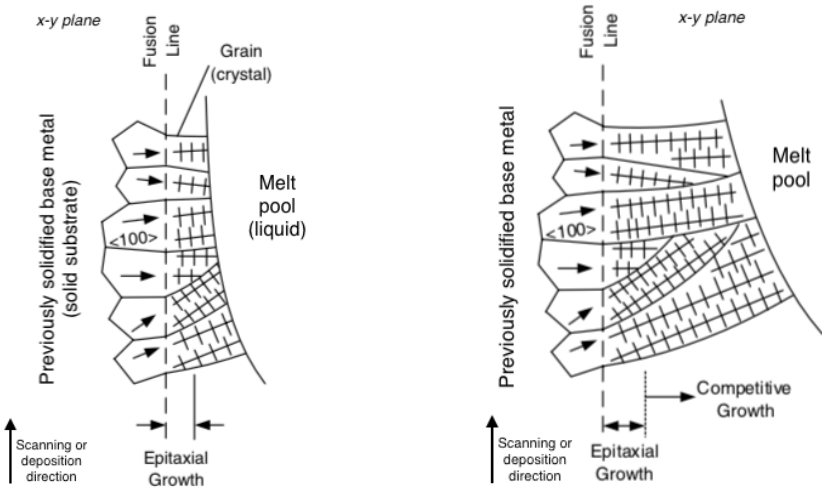

a b

Figure 1.12: Solidification of additively manufactured metal components: a) epitaxial grain growth starting from the fusion line correspondent to melt pool borders; b) competitive growth across melt pool (adapted from [19]).

Away from the fusion line, corresponding to the melt pool border, the solidification across the melt pool, follows the so-called competitive growth, as shown in Figure 1.12b. Indeed, grains grow perpendicularly to the melt pool border towards the core by following the direction of the maximum thermal gradient, hence the direction of maximum heat extraction. Concurrently, grains tend to grow following the easy-growth direction defined for each lattice structure, as reported in Table 1.1. Therefore, as indicated by arrows in Figure 1.12, grains whose easy-growth direction is perpendicular to the melt pool border are favored and might stop the growing of a less favored grain. However, it should be considered

that melt pool borders are curved and constantly in motion, thus it is possible that grains are initially favorably-oriented and, with changing in the curved solid/liquid interface, become unfavorably-oriented [22].

Crystal structure	***Easy-growth direction***
Face-centered-cubic (fcc)	<100>
Body-centered-cubic (bcc)	<100>
Hexagonal-close-packed (hcp)	<1010>
Body-centered-tetragonal (bct)	<110>

Table 1.1: Easy-growth direction for different crystal structure [19]

Epitaxial grain growth and consecutive competitive growth in case of LPBF have been documented by Chen et al. [23], as reported in Figure 1.13. In Figures 1.13a,b, melt pool border are indicated by the white dashed arrows while red arrows indicate growing directions: grains grow starting from the border by replicating the direction of the previously solidified layer. Evidence of the competitive growth occurring away from the melt pool border is given in Figure 1.13c where the encounter of different grain directions has been depicted.

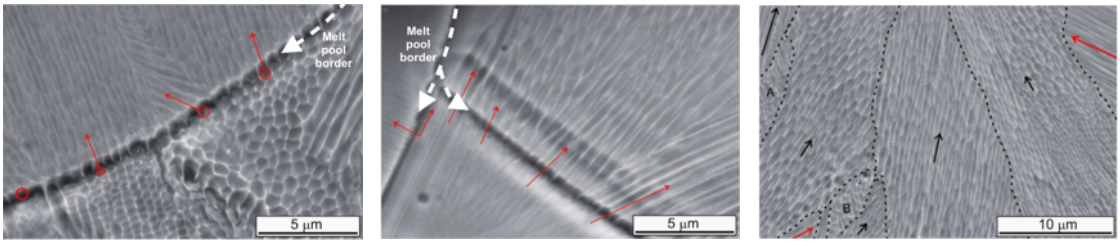

a b c

Figure 1.13: Grain growth of the LPBF C028Cr6Mo alloy: a) and b) epitaxial growth starting from melt pool boundaries (borders are indicated by white dashed arrows and growing direction by red arrows); c) competitive grow away from the melt pool boundaries. Adapted from [23].

The main outcome of epitaxial growth, as depicted in Figure 1.14, is the formation of macroscopic large columnar grains crossing-over layers responsible for a possible anisotropic mechanical behavior of additive components [4,7].

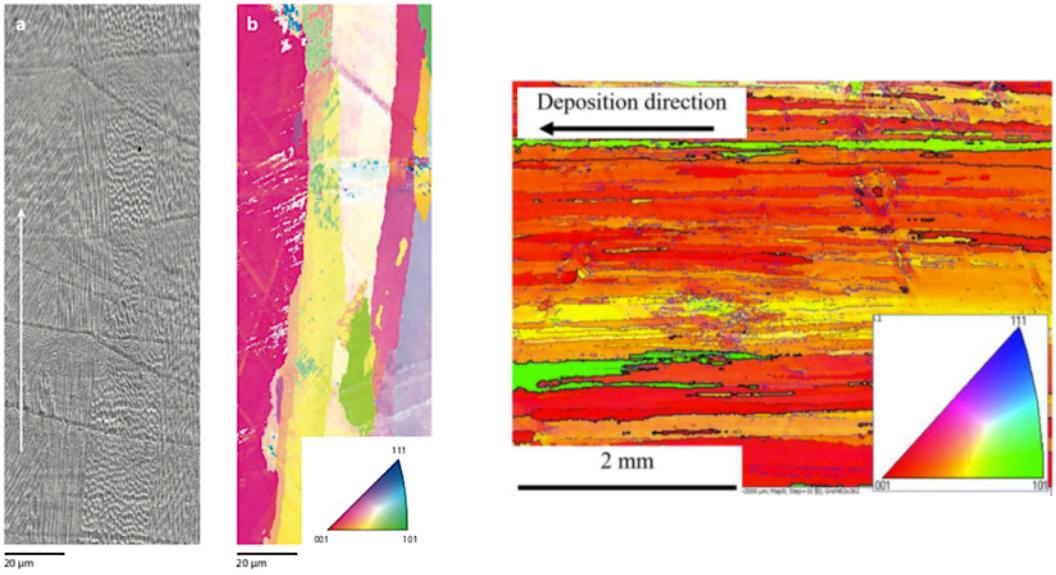

a b

Figure 1.14: Epitaxial grain growth crossing over layer as documented by EBSD analyses for: a) the Co28Cr6Mo LPBF alloy [24]; b) the AISI 316L WAAM stainless-steel [25].

It should be also mentioned that, by proper modification of chemical composition of deposition process, it is possible to limit the epitaxial growth of grains [21] , thus potentially reducing anisotropic behavior. In the particular case of aluminum alloys, recent literature studies reported that, with the addition of grain refiners such as Ti and TiB_2 nanosized particles, the formation of equiaxed grains rather than epitaxial ones was promoted, as showed in Figure 1.15. Similar results were reported for both LPBF [26,27] and WAAM [28] processes, proving that for both technologies equiaxed grains can be promoted by addition of grain refiners. Moreover, analogous effects were also achieved without any modification in the chemical composition, but by tailoring the arc modes for the Al6Mg alloy processed by variable polarity cold metal transfer (VP-CMT) WAAM process [29].

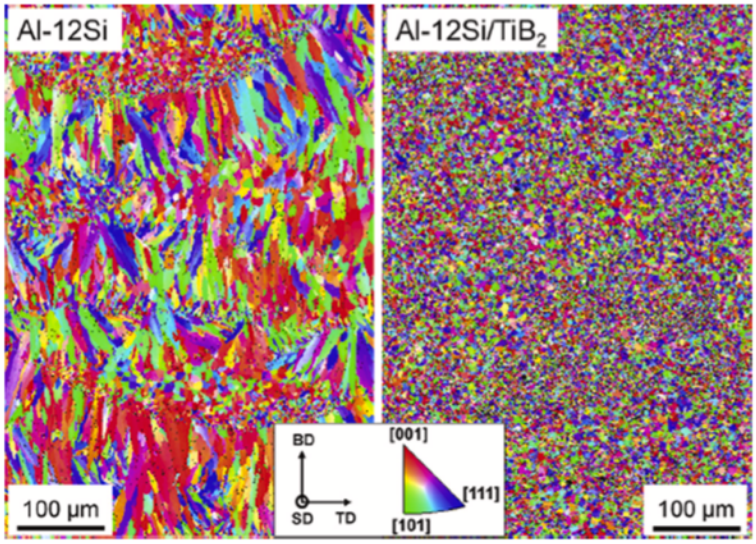

a b

Figure 1.15: EBSD results of an AlSi12 alloy processed with LPBF: a) un-modified alloys showing epitaxial grain growth; b) alloy modified with TiB_2 showing fine equiaxed grains [21].

1.2.3 Fine sub-structure within grains

Inside epitaxial grains a sub-structure is formed and can present different solidification structures, as evidenced also by Figures 1.13c and 1.14a. In case of metal alloys, that represent the focus of experimental analyses discussed in this dissertation, heat extraction and constitutional undercooling determine solidification structure. The constitutional undercooling is due to the different composition of solid and liquid phase and it is schematically represented in Figure 1.16a. During solidification, solute is rejected into the liquid phase leading to a concentration gradient (C_L) at the solid-liquid interface represented by orange curve in the Figure, accordingly, the liquidus equilibrium solidification temperature (T_L) is reduced, as represented by green curve in the same Figure. Based on the extent of heat extraction, that determines the slope of the T_A blue line, an area of constitutional undercooling is defined, in which the liquid phase survives below the solidification temperature. As represented in Figure 1.16b, the extent of such area determines solidification structure, passing from planar to

cellular to columnar and equiaxed dendritic, with increasing constitutional undercooling.

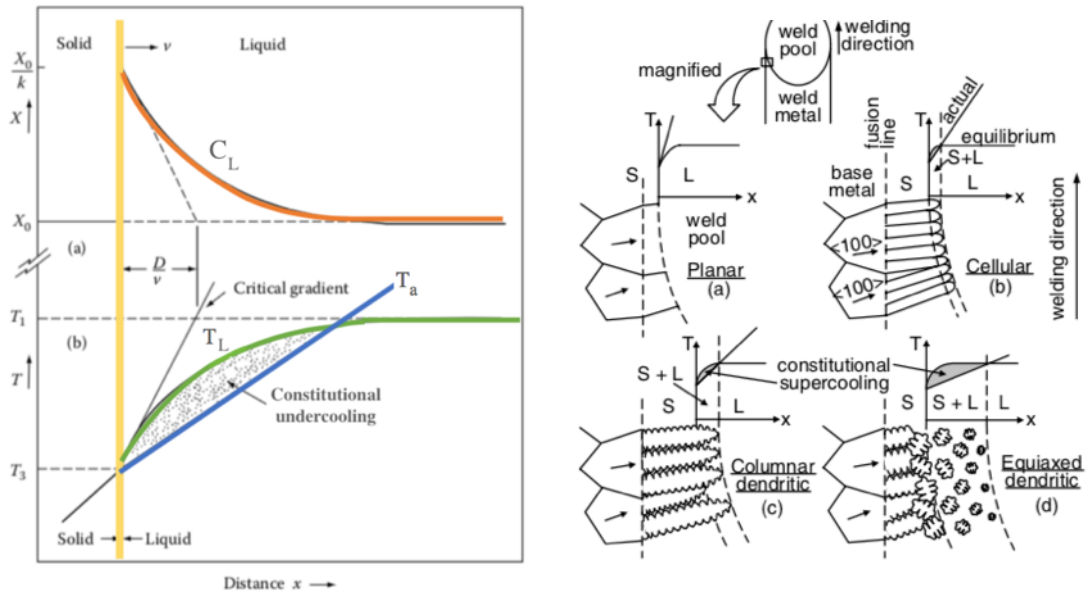

a b

Figure 1.16: Constitutional supercooling: a) definition (adapted from [30]), b) effect of on grain morphology [19].

Mathematically, constitutional undercooling condition is given by:

$$\frac{dT_a}{dx} < \frac{dT_L}{dx} \tag{6}$$

The term $\frac{dT_L}{dx}$ can be determined on the basis of the solute concentration gradient $\frac{dC_L}{dx}$, while $\frac{dT_a}{dx}$ is also known as temperature gradient G and it is determined by the manufacturing process and, specifically, by the extent of heat extraction.

At the solid-liquid interface two fluxes occur: the one due to the solute rejection by the solid, and the one due to the flux of solute in the liquid. At steady state, these two fluxes are balanced and, assuming a linear gradient into the liquid, the relation can be written as [22]:

$$R\,(C_L - C_o) = -D_L\left(\frac{dC_L}{dx}\right) \tag{7}$$

Where, in Equation 6:

R represents the solid-liquid interface growth

C_L is the liquid composition in the solid-liquid interface

C_0 is the nominal alloy composition

D_L is the solute diffusivity in the liquid

In case of phase diagram with a linear liquidus line, $\frac{dC_L}{dx}$ produces a corresponding $\frac{dT_L}{dx}$ given by:

$$\frac{dT_L}{dx} = m_L\left(\frac{dC_L}{dx}\right) \tag{8}$$

Where m_L is the liquidus line slope.

By combining equations from 6 to 8, the constitutional undercooling is given by [22]:

$$\frac{dT_a}{dx} = -\frac{Rm_L\,(C_L - C_0)}{D_L}$$

or (9)

$$\frac{G}{R} = -\frac{m_L\,(C_L - C_0)}{D_L}$$

According to Equation 9, the constitutional undercooling is determined by G and R, also known as solidification parameters, and by alloy composition. As represented in Figure 1.17a, the equation can be graphically represented and a more detailed version, reported in Figure 1.17b, is usually used to determine the solidification microstructure. The ratio G/R determines the morphology of solidification structure (cellular, columnar-dendritic and equiaxed dendritic)

while the product GR, that corresponds to the cooling rate, determines size of solidification structure.

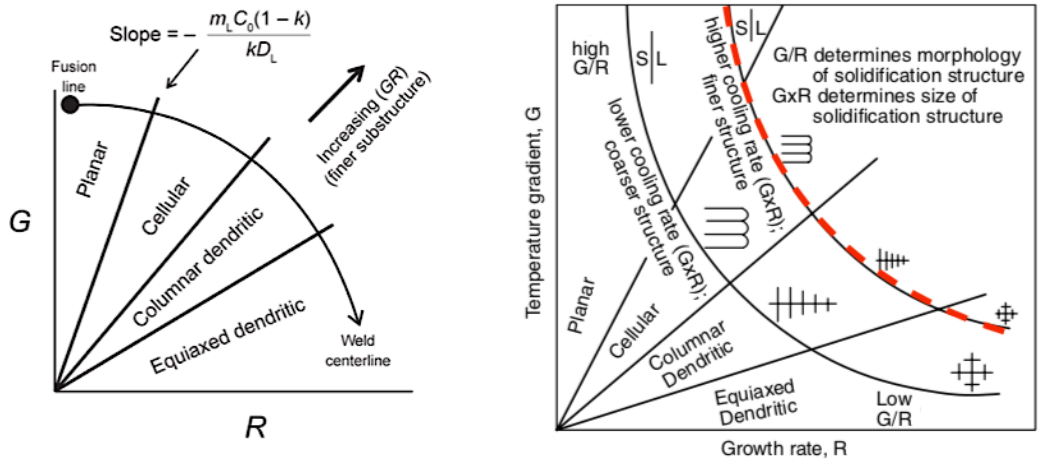

a b

Figure 1.17: Effect of temperature gradient G and solidification rate R on grain size and morphology: a) schematic representation, b) more detailed scheme (adapted from [19,22]).

Additive manufacturing technologies usually result in a very fine microstructure, being characterized by high cooling rates (GR), in the range 10^5-10^6 K s^{-1} in case of laser-based powder bed fusion [4,7], above the region defined by the red dashed line in Figure 1.17b. As will be more thoughtfully discussed in next sections, this very fine microstructure along with solid solution strengthening are responsible for the elevated mechanical properties often exhibited by additively manufactured components.

It should be noticed that the ratio G/R decreases from the fusion line towards the centerline of the weld or melt pool. More specifically, both G and R change continuously in the solid-liquid interface, as it is usually observed in conventional welding processes. As represented in Figure 1.18a, G is high in correspondence of region in direct contact with cold metal and small at the centerline of the melt pool. R instead varies as a function of the scanning speed (S in Figure 1.18b). Based on Figure 1.17b, the growth rate of the solid-liquid interface is given by:

$$R = \frac{S \cos\alpha}{\cos(\alpha - \beta)} \tag{10}$$

Where, in Equation 10:

S is the scanning or deposition speed

α is the angle between the scanning speed direction and the normal to the solid-liquid interface

β is the angle between the scanning speed direction and the [100] easy-growth direction for a cubic metal

In many cases, the term (α- β) is very small, thus it can be considered:

$$(\alpha - \beta) \simeq 0 \rightarrow \cos(\alpha - \beta) \simeq 1$$

and (11)

$$R = S \cos\alpha$$

Consequently, at the fusion line or melt pool border, where α=90°, R is equal to zero while at the centerline of the fusion zone it is α=0, thus R ≃ S.

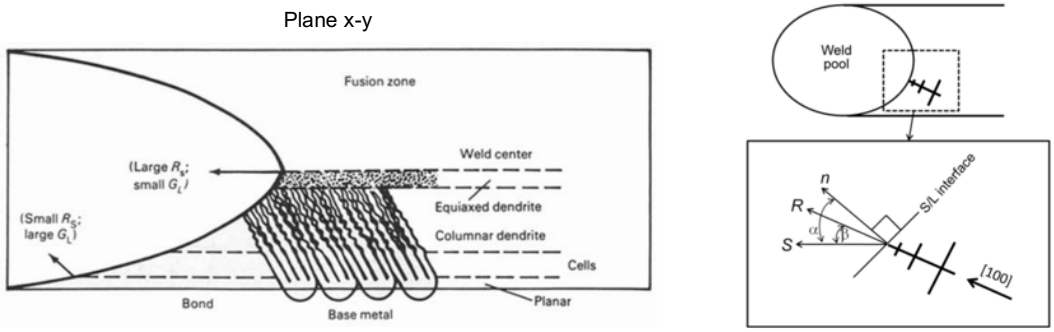

a b

Figure 1.18: Variation in grain morphology across the melt pool as consequence of the variation of G/R ratio (a); Geometric relation between growth rate R and the scanning speed S (b) [22].

Accordingly, with decreasing of the ratio G/R from the melt pool border to the center of the melt pool, the microstructure can change across the solidified melt pool from cellular to equiaxed morphology, as illustrated in Figure 1.18a. The transition between columnar and equiaxed grains is usually referred to as the

columnar-to-equiaxed transition (CET) and it has been observed also in some AM products [31].

In the experimental sections of the present dissertation, the specific sub-structure resulting from LPBF and WAAM process will be further discussed. Outcomes will show that in case of LPBF the studied alloys resulted in a peculiar cellular substructure while, in case of WAAM, a columnar-dendritic one was evidenced. The theory on the basis of the formation of the peculiar cellular structure of LPBF alloys in hereafter reported.

CELLULAR SOLIDIFICATION STRUCTURE

In the LPBF of most metal alloys, and in particular for the Co-Cr-Mo and Al-Si systems investigated in the present dissertation, the formation of an extremely fine cellular solidification structure inside melt pools was evidenced, with segregation of alloy element in correspondence of cell borders (Figure 1.19).

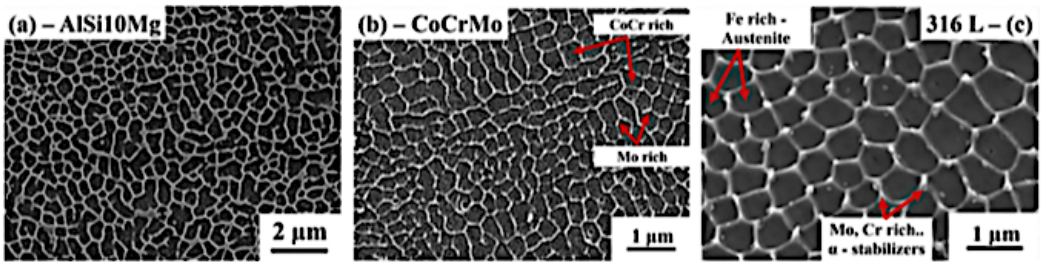

Figure 1.19: Cellular microstructure formed in the AlSi10Mg, Co28Cr6Mo and AISI 316L alloys processed by LPBF [32].

The development of such metastable cellular structure was investigated by Prashanth and Eckert [32]. As discussed by the authors [32], the above reported constitutional undercooling theory, that describes thermodynamical aspects involved in the determination of solidification morphology (ratio G/R), is not sufficient enough to explain the formation of cellular structure in LPBF. Actually, also kinetical and physical aspects should be taken into consideration. Kinetical aspects are determined by the velocity of solidification front and solute trapping occurring at the solid-liquid interface. Physical aspects are instead related to the

complex convective flow occurring inside melt pools (mainly Marangoni flow, as discussed in Section 1.2.1) that may cause solute accumulation along cell boundaries. In fact, surface tension gradients may lead to the formation of two different mechanisms: the Bernard Marangoni Surface Instability (BMI instability) and Particle Accumulated Structure mechanism (PAS mechanism). BMI and PAS involve several aspects (thermal gradients, grain growth rates, surface instability, mass transport and surface tension effects) and can be responsible for the formation of the metastable cellular structure with a distinct composition in the core of cells and along cell borders.

The formation of cellular microstructure can be explained according to Figure 1.20. The high cooling rates promote the solidification of the low-melting phase that, due to favorable kinetic conditions, solidifies first and entraps solute. In fact, as observed by several authors high cooling rates extend solid solubility of alloy elements and solute trapping might occur [4]. Concurrently, high melting-point alloy elements are ejected into the liquid phase, that become rich in solute, and eventually they are deposited along cell borders due to PAS mechanism [32]. As a result, the solidification of the metastable cellular microstructures is rather kinetically favored than thermodynamically.

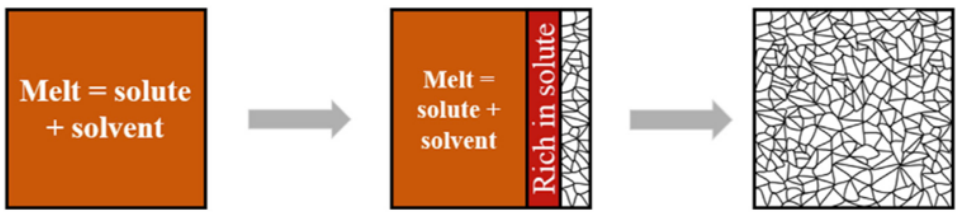

Figure 1.20: Schematic illustration of cellular structure formation in LPBF [32].

However, cellular structure is not observed in all LPBF metal alloys. Inconel and Ti alloys, for example, do not form a cellular structure since no solute atoms are ejected into the liquid at the solid-liquid interface [32].

Therefore, Prashanth and Eckert formulated the following criteria to be fulfilled for the formation of a cellular microstructure:

- A binary system is preferred, or a system that result in the formation of two phases.

- The solutes are immiscible with the solvent, or have a negligible solubility at the solid state.
- Melting temperature of the solutes must be higher than those of the solvent (the difference in the melting point should be higher than 673 K).

1.2.4 Thermal cycles

In additive manufacturing, melt pool are continuously formed during the processing of the layer and repeated for each consecutive layer. As a consequence, each solidified layer is re-heated and partially melted by the consecutive one, resulting in complex, uncontrolled, and repeated thermal cycles in the component, similarly to the conventional multi-pass welding (Figure 1.21a) [21]. Thermal gradients formed along melt pool develop localized and non-uniform expansion and consecutive contraction of the metal material, that can eventually result in residual stress. If the internal residual stress, compressive or tensile, locally overcomes the yield or ultimate strength of the material, deformations, distortions, and cracks might be developed. Residual stress characterizes additively manufactured components, to the extent that stress-relieving treatments are commonly applied as post-process treatments. Higher energy input technologies, as laser-based ones, develop higher residual stress, especially in case of powder bed fusion in which the energy is not uniformly introduced in the material due to the laser-beam interaction that will be later discussed.

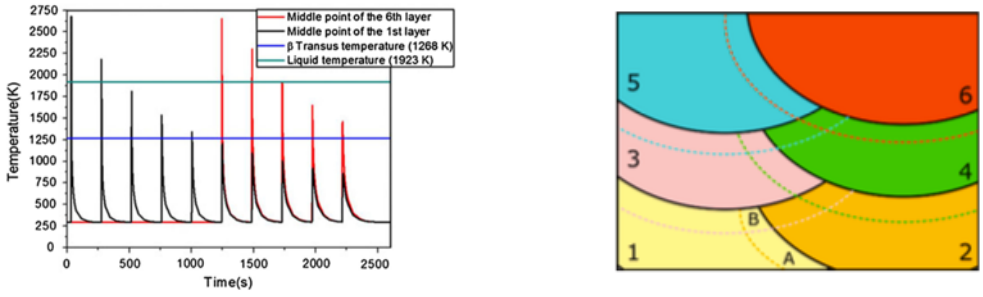

a b

Figure 1.21: Representative thermal cycles evaluated for the WAAM Ti6Al4V (a), subsequent solidified melt pools where heat-affected zones are indicated by dashed lines (b) [21,33]

It should be also considered that residual stress might be formed as a consequence of solid-state transformation due to re-heating. Indeed, by referring to Figure 1.21b, the microstructure in the proximity of the border of solidified melt pool can be re-heated once (zone *A*) or more than once (zone *B*) depending on the complexity of the deposition or scanning strategy. In the heat-affected zones, changes in the morphology of the microstructure, precipitation of second phases or solid-state phase transformations might occur. The actual quantity of heat introduced in the material is primarily function of the process parameter but it is also influenced by material-related aspects such thermal conductivity, specific heat and latent heat of melting. It is a common practice to quantify the energy input with linear, superficial and volumetric energy density (Table 1.2) [21]. However, it should be also mentioned that other process parameters, not considered in the energy density formula like scanning or deposition strategy and substrate platform pre-heating, might considerably affect thermal cycles and thus residual stress extent.

In the literature [8], the energy density has been also positively related to many macro and microstructural defects and features, as depicted in Figure 1.22. However, it should be noticed that energy density parameters are not sufficient enough to describe and control the whole process [34,35]. Its limitations are mainly related on the thermodynamic origin of these notations, that cannot consider all the complex physical phenomena related to the Marangoni flow and interaction between laser beam feedstock, as will be later described. In addition, as energy density depends on many process parameters, the same value can be obtained with several combination of parameters themselves, leading to different microstructural features. However, as will be further discussed in the experimental sections, energy density is still considered a reliable parameter in process optimization, specifically in the preliminary densification process where it has been proved to be positively related to final density and porosity content [36–39].

Table 1.2: Equations currently used for the definition of the energy/power input as a function of: laser power (P, W), hatch distance (h, mm), layer thickness (d, mm), speed (v, mm s^{-1}), laser spot diameter (dlaser, mm), laser/material interaction time (tint, s), track width (dt, mm), relative density of the powder bed (ρ_{bed}, a.u.), overlap distance (o, mm), powder feed rate (R, g min^{-1}), mean dimension of the feedstock material (gs, mm) and diameter of the heat source (dheatsource, mm). Adapted from [21].

Designation	***Unit of measure***	***Formula***
Linear heat input	J mm^{-1}	$LHI = \frac{P}{v}$
Effective energy density per unit of area	J mm^{-2}	$E_{eff} = \frac{P}{v\, d_{laser}}$
Energy density or volumetric fluency	J mm^{-3}	$F = \frac{t_{int}\, P}{h\, d\, o}$
Energy density	J mm^{-3}	$ED = \frac{P}{v\, h\, d}$ $ED = \frac{P}{\rho_{bed} d_{laser}\, h\, d}$ $ED = \frac{P}{\rho_{bed} d_{laser}\, h\, d}\ (2 - \frac{h}{d_t})$
Powder deposition density	g mm^{-2}	$PDD = \frac{R}{v\, d_{laser}}$
Dimensionless energy density	-	$ED = \beta \frac{P}{v\, h\, d}$ where $\beta = \frac{g_s}{d_{heat\ source}}$

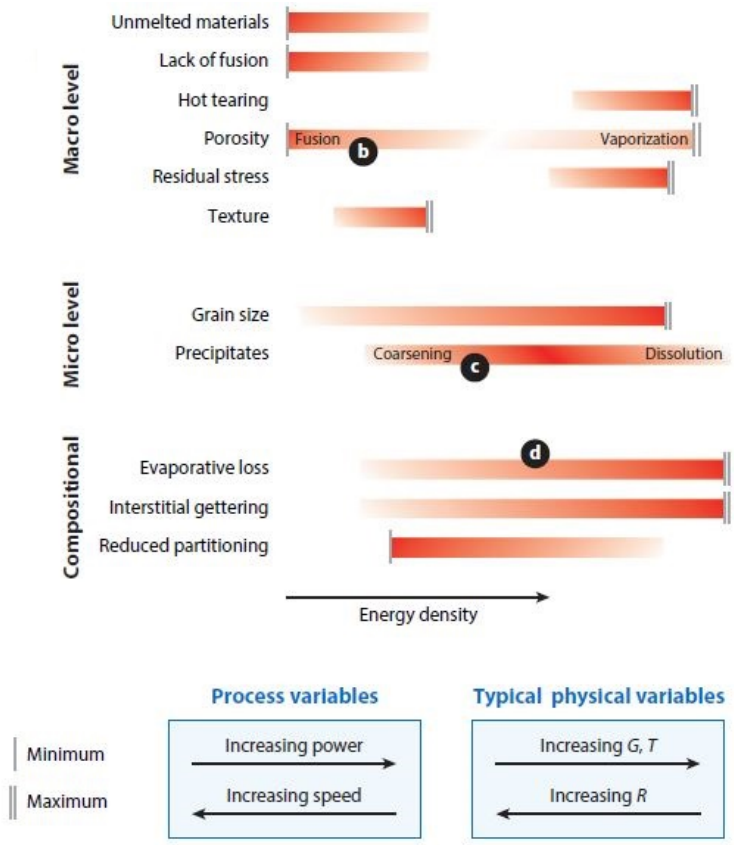

Figure 1.22: Effect of energy density on macro and microlevel microstructural features and variation in the chemical composition [8].

1.2.5 Defects

Additively manufactured parts are characterized by peculiar microstructural discontinuities, or defects. Defects will be thoughtfully investigated in the next sections regarding the experimental activities and can be synthetized as follows [4,7,8]:

- Porosity
    - Process-induced porosity due to both incomplete melting and keyhole phenomena. Incomplete melting, often termed lack of fusion, appears as an irregular cavity formed due to insufficient energy, in which un-melted material can be also observed. Keyhole phenomenon is usually observed when the power or energy density

is to elevated and a change in the heat exchange mode from conduction to keyhole occurs. As a result, gas might be entrapped into the melt pool.

  - Gas-induced porosity, usually present as micro (10-20 μm) spherical porosity and due to gas trapped into the melt pool or consequent to vaporization of one or more alloying elements. In powder bed fusion, gas porosity can be also due to the porosity content in the feedstock powders

- Cracking
  - Macroscopic cracks nucleated in correspondence of a macroscopic defects in the material or due to delamination (separation between two layers due to incomplete melting).
  - Microscopic, divided in solidification cracking and liquation cracking. Solidification cracking occurs along grain boundaries and it is related to the different contraction during cooling experienced by the latest layer and the previously deposited one. The upper layer will contract due to both thermal contraction and solidification shrinkage, the lower one, that experienced a lower temperature, will contract to a lesser extent. Consequently, a tensile stress is generated and, if it exceeds the strength of the material, a crack can be originated. Liquation cracking is observed in the partially melted zone where, upon re-heating due to the deposition of subsequent layer, the undesired melting of low-melting phases at grain boundaries occurs. During cooling and relative contraction, the liquid film can act as site for crack initiation. The alloys characterized by a large solidification range, solidification contraction, or thermal contraction are more prone to liquation cracking.

- Spatters are defined as portions of molten material ejected from the melt pool that can be recognized as large globular particles landed on the surface or on the processing layer. They are due to the interaction between the

material and the thermal source and can be limited by a proper protection of the pool carried out by the shielding gas.

- Balling that, as already discussed, is related to the surface tension and it is present as spherical particles that arise from the surface of the layer.

Most of the above-mentioned defects are related to the production process. Indeed, as will be analyzed in the following experimental sections, they can be minimized or limited by optimizing the process parameters. Others are, indeed, material-related and can be limited by a modification in the chemical composition as, for example, the addition of grain-refiners or alloying element that reduce the solidification range [21].

SURFACE QUALITY

Microstructural defects affect also the surface quality of additively produced metallic parts. In fact, surface finishing of AM parts is usually poor. According to Debroy et al. [4], causes for poor surface quality can be synthetized in: i) stair step effect, due to the layer-wise approach that leads to the approximation of curved and inclined surfaces (Figure 1.23a); ii) surface roughness caused by improper melting, spattering and balling phenomenon, as also evidenced by [40] (Figure 1.23b). While the first aspect is strongly related to process parameters such as layer thickness and building directions, the latter one is more related to typical defects of AM described in the previous paragraph, especially balling and spattering phenomena. In this view, as will be later discussed, WAAM is usually characterized by a poor surface quality mainly due to the large layer thickness adopted, while LPBF is mainly affected by partially melted powder adherent to later surfaces. Spattering phenomena, instead, can results from both technologies and spattering particles can adhere to the surface of produced parts, as showed in Figure 1.23b in case of LPBF.

a

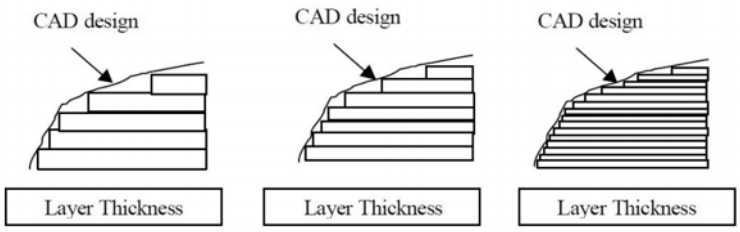

b

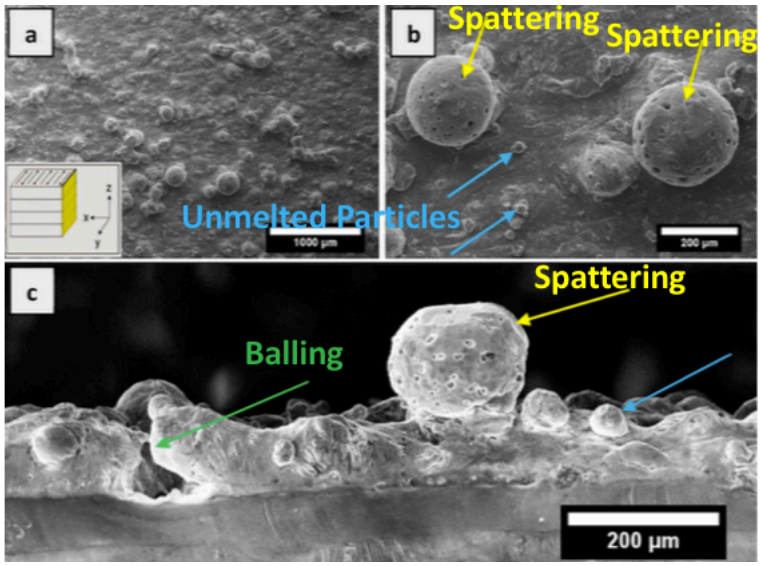

Figure 1.23: Principal aspects influencing the surface quality of AM parts: a) stair-step effect [41]; b) spattering, balling and un-melted particles on LPBF part surfaces [40].

Surface quality of AM parts will be further explored in the following Chapter concerning experimental analyses. Process parameters can, to some extent, be optimized to improve the surface quality of the final components. WAAM and LPBF as-built surface quality will be analyzed and discussed However, up to now, a post process surface treatment is usually employed, as also highlighted by this very recent review [42].

1.3 Peculiar aspects of LPBF

When considering the additive process based on powder bed fusion by means of a laser beam, a few more aspects related to the feedstock material and their interaction with the laser beam have to be considered, as discussed in the following sections.

1.3.1 Feedstock powder properties

Powder used as feedstock materials in LPBF technologies must fulfil peculiar characteristics and several aspects must be considered, such as:

- Chemical composition complying with requirements.
- Normal particle size distribution between 10 and 60 μm.
- Spherical shape.
- Smooth surface and without satellites.
- Absence of internal porosity.

Shape, morphology and particle size distributions directly affects the following properties that determine the proper distribution of an even powder bed:

- Flowability
- Density
    - Apparent (mass per unit volume naturally occupied by particles)
    - Tap (mass per unit volume occupied by tapped particles)

Flowability is favored by spherical and smooth particles and a high flowability promote the even distribution of the powder bad. Spherical and smooth particles contribute also to promote the packaging density of the powder bed. Packaging density of the powder bed is crucial in order to obtain full density parts and, as shown in Figure 1.24, it is also strongly dependent on the particles size distribution. Indeed, a normal distribution of particles size (Figure 1.24a) with and adequate balance between small and large particles improve the filling of the entire volume of the deposited layer (Figure 1.24b).

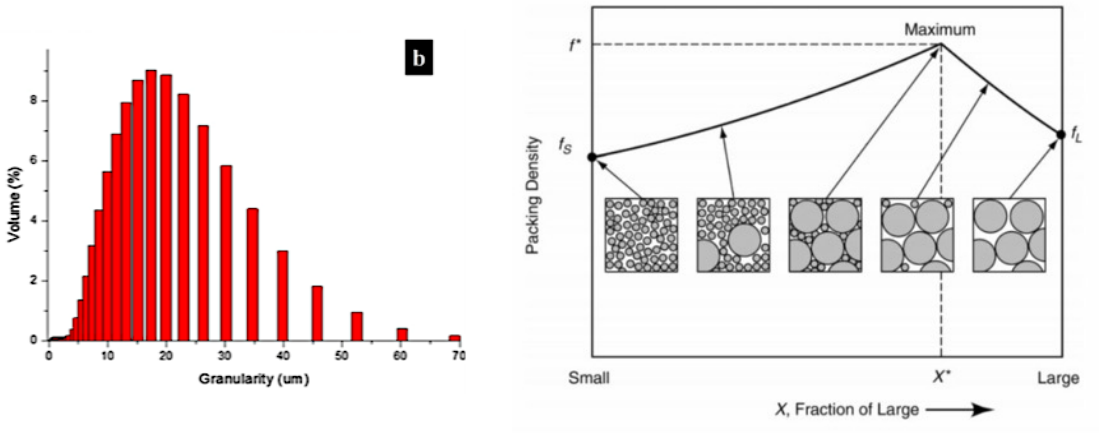

a b

Figure 1.24: Typical particle size distribution (a), influence of particle size distribution on packing density of the layer (b) [6,43].

Consequently, powders for LPBF are usually obtained via gas and plasma atomization, that can guarantee a proper control of shape and morphology [43]. In Figure 1.25 powder obtained via gas atomization (GA) and plasma rotating electrode process (PREP) are compared. Ideal spherical and smooth powder can be obtained via PREP, while a few defects can usually be found in GA powder, such satellites and internal pores. However, GA is a more versatile and economic process that can be applied to several metallic material while PREP is expensive and dedicated to specific material, such Ti-alloys.

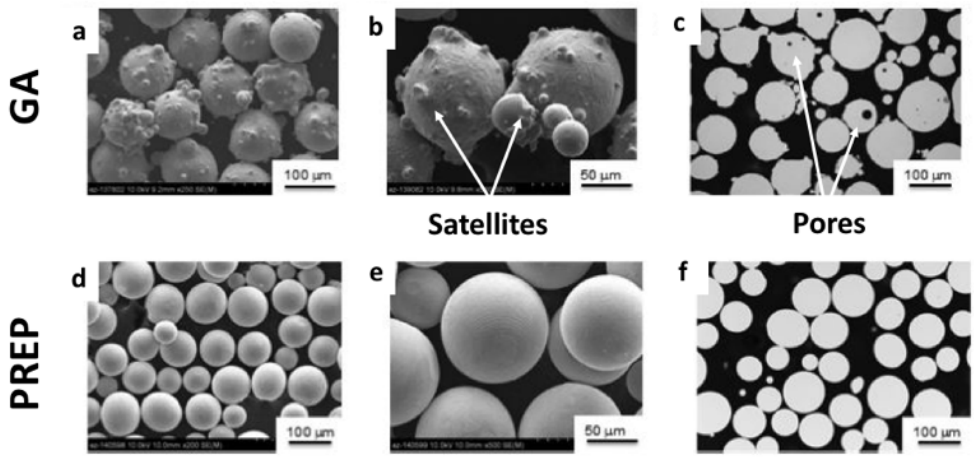

Figure 1.25: Comparison between powder obtained with gas atomization (a, b, c) and plasma rotating electrode process (d, e, f). Free powder and powder cross-section. Adapted from [7].

According to Hebert [44], properties of the feedstock material directly influence the quality of the powder bed and the process of heating and melting of powder, as already discussed in Section 1.1.1. Subsequently, also physical properties like melting and boiling temperature, thermal conductivity, heat capacity, latent heat of fusion, have to be taken into consideration. In addition, also the possible superficial oxidation and moisture absorption should be avoided and storage conditions should be properly controlled. All these aspects will be addressed in the following sections regarding the experimental activities carried out during the PhD course.

1.3.2 Powder-beam interaction

Prior to melting and solidification, several physical-chemical phenomena are involved in the interaction between laser beam and powder bed, that are addressed in the current section.

ABSORPTIVITY OF METALS POWDERS

Metallic powder particles are highly reflective and, as a consequence, LPBF technologies are considered as highly inefficient processes since only a small portion of the irradiance of the incoming beam is absorbed by the powder bed. As illustrated in Figure 1.26a, when the laser beam approaches the powder layer, scattering of rays occurs, leading to a power-loss. Concurrently, scattering of rays occurs also between metallic particles, as schematized in Figure 1.26b; this phenomenon is called multiple scattering and enhances the efficiency of LPBF, especially in case of highly reflective metals, such as Au, Al and Cu.

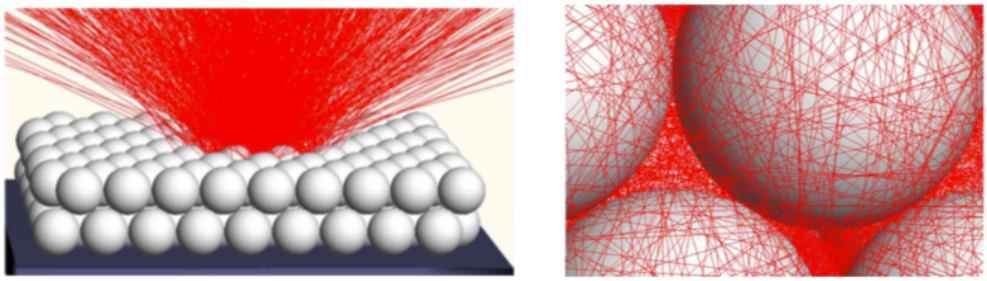

a b

Figure 1.26: Interaction between laser beam and powder bed: a) scattering of the incoming beam, b) multiple scattering between powder particles [45]

Consequently, the absorptivity of a single powder particle (ideally a sphere) is quite different from the absorptivity of a layer of powder; moreover, the absorptivity of a flat surface differs from the absorptivity of a layer of powder. Hence, when processing a layer of the powder bed, the total absorptance to be considered is the result of the system powder layer-solid substrate (i.e. the previously processed layer, melted and rapidly solidified). Boley et al. [45] performed a calculation of laser absorption by metal powder particles in additive manufacturing in case of a simplified powder layer consisting of spherical and smooths powders of identical size, closely packed. In their study, they considered the absorptivity of a single powder particle, a layer of powder and the system layer plus substrate. Referring to Table 1.3, the most important parameter in LPBF technologies is the total absorptivity by spheres and substrate, reported in column 9, noticeably higher than the one of an isolated sphere (column 5) or a flat surface (column 4). As mentioned before, the enhancement is due to the multiple scattering phenomena, crucial in the case of highly reflective material, as remarked by the relative absorptivity reported in column 10. By analysing data summarized in Table 1.3, it is possible to deduce that materials like stainless steels or titanium alloys are more easily processable than aluminium or copper. In addition, it is evident that most of the power is absorbed by the top of the powder layer (column 6), and only a small portion of it reaches the substrate (column 8) or even the bottom of the layer (column 7).

Table 1.3: Absorption measurements for several metallic material [45]

(1) Material	(2) Re(n)	(3) Im(n)	(4) α (Flat Surface)	(5) α (Isolated Sphere)	(6) α (Top Layer)	(7) α (Bottom Layer)	(8) α (Substrate)	(9) α (Spheres + Substrate)	(10) α (Spheres + Substrate)/α (Flat Surface)
Ag	0.23	7.09	0.018	0.020	0.072	.047	0.010	0.13	7.2
Al	1.244	10.	0.047	0.056	0.15	0.063	0.011	0.22	4.7
Au	0.278	7.20	0.021	0.024	0.081	0.050	0.011	0.14	6.7
Cu	0.35	6.97	0.028	0.032	0.101	0.055	0.011	0.17	6.1
SS	3.27	4.48	0.34	0.36	0.53	0.062	0.013	0.60	1.7
Ti	3.45	4.	0.38	0.40	0.56	0.062	0.014	0.64	1.7

*α denotes the absorptivity.

However, the actual powder morphology can be far from spherical and the spatial distribution of powder in the layer can be un-optimized, leaving voids. Size and spatial distribution of powder can lead to fluctuation in the total absorptivity, along with rough and oxidized powders surfaces [46,47]. Fluctuations can be almost negligible for moderately reflective metals, such as stainless steels, but become substantial for highly reflective ones, where size, morphology and distribution of the powders particles affects the multiple scattering phenomenon. Moreover, the absorptivity is also sensitive to the layer thickness and to the wavelength, diameter and distance of the laser beam, especially if its size is comparable to the particles one [33,45,48]. The dependence of the absorptivity from the wavelength of the laser beam is illustrated in Figure 1.27: most of the commercially available SLM machines works with laser source with a wavelength close to 1 µm (e.g. YAG:Nd), while CO_2 laser have a wavelength close to 10 µm.

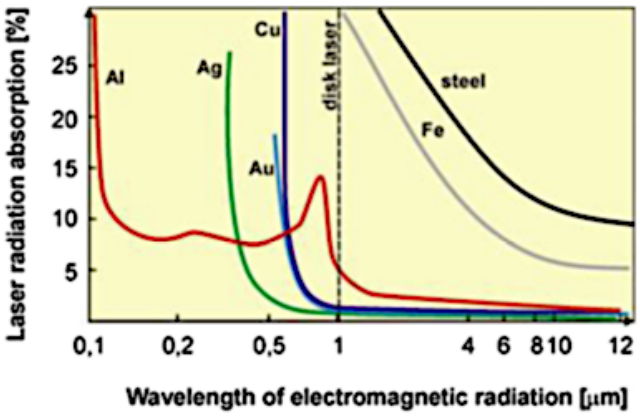

Figure 1.27: Laser radiation absorption of several metallic materials as a function of wavelength [33]

The absorptivity of metal increases with temperature [49]. Thus, during the heating and subsequent melting of powders the response to the incoming laser beam changes. In addition, during the process, part of the laser beam can be trapped by the complex phenomena generated, such as the vapor plume that will be discussed in the following paragraph. Measurements of the in-situ absorptivity of metallic powder during LPBF was performed by Trapp et al. [50] for the AISI 316L steel considering both the case of a flat disc and the powder-substrate system. Results are represented in Figure 1.28a: in the case of flat surface, absorptivity depends both on the laser power and on the scanning velocity and, for high power regime, reaches a saturation. By comparing the behavior of the flat disc with the one exhibited by the disc covered by a layer of powder (Figure 1.28b,c) it can be noticed that a low laser power regime the absorptivity of the powder is higher than the flat disc, in the reason of the previously discussed multi-scattering phenomenon. Then, when melting of the powders occurs, the absorptivity decreases rapidly and, by increasing the power, absorptivity raises again reaching the saturation level (approx. 0.6). In case of high scanning velocity, the absorptivity of the powders is higher than the one of the flat disc, and vice versa in case of low scanning velocity. The absorptivity at high power and high velocity is strongly related to the transition of the heat transfer from the conductive to the keyhole mode and to the vapor plume formed.

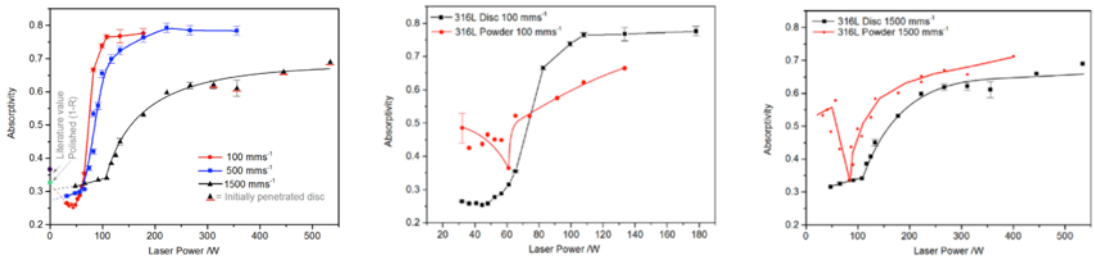

a b c

Figure 1.28: Absorptivity measurement on AISI 316L: a) flat surface, b) and c) comparison between flat surface and powder [50].

SPATTER AND DENUDATION

As schematized in Figure 1.29, as a consequence of the interaction between the laser beam and the powder bed, a laser-induced vapor plume is formed [51,52].

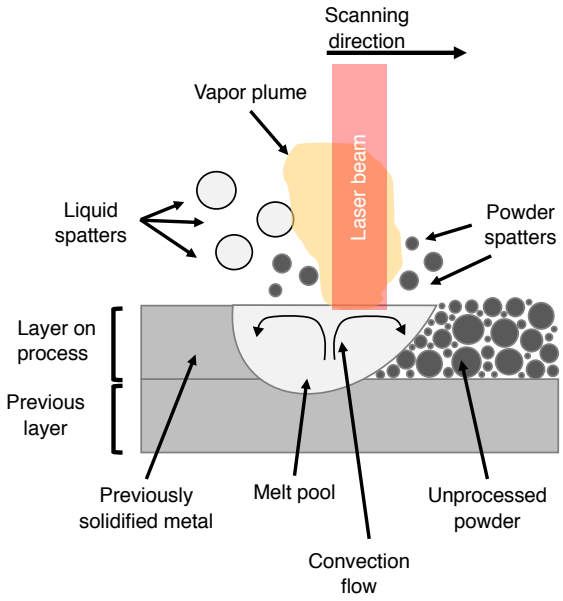

Figure 1.29: Schematic representation of the laser-beam interaction effects in LPBF

The vapor plume is the result of the combination of metal vapor and plasma generated above the melt pool. The vapor plume applies a recoil pressure on the melt pool and tends to eject metallic material away from the fusion zone, this phenomenon is known as spattering. As depicted in Figure 1.29, the material ejected can be in form of liquid (liquid spatters) of in form of powder (powder spatters). Driving forces of the dynamics of the melting process are the previously discussed Marangoni convection and the recoil pressure caused by the laser plume [51]. Indeed, while the Marangoni convection tends to evenly spread the molten material, the inward flow generated by the recoil pressure tends to eject the molten material away from the liquid pool. The balance between these two forces governs the stability of the molten pool and dynamics of solidification process. Another issue related to the laser-beam interaction is denudation that is defined as a depleting of powders in the regions surrounding laser tracks as a consequence of the recoil pressure [53]. Recent work focused on the analyses of the dynamics of fluid and particles [51,52] evidenced that laser power and scanning velocity have a major role in determining the extent of the vapor plume.

References

[1] EN ISO/ASTM 52900 Additive manufacturing — General principles — Terminology, (2015).

[2] Y. Zhang, L. Wu, X. Guo, S. Kane, Y. Deng, Y. Jung, J. Lee, J. Zhang, Additive Manufacturing of Metallic Materials : A Review, J. Mater. Eng. Perform. 27 (2018) 1–13. doi:10.1007/s11665-017-2747-y.

[3] A. Paolini, S. Kollmannsberger, E. Rank, Additive manufacturing in construction: A review on processes, applications, and digital planning methods, Addit. Manuf. 30 (2019) 100894. doi:10.1016/j.addma.2019.100894.

[4] T. DebRoy, H.L. Wei, J.S. Zuback, T. Mukherjee, J.W. Elmer, J.O. Milewski, A.M. Beese, A. Wilson-Heid, A. De, W. Zhang, Additive manufacturing of metallic components – Process, structure and properties, Prog. Mater. Sci. 92 (2018) 112–224. doi:10.1016/j.pmatsci.2017.10.001.

[5] T.G. Spears, S.A. Gold, In-process sensing in selective laser melting (SLM) additive manufacturing, Integr. Mater. Manuf. Innov. 5 (2016) 16–40. doi:10.1186/s40192-016-0045-4.

[6] C.Y. Yap, C.K. Chua, Z.L. Dong, Z.H. Liu, D.Q. Zhang, L.E. Loh, S.L. Sing, Review of selective laser melting: Materials and applications, Appl. Phys. Rev. 2 (2015) 041101–21. doi:10.1063/1.4935926.

[7] W.J. Sames, F.A. List, S. Pannala, R.R. Dehoff, S.S. Babu, The metallurgy and processing science of metal additive manufacturing, Int. Mater. Rev. 6608 (2016) 1–46. doi:10.1080/09506608.2015.1116649.

[8] P.C. Collins, D.A. Brice, P. Samimi, I. Ghamarian, H.L. Fraser, Microstructural Control of Additively Manufactured Metallic Materials, Annu. Rev. Mater. Res. 46 (2016) 63–91. doi:10.1146/annurev-matsci-070115-031816.

[9] B. Wu, Z. Pan, D. Ding, D. Cuiuri, H. Li, J. Xu, J. Norrish, A review of the wire arc additive manufacturing of metals: properties, defects and quality improvement, J. Manuf. Process. (2018). doi:10.1016/j.jmapro.2018.08.001.

[10] T.A. Rodrigues, V. Duarte, R.M. Miranda, T.G. Santos, J.P. Oliveira, Current status and perspectives on wire and arc additive manufacturing (WAAM), Materials (Basel). 12 (2019). doi:10.3390/ma12071121.

[11] S.W. Williams, F. Martina, A.C. Addison, J. Ding, G. Pardal, P. Colegrove, Wire + Arc additive manufacturing, Mater. Sci. Technol. (United Kingdom). 32 (2016) 641–647. doi:10.1179/1743284715Y.0000000073.

[12] C. Buchanan, L. Gardner, Metal 3D printing in construction: A review of methods, research, applications, opportunities and challenges, Eng. Struct. 180 (2019) 332–348. doi:10.1016/j.engstruct.2018.11.045.

[13] C.R. Cunningham, J.M. Flynn, A. Shokrani, V. Dhokia, S.T. Newman, Invited review article: Strategies and processes for high quality wire arc additive

manufacturing, Addit. Manuf. 22 (2018) 672–686. doi:10.1016/j.addma.2018.06.020.

[14] S. Kou, Fluid Flow and Metal Evaporation in Welding, in: Weld. Metall., Second edi, John Wiley & Sons, Hoboken, New Jersey, 2003: pp. 97–122.

[15] L. Aucott, H. Dong, W. Mirihanage, R. Atwood, A. Kidess, S. Gao, S. Wen, J. Marsden, S. Feng, M. Tong, T. Connolley, M. Drakopoulos, C.R. Kleijn, I.M. Richardson, D.J. Browne, R.H. Mathiesen, H. V. Atkinson, Revealing internal flow behaviour in arc welding and additive manufacturing of metals, Nat. Commun. 9 (2018) 1–7. doi:10.1038/s41467-018-07900-9.

[16] T. Mukherjee, H.L. Wei, A. De, T. DebRoy, Heat and fluid flow in additive manufacturing—Part I: Modeling of powder bed fusion, Comput. Mater. Sci. 150 (2018) 304–313. doi:10.1016/j.commatsci.2018.04.022.

[17] S.A. Khairallah, A.T. Anderson, A. Rubenchik, W.E. King, Laser powder-bed fusion additive manufacturing: Physics of complex melt flow and formation mechanisms of pores, spatter, and denudation zones, Acta Mater. 108 (2016) 36–45. doi:10.1016/j.actamat.2016.02.014.

[18] X. Zhou, X. Liu, D. Zhang, Z. Shen, W. Liu, Balling phenomena in selective laser melted tungsten, J. Mater. Process. Technol. 222 (2015) 33–42. doi:10.1016/j.jmatprotec.2015.02.032.

[19] S. Kou, The Fusion Zone, in: Weld. Metall., Second Edi, John Wiley & Sons, Hoboken, New Jersey, 2003: pp. 143–300.

[20] A. Basak, S. Das, Epitaxy and Microstructure Evolution in Metal Additive Manufacturing, Annu. Rev. Mater. Res. 46 (2016) 125–149. doi:10.1146/annurev-matsci-070115-031728.

[21] J.P. Oliveira, T.G. Santos, R.M. Miranda, Revisiting fundamental welding concepts to improve additive manufacturing: From theory to practice, Prog. Mater. Sci. 107 (2020) 100590. doi:10.1016/j.pmatsci.2019.100590.

[22] J.N. DuPont, Fundamentals of Weld Solidification, in: T. Lienert, T. Siewert, S. Babu, V. Acoff (Eds.), Weld. Fundam. Process., ASM International, 2011. doi:10.31399/asm.hb.v06a.a0005609.

[23] Z.W. Chen, M.A.L. Phan, K. Darvish, Grain growth during selective laser melting of a Co–Cr–Mo alloy, J. Mater. Sci. 52 (2017) 7415–7427. doi:10.1007/s10853-017-0975-z.

[24] A. Takaichi, Suyalatu, T. Nakamoto, N. Joko, N. Nomura, Y. Tsutsumi, S. Migita, H. Doi, S. Kurosu, A. Chiba, N. Wakabayashi, Y. Igarashi, T. Hanawa, Microstructures and mechanical properties of Co-29Cr-6Mo alloy fabricated by selective laser melting process for dental applications, J. Mech. Behav. Biomed. Mater. 21 (2013) 67–76. doi:10.1016/j.jmbbm.2013.01.021.

[25] L. Wang, J. Xue, Q. Wang, Correlation between arc mode, microstructure, and mechanical properties during wire arc additive manufacturing of 316L stainless steel, Mater. Sci. Eng. A. 751 (2019) 183–190.

doi:https://doi.org/10.1016/j.msea.2019.02.078.

[26] P. Mair, L. Kaserer, J. Braun, N. Weinberger, I. Letofsky-Papst, G. Leichtfried, Microstructure and mechanical properties of a TiB2-modified Al–Cu alloy processed by laser powder-bed fusion, Mater. Sci. Eng. A. 799 (2021) 140209. doi:https://doi.org/10.1016/j.msea.2020.140209.

[27] F. Belelli, R. Casati, M. Riccio, A. Rizzi, M.Y. Kayacan, M. Vedani, Development of a Novel High-Temperature Al Alloy for Laser Powder Bed Fusion, Met. . 11 (2021). doi:10.3390/met11010035.

[28] L. Wang, Y. Suo, Z. Liang, D. Wang, Q. Wang, Effect of titanium powder on microstructure and mechanical properties of wire + arc additively manufactured Al-Mg alloy, Mater. Lett. 241 (2019) 231–234. doi:https://doi.org/10.1016/j.matlet.2019.01.117.

[29] C. Zhang, Y. Li, M. Gao, X. Zeng, Wire arc additive manufacturing of Al-6Mg alloy using variable polarity cold metal transfer arc as power source, Mater. Sci. Eng. A. 711 (2018) 415–423. doi:10.1016/j.msea.2017.11.084.

[30] D.A. Porter, K.E. Easterling, M.Y. Sherif, Phase Transformations in Metals and Alloys, Thrid Edit, Taylor & Francis, 2009.

[31] P. Liu, Z. Wang, Y. Xiao, M.F. Horstemeyer, X. Cui, L. Chen, Insight into the mechanisms of columnar to equiaxed grain transition during metallic additive manufacturing, Addit. Manuf. 26 (2019) 22–29. doi:10.1016/j.addma.2018.12.019.

[32] K.G. Prashanth, J. Eckert, Formation of metastable cellular microstructures in selective laser melted alloys, J. Alloys Compd. 707 (2017) 27–34. doi:10.1016/j.jallcom.2016.12.209.

[33] C. Galy, E. Le Guen, E. Lacoste, C. Arvieu, Main defects observed in aluminum alloy parts produced by SLM: From causes to consequences, Addit. Manuf. 22 (2018) 165–175. doi:10.1016/j.addma.2018.05.005.

[34] K.G. Prashanth, S. Scudino, T. Maity, J. Das, J. Eckert, Is the energy density a reliable parameter for materials synthesis by selective laser melting?, Mater. Res. Lett. 5 (2017) 386–390. doi:10.1080/21663831.2017.1299808.

[35] U. Scipioni Bertoli, A.J. Wolfer, M.J. Matthews, J.P.R. Delplanque, J.M. Schoenung, On the limitations of Volumetric Energy Density as a design parameter for Selective Laser Melting, Mater. Des. 113 (2017) 331–340. doi:10.1016/j.matdes.2016.10.037.

[36] T. De Terris, O. Andreau, P. Peyre, F. Adamski, I. Koutiri, C. Gorny, C. Dupuy, Optimization and comparison of porosity rate measurement methods of Selective Laser Melted metallic parts, Addit. Manuf. 28 (2019) 802–813. doi:10.1016/j.addma.2019.05.035.

[37] M. Guo, D. Gu, L. Xi, H. Zhang, J. Zhang, J. Yang, Selective laser melting additive manufacturing of pure tungsten : Role of volumetric energy density on densification, microstructure and mechanical properties, Int. J. Refract.

Metals Hard Mater. 84 (2019) 105025. doi:10.1016/j.ijrmhm.2019.105025.

[38] Z.A. Mierrzejewska, Effect of Laser Energy Density, Internal Porosity and Heat Treatment on Mechanical Behavior of Biomedical Ti6Al4V Alloy Obtained with DMLS Technology, Materials (Basel). 12 (2019) 2331. doi:doi:10.3390/ma12142331.

[39] J.H. Yi, J.W. Kang, T.J. Wang, X. Wang, Y.Y. Hu, T. Feng, Y.L. Feng, P.Y. Wu, Effect of laser energy density on the microstructure, mechanical properties, and deformation of Inconel 718 samples fabricated by selective laser melting, J. Alloys Compd. 786 (2019) 481–488. doi:10.1016/j.jallcom.2019.01.377.

[40] M. Hamidi Nasab, D. Gastaldi, N. Lecis, M. Vedani, On Morphological Surface Features of the Parts Printed by Selective Laser Melting (SLM) On morphological surface features of the parts printed by selective laser melting (SLM), Addit. Manuf. 24 (2018) 373–377. doi:10.1016/j.addma.2018.10.011.

[41] B. Vasudevarao, D. Prakash Natarajan, M. Henderson, Sensitivity Of RP Surface Finish To Process Parameter Variation, in: Solid Free. Fabr. Symp. - An Addit. Manuf. Conf., 2000.

[42] E. Maleki, S. Bagherifard, M. Bandini, M. Guagliano, Surface post-treatments for metal additive manufacturing: Progress, challenges, and opportunities, Addit. Manuf. (2020) 101619. doi:10.1016/j.addma.2020.101619.

[43] J.H. Tan, W.L.E. Wong, K.W. Dalgarno, An overview of powder granulometry on feedstock and part performance in the selective laser melting process, Addit. Manuf. 18 (2017) 228–255. doi:10.1016/j.addma.2017.10.011.

[44] R.J. Hebert, Viewpoint: metallurgical aspects of powder bed metal additive manufacturing, J. Mater. Sci. 51 (2016) 1165–1175. doi:10.1007/s10853-015-9479-x.

[45] C.D. Boley, S.A. Khairallah, A.M. Rubenchik, Calculation of laser absorption by metal powders in additive manufacturing, Appl. Opt. 54 (2015) 2477–2482.

[46] C.D. Boley, S.C. Mitchell, A.M. Rubenchik, S.S.Q. Wu, Metal powder absorptivity: modeling and experiment, Appl. Opt. 55 (2016) 6496. doi:10.1364/ao.55.006496.

[47] A. Rubenchik, S. Wu, S. Mitchell, I. Golosker, M. LeBlanc, N. Peterson, Direct measurements of temperature-dependent laser absorptivity of metal powders, Appl. Opt. 54 (2015) 7230. doi:10.1364/ao.54.007230.

[48] T. Laoui, X. Wang, T.H.C. Childs, J.P. Kruth, L. Froyen, LASER PENETRATION IN A POWDER BED DURING SELECTIVE LASER SINTERING OF METAL POWDERS: SIMULATIONS VERSUS EXPERIMENTS, in: 2000 Int. Solid Free. Fabr. Symp., 2000: pp. 453–460. doi:http://dx.doi.org/10.26153/tsw/3071.

[49] M. V Allmen, A. Blatter, Laser-Beam Interactions with Materials, Springer-Verlag, Berlin, Heidelbelg, 1995. doi:10.1007/978-3-642-57813-7.

[50] J. Trapp, A.M. Rubenchik, G. Guss, M.J. Matthews, In situ absorptivity measurements of metallic powders during laser powder-bed fusion additive manufacturing, Appl. Mater. Today. 9 (2017) 341–349. doi:10.1016/j.apmt.2017.08.006.

[51] C. Qiu, C. Panwisawas, M. Ward, H.C. Basoalto, J.W. Brooks, M.M. Attallah, On the role of melt flow into the surface structure and porosity development during selective laser melting, Acta Mater. 96 (2015) 72–79. doi:10.1016/j.actamat.2015.06.004.

[52] D. Wang, S. Wu, F. Fu, S. Mai, Y. Yang, Y. Liu, C. Song, Mechanisms and characteristics of spatter generation in SLM processing and its effect on the properties, Mater. Des. 117 (2017) 121–130. doi:10.1016/j.matdes.2016.12.060.

[53] M.J. Matthews, G. Guss, S.A. Khairallah, A.M. Rubenchik, P.J. Depond, W.E. King, Denudation of metal powder layers in laser powder bed fusion processes, Acta Mater. 114 (2016) 33–42. doi:10.1016/j.actamat.2016.05.017.

Part A

LASER-BASED POWDER BED FUSION

Chapter 2

LASER-BASED POWDER BED FUSION OF COCRMO BIOMEDICAL ALLOYS
A LITERATURE REVIEW

2.1 CoCrMo as biomedical material

2.1.1 Historical background

Cobalt-Chromium alloys with a significant content of refractory elements (i.e. tungsten) were firstly developed in the early 20th century and, in the reason of their high corrosion resistance, wear resistance and strength, they were soon adopted for the production of removable dental devices, replacing stainless steels as a low-cost alternative to gold-base alloys [1]. Subsequently, C and Cr content were adjusted and cast Co-Cr-W alloys were frequently used for the fabrication of orthopedic fracture-fixation devices, such as plates and screws. In the 1930s, W was substituted with Mo since at the time in North America Mo was easier to provide than W, and the addition of Mo in Co-Cr alloys enhanced their corrosion resistance, allowing the adoption of such materials for permanent orthopedic implants for joint reconstruction, like semi and total hip implants, mandibular plates as well as partial and total knee replacements. These early devices were produced by investment casting, due to complex geometries achievable with this technique and high carbon content (approx. 0.2 wt.%) was considered to promote castability. However, it is well known that casting products have generally low mechanical strength with respect to wrought components, thus wrought CoCrWNi alloys with low carbon content (approx. 0.05 wt.%) were developed in the early 1940s. Wrought CoCrWNi alloys were characterized by lower corrosion ad wear

resistance than cast CoCrMo alloys, as a consequence in the 1970s high-carbon CoCrMo alloys for thermomechanical forging were developed. Concurrently, by the end of 1980s, powder metallurgy technologies were exploited for the production of high-carbon CoCrMo components starting from gas atomized powders.

Nowadays, orthopedic and dental implants still represent the main application of cast and wrought CoCrMo alloys, while in other medical areas such as orthodontics and cardiovascular surgery they are gradually replaced by titanium and platinum-base alloys, respectively.

2.1.2 Biomaterial requirements

A biomaterial is defined as: "*any biocompatible material, natural or man-made, which is used to replace or assist part of an organ or tissue, while in intimate contact with it*" [2]. Metals are widely used biomaterials, especially for structural application such as implants, scaffolds and pins. The main reason is related to their excellent mechanical properties that make metals suitable for load-bearing medical devices. Not all metallic materials can be used as biomaterials. In fact, four main families of metals are the most commonly used: stainless steels, titanium alloys, shape memory alloys and CoCrMo alloys. More specifically, metals must fulfil well-defined requirements, in order to be considered as biomaterials [2–5]:

- Excellent corrosion resistance (particularly *in vivo*);
- Good mechanical properties;
- Good wear resistance;
- Excellent biocompatibility;
- Good osseointegration (in case of implants).

The applicability of the above-mentioned metal alloys as biomaterials relies in the formation of a protective thin oxide film that assures an excellent corrosion resistance. The biocompatibility, instead, "*implies that the local or systemic response does not impair the device function or the health of the patient, which requires that it does not induce a tumorigenic (cancer) nor a toxicological (e.g., cell*

death and tissue necrosis) response" [6]. Lastly, the osseointegration is defined as the stable union formed between the bone and the implanted device. Titanium has the best biocompatibility, it is inert and its oxide film is thermodynamically stable and capable to resist in all human body fluids. However, titanium-based alloys are not suitable for application requiring a high wear resistance, such as joint replacement devices, for which CoCr alloys are preferred [2,7]. Therefore, CoCrMo alloys are used for the fabrication of permanent joint replacement implants due to their excellent wear resistance. They also show a satisfying biocompatibility and corrosion resistance that is assured by the formation of the Cr_2O_3 oxide film [8].

2.1.3 Additive manufacturing in the biomedical field

One of the major drawbacks concerning CoCrMo alloys is related to the manufacturing process. These alloys have a high melting point (1350-1450 °C) and are also difficult to machine, so they are commonly manufactured via forging processes. Only in case of complex design, such as the femoral component of a knee prosthesis, investment casting or metal injection molding (MIM) is adopted. Wrought alloys are manufactured through a series of forming, reheating, and further forming steps starting from high temperature (930-1190 °C), that make the whole process expensive [9]. As a consequence of the described processing routes, medical implants are commonly realized in a limited number of sizes and shapes, that reasonably cannot fit all patients. In this view, additive manufacturing technologies can be proficiently applied to the biomedical field for the processing of CoCrMo alloys and for the fabrication of tailored devices, enhancing the patient's quality of life and preventing revision surgery [10]. Actually, the possibility has been already investigated and a standard procedure proposed, as displayed in Figure 2.1 [11]. The adoption of additive manufacturing technology, specifically powder bed fusion, can also promote reduction of the stress shielding effect occurring when bone and implant are joint. The elastic modulus of the cortical bone (10-30 GPa) is lower than elastic modulus of metals. This difference is enhanced in case of CoCrMo alloys, whose modulus is 240 GPa. As a consequence, the metal implant acts as load bearing element, replacing the bone and inducing biological responses, such as atrophy [2]. The fabrication via additive

manufacturing of tailored prostheses, with complex lattice structures and engineered stiffness, might mitigate the occurrence of this phenomenon and, concurrently, improve osseointegration [10,12,13].

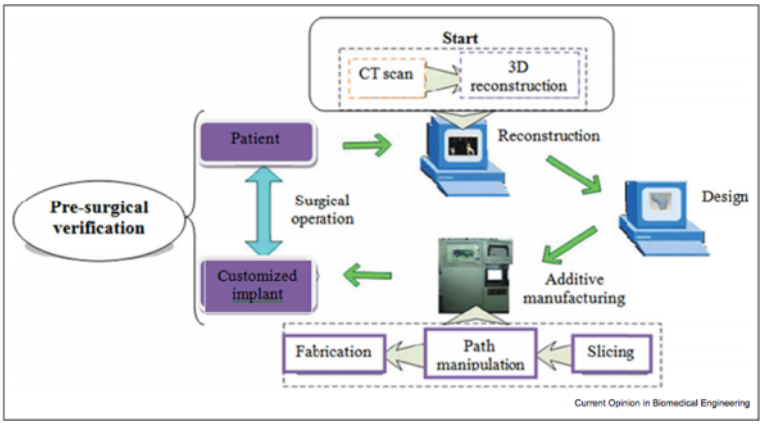

Figure 2.1: Procedure for the fabrication of customized implant via additive manufacturing [11]

2.2 Metallurgy of conventionally processed Co28Cr6Mo alloy

By focusing on the orthopedic applications, the Co28Cr6Mo alloys are currently used for permanent implant devices, such as ankle and knee prostheses. According to the ASTM designation system, Co28Cr6Mo alloys are classified on the basis of the processing route, as summarized in Table 2.1. As mentioned in the previous section, investment casting and warm/hot working represent the manufacturing route conventionally adopted for these alloys. Among the alloys, small variations in the chemical composition can be found, mainly related to the carbon content that can vary between C=0.14-0.35 wt.%, while all of them have a low Ni content, set up to a maximum of 0.5 wt.% for the cast alloy and 1.0 wt.% for the wrought alloy, in order to prevent Ni-sensitization. The nominal chemical composition of the Co28Cr6Mo alloys and the role of major alloy elements are reported in Tables 2.2 and 2.3 respectively. Among alloy elements, the most relevant is Cr that, by forming the protective Cr_2O_3 passivation film, gives this alloy an adequate corrosion resistance, enhanced by the presence of Mo. However, due to the presence of C, carbides might form. Carbides formation can be detrimental for

corrosion resistance, since they deplete the Cr and Mo content in the matrix. At the same time, carbides increase wear resistance of the alloy, relevant for the final applications. Therefore, the two aspects have to be proper balanced. It should be also noticed that, since Co is an allotropic element, alloy elements may contribute to stabilize the hcp (hexagonal compact) equilibrium phase or the metastable fcc (face-centered cubic) phase [1].

Table 2.1: ASTM designation for Co28Cr6Mo alloys for orthopedic implants

Alloy	Processing Route	Carbon content	Pros	Cons
ASTM F75	Investment casting	High	High wear resistance due to carbide distribution and work-hardening ability.	Large grain size, porosity and shrinkage.
ASTM F1537	Wrought/Forging	Low	High tensile and fatigue strength due to the FCC to HCP transformation occurring during cold working	Low wear resistance.
ASTM F799		High		Good wear resistance but more difficult to process.
ASTM F1377	Powder for coating	High		

Table 2.2: Nominal chemical composition for the Co28Cr6Mo alloy [14,15]

Elements (wt.%)								
Co	***Cr***	***Mo***	***C***	***Si***	***Fe***	***Ni***	***Mn***	***N***
Bal.	26.0 – 30.0	5.0 – 7.0	0.14-0.35	1.0 max	0.75 max	1.0 max	1.0 max	0.25 max

Table 2.3: Role of major alloy elements in the Co28Cr6Mo alloy [1]

Element	*Role*
Cr	Responsible for the high corrosion resistance of the alloy (forms the protective Cr_2O_3 oxide film). Tends to form M_7C_3 and $M_{23}C_6$ carbides. Helps stabilizing hcp Co phase.
Mo	Improves corrosion resistance. May forms M_6C and $M_{12}C$ carbides. Helps stabilizing hcp Co phase.
C	Improves castability and decreases formability of the alloy. Forms carbides (beneficial for wear resistance but detrimental for corrosion resistance). Helps stabilizing fcc Co phase.
Ni	Improves formability of the alloy. Helps stabilizing fcc Co phase. May cause Ni-sensitization.

Wrought alloys are usually delivered in the hot/warm worked and annealed condition, while the cast alloy is usually subjected to a final solution treatment or hot isostatic pressing (HIP) to reduce solidification defects. More recently, powder metallurgy processes like metal injection molding (MIM) have been adopted for the processing of this alloy [16]. For comparison purposes with the LPBF alloy, the metallurgy of the Co28Cr6Mo cast alloy will be discussed below.

2.2.1 Co28Cr6Mo investment casting alloy

Cast Co28Cr6Mo alloy is processed by investment casting, also known as lost wax process. As disclosed in Figure 2.2, the process is based on initial designs made of wax and assembled in the so-called casting tree, that is later coated with a thick

layer made of refractory slurry. Once the casting tree is dried and dewaxed, the molten alloy is poured into the casting tree and, once solidified, the metal part is extracted from the tree by destroying the ceramic shell. The Co28Cr6Mo alloy melts at approximately 1350-1450 °C, depending on the exact composition, and it is poured in the shell pre-heated at approximately 1200 °C [17]; as a result, the whole investment casting process is quite expensive and intricated, since it involves several specific steps.

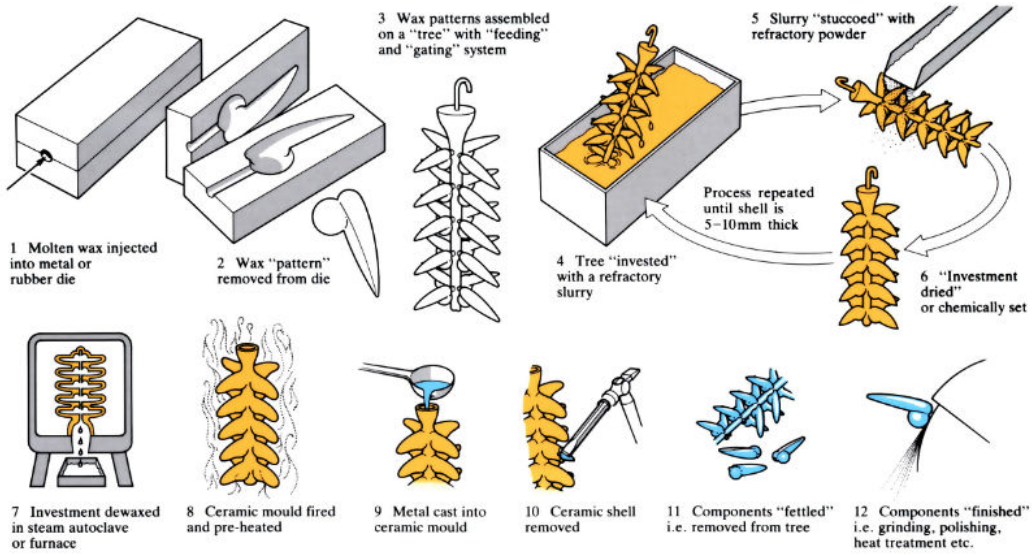

Figure 2.2: The investment casting process, a step by step illustration [18]

The as-cast microstructure (Figure 2.3) is generally coarse and highly cored. It consists of a cobalt-rich dendritic phase (γ-fcc metastable phase) and precipitates at grain boundaries and interdendritic regions. These precipitates are enriched in alloy elements and can be identified as: blocky carbides (mainly $M_{23}C_6$), a brittle intermetallic σ-phase, and a coarse lamellar structure consisting of interlayered plates of γ-fcc (also referred to as α-fcc in the literature) and $M_{23}C_6$ phases [17,19].

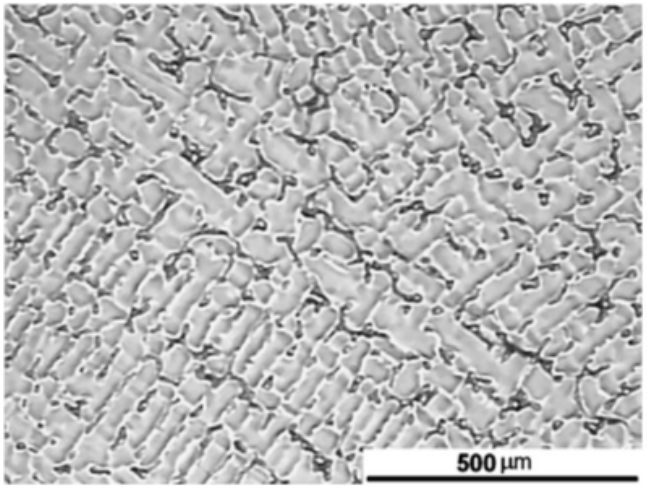

a

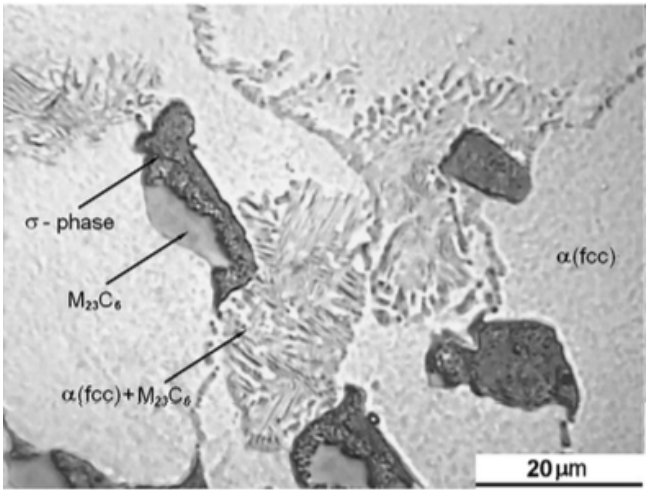

b

Figure 2.3: As-cast microstructure of the Co28Cr6Mo alloy: a) low magnification showing dendritic structure; b) detail of interdendritic region [19]

With reference to the Co-Cr phase diagram in Figure 2.4, the equilibrium phase at room temperature for this alloy is the ε-hcp phase. However, since the γ-fcc to ε-hcp phase transformation, occurring at approximately 890-950 °C, is sluggish and not kinetically favored, the metastable γ-fcc is usually retained at room temperature [1,17]. The γ-fcc to ε-hcp transformation can be promoted by post-

process isothermal heat treatments, work hardening, and water quenching, that might induce a martensitic transformation [20].

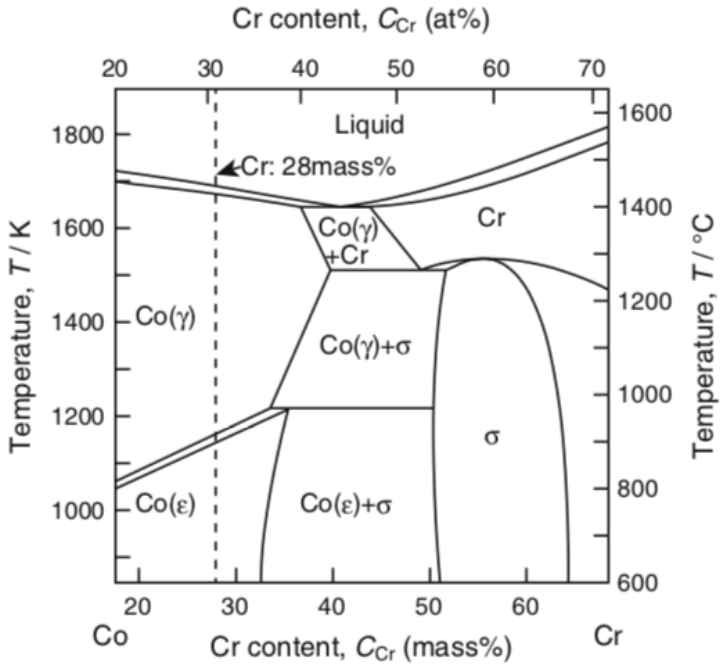

Figure 2.4: Co-Cr binary phase diagram, the vertical dashed line refers to the Co28Cr6Mo composition [21]

The complete list of phases and precipitates in biomedical Co-Cr-Mo alloys can be found in Table 2.4, as reported by Narushima et al. [22]. According to their works, second phases in Co-Cr-Mo alloys strictly depend on the carbon and nitrogen content. Based on their nomenclature, in the definition of M_2X, $M_{23}X_6$, M_7X_3 phases the letter M stands for metal element and X for carbon or nitrogen. χ phase is an intermetallic compound which is promoted by the presence of Si and a relatively low carbon content. The η and π phases are carbon rich carbonitrides. Both M_6X and $M_{12}X$ compounds belong to the η phase, that is enriched in Mo. π phase forms at high temperatures (1275-1350 °C) where partial melting of the alloy occurs and its presence depends on the cooling rate from these temperatures: a high cooling rate may promote the retainment of such phase while slower cooling rates promote the transformation π → Co(γ-fcc) + $M_{23}X_6$. Therefore, it is plausible that in investment casting products the π-phase is usually not observed. The M_2X is a nitrogen-rich carbonitride, while the $M_{23}X_6$ phase is nearly a carbide and it is mainly composed by Cr, as disclosed by the chemical composition in Table 2.4.

Table 2.4: Chemical composition and crystal structure of phases detected on CoCr biomedical alloys [22]. The acronym N.A. stands for not available.

Phase	*Crystal Structure*	*Chemical composition (at.%)*						
		Co	***Cr***	***Mo***	***C***	***N***	***Si***	***Mn***
M_2X		3.7	62.9	5.5	12.7	15.2	-	-
$M_{23}X_6$	Cubic	12.6-14.6	58.6-61.6	5.2-6.0	17.5-22.1	N.A.	N.A.	0-0.1
M_7X_3	Cubic	Co:Cr:Mo = 26.0 : 65.8 : 8.2						
π	Cubic	31.0-38.0	38.9-43.7	9.6-12.0	11.9-14.3	0-3.3	0-2.5	0-1.1
σ	Topologically closed-packed	Co:Cr:Mo = 44-47.6 : 41.1-44 : 11.2-12 (C content non measured)						
η	β-Mn	29.4-31.1	23.4-23.5	22.6-22.7	10.8-13.1	0-4.0	8.0-11.4	-
χ	α-Mn	48.5	34.6	12.7	N.A.	-	4.3	-

As mentioned above, carbon content has a major role in the formation of second phases, followed by nitrogen and silicon. The graph reported in Figure 2.5a shows the variation in the relative intensity of the strongest peak of second phases as a function of C content, as determined by XRD analyses of extracted particles (Figure 2.5b) [22]. The effect of N and Si is instead depicted in Figure 2.6a,b.

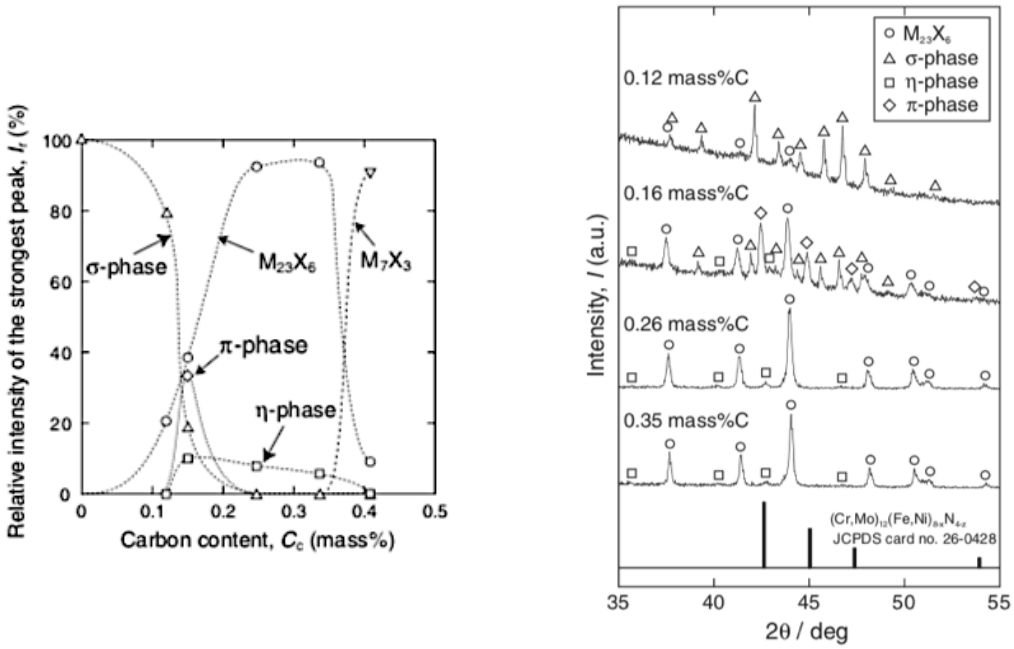

a b

Figure 2.5: Analyses of second phases for the Co28Cr6Mo alloy: a) relative intensity of the strongest peak as a function of C content; b) relative XRD spectra [22].

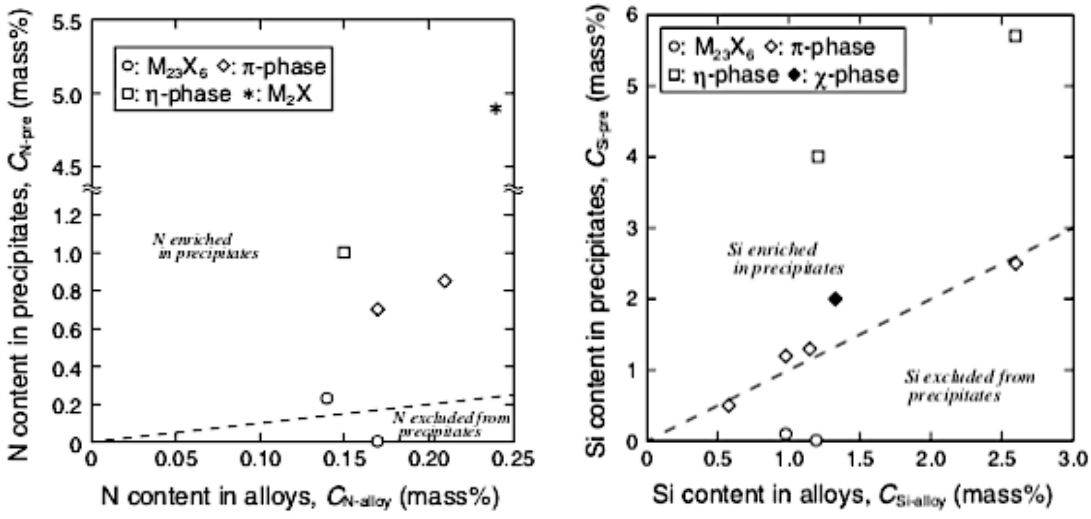

a b

Figure 2.6: Effect of minor alloy elements on second phases for the Co-Cr-Mo alloys: a) nitrogen; b) silicon [22].

HEAT TREATMENT

To partially homogenize the microstructure, the as-cast components are subjected to a short (1-3 h) solution treatment in the range 1200-1225 °C, and in any case below 1235 °C that corresponds to the melting point of the Cr, Mo, C-enriched eutectic interdendritic regions. The solution treatment results in a partial dissolution of carbides, even if some are retained since they enhance the wear resistance of the alloy. In order to reduce also solidification defects such as internal porosity and interdentritic shrinkages, solution treatment can be replaced by a HIP process, performed at 1220-1230 °C with an isostatic pressure of 105 MPa and holding for 2 h. Both solution treatment and HIP have to be performed in an inert atmosphere. From the solution treatment temperature, the alloy is rapidly cooled by water quenching, in order to avoid the precipitation of brittle $M_{23}C_6$ carbides, occurring in the 1100-800 °C range [17]. After quenching, the alloy may undergo an isothermal aging treatment (also referred to as an aging anneal) at approximately 890-900 °C, where ε-hcp is stable according to phase diagram, to promote the formation of the so-called isothermal martensite platelets or bands, that typically form transgranularly. Aging treatments also induce the formation of stacking faults by partial dislocation within γ-fcc phase and faulted zone themselves, resulting in a two-phase fcc-hcp structure. Moreover, aging treatment promotes the precipitation of finely dispersed carbides (mainly $M_{23}C_6$) among the hcp zones or at the hcp-fcc boundaries [1]. The heat treatment conditions for the cast Co28Cr6Mo alloy are summarized in Table 2.5, while typical mechanical properties are reported in Table 2.6.

Table 2.5: Heat treatment condition for the Co28Cr6Mo cast alloy

Solution treatment		***Water Quenching***	***Artificial aging treatment***	
Temperature [°C]	*Time at temperature [h]*		*Temperature [°C]*	*Time at temperature [h]*
1200-1225	1 to 3		890 - 900	-

Table 2.6: Typical mechanical properties for the cast Co28Cr6Mo alloy [14,17]

	Tensile properties			*Fatigue resistance*
HRC Hardness				
	Ys [MPa]	***UTS [MPa]***	***A%***	**[MPa]**
25-35	450-530	655-890	11-17	207-310

Micrographs showing the evolution in the microstructure during aging up to 16 h are reported in Figure 2.7. Micrographs show that in the early stages of aging (4 and 8 h), a progressive precipitation of M23C6 carbides at grain boundaries and inside grains occurs [23]. By increasing aging time (16 h) the lamellar structure, growing from grain boundaries, becomes the dominant feature in the microstructure.

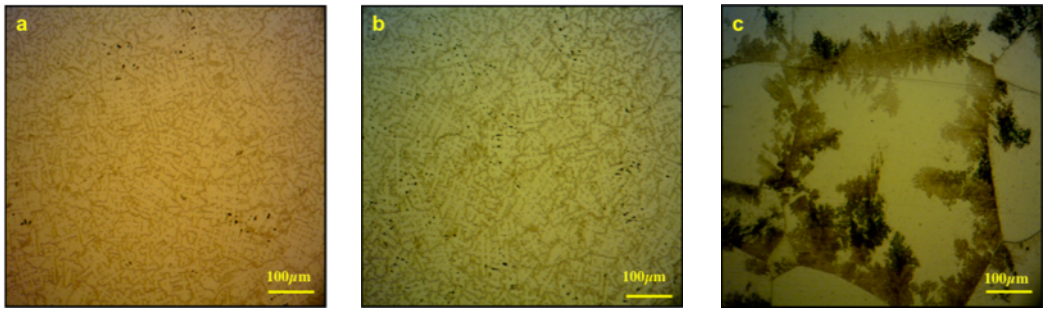

Figure 2.7: Optical micrographs of solutionized and isothermally aged Co28Cr6Mo cast alloy at 950 °C for, (a) 4 h, (b) 8 h, (c) 16 h [23].

Aging response of the Co28Cr6Mo solution-treated cast alloy was investigated by Taylor and Waterhouse [24] who proposed the time-temperature-precipitation (TTP) diagram reported in Figure 2.8. In their study, only $M_{23}C_6$ carbides were evidenced by XRD analyses of the extracted particles of solution-treated and aged alloy. According to their findings, precipitation started with feathery, interdendritic phase and lamellar structure at grain boundaries. In the range 650-

900 °C, $M_{23}C_6$ carbides nucleated and grew in association with stacking faults within the γ-fcc Co phase and developed as blocky carbides at grain boundaries. For temperatures higher than 900 °C, the precipitation mechanism changed as $M_{23}C_6$ nucleated on dislocations. At temperature above 900 °C, indeed, the γ-fcc Co phase became instable and diffusion processes are promoted, thus justifying the change in the precipitation mode.

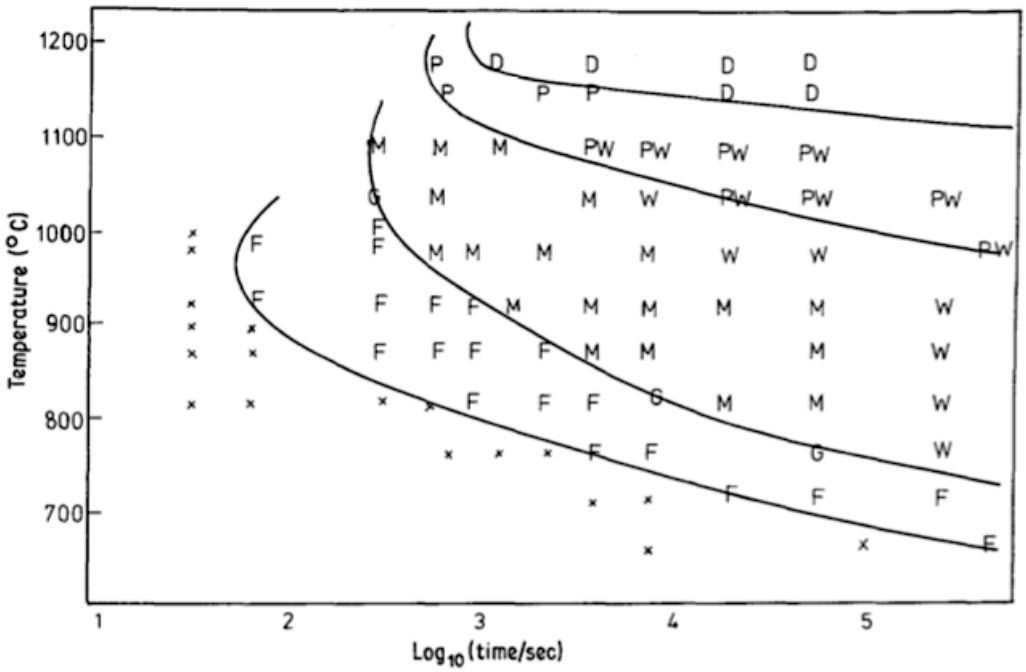

Figure 2.8: Time-temperature-precipitation diagram for the Co28Cr6Mo solution treated cast alloy: x stands for no precipitation; F stands for feathery, interdendritic precipitate, and lamellar structure at grain boundaries; G stands for blocky grain boundary phase; M indicates change in morphology; W indicates orientation effects in the matrix phase; P stands for no lamellar structure; PW stands for spheroidized, agglomerated lamellae; D represents dissolution apparent [24].

2.3 Wear of biomedical implants

Human synovial joints are a load bearing dynamic structure that operates, in average, for a total lifetime of 70 years and 10^8 loading cycles (Figure 2.9a). They are naturally lubricated by the synovial fluids and, in fully operating conditions, have a low friction coefficient and wear rate, set at 0.02 and 10^{-6} mm^3 N^{-1}

respectively [25]. However, they may deteriorate as a consequence of natural aging, trauma and diseases. When the natural joint cannot operate anymore, it can be replaced with an artificial orthopedic implant (Figure 2.9b).

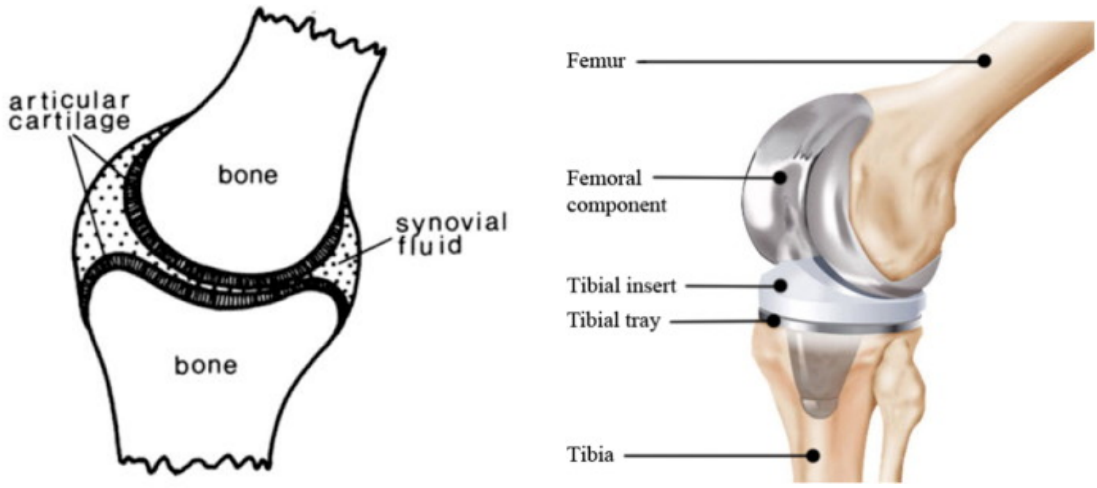

a b

Figure 2.9: Synovial joint (a); knee joint replacement (b) [25,26].

To guarantee the proper mechanical strength and adequate wear resistance, implant for joint replacement are often made of CoCrMo biomedical alloys, especially in case of knee and ankle joints. Failure of the implant usually does not occur due to excessive wear of the device. However, wear debris of the artificial joint might induce a biologic response in the system causing inflammation, local osteolysis and also local or systemic hypersensitivity. As a consequence, wear behavior of the CoCrMo alloy is crucial in order to reduce implant loosening due to the aforementioned biological reactions that affect the bone-prosthesis interface that can eventually lead to implant failure [27]. By focusing on the CoCrMo alloys, it should also be mentioned that neurotoxicity of Co consequent to metal release from orthopedic implants is under investigation [28]. The scheme in Figure 2.10 synthetizes the reported causes of implant failure, that can eventually lead to a revision surgery. From the scheme, it is quite evident that debris generated by wear

and corrosion phenomena play a major role in determining the success of the arthroplasty and patients' quality of life.

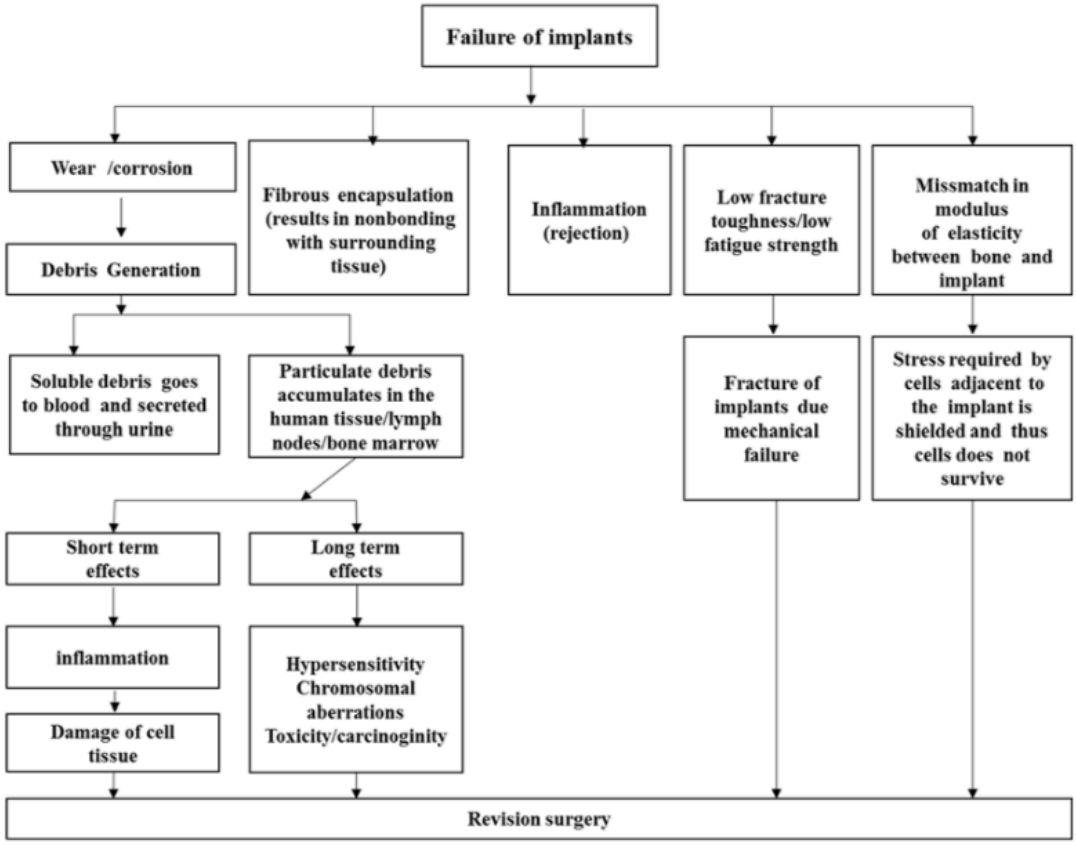

Figure 2.10: Reported causes for implant replacement failure [29]

Historically, artificial joints were made as metal-on-metal implants, where load-bearing surfaces of the artificial joint where directly in contact. Even if this solution was not convenient from the tribological point of view, as direct contact of identical metals should be avoided, it was an acceptable balance between wear and corrosion properties. In fact, by using two identical metals, electrochemical corrosion, due to electrolytic reaction between different metals, can be avoided. Modern implants belong instead to the metal-on-polymer type where, as showed in Figure 2.9b, a polymeric insert is interposed between metallic surfaces. This adoption results in the reduction of the frictional torque of the artificial joint and prevents implant loosening. In metal-on-polymer implants wear debris are mainly composed by polymeric elongated micrometric particles [27]. However, wear of the metal alloy can occur as a consequence of tribo-corrosion phenomena in

correspondence of metal-on-metal modular junctions where micro-motions between the two components might be developed [30].

The artificial joint is a complex tribological system that can be investigated at different levels:

- Laboratory scale wear tests (pin-on-disk, ball-on-disk, block-on-disk configurations) for wear mechanism evaluation;
- Joint simulators to study the whole implant;
- In-vivo experiments to assess the response of the whole joint replacement.

As reported in the review by Hussein et al. [29], laboratory scale tests were quite extensively adopted to study wear mechanisms of the main metallic biomaterials. Even though literature studies are usually obtained in very different conditions making results hardly comparable, among metallic biomaterials the Co-based ones are generally characterized by the highest wear resistance.

2.4 LPBF of Co28Cr6Mo alloy

Due to the relevance of additive manufacturing in the biomedical field, many literature studies focused on the application of AM techniques, particularly powder bed fusion ones, to CoCrMo alloys. However, most of the experimental works dealt with the alloy specific for dental application, that contains also W as alloy element (approx. 4–6 wt.%). Fewer researches have been specifically devoted to the orthopedic alloys, with composition complying with the requirements reported in Table 2.2. From the process point of view, the Co28Cr6Mo alloy is considered an easily printable material and the majority of the consulted literature works reported successful fabrication of near-full-density parts. Process parameters adopted in the literature are not reported in the present section but the role of process parameters in the optimization of LPBF process of this alloy will be thoroughly investigated in the next chapter regarding experimental activities. From the metallurgical point of view, literature data evidenced that the Co28Cr6Mo alloy, when processed via LPBF, solidifies in a hierarchical

microstructure (Figure 2.11) consisting of epitaxial columnar grains, crossing-over layers and sub-micron sized cellular structure, as for many other metal alloys [31]. The solidified semi-circular melt pools are clearly identifiable in the low magnification micrograph in Figure 2.11a, while columnar grain growth due to epitaxy were evidenced by EBSD analyses in Figure 2.11b. High magnification microscopy allowed to further highlight the developed cellular structure and the competitive growth starting from melt pool borders (Figure 2.11c,d).

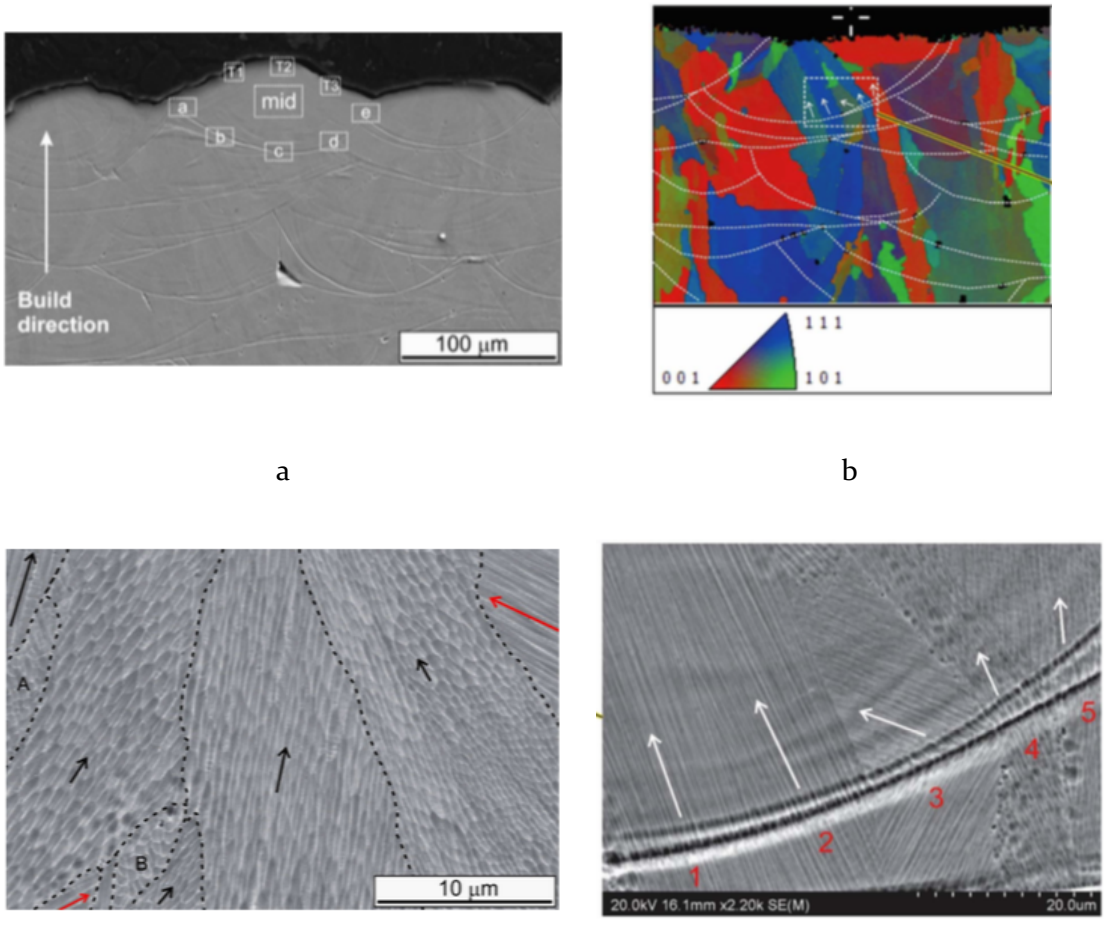

a b

c d

Figure 2.11: Hierarchical microstructure of the LPBF Co28Cr6Mo alloy resulting from scanning electron microscope analyses: a) low magnification SEM micrographs highlighting melt pool borders, b) EBSD analyses revealing columnar epitaxial grains crossing over layers, c) high magnification SEM micrograph of melt pool core ("mid" area in figure a), d) SEM high magnification micrograph of melt pool border where grain grow direction are evidenced by white arrows (adapted from [32,33]).

The development of the cellular microstructure was explained by Prashanth and Eckert [34]. CoCrMo is a ternary system, however, Mo content in the Co28Cr6Mo alloy is not sufficient to form the ternary phase $Co_{49}Cr_{21}Mo_{30}$. Thus, the ternary CoCrMo diagram can be considered as a pseudo-binary diagram, with CoCr and Mo as main phases. During solidification, the low-melting CoCr phase forms directly from the liquid, ejecting the high-melting Mo phase, due to negligible solubility of Mo in the CoCr phase. As a consequence, Mo is segregated on cell boundaries. Micro-segregation between cell core and border was supported by SEM and TEM analyses, reported in Figure 2.12, that revealed accumulation of Cr and Mo (Figure 2.12a) and C (Figure 2.12b) in correspondence of cell borders. In view of these findings, it is possible that the fine network surrounding Co-based cells mainly consists of carbides [35,36].

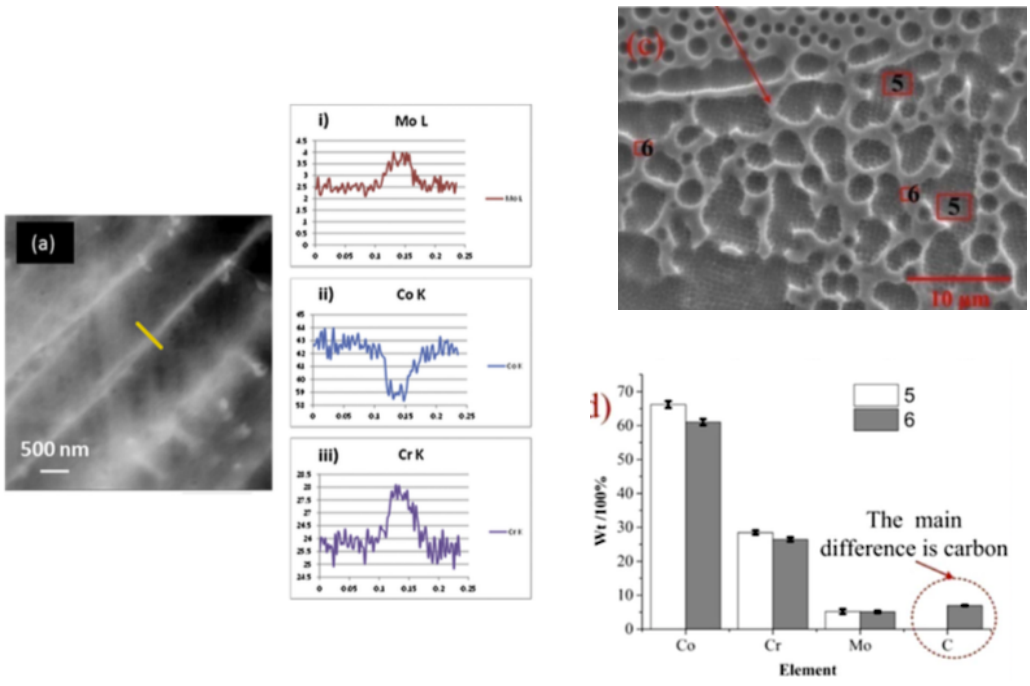

a b

Figure 2.12: Semiquantitative analyses revealing solute concentration at cell borders: a) TEM analyses showing segregation of Cr and Mo, b) SEM-EDS analyses revealing a higher C content (adapted from [36,37]).

As regards phase composition, several authors report the co-existence in the as-built alloy of both γ-fcc and ε-hcp, from a 7:3 ratio up to almost equal proportions

[35,38,39]. Therefore, the LPBF process, presumably due to repetitive thermal cycles during building, promoted the partial transformation to the equilibrium phase. In one case [35], XRD analyses revealed also the presence of approximately 2% carbides ($M_{23}C_6$) content, supporting the previously discussed metallographic analyses on the fine carbide-based network that surrounds Co cells.

Mechanical properties, in terms of tensile behavior, are summarized in Table 2.7. Literature data for the LPBF Co28Cr6Mo alloy reports quite elevated mechanical properties, especially if compared to the cast counterpart (Table 2.6). The increase in yield and ultimate tensile strength occurred without a detrimental effect on the ductility, that is comparable to the cast alloy. The strength increase is ascribable to the refined cellular structure and to solid solution strengthening, as occurs for many LPBF-processed metal alloys [31]. Tensile data fulfill also the minimum requirement established by the ASTM F3213 standard for final properties of Co28Cr6Mo PBF product.

Table 2.7: Tensile properties of the LPBF Co28Cr6Mo alloy, as reported in the literature [37,40,41].

Tensile properties		
Ys [MPa]	***UTS [MPa]***	***A%***
730-870	1140-1300	10-15

2.4.1 Heat treatment of LPBF Co28Cr6Mo alloy

Quite limited research about the heat treatment of Co28Cr6Mo LPBF alloy is currently reported in the literature. The investigated heat treatment conditions can be summarized as follows [39,42–45]:

- solution treatment (1150-1220 °C 1-6 h);
- solution treatment (1150 °C x 1 h) + isothermal aging (800 °C x 4 h);
- solution treatment (1200 °C x 1 h) + isothermal aging (900 °C x 0.5-10 h);
- solution treatment (1200 °C x 1 h) + isothermal aging (750 °C x 0.5-10 h);
- annealing at 750, 900, 1050, 1150 °C x 6 h.

In few cases, only the conventional solution treatment was applied to the as-built alloy [36,43,44]. Several authors, instead, applied the complete heat treatment that combines a high-temperature solution treatment followed by quenching and isothermal aging in the range 750-900 °C [39,42]. Finally, only one study was focused on direct aging anneal treatment at different temperatures for a total holding time of 6 h [45] with a primary focus on stress-relieving. Solution treatment induced a decrease in yield and ultimate tensile strength. Solution treatment followed by aging induced an increase in hardness and ultimate strength, justified by the γ-fcc to ε-hcp phase transformation occurring during isothermal aging and a nearly 100% ε-hcp can be obtained after long-time aging (900 °C x 10 h) [39]. When only aging anneal treatment was applied directly to the as-built condition, a progressive decrease in the hardness and ultimate tensile strength was observed with increasing temperature. Concurrently, ductility of the alloy was enhanced and these results were related with the decrease of the ε-hcp phase content with increasing aging temperatures. Partial γ-fcc to ε-hcp phase transformation occurred after aging at 750 °C then, for higher treatment temperatures, the ε-hcp phase content gradually decreased and disappeared after 1150 °C treatment [45]. From a microstructural point of view, all the investigated treatment induced modification in the alloy, as depicted in Figure 2.13. The aging anneal treatment up to 1050 °C affected the cellular structure and promoted the precipitations of second phases inside grains (Figure 2.13a) [45], while for all

treatments performed in the range 1150-1220 °C a more profound change occurred (Figure 2.13b,c) [39,42–44]. As schematically illustrated in Figure 2.14, homogenization, relief of residual stress and recrystallization occurred, resulting in an equiaxed grain with precipitation of granular second phases along grain boundaries [39,45]. In the mentioned studies, since no external plastic strain was induced in the alloy, the rapid solidification, the formation of dense dislocation, and the accumulation of residual thermal stress resulting from LPBF acted as driving force of recrystallization process, made possible by the high temperature treatment.

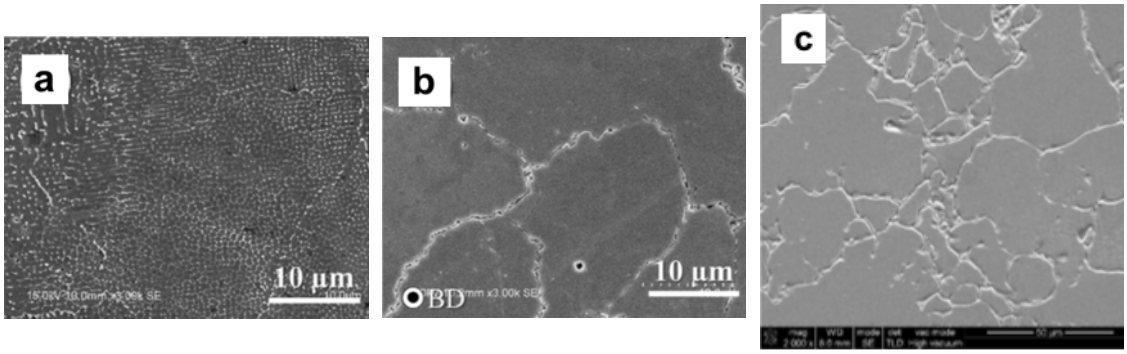

a b c

Figure 2.13: Evolution in the microstructure of the LPBF Co28Cr6Mo alloy after: a) aging at 900°C for 6h, b) solution treatment at 1050°C, c) solution treatment+aging at 900°C for 1h (adapted from [39,45]).

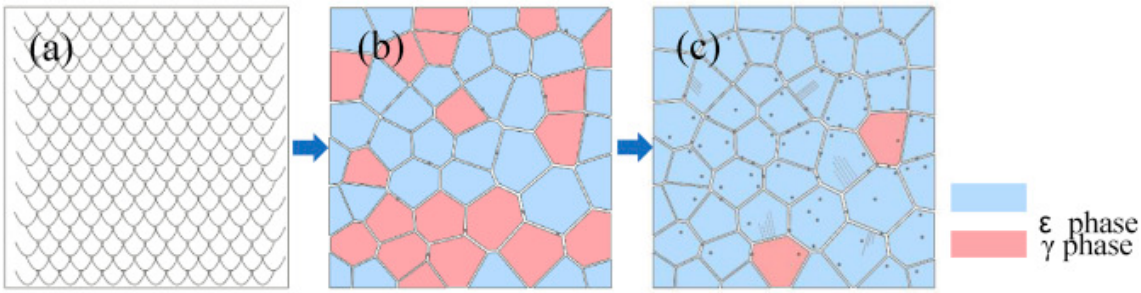

Figure 2.14: Schematic representation of the evolution of the LPBF Co28Cr6Mo alloy: a) as-built cellular structure, b) after solution treatment and short aging, c) after solution treatment and long aging [39].

References

[1] R. Pillar, S.D. Ramsay, Cobalt-base alloys, in: R.J. Narayan (Ed.), Mater. Med. Devices, ASM Interbational, 2012: pp. 211–222. doi:10.31399/asm.hb.v23.a0005669.

[2] Q. Chen, G.A. Thouas, Metallic implant biomaterials, Mater. Sci. Eng. R Reports. 87 (2015) 1–57. doi:10.1016/j.mser.2014.10.001.

[3] G.A. dos Santos, The Importance of Metallic Materials as Biomaterials, Adv. Tissue Eng. Regen. Med. Open Access. 3 (2017) 300–302. doi:10.15406/atroa.2017.03.00054.

[4] N. Patel, P. Gohil, A review on biomaterials: scope, applications & human anatomy significance, Int. J. Emerg. Technol. Adv. Eng. 2 (2012) 91–101.

[5] H. Breme, V. Biehl, N. Reger, E. Gawalt, Metallic Biomaterials: Introduction, in: W. Murphy, J. Black, G. Hastings (Eds.), Handb. Biomater. Prop., Second, Springer, 2016: pp. 151–159. doi:10.1007/978-1-4939-3305-1.

[6] D. Gibbons, Introduction to Medical Implant Materials, in: R.J. Naraya (Ed.), Mater. Med. Devices, ASM International, 2015: pp. 3–5.

[7] I. Peter, L. Matekovits, M. Rosso, Up-to-Date Knowledge and Outlooks for the Use of Metallic Biomaterials: Review Paper Ildiko, in: Biomater. Regen. Med., InTech Open, 2012: pp. 45–63. doi:10.5772/intechopen.69970 47.

[8] S.J. Gobbi, V.J. Gobbi, Y. Rocha, Requirements for Selection/Development of a Biomaterial, Biomed. J. Sci. Tech. Res. 14 (2019) 10674–10679. doi:10.26717/bjstr.2019.14.002554.

[9] T. Ozel, P. Bartolo, E. Ceretti, J. De Ciurana Gay, C.A. Rodriguez, J.V.L. Da Silva, Biomedical Devices: Design, Prototyping and Manufacturing, John Wiley & Sons, 2017. doi:10.1002/9781119267034.

[10] M. Lowther, S. Louth, A. Davey, A. Hussain, P. Ginestra, L. Carter, N. Eisenstein, L. Grover, S. Cox, Clinical, industrial, and research perspectives on powder bed fusion additively manufactured metal implants, Addit. Manuf. 28 (2019) 565–584. doi:10.1016/j.addma.2019.05.033.

[11] S. Singh, S. Ramakrishna, Biomedical applications of additive manufacturing: Present and future, Curr. Opin. Biomed. Eng. 2 (2017) 105–115. doi:10.1016/j.cobme.2017.05.006.

[12] L. Bai, C. Gong, X. Chen, Y. Sun, J. Zhang, L. Cai, S. Zhu, S.Q. Xie, Additive manufacturing of customized metallic orthopedic implants: Materials, structures, and surface modifications, Metals (Basel). 9 (2019) 1–26. doi:10.3390/met9091004.

[13] S. Bose, D. Ke, H. Sahasrabudhe, A. Bandyopadhyay, Additive manufacturing of biomaterials, Prog. Mater. Sci. 93 (2018) 45–111. doi:10.1016/j.pmatsci.2017.08.003.

[14] ASTM F75-18, Standard Specification for Cobalt-28 Chromium-6 Molybdenum Alloy Castings and Casting Alloy for Surgical Implants (UNS R30075), (2018). doi:https://doi.org/10.1520/F0075-12.

[15] ASTM F1537-20, Standard Specification for Wrought Cobalt-28Chromium-

6Molybdenum Alloys for Surgical Implants (UNS R31537, UNS R31538, and UNS R31539), (2020). doi:10.1520/F1537-20.

[16] P. V. Muterlle, M. Zendron, M. Perina, R. Bardini, A. Molinari, Microstructure and tensile properties of metal injection molding Co-29Cr-6Mo-0.23C alloy, J. Mater. Sci. 45 (2010) 1091–1099. doi:10.1007/s10853-009-4051-1.

[17] R. Pillar, Metallic Biomaterials, in: R. Narayan (Ed.), Biomed. Mater., Springer US, 2009: pp. 41–81. doi:10.1007/978-0-387-84872-3.

[18] Open University, (n.d.). https://www.open.edu/openlearn/science-maths-technology/engineering-technology/manupedia/investment-casting.

[19] J. V. Giacchi, C.N. Morando, O. Fornaro, H.A. Palacio, Microstructural characterization of as-cast biocompatible Co-Cr-Mo alloys, Mater. Charact. 62 (2011) 53–61. doi:10.1016/j.matchar.2010.10.011.

[20] K. Yamanaka, M. Mori, Y. Koizumi, A. Chiba, Local strain evolution due to athermal γ→ε martensitic transformation in biomedical CoCrMo alloys, J. Mech. Behav. Biomed. Mater. 32 (2014) 52–61. doi:10.1016/j.jmbbm.2013.12.019.

[21] T. Narushima, K. Ueda, Alfirano, Cobalt-Base Alloys as effective Metallic Biomaterials, in: M. Niinomi, T. Narushima, M. Nakai (Eds.), Adv. Met. Biomater., Springer, Berlin, Heidelbelg, 2015: pp. 157–178. doi:10.1007/978-3-662-46836-4_7.

[22] T. Narushima, S. Mineta, Y. Kurihara, K. Ueda, Precipitates in biomedical Co-Cr alloys, Jom. 65 (2013) 489–504. doi:10.1007/s11837-013-0567-6.

[23] S. Zangeneh, H.R. Lashgari, A. Roshani, Microstructure and tribological characteristics of aged Co-28Cr-5Mo-0.3C alloy, Mater. Des. 37 (2012) 292–303. doi:10.1016/j.matdes.2011.12.041.

[24] R.N.J. Taylor, R.B. Waterhouse, A study of the ageing behaviour of a cobalt based implant alloy, J. Mater. Sci. 18 (1983) 3265–3280. doi:10.1007/BF00544151.

[25] D. Dowson, Friction and Wear of Medical Implants and Prosthetic Devices, in: R. Narayan (Ed.), Mater. Med. Devices, ASM International, 2012: pp. 187–195. doi:10.31399/asm.hb.v23.9781627081986.

[26] A. Hafezalkotob, A. Hafezalkotob, Comprehensive MULTIMOORA method with target-based attributes and integrated significant coefficients for materials selection in biomedical applications, Mater. Des. 87 (2015) 949–959. doi:https://doi.org/10.1016/j.matdes.2015.08.087.

[27] N.J. Hallab, Biologic aspects of implants wear, in: R. Narayan (Ed.), Mater. Med. Devices, ASM International, 2012: pp. 157–168. doi:10.31399/asm.hb.v23.9781627081986.

[28] S. Catalani, M.C. Rizzetti, A. Padovani, P. Apostoli, Neurotoxicity of cobalt, Hum. Exp. Toxicol. 31 (2012) 421–437. doi:10.1177/0960327111414280.

[29] M.A. Hussein, A.S. Mohammed, N. Al-Aqeeli, Wear characteristics of metallic biomaterials: A review, Materials (Basel). 8 (2015) 2749–2768. doi:10.3390/ma8052749.

[30] M. Merola, S. Affatato, Materials for Hip Prostheses: A Review of Wear and Loading Considerations, Materials (Basel). 12 (2019) 495. doi:10.3390/ma12030495.

[31] T. DebRoy, H.L. Wei, J.S. Zuback, T. Mukherjee, J.W. Elmer, J.O. Milewski, A.M.

Beese, A. Wilson-Heid, A. De, W. Zhang, Additive manufacturing of metallic components – Process, structure and properties, Prog. Mater. Sci. 92 (2018) 112–224. doi:10.1016/j.pmatsci.2017.10.001.

[32] Z.W. Chen, M.A.L. Phan, K. Darvish, Grain growth during selective laser melting of a Co–Cr–Mo alloy, J. Mater. Sci. 52 (2017) 7415–7427. doi:10.1007/s10853-017-0975-z.

[33] K. Darvish, Z.W. Chen, M.A.L. Phan, T. Pasang, Selective laser melting of Co-29Cr-6Mo alloy with laser power 180–360 W: Cellular growth, intercellular spacing and the related thermal condition, Mater. Charact. 135 (2018) 183–191. doi:10.1016/j.matchar.2017.11.042.

[34] K.G. Prashanth, J. Eckert, Formation of metastable cellular microstructures in selective laser melted alloys, J. Alloys Compd. 707 (2017) 27–34. doi:10.1016/j.jallcom.2016.12.209.

[35] A. Molinari, The structural metastability of metallic alloys produced by Selective Laser Melting, La Metall. Ital. 1 (2017) 21–27.

[36] C. Song, M. Zhang, Y. Yang, D. Wang, Y. Jia-kuo, Morphology and properties of CoCrMo parts fabricated by selective laser melting, Mater. Sci. Eng. A. 713 (2018) 206–213. doi:10.1016/j.msea.2017.12.035.

[37] B. Qian, K. Saeidi, L. Kvetková, F. Lofaj, C. Xiao, Z. Shen, Defects-tolerant Co-Cr-Mo dental alloys prepared by selective laser melting, Dent. Mater. 31 (2015) 1435–1444. doi:10.1016/j.dental.2015.09.003.

[38] Z. Guoqing, Y. Yongqiang, L. Hui, S. Changhui, Z. Zimian, Study on the Quality and Performance of CoCrMo Alloy Parts Manufactured by Selective Laser Melting, J. Mater. Eng. Perform. 26 (2017) 2869–2877. doi:10.1007/s11665-017-2716-5.

[39] M. Zhang, Y. Yang, C. Song, Y. Bai, Z. Xiao, An investigation into the aging behavior of CoCrMo alloys fabricated by selective laser melting, J. Alloys Compd. 750 (2018) 878–886. doi:10.1016/j.jallcom.2018.04.054.

[40] M.V. Mergulhão, C.E. Podestá, M.D.M. das Neves, Valuation of Mechanical Properties and Microstructural Characterization of ASTM F75 Co-Cr Alloy Obtained by Selective Laser Melting (SLM) and Casting Techniques, Mater. Sci. Forum. 899 (2017) 323–328. doi:10.4028/www.scientific.net/MSF.899.323.

[41] E. Liverani, A. Fortunato, A. Leardini, C. Belvedere, S. Siegler, L. Ceschini, A. Ascari, Fabrication of Co-Cr-Mo endoprosthetic ankle devices by means of Selective Laser Melting (SLM), Mater. Des. 106 (2016) 60–68. doi:10.1016/j.matdes.2016.05.083.

[42] M. Béreš, C.C. Silva, P.W.C. Sarvezuk, L. Wu, L.H.M. Antunes, A.L. Jardini, A.L.M. Feitosa, J. Žilková, H.F.G. de Abreu, R.M. Filho, Mechanical and phase transformation behaviour of biomedical Co-Cr-Mo alloy fabricated by direct metal laser sintering, Mater. Sci. Eng. A. 714 (2018) 36–42. doi:10.1016/j.msea.2017.12.087.

[43] S.L. Sing, S. Huang, W.Y. Yeong, Effect of solution heat treatment on microstructure and mechanical properties of laser powder bed fusion produced cobalt-28chromium-6molybdenum, Mater. Sci. Eng. A. 769 (2020) 138511. doi:10.1016/j.msea.2019.138511.

[44] S.M.J. Razavi, A. Avanzini, G. Cornacchia, L. Giorleo, F. Berto, Effect of heat treatment on fatigue behavior of as-built notched Co-Cr-Mo parts produced by Selective Laser Melting, Int. J. Fatigue. 142 (2021) 105926. doi:10.1016/j.ijfatigue.2020.105926.

[45] Y. Kajima, A. Takaichi, N. Kittikundecha, T. Nakamoto, T. Kimura, N. Nomura, A. Kawasaki, T. Hanawa, H. Takahashi, N. Wakabayashi, Effect of heat-treatment temperature on microstructures and mechanical properties of Co–Cr–Mo alloys fabricated by selective laser melting, Mater. Sci. Eng. A. 726 (2018) 21–31. doi:10.1016/j.msea.2018.04.048.

Chapter 3

LASER-BASED POWDER BED FUSION OF CO28CR6MO BIOMEDICAL ALLOY

EXPERIMENTAL ANALYSES

Foreword

The present Chapter synthetizes the experimental activities carried out during the PhD research project on Co28Cr6Mo alloy for orthopedic implants processed by Laser-based Powder Bed Fusion (LPBF). Experimental analyses were firstly focused on investigating the relation between the LPBF process and sample properties. Once identified the optimized processing window, research effort was devoted at exploring low temperature aging treatment of the LPBF alloy and assessment of the effects on the most important properties required by final applications. The latter represents, with respect to the state of art described in the previous Chapter, the most important novelty of the presented work.

Therefore, the work focused on two main topics:

- Process optimization and investigation of the effect of Laser Energy Density (LED) on final samples properties (density, surface morphology, microstructural features, hardness).
- Optimization of post-process aging treatment and assessment of the wear and corrosion behavior of the untreated and heat-treated alloy.

The Chapter is mainly based on the following papers, for which I was involved as corresponding and first author:

- "*CoCr alloy processed by Selective Laser Melting (SLM): effect of Laser Energy Density on microstructure, surface morphology, and hardness*" by L. Tonelli, A. Fortunato and L. Ceschini published in the *Journal of Manufacturing Processes (vol.52:106–119, 2020)*

- The pre-print "*Aging treatment of the additively manufactured Co28Cr6Mo biomedical alloy and its effects on the wear and corrosion behavior*" by L. Tonelli, M. Seyedi, A. Balbo, C. Monticelli, M. Z. Ahmed, A. Fortunato, E. Liverani, L. Ceschini currently unpublished.

3.1 Process optimization: role of laser energy density on morphology, hardness and microstructure

This section contains selected parts of the published paper "*CoCr alloy processed by Selective Laser Melting (SLM): effect of Laser Energy Density on microstructure, surface morphology, and hardness*" (© 2020. This manuscript version is made available under the Creative Common license CC-BY-NC-ND 4.0). The published version of the paper can be accessed by the following link https://doi.org/10.1016/j.jmapro.2020.01.052

Journal of Manufacturing Processes 52 (2020) 106–119

Contents lists available at ScienceDirect

Journal of Manufacturing Processes

journal homepage: www.elsevier.com/locate/manpro

CoCr alloy processed by Selective Laser Melting (SLM): effect of Laser Energy Density on microstructure, surface morphology, and hardness

Lavinia Tonelli[a,*], Alessandro Fortunato[a], Lorella Ceschini[b]

[a] Department of Industrial Engineering (DIN), Alma Mater Studiorum - University of Bologna, Viale Risorgimento 2, 40136, Bologna, Italy
[b] Department of Civil, Chemical, Environmental and Materials Engineering (DICAM), Alma Mater Studiorum - University of Bologna, Viale Risorgimento 2, 40136 Bologna Italy

3.1.1 Aim and Scope

The benefits that additive manufacturing (AM) technologies, like laser-based powder bed fusion (also known as Selective Laser Melting, SLM), can bring to the biomedical field have already been illustrated in the literature [1–3]. Firstly, they allow an affordable customization to make the device fit the patient anatomy. In addition, for the specific case of Ti and Co-based alloys, AM process enables to overcome the limits imposed by the conventional manufacturing routes [4,5]. Several studies have been carried out on CoCrMo alloys processed with LPBF to realize such medical devices [6–13]. However, most of these studies focus on the technological and mechanical aspects and a comprehensive analysis of the effect

of different process parameters on the surface quality, microstructure and properties of the final components is currently lacking. Hence, the aim of the present study was to correlate the Laser Energy Density (LED) to surface quality of the as-build samples, microstructure and hardness. LED, defined by the $LED = P/(v \cdot h \cdot d)$ [J mm^{-3}], combines four major process parameters: laser power P [W], scanning velocity v [mm s^{-1}], distance between two consequent laser scans h [mm] and layer thickness d [mm]. Experimentally, several recent publications have indeed demonstrated that LED is directly related to some of the features involved in the densification process such as density, porosity content and defect formation mechanisms [14–17]. Based on the above, a number of CoCrMo samples have been processed via LPBF setting various process parameters in order to obtain a wide range of LED values, then a full microstructural investigation was carried out, along with the characterization of surface morphology and macro and micro hardness tests. The final purpose was to identify major process-related features (including material discontinuities) and to define an optimized LED interval.

3.1.2 Experimental Procedure

Gas atomized CoCrMo powder, provided by LPW Technology (LPW Technology Ltd, Runcorn, UK) were used for samples production. Powder particles were nominally spherical in shape and with size ranging from 15 to 45 μm. Their nominal chemical composition, given by the supplier, complied with the requirements of the ASTM F75 standard (Co-28Cr-6Mo casting alloy). Samples in form of blocks (20 x 6 x 30 mm^3) were realized using the LPBF equipment SISMA MYSINT100 provided with an Yb-fiber laser (λ = 1070 nm), a maximum power of 200 W and a nominal focused spot diameter of 50 μm. Samples were built in a nitrogen atmosphere with a low residual content of oxygen (0.3 vol%). Process parameters and scanning strategy were settled using MARCAM AutoFab software. A wide range of process parameters, reported in Table 3.1, were considered, in order to obtain several LED values. Scanning strategy of each layer was designed as a chessboard: the layer is divided in 3x3 mm blocks then the laser beam scans each block following parallel lines whose direction is perpendicular to the one of the adjacent blocks. Every next layer, the chessboard pattern is rotated by 45°.

Building direction of samples was unique and perpendicular to the un-heated base plate.

Table 3.1: Process parameters adopted for the production of samples, leading to different values of $LED = P/(v \cdot h \cdot d)$.

P [W]	***v [mm s^{-1}]***	***h [mm]***	***d [mm]***	***LED [J mm^{-3}]***
70; 90; 110; 130; 150	500; 700; 900; 1100	0.04; 0.06; 0.08	0.02; 0.03	43.21 - 267.86

Shape, morphology and chemical composition of powders were characterized by a Scanning Electron Microscope equipped with an Energy Dispersive X-ray Spectroscope (SEM-EDS, Zeiss EVO 50). The presence of internal porosity was assessed with Optical Microscopy (OM, Zeiss Imager A1) and SEM analyses of powders cross-sections. Both lateral and top surfaces of LPBF samples (as represented in Figure 3.1), were characterized by SEM-EDS analyses and surface roughness was evaluated with a stylus profilometer (Hommelwerke T2000, 5 µm tip radius). The density of all LPBF samples was determined following Archimedes' principle; at least three measurements were performed on each sample using an analytical balance (precision ± 0.0001 g). With respect to the building direction, the microstructural characterization was carried out both on longitudinal (L) and transverse (T) cross-sections, as shown in Figure 3.1. Prior to the microstructural characterization, standard metallographic techniques were used for samples preparation, including mechanical grinding (with 180–2500 grit SiC papers) and polishing up to 1 µm diamond suspension. Electrochemical etching was performed at 4 V for 20 s, in a solution of hydrochloric acid and ferric chloride dissolved in distilled water (5 mL HCl, 10 g $FeCl_3$, 100 mL H_2O) [18]. OM and SEM-EDS analyses were accomplished on both L and T samples produced under a wide range of LED values. With the aim to correlate the process parameters, in terms of LED, and the resulting microstructure, a number of measurements (such as porosity evaluation and estimation of laser tracks) were carried out using the ImageJ software for image analysis on both OM and SEM micrographs. Phase composition of samples produced with high, medium and low LED was determined by X-Ray Diffraction

(PANalytical Expert PRO with Xcelerator detector) provided with a Cu-Kα radiation source (λ = 0.15405 nm) and carrying out θ - 2θ scans from 30° to 100° with a 0.017° step size and a 15 s dwell time, performed at 40 kV and 40 mA. Hardness of the LPBF parts were evaluated both by Rockwell (HRC [19]) and Vickers (HV0.5, 10 s dwell time [20]) tests.

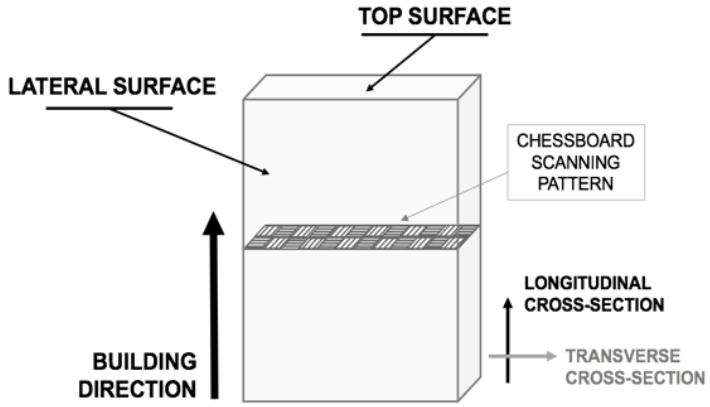

Figure 3.1: Scheme of surfaces for morphological investigations (Top and Lateral) and directions for metallographic samples extraction (Longitudinal and Transverse) from LPBF specimens.

3.1.3 Results and Discussion

POWDER CHARACTERIZATION

Powders particles were mainly spherical in shape even if satellites and collapsed particles were also detected on the surface of powders, making powders morphology uneven, as shown in Figure 3.2. Particles showed a fine dendritic structure, as highlighted by white arrows in Figure 3.2b. Dendritic phase is, indeed, distinctive of the feedstock powder since LPBF components, on the contrary, solidify with a cellular microstructure [21]. The chemical composition was investigated by SEM-EDS analyses on free powders and the results matched the standard of ASTM F75 [22]. As reported by Hebert [23] and Sames et al. [24], gas trapped in the feedstock powders might negatively influence the quality of the final parts, leading to the formation of bubbles in the melt pool. In this view, powders cross-sections were analyzed and, as shown in Figure 3.2c, no internal porosities were generally detected.

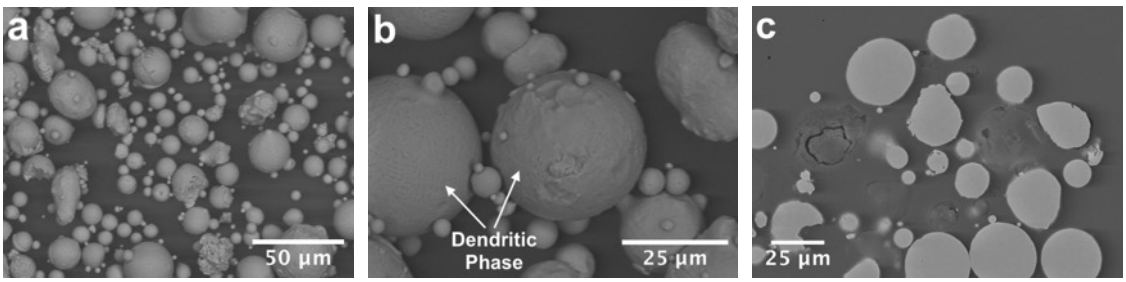

Figure 3.2: SEM micrographs: low (a) and high (b) magnification of free powder particles, (c) particles cross-section.

It is worth mentioning that in few cases it was possible to identify powders with an anomalous morphology, due to the presence of round darker regions, as reported in Figure 3.3. The particle showed an almost perfect spherical shape and a smooth surface, dendritic phase was clearly recognizable but darker areas could be also detected on the surface. SEM-EDS analyses, also reported in Figure 3.3, suggested the presence, in correspondence of darker areas, of oxides with a higher Si and Mn content and the presence of Al and Ca, while the chemical composition of dendritic phases still complied requirements for the ASTM F75 alloy [22].

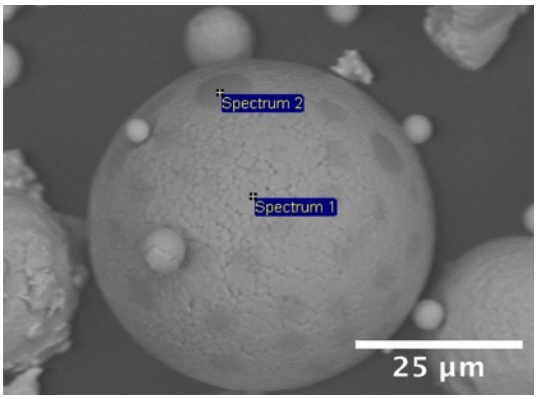

	O	Al	Si	Ca	Cr	Mn	Co	Mo
Spectrum 1	2.93	-	0.99	-	28.15	0.99	61.24	5.69
Spectrum 2	30.83	1.92	12.01	0.31	25.62	11.46	16.65	1.13

Figure 3.3: SEM-EDS analyses performed on anomalous powder particle: chemical composition (wt.%) of dendritic phase (Spectrum 1) and darker areas (Spectrum 2).

SAMPLES CHARACTERIZATION

Density measurements were carried out following the well-known Archimedes' method, repeating the measurement at least three times for each LPBF sample. For

the same alloy produced by additive manufacturing, this method proved to be quite accurate even when compared with more sophisticated technologies [25]. Results of density measurements as a function of LED are reported in Figure 3.4, where the nominal density of the conventional Co-28Cr-6Mo investment casting alloy, as specified in the ASTM F75 standard [22], is reported for comparison (dotted line). From density measurements, it is possible to define a critical value of LED (100 J mm^{-3}) beyond which samples produced by LPBF exhibited a density comparable to a conventional casting component. In few cases, the measured density was even higher than the reference one, presumably due to the superficial roughness of LPBF component and open porosities on the surface that might compromise the correct determination of sample weight when immersed in water. In this view, in order to verify the correspondence of density measurements with porosity content of LPBF parts, the actual area occupied by internal porosities was measured on polished cross-sections of selected samples using the ImageJ software for image analysis, results are still reported in Figure 3.4. By increasing the LED, internal porosity content decreased reaching the minimum value (approx. 0.1 area%) for LED value higher than 150 J mm^{-3}. Therefore, even if a LED value beyond 100 J mm^{-3} is sufficient to obtain parts with a density comparable to the conventional one, in order to obtain a sound component with an extremely low porosity content, such value has to be equal to or higher than 150. Based on these preliminary results and with the aim to better highlight the relationship between microstructural features and process parameters, the LPBF samples have been separated in three different classes, according to the LED applied during the process: low (up to 100 J mm^{-3}), medium (100-150 J mm^{-3}) and high (150-270 J mm^{-3}) LED classes. A total of 30 samples were produced in the current study, distributed as follows: 15 for the low, 10 for the medium and 5 for the high LED class. Low LED results in inadequate density and high porosity content, so in a poor quality of LPBF parts. Medium LED returns a porosity content less than 1 area%, while high LED values lead to almost defect-free samples.

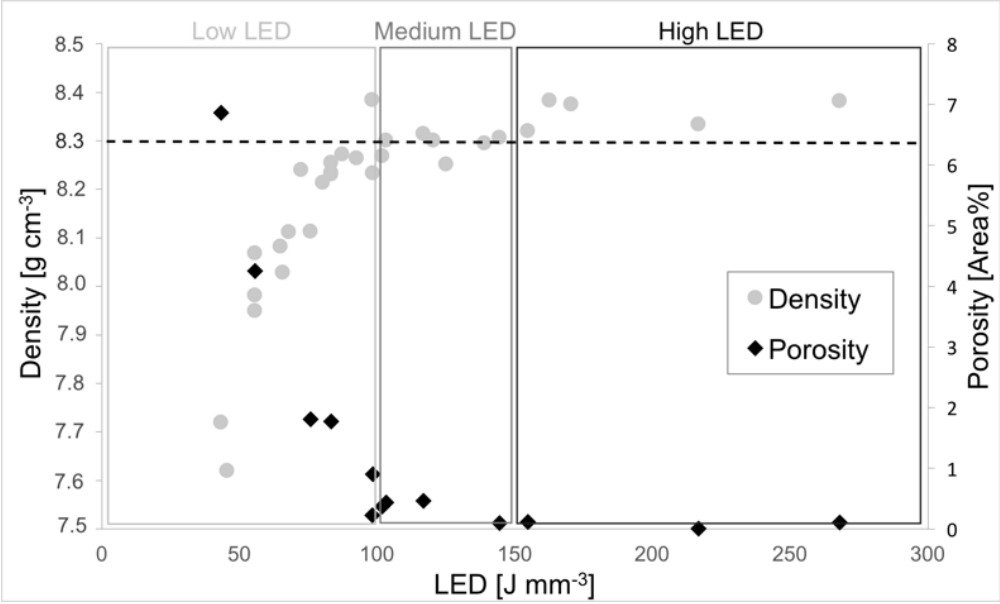

Figure 3.4: Density and internal porosity of LPBF samples as a function of LED, measured by Archimedes' method and image analysis on polished cross sections, respectively. Dotted line defines the reference value of a conventional cast component (8.3 g cm^{-3}) while frames define ranges of low, medium and high LED.

It is well known that an important feature of LPBF components is represented by surface quality and part of the recent literature has been focused on classifying the proper methodologies to perform surface metrology of AM products [26]. This technology, in fact, generates high surface roughness and, generally, LPBF parts need post-process finishing. With the aim to investigate the relationship between energy density and surface quality, the lateral and top surfaces of samples were characterized in the as-built conditions. Qualitative SEM analyses of the morphology of lateral surfaces, reported in Figure 3.5, showed no remarkable differences between sample processed with low, medium or high LED. Lateral surfaces are indeed mainly characterized by sintered or semi-molten powders, clearly identifiable by the dendritic phase, and porosities (as shown by the cross-section in Figure 3.6).

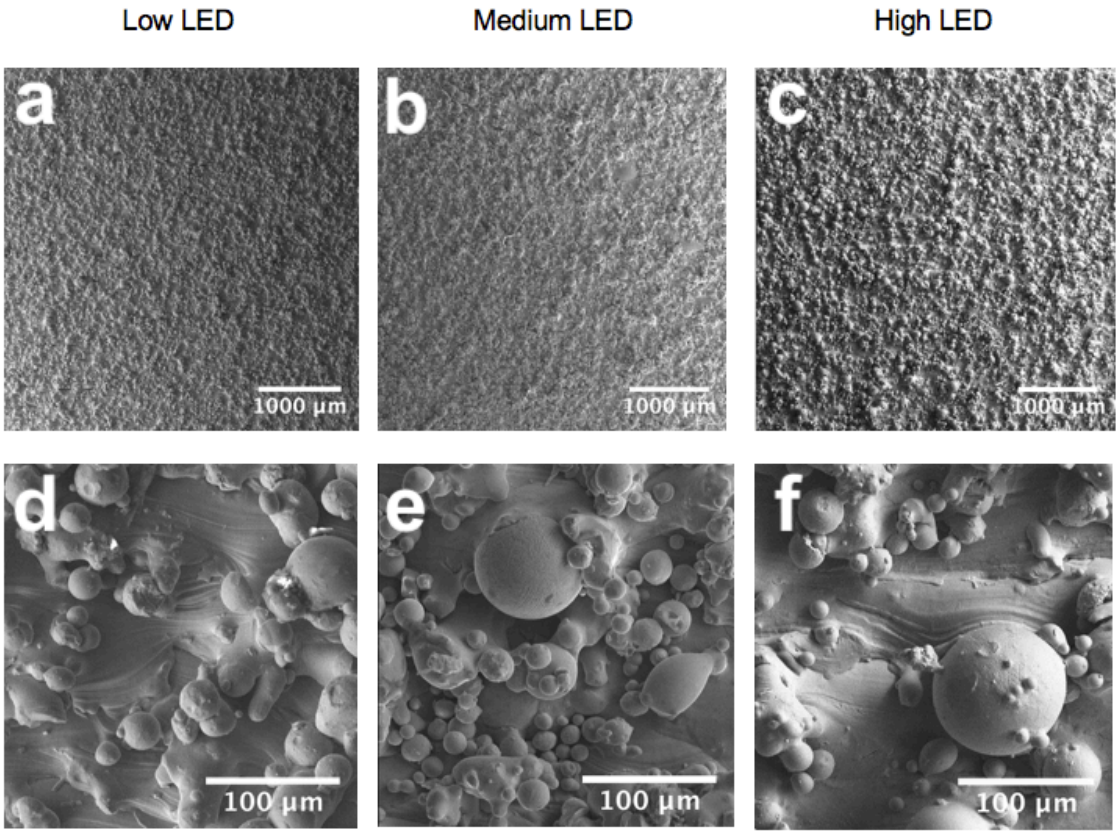

Figure 3.5: Low and high magnification SEM micrographs on lateral surface of representative samples processed with: (a) and (d) Low LED, (b) and (e) Medium LED, (c) and (f) High LED.

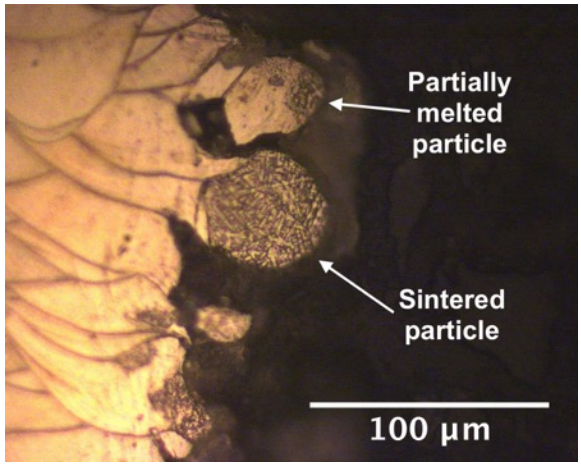

Figure 3.6: Optical Micrograph of a polished cross-section of a representative lateral surface

Profilometric measurements, summarized in Figure 3.7, confirmed the results of SEM analyses: they returned values of average surface roughness in the range Ra=8-12 μm and they are not directly related to LED. On the basis of these outcomes, it appears that stochastic phenomena, in terms of powders distribution in the layer, dominate the resulting roughness of lateral surfaces (in direct contact with the powder bed).

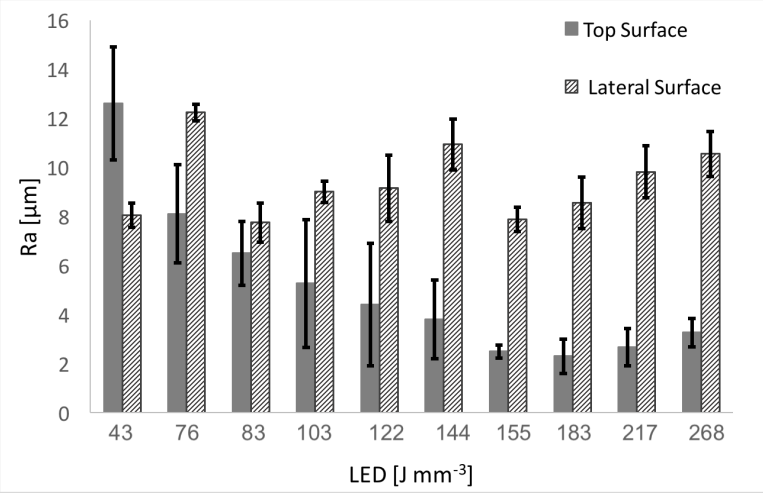

Figure 3.7: Average surface Roughness (Ra) measured on both lateral and top surface on samples with increasing LED values.

The roughness of the top surface, instead, was strongly dependent on LED: a low energy applied on the powder bed led to high roughness (max Ra=13 μm), while increasing LED produced smoother surfaces, reaching the lowest surface roughness value (Ra=2.5-3 μm) in case of samples produced with high LED (over 150 J mm^{-3}). The observation of top surfaces with the aid of SEM (Figure 3.8) allowed to explain the profilometric results: while for medium and high LED (Figure 3.8d,f) the chessboard scanning pattern was easily recognizable and laser scans were even and regular, in case of low LED (Figure 3.8a) the resulting surface is irregular, with discontinuous scans and cavities. High magnification micrographs of medium and high LED samples (Figure 3.8e,g) showed regular and narrowed laser scans, representing the solidified elongated molten pools with an analogue morphology for both samples, already observed by Zhou et al. [27]. It is worth mentioning that top surfaces of the as-built samples represent a single layer

of melted and solidified powder, consequently the analysis and observation of these surfaces are fundamental in order to appreciate melt pool dynamics and principal related aspects. Another important factor regarding surface quality is related to the deposition of the following layer of powders: a smooth surface, in fact, will improve flowability of particles. On the contrary, a rough surface might lead to an uneven distribution of powder particles with an evident downside on the quality of the final part. As already illustrated by other authors [28,29], the discontinuous and chaotic morphology showed by low LED samples is the result of an unstable melt flow that leads to the incomplete wetting and spreading of the molten material during the process. Therefore, irregularities can be ascribed to defects of material filling or localized lacks of fusion, as well as spatter ejection of molten material from the pool, bringing to cavities and coarseness, as showed in Figure 3.8b. As a consequence, porosities and partially melted powder particles can be easily detected on the surface of low LED samples, as represented in Figure 3.8c. Recent works [30–32] analyzed the dynamics of fluid and particles during laser powder bed fusion, highlighting that spatter ejection and denudation are phenomena strictly related to this technology and dependent on process parameters. The denudation is defined as a depleting of powders in the regions surrounding laser tracks [33], while spatter ejection is promoted by the so-called laser-induced plume. The laser plume tends to eject molten material away from the liquid pool and particles ejected from the liquid pool solidify before falling down on the powders bed and, by reacting with the residual oxygen in the chamber atmosphere, they may change their chemical composition [30]. The stability of the molten pool is dominated by the balance between spatter ejection due to the laser plume and Marangoni convection, that tends to spread molten material from the center of the melt pool to the outer regions [31]. Since the direction of the plume and its temperature are mainly dependent on scanning velocity, as well as on pattern and laser power, so on LED, a careful optimization of these parameters must be performed [32]. The relation between energy input and spatter ejection has been also investigated by Wang et al. [30] for a CoCrMoW dental alloy, showing that raising in the energy input leads to an increased spattering. In the present work, while in samples processed with low LED the molten pool was clearly unstable leading to a disarranged top surface, in samples processed with medium

and high LED the morphology of the top surface was even and regular and only a few discontinuities on the laser pattern could be observed (Figure 3.8d,e). Two kinds of defects were detected on the surface of medium and high LED samples: spattering and Marangoni flow related phenomena, represented in Figure 3.8h. Spattering appears as fully re-melted spherical particles that have been reincorporated in the layer. Marangoni flow is, instead, related to the local changes of surface tensions that affects the stability of the melt pool, so the proper wetting and spreading of the liquid. Oxygen content, in particular, plays an important role on local changes of surface tension by dramatically reducing it. Reduction in the surface tension reverses the direction of the Marangoni flow, leading to the formation of large globular islands, as already observed in the LPBF of tungsten [28].

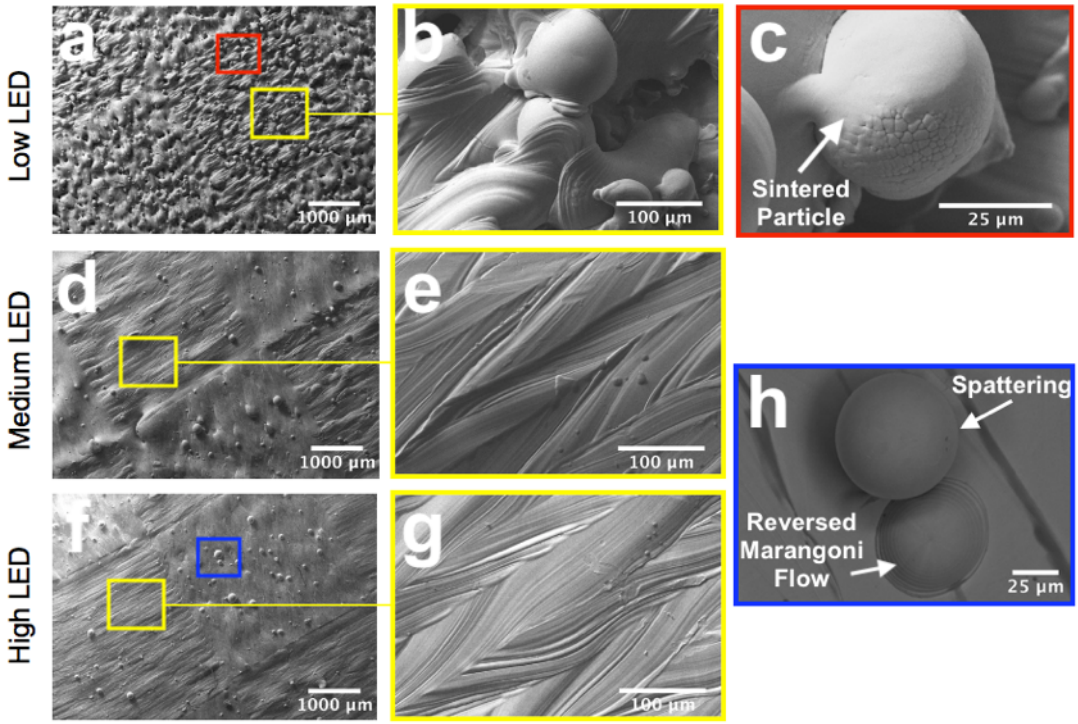

Figure 3.8: SEM analyses on top surface: (a), (d), (f) low magnification of low, medium and high LED samples; (b), (e), (g) details of area defined by yellow frames of low, medium and high LED samples, (c) details of area defined by red frame showing a sintered particle on low LED samples, (h) details of area defined by blue frame showing spattering and Marangoni-related defects on high LED samples.

Cross-sections analyses of the main defects observed on the top surfaces are reported in Figure 3.9: sintered particles (Figure 3.9a) were defined by the dendritic phase as previously observed in the feedstock powders; spattering defects (Figure 3.9c) showed no dendritic phase, proving that material underwent melting and then rapidly solidified into a spherical shape. Reversed Marangoni phenomena (Figure 3.9b) were clearly characterized by a centripetal, instead of a centrifugal, flow that moved the molten material from the outside into the center of the pool.

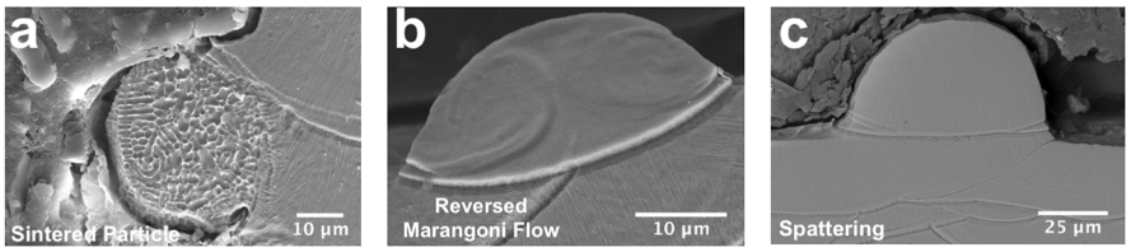

Figure 3.9: SEM micrographs of representative defects detected on top surfaces: (a) sintered particle on low LED samples, (b) reversed Marangoni flow and spattering defects on medium and high LED samples.

The presence of a local segregations along laser tracks was also verified via SEM-EDS analyses (Figure 3.10). Results showed that darker area (corresponding to the center and outer region of the melt pool) were characterized by a higher Si and Mn content (wt.%), with also a not negligible content of oxygen, Al and Mg, in particular located at the center of the track. Similar outcomes have been previously reported in the case of feedstock powders and, presumably, the two phenomena are related. It is possible that Al-O-Si compounds derive from the feedstock powder and, during solidification of the melt pool, high melting compounds are ejected into the liquid phase and segregation might occur, by the reason of the spreading of liquid phase driven by Marangoni flow from the center to the outer regions of the melt pool [21,31].

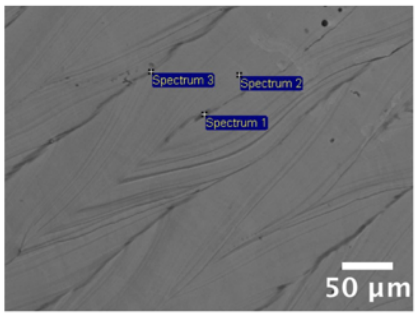

	O	Mg	Al	Si	Cr	Mn	Co	Mo
Spectrum 1	28.63	0.21	0.69	8.14	23.58	6.43	29.89	2.43
Spectrum 2	-	-	-	0.87	28.24	1.13	63.13	6.63
Spectrum 3	1.66	-	-	1.12	28.28	1.22	61.07	6.38

Figure 3.10: SEM-EDS analyses performed on a laser track on the top surface: micrograph showing the investigated regions and relative chemical composition (wt.%).

It is well known that LPBF parts are characterized by a hierarchical microstructure that can be divided in macro-level and micro-level microstructural features. Material discontinuities (i.e. defects) and texture fall within the first category, while morphology and size of grains and phase composition fall in the second one [34]. Next sections report on these macro and micro-level microstructural features.

MACRO-LEVEL MICROSTRUCTURAL FEATURES

Representative micrographs of T and L cross-sections of samples produced with different LED levels are illustrated in Figure 3.11. They clearly prove that process parameters, in terms of applied energy, have a noticeable influence on the final microstructure. Low LED values (Figure 3.11a,d) led to a chaotic microstructure, with a large extent of internal porosity and lacks of fusion, while medium (Figure 3.11b,e) and high values of LED (Figure 3.11c,f) led to a more regular and continuous microstructure, with a negligible presence of porosities, as also previously reported. On transverse cross-sections, the pattern resulting from the chessboard scanning strategy of each layer can be clearly identified, since laser tracks appear well highlighted by the etching. Longitudinal cross-sections, instead, evidence the melt pool overlap, due the highly localized melting of powder.

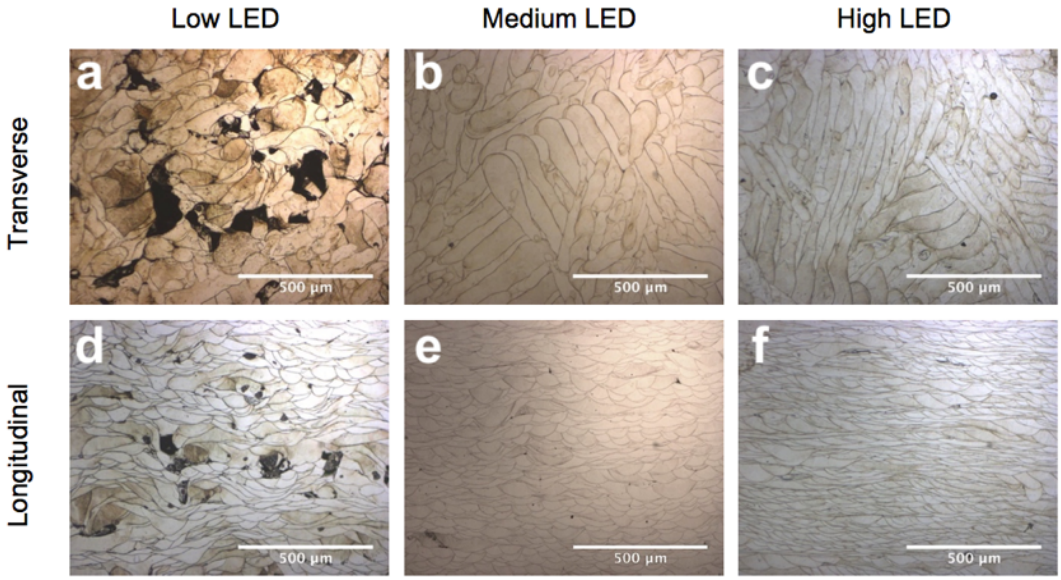

Figure 3.11: Low magnification optical micrographs of transverse and longitudinal cross sections samples produced with low (a) and (d), medium (b) and (e) and high (c) and (f) LED. Layer thickness was 0.03 mm for low LED sample and 0.02 mm for the medium and high ones.

On sound components, exhibiting an even microstructure and few solidification defects, a number of microstructural analyses were carried out: the width of the tracks left by the subsequent passages of the laser was evaluated on T-sections and an attempt to estimate the mean size of the residual melt pool area was carried out on L ones. In order to obtain a reliable value of the laser track widths, a total of 54 different measurements for each sample, distributed in different region of the T section, were accomplished and the results are showed in Figure 3.12a. According to the manufacturer, the nominal spot diameter for the LPBF machine used in this experiment is 50 µm and the majority of the investigated samples exhibited residual tracks wider than 50 µm, thus indicating that the actual volume of material involved in the melting process is wider than the one directly affected by the beam, on account of heat conduction.

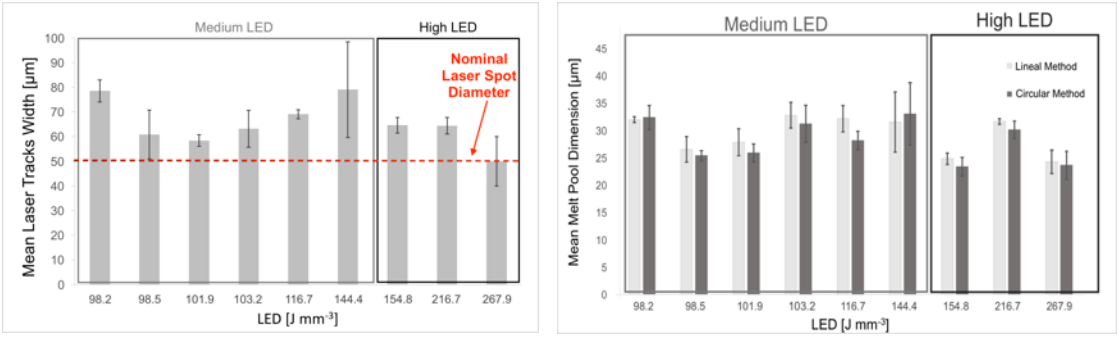

a b

Figure 3.12: Measurements performed on solidified laser tracks, displayed as a function on increasing LED: a) mean laser tracks widths measured on transverse cross-section of samples, the red dashed line defines the reference value of the nominal laser spot diameter; b) average dimension of the residual melt pool area measured with both diagonal and circular method (ASTM E112-12) on longitudinal cross-section of samples.

The dimension of the residual mean melt pool area was estimated by adapting conventional procedures for the evaluation of the average grain size described in the ASTM E112-12 standard [35]. The analysis was carried out with the aim to evaluate the average dimension of the residual melt pool area resulting from the whole LPBF process, that involves re-melting due to the processing of subsequent layers and complex scanning strategy, as the chessboard pattern rotated by 45° every next layer. Two methods were considered, based on the lineal and on the circular intercept procedure, being the first usually recommended for equiaxed grains and the latter suitable for deformed grains. The average dimension of the residual melt pool area was obtained by merely dividing the length of the intercepts for the number of crossed melt pools: a total of 9 different regions for each sample in the L section were investigated. The two methods returned comparable values for the average dimension of residual melt pool area (Figure 3.12b), ranging approximately from 25 to 35 µm. Since melt pools are almost semi-circular in shape and their sizes are related to the beam diameter (width) and layer thickness (depth) [21], it can be inferred that the measurements returned an estimation of the depth of the residual melt pool area (in this work layer thickness was set at 20 and 30 µm). The LED applied seems to have no direct connection to

the extent of the residual melt pool. It is possible that, by considering the value of the energy density, the single contribution of parameters such as laser power, layer thickness and hatch spacing was hidden. For instance, other researchers, through in-situ monitoring of the melt pool dynamic and analyses of laser tracks, demonstrated that laser power has an important role in determining the size and geometry of the pool: higher laser powers lead to deeper melt pool thus impacting the aspect ratio of the melt pool [31,36].

A preliminary characterization of material discontinuity (defects) was performed by optical microscopy (Figure 3.13).

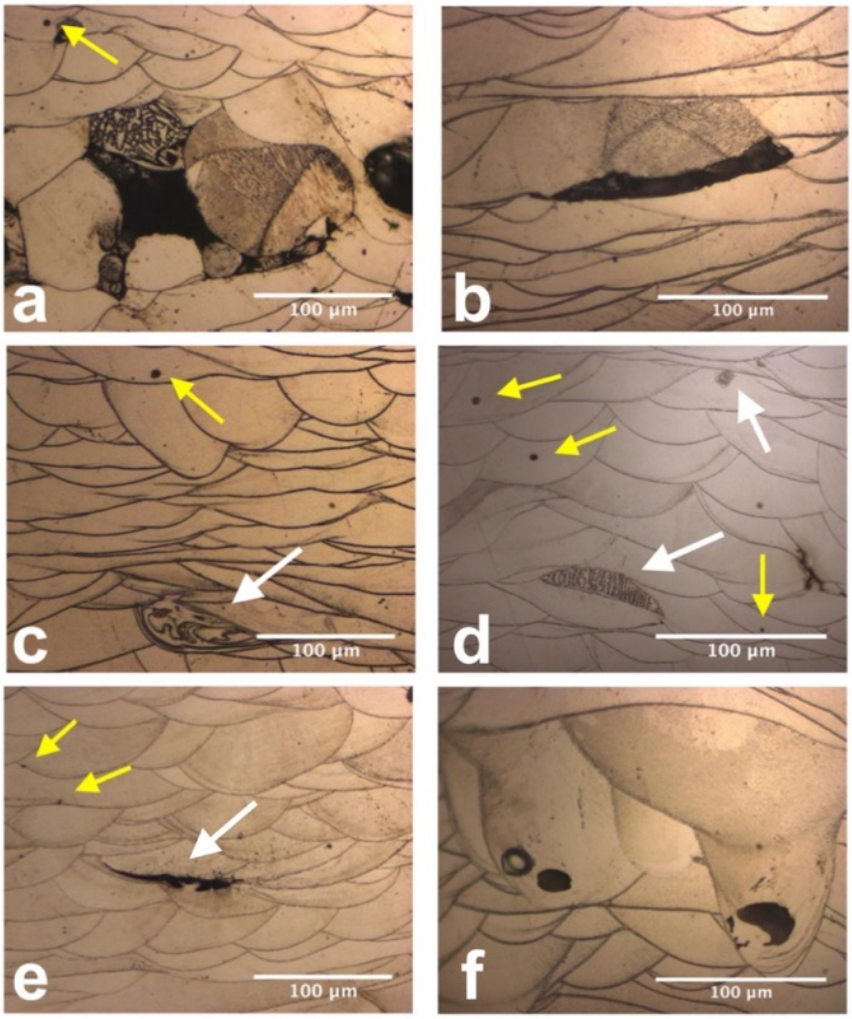

Figure 3.13: OM micrographs showing microstructural discontinuities found in longitudinal cross-sections of LPBF parts: a) and b) lack of fusion, c) Marangoni related phenomena (white arrow) and microporosities (yellow arrow), d) partially un-melted particles (white arrows) and microporosities (yellow arrows), e) crack (white arrow) and microporosities (yellow arrows), f) Keyhole phenomena.

According to Zhand et al. [37], common defects in LPBF parts can be classified in three categories: cavities due to incomplete fusion, porosities and cracks. Process parameters play a key role in determining type, amount and magnitude of such defects. Incomplete melting (Figure 3.13a,b), also named lack of fusion, is the most common defect in samples processed with a low LED value, where the applied energy is not sufficient enough to melt the whole material and leads to an unstable molten pool, as previously discussed. Lacks of fusion may present themselves as large and irregular cavities, where un-melted powders particles can be easily recognizable by their spherical shapes and dendritic phase, as represented in Figure 3.13a, or as cavities, located at the bottom of a melt pool, due to poor bonding to the underlying layer, as shown in Figure 3.13b. A number of porosities, indicated by the yellow arrows in Figure 3.13c,e could be detected on sample processed in the full range of parameters; these defects had the typical spherical shape of gas porosities and their size was generally lower than 10 μm. In the molten pool, due to high temperature, the gas solubility in the liquid metal is elevated and, since cooling rate is extremely high, the dissolved gas might remain trapped in the solidified metal, forming the characteristic spherical porosities. Considering that feedstock powders have been previously proved to be free of internal defects, such porosities might be process-related and consequent to both vaporization of alloy elements or dissolution of gas entrapped between metal powder during layer deposition. It is also possible to observe, in the L-sections of sound component, the classic Marangoni convection related phenomena, as indicated by the white arrow in Figure 3.13c. As formerly exposed, in the case of local changes of surface tension, the flow of molten material is reversed (from the edge of the molten pool to the center) and, once solidified, it results in a microstructural discontinuity. On sample cross-sections it is not uncommon to observed partially un-melted particles, identifiable by the dendritic structure as indicated by white arrows in Figure 3.13d. These defects could be found also in regular and homogenous microstructure, resulting from medium and high LED, where large cavities and major lacks of fusion were not present. An example of solidification crack is represented in Figure 3.13e. According to [38], three types of crack can be observed in AM components: solidification cracking occurring along the solidifying layer and due to the tensile stresses induced by thermal contraction, liquation cracking

that affects the partially melted zone, and delamination. Usually, solidification cracks can be easily distinguished from poor bonding cavities, even if they are both generally located at the bottom of a solidified melt pool: the latter are surrounded by irregular melt pool with a coarser microstructure (darker area in Figure 3.13b), while cracks can be found in a homogeneous and regular microstructure. It is worth mentioning that cracks were not very recurring in the analyzed samples, regardless of the LED value. According to Collins et al. [34], hot tearing is particularly related to high energy densities applied to the powders bed, therefore it is possible to hypothesize that the critical value of LED, beyond which hot tearing become substantial, was not reached in the present work. Finally, keyhole collapses can occur during powder bed fusion, leading to final defects similar to the one showed in Figure 3.13f. Keyhole melting mode was originally studied for laser welding [39] where, for a certain combination of process parameters (i.e. laser power, speed and beam diameter), material can experience a transition in the melting mode, changing from conduction to keyhole-mode. For low laser intensity (nominally lower than 10^5 MW cm^{-2}), heat transfer in the molten pool occurs by conduction; in the case of keyhole-mode the laser energy density is high enough to cause partial vaporization of elements, leaving a cavity inside the liquid pool, thus allowing the laser to penetrate more deeply in the material. The same mechanism has already been observed in LPBF parts [40,41]: the conduction mode lead to the formation of almost semi-circular solidified melt pool, with a ratio between depth and width of approximately 1:2. When keyhole collapse occurs, the shape is no longer semi-circular, the depth is greater and the 1:2 ratio is no more respected. For the same reasons previously exposed, the gas formed by vaporization of elements can be entrapped in the solidified material, generating porosity in the final microstructure located at the end of the collapsed melt pool, as reported in Figure 3.13f. Keyhole formation is strongly related to the laser-powder interaction: preliminary studies demonstrated that, by increasing the time of interaction between the laser and the material, keyhole collapse is favored [31,41], thus laser speed is a relevant parameter. For a fixed time of interaction, instead, higher laser power may cause the transition from conduction to keyhole melting mode, leading to an unstable liquid pool and the formation of pores

located at the bottom of the melt pool [31]. In this work it was found that keyhole phenomenon is rather limited if LED is lower than 200 J mm^{-3}.

The same microstructural discontinuities were also observed by SEM and common detected defects are represented in Figure 3.14: lack of fusion (Figure 3.14a), porosity located at the bottom of the melt pool (Figure 3.14b), solidification cracking to the high thermal gradient (Figure 3.14c) and reversed Marangoni flow (Figure 3.14d). In the cavity, consequent of insufficient melting, the feedstock powder particles almost unaffected by the laser beam can be easily recognized, as well as the partially melted material and cracks propagating from the cavity to the surrounding solidified material. Gas porosity and hot tearing were usually discovered in regular and homogeneous microstructure, as showed in Figures 3.14b,c. Finally, when the convection flow due to Marangoni effect is reversed, the molten material solidified in a very chaotic and inhomogeneous microstructure (Figures 3.14d), where a few micro-porosities could be detected but no evidence of segregation was ascertained.

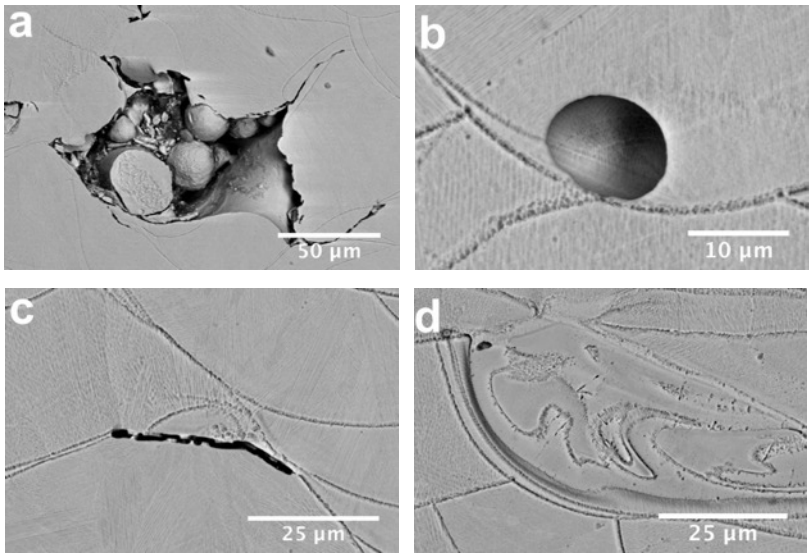

Figure 3.14: SEM micrographs showing discontinuities found in longitudinal cross sections of LPBF parts: a) lack of fusion, b) porosity, c) crack d) Marangoni related phenomena.

On samples L and T sections a few inhomogeneities, peculiar of CoCr alloys, were detected. For instance, a Si-rich particle is represented in Figure 3.15a; such

spherical inclusions have been already observed in the Co-28Cr-6Mo alloy processed with investment casting [42,43] and in a CoCrW dental alloy produced by three different processes (casting, milling and SLM) [44]. In the present study, a Si-rich oxide film was observed also in correspondence of a crack (Figure 3.15b). Similar inclusions have been previously observed in the feedstock powders and on the top surfaces of LPBF samples. SEM-EDS analyses performed on such inclusions revealed, as reported before, a higher content of Si, O and Al, as observed also by Giacchi et al. [43].

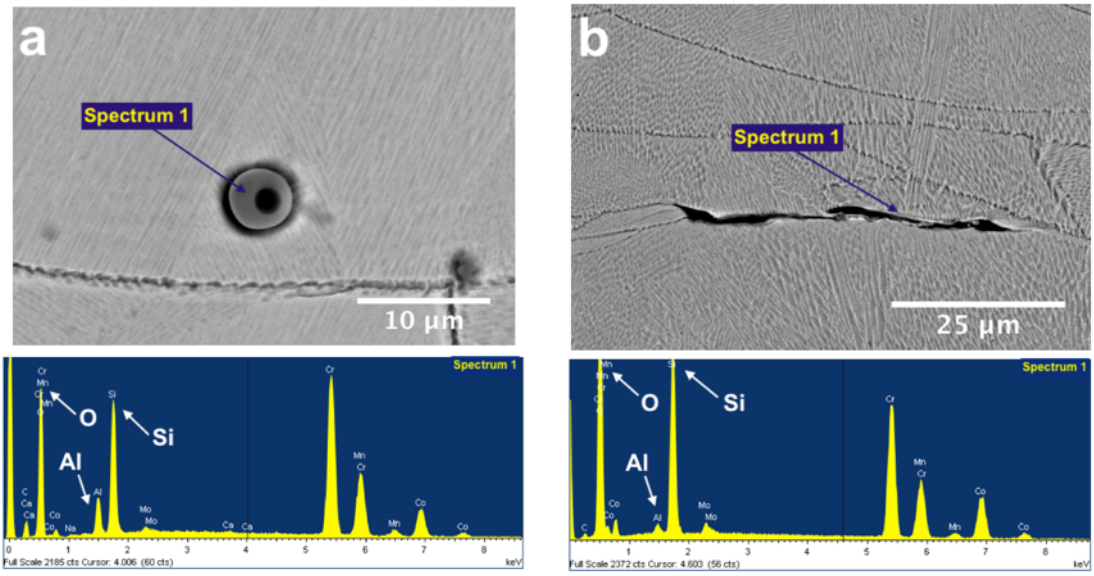

Figure 3.15: SEM-EDS analysis of microstructural discontinuities peculiar of CoCr alloy: a) Si-rich particle, b) crack with a Si-rich film.

Electrochemical etching of polished cross-sections and following observation under polarized light microscopy (Figure 3.16), revealed a texture showing preferential solidification and columnar grain growth in the direction of the highest temperature gradient, as already observed by other researchers for the same alloy [6,8,36] and generally for some metals processed by LPBF [34]. In the representative optical micrographs of the L section (Figures 3.16c,d) it is possible to observe that columnar grain growth crossed over layers, generally replicating the grain orientation of the previous layer (epitaxial growth). The epitaxial growth

is governed by the heat flux and the orientation of the underlying solidified material, namely the previous processed layer. Grain growth is not oriented exactly in the same direction of the heat flux, therefore perpendicular to the layer; instead, for Co-Cr alloy [6,8] as well in the case of different metals with a cubic structure [45,46], it follows a preferential crystallographic orientation, usually one of the <100> family, close to the thermal gradient direction. However, by alternating the laser scanning direction and by rotating the scanning pattern across layers, it is possible to alternate heat flux direction resulting in a preferential <111> orientation [21,33,47]. It appears that the solidification process started in correspondence of pool boundaries and grains have grown directly from the previous layer, without changing direction. The real-time monitoring of LPBF technology applied on Ti6Al4V alloy [31] demonstrated that solidification begins from boundaries of the semi-circular liquid pool and that grain growth is radial, approximately oriented along a direction comprised between the maximum local thermal gradient and the preferential growth orientation.

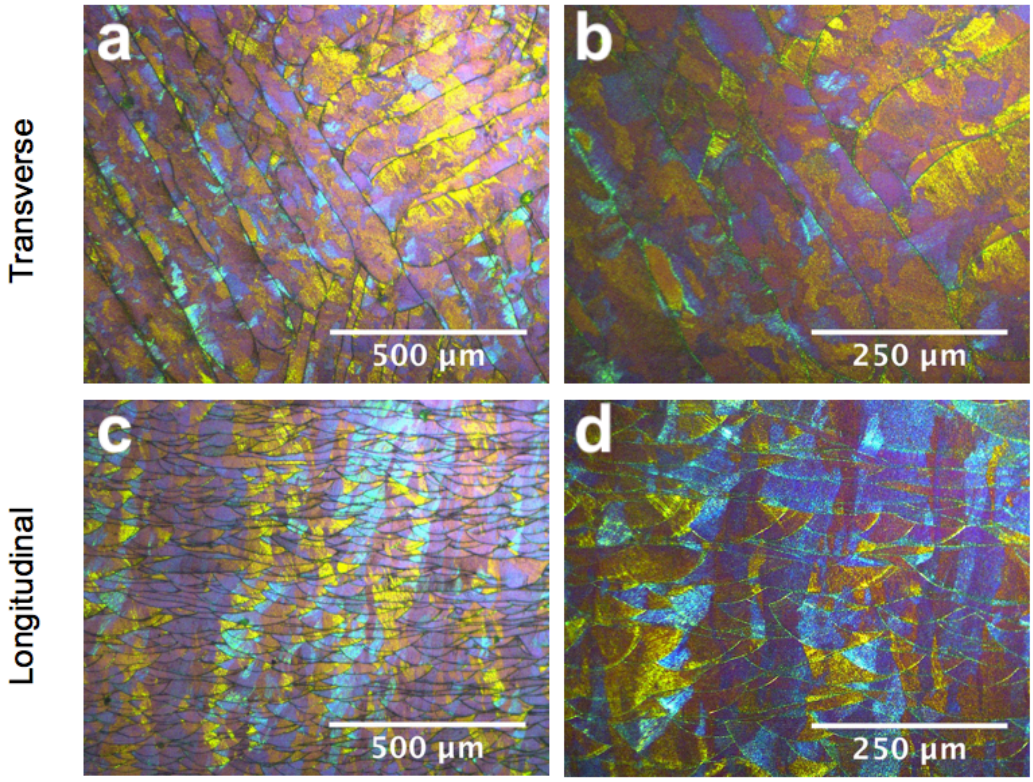

Figure 3.16: Optical micrographs in polarized light of a representative sample produced with LED higher than 150 J mm^{-3}: (a) low and (b) high magnification of transverse cross-section, (c) low and (d) high magnification longitudinal cross-section.

MICRO-LEVEL MICROSTRUCTURAL FEATURES

At the micro-level scale all investigated samples, regardless the LED value, exhibited the same microstructural features, peculiar of the LPBF technology and consequent to the extremely rapid solidification that leads to the formation of a metastable cellular microstructure [21]. Representative high magnification SEM micrographs are reported in Figure 3.17. The previously discussed epitaxial grain growth crossing over layers is evident in Figure 3.17a: at least two growing directions can be clearly recognized, where elongated columnar grains can be identified. In the same image the collision between two growing directions is represented, as indicated by the white arrow in Figure 3.17a. It has indeed been reported [8,34] that grain growth is competitive and, when two different directions intercept, one of them might stop. The analyses revealed the presence, inside the solidified melt pools, of an extremely fine sub-micron sized cellular grain structure. These results are consistent with the outcomes reported by other authors for the same alloy processed via LPBF [6–8,11]. Size and morphology of cellular grains can change between melt pools and even locally inside the same one: as represented in Figure 3.17b, cellular grains can be either almost circular or elongated, and grain size may vary from adjacent melt pools. Following the work done by Darvish et al. [36], an evaluation of the primary spacing of dendrites/cells (λ_1) was carried out on samples processed with low, medium and high LED, in order to verify if a correlation between the energy density and λ_1 exists. From this preliminary investigation it seems that the energy density does not exert a determinant influence on cells size; the average value measured in this experiment for λ_1 is 0.6 μm and it is consistent with literature data [36]. In addition, it is worth mentioning that very fine spherical porosities, with dimension lower than 1 μm, can be found in the microstructure, as highlighted by the white circle in Figure 3.17b. A SEM image at higher magnification of a melt pool boundary is reported In Figure 3.17c. According to the literature [6,7,10] a micro-level segregation between the core of cell grain and boundaries exists: center of the cell is rich in CoCr, while a higher concentration of Mo can be found at the grain boundaries. A number of SEM-EDS analyses were carried out in correspondence of track (melt pool) boundaries, with

the aim to verify possible segregation, but no evidence of enrichment of any of the alloy elements was found.

According to Prashanth and Eckert [21], rapid solidification favors the formation of a cellular microstructure in which the CoCr phase directly forms from the liquid and grows epitaxially from melt pool borders, ejecting Mo into the liquid. As a result, Mo is deposited on cellular boundaries. The formation of the cellular microstructure involves thermodynamic and kinetic theories, as well as physical aspects such as high thermal gradients and surface tension, that lead to the previously mentioned Marangoni convection flow that can cause solute accumulation [21]. The occurrence of solute accumulation was also confirmed by Qian et al. [7] by reporting TEM analyses that revealed Cr and Mo enrichment in correspondence of cellular boundaries. SEM-EDS analyses were also performed on different areas of low, medium and high LED samples, with the purpose to verify if chemical composition of final LPBF samples diverges from the one of the powders and if major vaporization of alloy elements occurs at high LED level. The results showed that the average chemical composition complied with the requirements and no differences between samples were highlighted. No massive vaporization of elements was documented, even at high LED value.

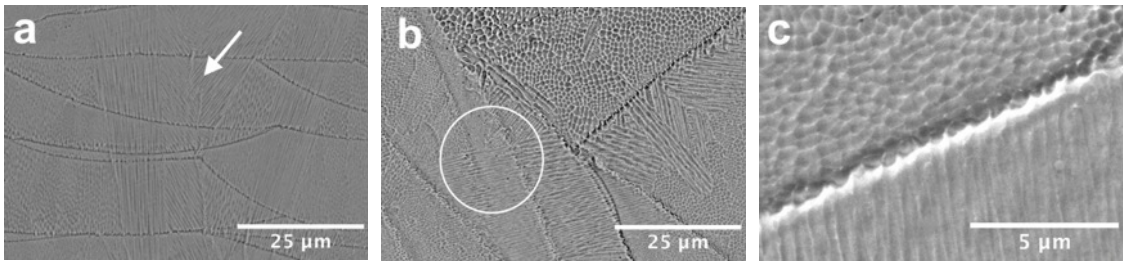

Figure 3.17: High magnification SEM micrographs of LPBF parts cross-sections: the white arrow in a) indicates the intersection between two growing directions, the white circle in b) underlines sub-micro-sized porosities, c) magnification of a melt pool boundary.

Results of the X-ray diffraction analyses performed on longitudinal section of samples obtained at the three different level of LED are reported in Figure 3.18. The XRD spectra show that LPBF samples mainly consist of γ (Co-fcc, ICDD:15-

806) and ε (Co-hcp, ICDD:5-727) phases. At high LED value, the ε phase is slightly reduced in favor of the γ phase, while at low LED the two phases are almost equally present. This result suggests that different volume energies lead, as mentioned before, to different thermal gradients, thus facilitating or hindering the γ to ε transformation. Similar results were also reported by Molinari [48], for the same alloy produced by LPBF under different process conditions. It is worth nothing that, according to the equilibrium phase diagram, the ε-hcp phase is stable at room temperature, while the γ-fcc phase is the high temperature stable phase (900-950°C). However, as also observed in conventional CoCr castings, since the transformation from fcc to hcp phase, occurring during cooling, is sluggish, usually the γ-fcc phase still exists at room temperature [49]. In addition, high cooling rates and small grain size (<100 μm), peculiar of the LPBF technology, might suppress the γ - ε transformation [6].

Due to the superposition of reflections of γ and ε phases, peaks approximately located at 2θ=44,75 and 92° correspond to both phases. For all samples, the highest intensity peaks were the ones located at about 2θ=44°, corresponding to γ(111) and ε(002), and at about 2θ=47.5°, corresponding to ε(101). This result confirmed a preferential crystal orientation, as reported in the literature and previously discussed in the present research.

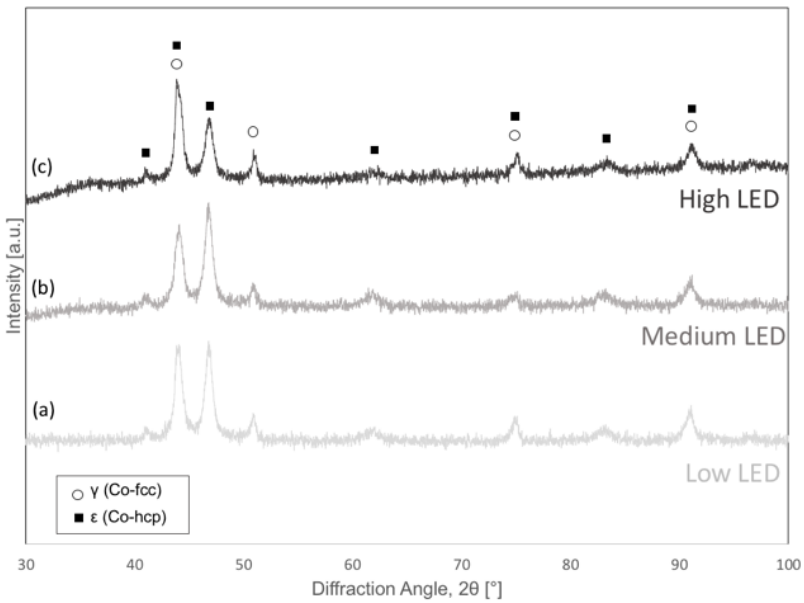

Figure 3.18: XRD analysis performed on representative LPBF samples processed with: a) low, b) medium, and c) high LED.

HARDNESS MEASUREMENTS

Both macro (HRC) and micro (HV0.5) hardness were evaluated for the investigated samples, and reported in Figure 3.19 as a function of LED. Standard requirement for samples produced with conventional casting is 25-35 HRC in the as-cast condition [22]. As a result of the extremely fine microstructure, all but two samples fulfill the requirement, even in the case of low energy density, thus an elevated porosity content (Figure 3.19a). Most of the samples exhibited even greater hardness, especially when their density was high (meaning LED>100 J mm^{-3}): samples of near-full-density presented an average hardness value of 36 ± 1 HRC. Microhardness measurements (HV0.5) were also performed on single melt pools, both on transverse and longitudinal cross sections, and the results are reported in Figure 3.19b. So as for the micro-level microstructure, the laser energy density did not show a direct influence on microhardness of the LPBF samples, since samples processed with very different LED returned a very similar microhardness. Average microhardness values lied in the range 380-430 HV0.5 and, for the majority of samples, transverse cross-sections exhibited a lower hardness than the corresponding longitudinal ones, even if a high standard deviation was registered. These results might be ascribed to the intrinsic anisotropy that the LPBF technology induces on the as built components, as a result of the strongly oriented columnar grain growth. Microhardness values are consistent with the ones reported for the Co-28Cr-6Mo alloy processed via LPBF by Mergulhão et al. [11] and slightly lower than those measured by Qian et al. [7].

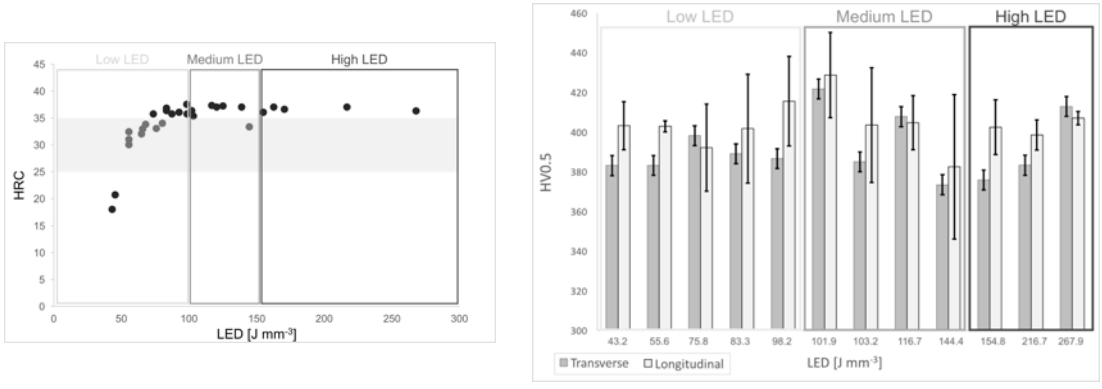

Figure 3.19: Hardness measurements of LPBF samples as a function of LED: a) HRC results where grey band defines requirements given by ASTM F75 for a conventional cast component; b) HV0.5 performed on metallographic cross-sections.

3.1.4 Conclusions

In the present work, surface, microstructural and hardness properties of Co-28Cr-6Mo samples realized by LPBF were thoroughly analyzed, with the aim to establish a correlation between the aforementioned properties and process parameters. A wide range of process parameters were considered, in order to explore a wide range of energy densities (LED=43.2 - 267.9 J mm^{-3}). Hence, all outcomes have been related to three different classes of LED: low (up to 100 J mm^{-3}), medium (100-150 J mm^{-3}) and high (150-270 J mm^{-3}). The following conclusion can be drawn:

- Low LED is not enough to fully melt the feedstock powder particles and results in a liquid pool highly unstable. In account of extensive lacks of fusion, being the dominant defect, LPBF samples exhibited a porosity content in the range 1-7 area%, high roughness on the top surface (Ra=13-7 μm) and a considerable variability in the microhardness of samples, ranging from 18 to 36 HRC.
- Medium and high LED succeeded in complete melting and returned sound components, with a very low porosity content (0.5-0.1 area%) and smother top surfaces (Ra=5-2.5 μm); in addition, hardness values settled at 36 ± 1 HRC, with a very low variability. Dominant defects were micro-sized gas porosities although, if the energy density is to high (LED > 200 J mm^{-3}), keyhole collapses occasionally occurred.
- The energy density seems to have no direct effect on the quality of lateral surfaces of samples and on the laser tracks size, both on the transverse and longitudinal sections. In this view, further investigations might be conducted with the aim to identify the role of single process parameters. However, a promising roughness lower than Ra=10 μm for lateral surfaces and lower than Ra=4 μm for top surfaces, was obtained.
- At a micro-level scale, the microstructure of all samples exhibited similar features: cellular grains with epitaxial growth crossing over layers, oriented along the direction of the maximum heat gradient. Moreover, micro-hardness on single melt pools seems to have no direct correlation with LED

values and measurements performed on transverse and longitudinal sections highlighted a minor anisotropic behavior.

3.2 Heat treatment, wear and corrosion behavior

This section contains selected parts of the currently unpublished paper "*Aging treatment of the additively manufactured Co28Cr6Mo biomedical alloy and its effects on the wear and corrosion behavior*".

3.2.1 Aim and Scope

Co28Cr6Mo alloy is commonly used as biomaterial for the production of orthopedic prostheses and can be proficiently processed with laser-based additive manufacturing technology for the production of customized implants. Apart from biocompatibility and high corrosion resistance, the major properties required by load-bearing applications are elevated mechanical strength and wear resistance. While mechanical properties of the LPBF alloy, in terms of tensile and compression, have already been investigated in the literature [7,9,11], the assessment of wear behavior is currently lacking. In addition, the conventional cast Co28Cr6Mo alloy is usually subjected to post-process heat treatment in order to homogenize the as-cast cored microstructure and to induce the transformation from γ-fcc to ε-hcp phase, that is characterized by a higher strength. As regards the Co28Cr6Mo LPBF alloy, literature works up to know have been devoted to study the high-temperature (1150-1220 °C) solution treatment with and without a subsequent aging treatment (750-900 °C) [12,50–52], as well as to investigate long-time annealing (750-1150 °C)[53] and to assess their effects on microstructure and mechanical properties. Based on the above, in view of the extremely fine, supersaturated and metastable microstructure resulting from LPBF, in the present work only short-time (30-180 min) aging treatments in the range 600-900 °C, without a preliminary solution treatment, were considered and effects on hardness

and microstructure were investigated. Once identified the optimized aging treatment, wear tests were conducted on the as-built and heat-treated alloy and compared to the conventional Co28Cr6Mo wrought alloy, currently used as a standard material for orthopedic implants. Finally, preliminary evaluation on the corrosion resistance in a phosphate-buffered saline solution for the conventional wrought alloy and the LPBF as-built and heat-treated alloy was carried out.

3.2.2 Experimental Procedure

Based on the results obtained from the experimental work discussed in Section 3.1 and using the same powder batch and printing machine, samples were fabricated in the range of Laser Energy Density (LED=120-170 Jmm^{-3}) close to the optimized one, using parameters disclosed in Table 3.2. Samples in the form of blocks (6x20x30 mm^3) were fabricated in a nitrogen atmosphere with a vertical building direction and adopting the previously discussed chessboard scanning strategy. Samples were classified in three different sets as follows: heat-treatment (HT), wear tests (W), and corrosion tests samples. HT samples were used for the preliminary heat treatments investigation with the aim to define the optimized heat treatment conditions. The other sets of samples (W1, W1HT, W2, W2HT, W3, W3HT and C1, C1HT, C2, C2HT) were dedicated to wear and corrosion tests and, with the aim to assess the influence of LED on tribological and corrosion properties, samples have been produced with different values of LED. As a reference, the commercially available conventional ASTM F1536 wrought alloy supplied in the warm worked condition has been subjected to wear tests.

Table 3.2: Process parameters adopted for the fabrication of Co28Cr6Mo LPBF samples

Samples	***Laser Power [W]***	***Scanning velocity [mm s^{-1}]***	***Layer Thickness [mm]***	***Hatching Space [mm]***	***LED [J mm^{-3}]***
HT	90; 130; 150	900; 500; 1100	0.02	0.04; 0.06; 0.08	120-170
W1, W1HT	150	1100	0.03	0.06	97
W2, W2HT	130	700	0.02	0.06	155
W3, W3HT	150	500	0.02	0.06	250
C1, C1HT	90	500	0.02	0.06	150
C2, C2HT	150	500	0.03	0.06	167

Heat treatments, whose conditions are synthetized in Table 3.3, were carried out on as-built samples in a muffle furnace operating in ambient atmosphere and were followed by water quenching. As mentioned above, HT samples were used for the assessment of aging behaviour of the alloy and were subjected to all heat treatments, while only the optimized treatment was applied to the wear (W1HT, W2HT, W3HT) and corrosion (C1HT and C2HT) samples. Temperatures for heat treatment assessment were chosen on the basis of the time-temperature-precipitation (TTP) curves for the Co28Cr6Mo cast alloy published by Taylor et al [54], with the aim to induce aging of the alloy. Due to the very fine microstructure of the additively manufactured alloy and consequent its short diffusion paths, only short soaking times were considered (30, 90, 180 minutes) in order to avoid undesired grain growth.

Table 3.3: Conditions (temperature and soaking time) of heat treatment applied to the sets of Co28Cr6Mo LPBF samples

Samples	***Temperature [°C]***	***Time [minutes]***
HT	600, 700, 750, 800, 850, 900	30, 90, 180
W1HT W2HT W3HT	850	180
C1HT C2HT	850	180

With the aim of verifying the repeatability of heat treatments within the range of optimized LED, firstly the response to aging treatment was assessed on HT samples processed with LED=120 J mm^{-3}, then the same treatments were repeated for samples processed at LED=170 J mm^{-3}. As a first evaluation of the effect of heat-treatments, aging curves have been obtained for HT samples, by measuring Rockwell hardness (HRC [19]) for each temperature-time combination. Micro-

hardness (HV0.5 [20]) was estimated by Vickers tests carried out, with a 500 g load and a 15 s dwell time, on polished surfaces of samples already used for microstructural analyses.

Microstructural analyses were carried out via optical (OM, Zeiss Imager A1) and scanning electron (SEM, Zeiss EVO 50) microscopy on polished and etched surfaces of both heat-treated and as-built samples. The microstructure of samples was characterized on cross-sections obtained along the building direction (longitudinal cross-section) that followed the same metallographic procedure already described for the microstructural analyses (Section 3.1.2). Phase composition of as-built and heat-treated samples was obtained with X-ray diffraction analyses (XRD, PANalytical Expert PRO with Xcelerator detector) operating with a CuKα tube (λ = 0.15406 nm) at 40 mA and 40 kV. Spectra were acquired in the range 30-100° with 0.05° step size and 15 s dwell time. Phase identification on XRD spectra was then performed with the Xpert Highscore Plus software. A differential thermal analyzer (DTA, Rheometric Scientific STA 1500) was used to perform thermal analyses on the as-built samples. Scans were recorded in the range 30-1200 °C by heating specimens of about 100 mg in Ar atmosphere with a heating rate of 10 °C min^{-1} in an Al_2O_3 crucible. DTA curves were then elaborated with the RSI Orchestrator software.

Sliding wear tests under unlubricated and ambient temperature conditions were conducted in order to compare the friction and wear behavior of as-built, heat-treated and conventional conditions. To this aim, a standard bearing steel (AISI 52100) was chosen as a counter material, heat-treated to 62 HRC hardness. Dry-sliding wear tests were carried out on a slider-on-cylinder tribometer (block-on-ring contact geometry [55]) and sliders (5x5x30 mm^3) were extracted from the LPBF samples. Prior to tribological tests, surface roughness and hardness on sliders and cylinder were measured by means of a stylus profilometer with a tip radius of 5 μm (Hommelwerke T2000) and HRC hardness test, respectively. Wear test parameters are reported in Table 3.4; in the same table, also contact pressures can be found, estimated according to the Hertzian theory [56]. In the formula, while a reference value of 208 GPa for the elastic modulus of AISI 52100 was implemented [57], the elastic modulus for the LPBF CoCr alloy was experimentally measured on as-built samples via non-destructive ultrasonic method, whose principle is

described in the literature [58]. An average value of 240 ± 12 GPa was found. Coefficient of friction (COF) was continuously recorded during the tests by means of load bending cells, then for each test the steady-state COF was calculated as average value after the run-in distance, set at 500 m. Wear scars dimensions on sliders, in term of depth and width, were characterized by stylus profilometry while wear mechanisms were investigated by means of SEM-EDS analyses. The phase composition of the oxide layers formed on wear scars was evaluated by μRaman spectroscopy.

Table 3.4: Wear tests conditions and relative Hertzian contact pressures

Samples	*Applied Normal Load [N]*	*Sliding Distance [m]*	*Sliding velocity [m s^{-1}]*	*Peak Contact Pressure [MPa]*	*Mean Contact Pressure [MPa]*	*Counter-material*
W1, W1HT W2, W2HT W3, W3HT Wrought alloy	5; 10	5000	0.3	44; 62	35; 49	AISI 52100

Preliminary tests on corrosion resistance were carried out with electrochemical impedance spectroscopy after 1- and 15-days immersion in Phoshate-Buffered Saline (PBS) solutions at pH 4 with 20 mM of H_2O_2.

3.2.3 Results and Discussion

AGING RESPONSE

Hardness evolution as a result to the exposure at high temperature for a given time are represented in the aging curves of Figure 3.20. In the same figure, as a reference, also the hardness of the as-built alloy, whose mean value is 37±1 HRC, is reported (black dashed line). All treatments induced strengthening with the greatest hardness obtained for 800 and 850 °C treatments. For all treatments performed in the range 600-850 °C the increase in HRC hardness as a function of

soaking time was progressive and almost linear, reaching the maximum of 40 HRC in case of low-temperature treatments (600-750 °C) and approximately 47 HRC for the high temperature ones (800-850 °C). Aging treatment at 900°C, instead, showed a drop in hardness after holding for 180 min. Microhardness measurements ($HV_{0.5}$) showed comparable results and, by focusing on the condition of soaking for 180 minutes (Table 3.5), it can be noticed that microhardness progressively increased up to the temperature of 850 °C, and then dropped to value comparable to the as-built condition for the 900 °C treatment. As a consequence, based on hardness measurements, the 850 °C for 180 min treatment was found to be the most efficient to induce alloy strengthening. As mentioned in the experimental section, aging treatments were performed for samples obtained with LED=120 J mm^{-3} and LED=170 J mm^{-3} and in both cases the same results were obtained.

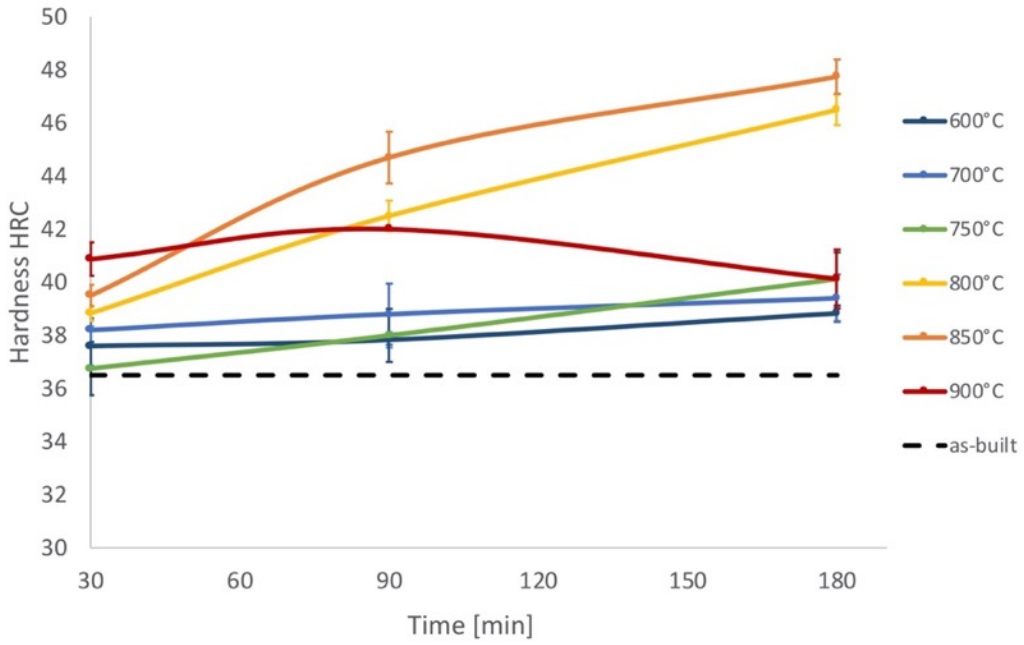

Figure 3.20: HRC hardness as a function of aging time and temperature (aging curves) for the LPBF Co28Cr6Mo alloy

Table 3.5: Micro-hardness values (HV0.5) for the LPBF Co28Cr6Mo alloy heat-treated at different temperatures for 180 min, compared to the as-built condition

	Sample condition						
	As-built	*600°C 180min*	*700°C 180min*	*750°C 180min*	*800°C 180min*	*850°C 180min*	*900°C 180min*
$HV_{0.5}$	422 ±19	446 ± 15	455 ± 9	463 ± 10	512 ± 14	534 ± 12	430 ± 10

XRD and thermal analyses (Figure 3.21) were performed to assess changes occurring in the phase composition of the alloy due to the high temperature exposure. The differential thermal analysis (DTA) of the as-built alloy, reported in Figure 3.21a, showed an exothermal peak (A) located at about 600 °C, followed by an endothermic peak (B) around 830 °C. According to data reported in the literature [12,59], peaks recorded by thermal analysis are related to the allotropic γ(Co-fcc) to ε(Co-hcp) transformation. Specifically, the exothermic peak (A) is related to the fcc→hcp transformation, while the endothermic peak (B) to the following hcp→fcc transformation. According to the literature, peak A is located at about 600 °C, as in the present study, while peak B is usually located at 950 °C. Conforming to the binary Co-Cr phase diagram [60], ε(Co-hcp) is the equilibrium phase stable at room temperature and the transformation to the γ(Co-fcc) phase occurs in the range 900-950 °C. However, it should be noticed that the microstructure resulting from LPBF process is metastable, thus it is safe to assume that equilibrium diagrams might be no longer verified [21]. Since peak B in the present study is moved to a lower temperature, suggesting that the change from hcp to fcc phase is anticipated, it could be inferred that a modification in the kinetics of the transformation occurred, as also observed for other LPBF alloys [61].

The occurrence of the fcc→hcp transformation (peak A) was also supported by XRD analyses in Figure 3.21b, in which as-built and heat-treated (180 min) alloys are compared. In fact, as previously discussed, the LPBF as-built alloy showed the presence of both ε (ICDD:5-727) and γ (ICDD:15-806) Co-phases. However, heat treatments changed phase composition of the alloy. By focusing on the peaks related to only ε phase (located approximately at 2θ=41.4, 47, 62.5, 83.8°) it is possible to observe that presence of ε phase increased with increasing temperature,

especially after the 800 °C and 900 °C treatment. By comparing these outcomes with aging curves, the fcc to hcp transformation can be, indeed, ascribed to the observed hardness increase of the alloy.

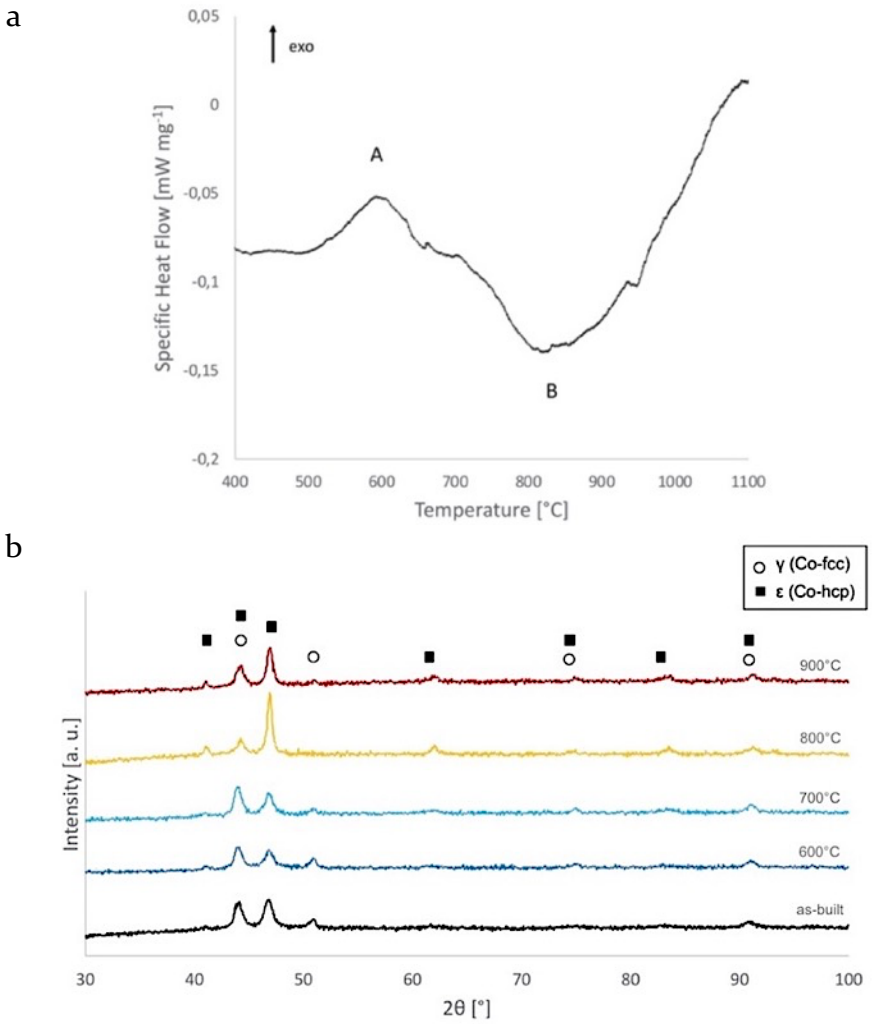

Figure 3.21: Microstructural characterization: a) differential thermal analysis (DTA) on the LPBF as-built Co28Cr6Mo alloy, b) phase composition (XRD) analyses on as-built and heat-treated samples for 180 min at 600, 700, 800 and 900°C

The modifications in the microstructure induced by aging treatments are shown in Figure 3.22, where the as-built condition is compared to one of the low-temperature (750 °C) and to the highest temperature (850 and 900 °C) treatments. In the optical micrograph of as-built alloy (Figure 3.22a), solidified semi-circular melt pools typical of LPBF components can be clearly identified, whose boundaries

became less clear after the exposure to increasing temperatures (Figures 3.22c,e,g), even if in the heat-treated samples a layered microstructure, due to the additive process, can still be recognized. In fact, as reported by previous studies, recrystallization and homogenisation of the microstructure occurs at higher temperature (1150-1220 °C) [50–52,62]. Optical analyses showed the development of new microstructural features that initially (Figure 3.22c) involved boundaries of the large columnar grains crossing-over layers and, with increasing temperature, affected the whole microstructure. SEM analyses highlighted that the cellular microstructure along with the melt pool boundaries of the as-built alloy (Figure 3.22b) progressively disappeared when the alloy is subjected to heat-treatment from 750 to 900 °C (Figures 3.22d,f,h). In addition, the fine cellular microstructure was replaced by a fine distribution of sub-micro sized globular particles that reached their maximum density in the 850 °C for 180 min heat-treated alloy (Figure 3.22f), that as previously discussed exhibited also the highest value of both hardness and microhardness. After the 900 °C for 180 min treatment, instead, most part of the particles were dissolved, possibly explaining the drop in hardness evidenced by this aging condition.

For the purpose of the present study, the optimized condition was found in the 850 °C for 180 min heat-treatment, that produced the highest hardness and a deep change in the microstructure, both in terms of phase composition and grain morphology. Further analyses were conducted on the 850 °C for 180 min condition, with the aim to highlight the composition of sub-micro sized globular particles that replaced the cellular structure. SEM-EDS analyses are reported in Figure 3.23, showing an enrichment in alloy elements, especially Mo, in correspondence of these particles. Based on the results reported in the literature, showing a Mo segregation in cellular boundaries [7,12], it can be inferred that globular particles formed from cell borders and, presumably, are carbide particles.

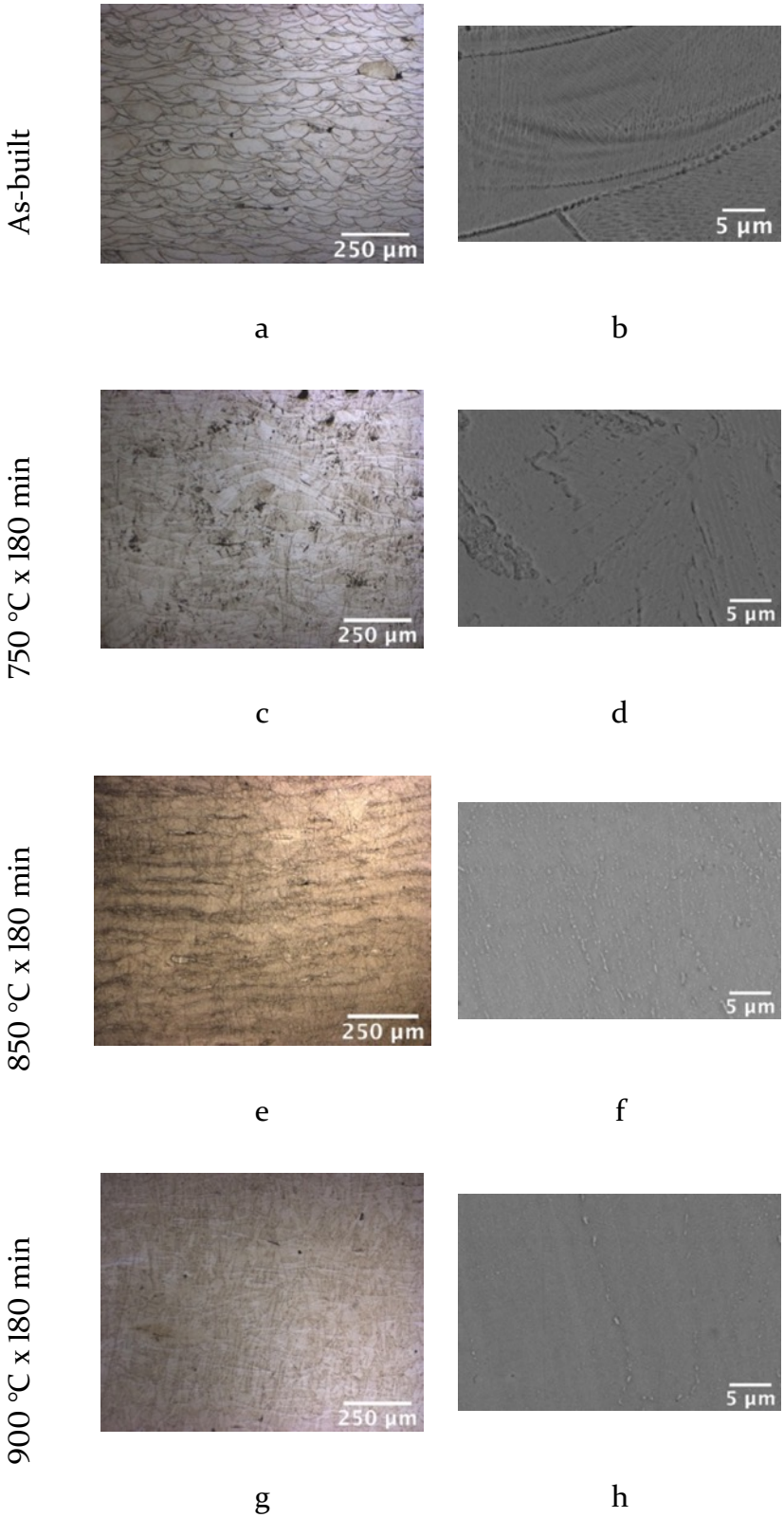

Figure 3.22: Microstructural characterization: a), c), e), g) OM and b), d), f), h) SEM micrographs of LPBF Co28Cr6Mo as-built and heat-treated samples for 180 min at 750, 850 and 900 °C

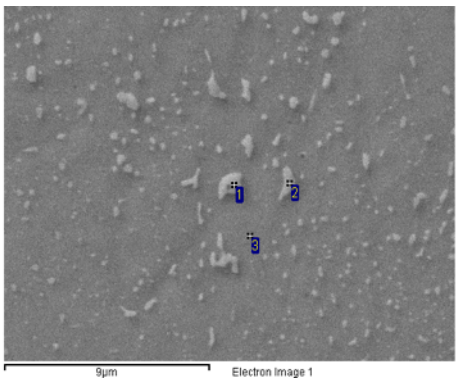

	Element (wt.%)						
Spectrum	**C**	**O**	**Si**	**Cr**	**Mn**	**Co**	**Mo**
1	5.74	0.00	1.60	26.11	0.83	56.16	**9.55**
2	5.67	0.00	2.65	26.32	0.56	51.55	**13.24**
3	4.07	1.64	1.02	27.07	0.87	59.25	**6.08**

Figure 3.23: SEM-EDS analyses of globular particles in heat-treated sample at 850°C x 180 min

WEAR BEHAVIOR

Dry sliding wear tests were carried out on as-built and heat-treated samples in the optimized condition (850 °C for 180 min), with the aim to assess the effect of hardness increase on wear resistance of the alloy. In addition, since to the best of authors' knowledge no wear data are currently reported in the literature for the Co28Cr6Mo LPBF alloys, samples for wear test were produced with a different value of LED in order to investigate the influence of LED on tribological behavior of this alloy produced by LPBF. In particular, it was chosen the optimal LED range (samples W2 and W2HT), a value lower than the optimal one (W1 and W1HT) and a value higher than the optimal one (W3 and W3HT). Lastly, the same were compared to the conventionally manufactured wrought Co28Cr6Mo alloy [63] that represents the current standard for knee and ankle implants. Before tests, both sliders and countermaterial, were characterized in terms of hardness and surface roughness (Table 3.6). As for the latter, all sliders were prepared with the same surface roughness (Ra=0.22 ± 0.02 µm), while the steel cylinder was mechanically polished to Ra=0.13 ± 0.02 µm. Regarding hardness, it is worth noticing that heat treatment succeeded in remarkably increasing the value of the low LED alloy, by comparison with the as-built condition, going from 29 to 42 HRC, while the high LED sliders exhibited the lowest increase, going from 35 to 44 HRC. The conventional wrought alloy, instead, was characterized by a hardness value of 39

HRC. However, hardness of the steel countermaterial was higher than all tested sliders, and equal to 62 HRC.

Table 3.6: HRC hardness and surface roughness of sliders and cylinder used for wear tests

	Sliders							***Cylinder***
	W1	*W1HT*	*W2*	*W2HT*	*W3*	*W3HT*	*Wrought alloy*	
HRC	29 ± 1	42 ± 2	36 ± 1	47 ± 1	35 ± 2	44 ± 2	39 ± 1	62 ± 1
Ra [μm]	0.22 ± 0.02							0.13 ± 0.02

Wear tests results are reported in Figure 3.24 and 3.25, in term of steady-state coefficient of friction (COF) and maximum wear depth measured by profilometry on sliders, respectively. Average COF ranged between 0.5 and 0.9 for all tested samples, with the maximum obtained for the conventional wrought alloy with 5 N of applied load (Figure 3.24a). The LPBF as-built showed little variation in the COF by increasing the applied load from 5 to 10 N, with the only exception of W2 sliders for which it raised (Figure 3.24b). Among all the tested samples, the conventional wrought alloy exhibited the highest load-dependence of COF, that decreased in case of tests performed with 10 N load. Generally, the heat treatment induced a decrease in the COF and both W1HT and W2HT showed a little influence of the applied load after heat-treatment, while the COF of W3HT increased for 10 N tests.

By comparing wear depths, it is worth noticing that for 5 N tests, the wear resistance of all LPBF as-built sliders was higher than the wrought one (Figure 3.25a), while in case of 10 N tests the wrought alloy exhibited a higher wear resistance (Figure 3.25b). This is a remarkable result since the mean contact pressure experienced by prosthetic implants during service life in vivo conditions is in the range of 10-30 MPa with occasional peaks up to 50 MPa [64,65], thus better represented by 5 N tests (Table 3.4). Apart from the wrought alloy, all samples showed increased wear depths for tests performed at 10 N (Figure 3.25b). The effect of heat treatment was not obvious, since it produced different outcomes on the basis of LED values. For low LED samples (W1HT), the heat treatment

succeeded in improving the wear resistance, especially for 10 N load, probably due to the great increase in hardness. For high LED samples (W3HT), in case of 5 N tests the wear resistance was almost unaffected by heat treatment, while for 10 N tests it was drastically reduced. For the samples obtained in the medium LED range (W2HT), the heat-treatment was detrimental for the wear resistance at both 5 and 10 N.

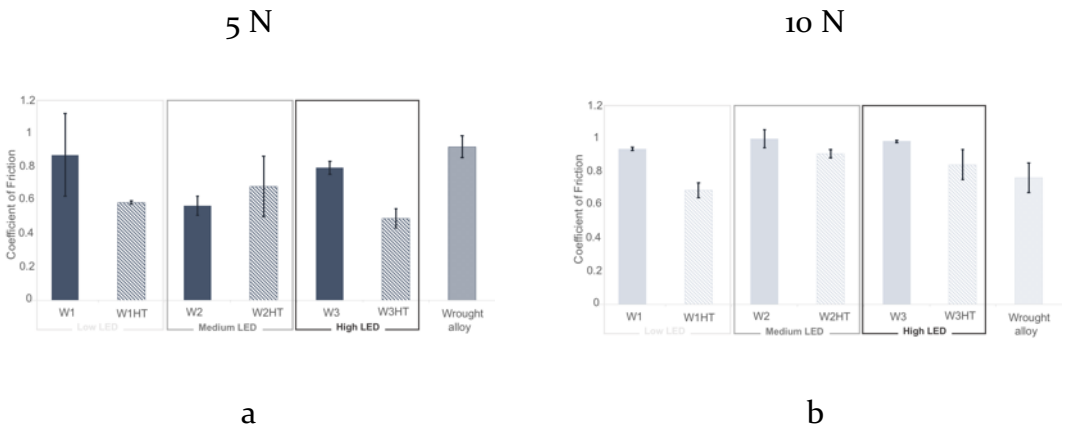

Figure 3.24: Steady-state COF for: a) 5 N load; b) 10 N load.

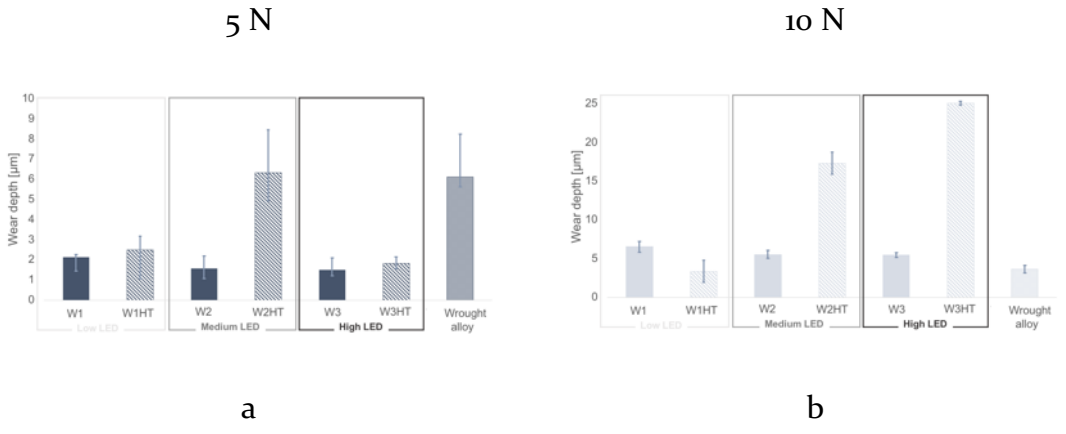

Figure 3.25: Maximum wear depth on sliders: a) 5 N load; b) 10 N load.

Further investigation of wear behavior was conducted via wear scars characterization performed by means of SEM-EDS. Accordingly, as summarized in

Table 2.7, two main wear mechanisms were identified: i) a mild-oxidative wear regime experienced by the majority of sliders, ii) a severe wear regime.

Table 2.7: Summary of wear regime established during wear tests, as a function of LED range, heat-treatment condition and applied normal load.

Samples	***Heat treatment***	***LED range***	***Normal Load [N]***	***Wear regime***	
				Mild-oxidative	*Severe delamination*
W1	No	low	5	✓	
			10	✓	
W1HT	Yes		5	✓	
			10	✓	
W2	No	medium	5	✓	
			10	✓	
W2HT	Yes		5		✓
			10		✓
W3	No	high	5	✓	
			10	✓	
W3HT	Yes		5	✓	
			10		✓
Wrought alloy	-	-	5		✓
			10	✓	

As shown in Figure 3.26, mild-oxidative wear regime resulted in a low wear damage of the sliders in the reason of protective oxidative tribo-film formed between the sliding surfaces of both sliders and cylinder. The presence of oxidative tribo-film was also confirmed by EDS maps in Figure 3.27, where the presence of an Fe-based oxide, due to the wear of the steel cylinder countermaterial, was revealed on sliders characterized by a low wear depth. However, two different behavior in case of mild-oxidative wear were observed: i) in case of 5 N tests, a thick and compact reddish layer was formed (Figures 3.26a and 3.27a), ii) for 10 N tests the layer was thinner, darker and did not homogeneously cover the scar (Figures 3.26b and 3.27b). Raman analyses, not reported here, confirmed that the

oxides formed in case of 5 N were mainly composed of hematite, while at 10 N were mainly made of magnetite. On the other hand, when severe wear regime was established no protective tribo-layer was formed (Figures 3.26c and 3.27c), resulting in high wear depths. The majority of LPBF samples showed a mild-oxidative wear regime, with the exception of W2HT and W3HT. This outcome is presumably related to the fracture toughness of the heat-treated alloy. W2HT and W3HT sliders exhibited indeed the highest hardness, equal to 44 and 47 HRC respectively. Indeed, according to the Archard's law, wear rate of metal alloys is inversely related to the alloy hardness. Thus, for a metal characterized by a high hardness value a high wear resistance should be expected. However, the decrease in the fracture toughness induced by increased alloy hardness, can induce different wear mechanisms involving microcracking. In this condition the Archard's law can be no longer valid and elevated wear rate can be obtained, even in case of a high hardness value [66]. Finally, it should be noticed that wear mechanism of the conventional wrought alloy changed, confirming the load-dependence of the tribological behavior showed also by COF. For the 5 N tests, severe wear of the wrought alloy occurred, while during tests performed at 10 N load a mild-oxidative regime was established by the formation of the aforementioned oxidative tribo-film.

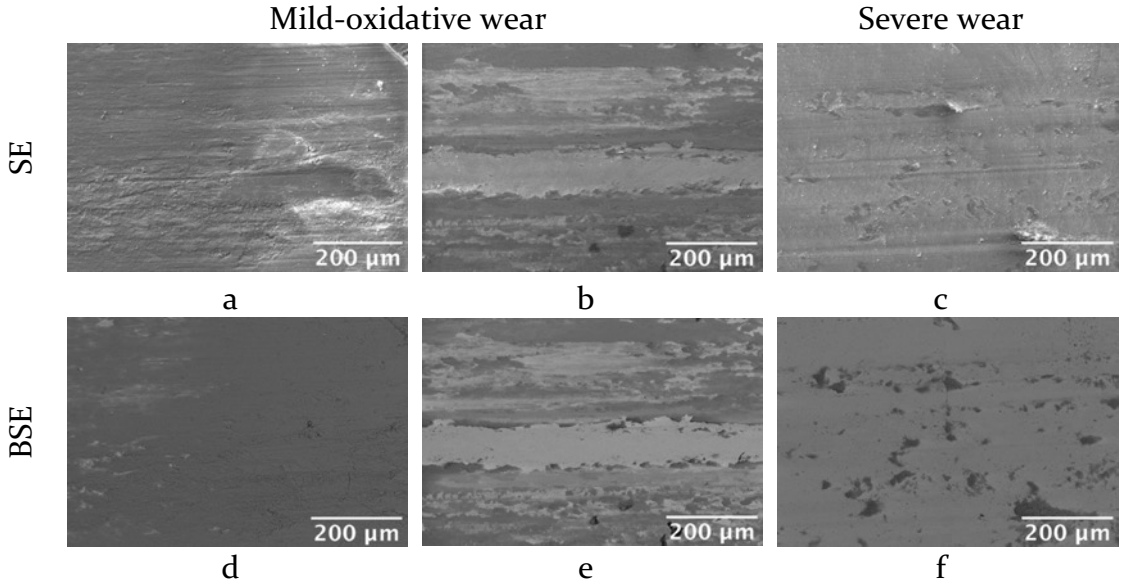

Figure 3.26: Secondary and back scattered electrons SEM analyses of sliders wear scars: a), b), d), e) mild-oxidative regime; c), f) severe wear regime.

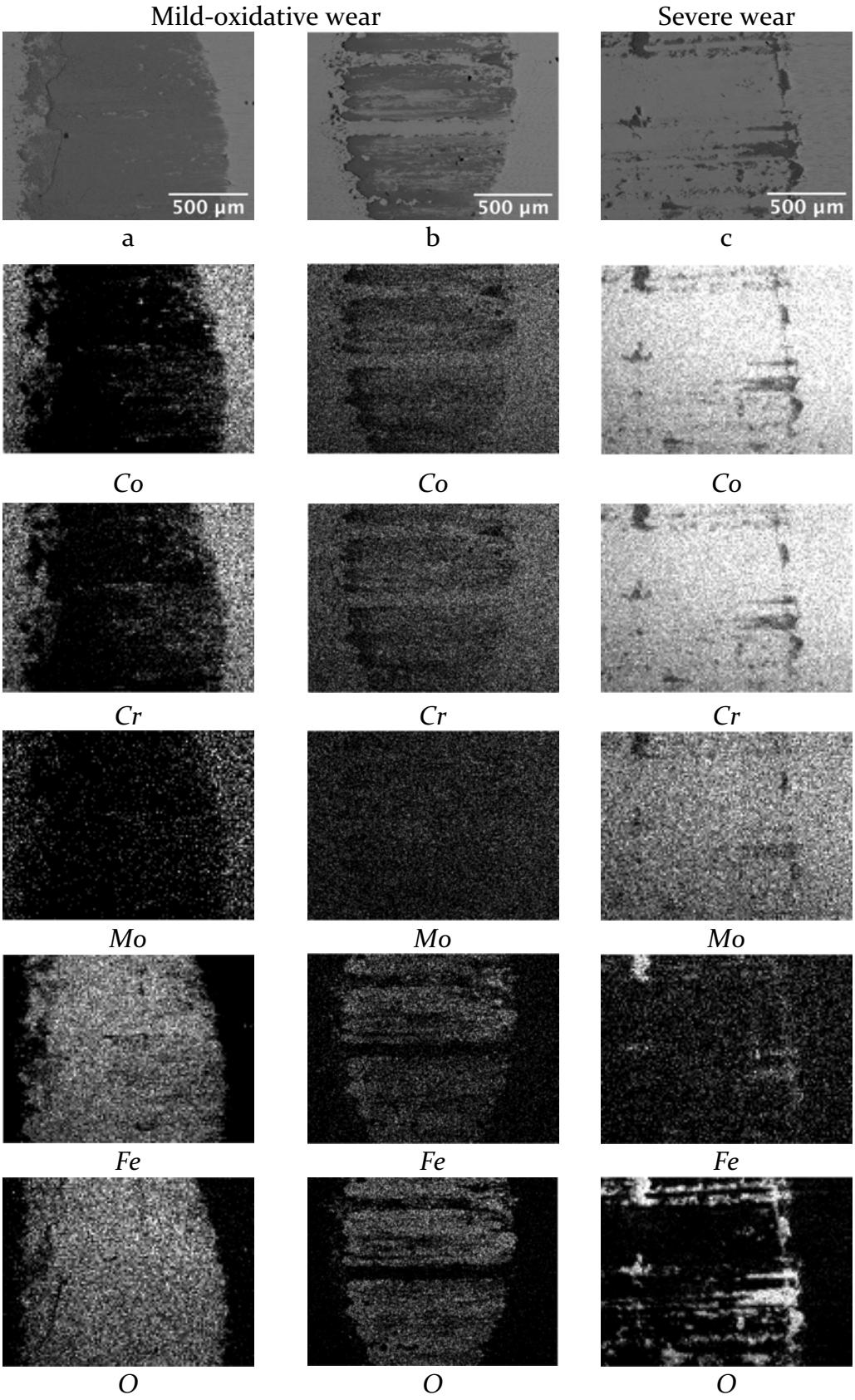

Figure 3.27: SEM-EDS maps of wear scars for: a), b) mild-oxidative regime; c) severe wear regime.

CORROSION RESISTANCE

Preliminary assessment of corrosion resistance is reported in Figure 3.28, showing the polarization resistance (Rp) as a function of time in PBS solution. Samples that exhibit a higher Rp are characterized by a better corrosion resistance. From the preliminary results, LPBF as-built sample C1 exhibited a corrosion resistance comparable to the conventional wrought alloy and, after heat treatment (C1HT), the corrosion behavior significantly increased. Heat treatment succeeded also in increasing polarization resistance of the LPBF as-built sample C2 samples. However, it should be noticed that the corrosion behavior was influenced by process parameters. Further analyses will be needed in order to understand the effect of process parameters and heat treatments on corrosion behavior of the LPBF Co28Cr6Mo alloy.

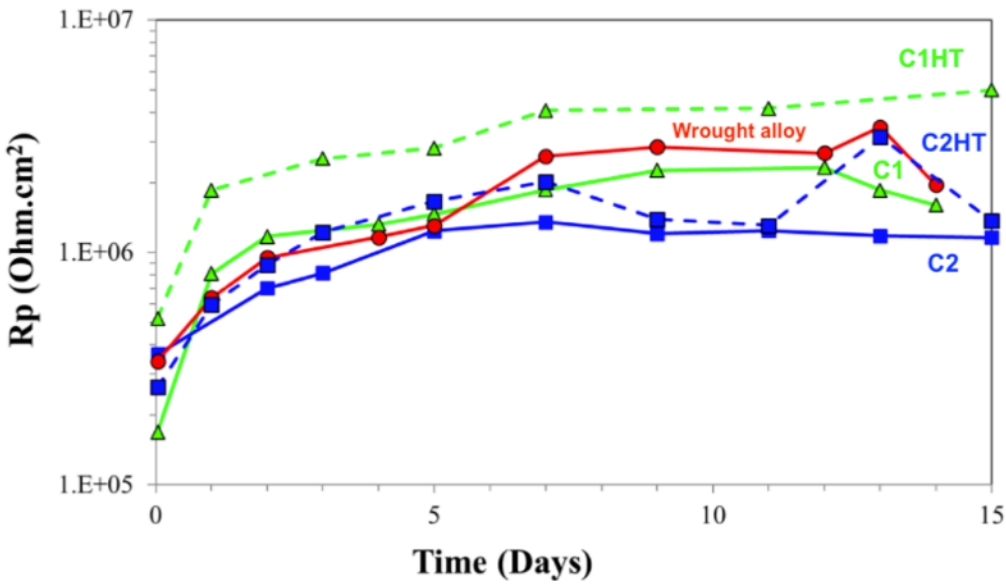

Figure 3.28: Resistance potential for the Co28Cr6Mo alloy immersed in PBS solution

3.2.4 Conclusions

In the present work, the effect of a direct aging treatment of the as-built LPBF alloy, without any prior solution treatment, on hardness and microstructure for the LPBF Co28Cr6Mo alloy was investigated. Temperatures in the range 600-900 °C were considered for a holding time between 30 and 180 min. Once defined the optimized heat treatment conditions, dry sliding wear tests were conducted on as-built and heat-treated alloy processed with different value of laser energy density. As a reference, also the wear behavior of the conventional wrought alloy was evaluated. Based on the results, the following conclusions can be summarized:

- For all the investigated temperatures (600-900 °C) strengthening of the alloy occurred, related to both fcc to hcp phase transformation, as a result of the isothermal treatment, and precipitation of very fine and homogenously dispersed Mo-based second phases. The formation of these globular fine particles was influenced by both aging temperature and holding time and reached it maximum density for 180 min at 850 °C aging treatment.
- In the range of contact pressures relevant for biomedical applications (10-50 MPa), the as-built LPBF alloy was characterized by a higher wear resistance than conventional wrought alloy currently adopted for orthopedic implants. In most cases, the optimized aging treatment did not affect the wear behavior of the alloy, even if it should be noticed that for the heat-treated alloy characterized by the highest hardness a change in the wear behavior occurred and wear resistance became comparable to the wrought alloy.
- For a specific combination of process parameters, preliminary results on corrosion behavior of the alloy showed that the LPBF as-built alloy might have higher corrosion resistance than the conventional wrought alloy. Furthermore, the optimized heat treatment succeeded in increasing the corrosion resistance of the LPBF alloy obtained with both process parameters combinations so far investigated.

References

[1] W.S.W. Harun, M.S.I.N. Kamariah, N. Muhamad, S.A.C. Ghani, F. Ahmad, Z. Mohamed, A review of powder additive manufacturing processes for metallic biomaterials, Powder Technol. 327 (2018) 128–151. doi:10.1016/j.powtec.2017.12.058.

[2] S. Bose, D. Ke, H. Sahasrabudhe, A. Bandyopadhyay, Additive manufacturing of biomaterials, Prog. Mater. Sci. 93 (2018) 45–111. doi:10.1016/j.pmatsci.2017.08.003.

[3] L. Kunčická, R. Kocich, T.C. Lowe, Advances in metals and alloys for joint replacement, Prog. Mater. Sci. 88 (2017) 232–280. doi:10.1016/j.pmatsci.2017.04.002.

[4] T. Ozel, P. Bartolo, E. Ceretti, J. De Ciurana Gay, C.A. Rodriguez, J.V.L. Da Silva, Biomedical Devices: Design, Prototyping and Manufacturing, John Wiley & Sons, 2017. doi:10.1002/9781119267034.

[5] Q. Chen, G.A. Thouas, Metallic implant biomaterials, Mater. Sci. Eng. R Reports. 87 (2015) 1–57. doi:10.1016/j.mser.2014.10.001.

[6] A. Takaichi, Suyalatu, T. Nakamoto, N. Joko, N. Nomura, Y. Tsutsumi, S. Migita, H. Doi, S. Kurosu, A. Chiba, N. Wakabayashi, Y. Igarashi, T. Hanawa, Microstructures and mechanical properties of Co-29Cr-6Mo alloy fabricated by selective laser melting process for dental applications, J. Mech. Behav. Biomed. Mater. 21 (2013) 67–76. doi:10.1016/j.jmbbm.2013.01.021.

[7] B. Qian, K. Saeidi, L. Kvetková, F. Lofaj, C. Xiao, Z. Shen, Defects-tolerant Co-Cr-Mo dental alloys prepared by selective laser melting, Dent. Mater. 31 (2015) 1435–1444. doi:10.1016/j.dental.2015.09.003.

[8] Z.W. Chen, M.A.L. Phan, K. Darvish, Grain growth during selective laser melting of a Co–Cr–Mo alloy, J. Mater. Sci. 52 (2017) 7415–7427. doi:10.1007/s10853-017-0975-z.

[9] E. Liverani, A. Fortunato, A. Leardini, C. Belvedere, S. Siegler, L. Ceschini, A. Ascari, Fabrication of Co-Cr-Mo endoprosthetic ankle devices by means of Selective Laser Melting (SLM), Mater. Des. 106 (2016) 60–68. doi:10.1016/j.matdes.2016.05.083.

[10] M. Seyedi, F. Zanotto, C. Monticelli, A. Balbo, E. Liverani, A. Fortunato, Microstructural characterization and corrosion behaviour of SLM CoCrMo alloy in simulated body fluid, Metall. Ital. 110 (2018) 45–50.

[11] M.V. Mergulhão, C.E. Podestá, M.D.M. das Neves, Valuation of Mechanical Properties and Microstructural Characterization of ASTM F75 Co-Cr Alloy Obtained by Selective Laser Melting (SLM) and Casting Techniques, Mater. Sci. Forum. 899 (2017) 323–328. doi:10.4028/www.scientific.net/MSF.899.323.

[12] C. Song, M. Zhang, Y. Yang, D. Wang, Y. Jia-kuo, Morphology and properties of CoCrMo parts fabricated by selective laser melting, Mater. Sci. Eng. A. 713 (2018) 206–213. doi:10.1016/j.msea.2017.12.035.

[13] C. Song, Y. Yang, Y. Wang, D. Wang, J. Yu, Research on rapid manufacturing of CoCrMo alloy femoral component based on selective laser melting, Int. J. Adv. Manuf. Technol. 75 (2014) 445–453. doi:10.1007/s00170-014-6150-7.

[14] T. De Terris, O. Andreau, P. Peyre, F. Adamski, I. Koutiri, C. Gorny, C. Dupuy,

Optimization and comparison of porosity rate measurement methods of Selective Laser Melted metallic parts, Addit. Manuf. 28 (2019) 802–813. doi:10.1016/j.addma.2019.05.035.

[15] M. Guo, D. Gu, L. Xi, H. Zhang, J. Zhang, J. Yang, Selective laser melting additive manufacturing of pure tungsten : Role of volumetric energy density on densification, microstructure and mechanical properties, Int. J. Refract. Metals Hard Mater. 84 (2019) 105025. doi:10.1016/j.ijrmhm.2019.105025.

[16] Z.A. Mierrzejewska, Effect of Laser Energy Density, Internal Porosity and Heat Treatment on Mechanical Behavior of Biomedical Ti6Al4V Alloy Obtained with DMLS Technology, Materials (Basel). 12 (2019) 2331. doi:doi:10.3390/ma12142331.

[17] J.H. Yi, J.W. Kang, T.J. Wang, X. Wang, Y.Y. Hu, T. Feng, Y.L. Feng, P.Y. Wu, Effect of laser energy density on the microstructure, mechanical properties, and deformation of Inconel 718 samples fabricated by selective laser melting, J. Alloys Compd. 786 (2019) 481–488. doi:10.1016/j.jallcom.2019.01.377.

[18] G.F. Vander Voort, ASM Handbook Volume 9 - Metallography and Microstructures, ASM Interbational, 2004. doi:https://doi.org/10.31399/asm.hb.v09.9781627081771.

[19] ISO 6508-1 - Metallic materials - Rockwell hardness test, (2016) 1–32.

[20] EN ISO 6507 Metallic materials – Vickers hardness test, (2018).

[21] K.G. Prashanth, J. Eckert, Formation of metastable cellular microstructures in selective laser melted alloys, J. Alloys Compd. 707 (2017) 27–34. doi:10.1016/j.jallcom.2016.12.209.

[22] ASTM F75-18, Standard Specification for Cobalt-28 Chromium-6 Molybdenum Alloy Castings and Casting Alloy for Surgical Implants (UNS R30075), (2018). doi:https://doi.org/10.1520/F0075-12.

[23] R.J. Hebert, Viewpoint: metallurgical aspects of powder bed metal additive manufacturing, J. Mater. Sci. 51 (2016) 1165–1175. doi:10.1007/s10853-015-9479-x.

[24] W.J. Sames, F.A. List, S. Pannala, R.R. Dehoff, S.S. Babu, The metallurgy and processing science of metal additive manufacturing, Int. Mater. Rev. 6608 (2016) 1–46. doi:10.1080/09506608.2015.1116649.

[25] J.A. Slotwinski, E.J. Garboczi, K.M. Hebenstreit, Porosity Measurements and Analysis for Metal Additive Manufacturing Process Control, J. Res. Natl. Inst. Stand. Technol. 119 (2014) 494–528. doi:10.6028/jres.119.019.

[26] A. Townsend, N. Senin, L. Blunt, R.K. Leach, J.S. Taylor, Surface texture metrology for metal additive manufacturing: a review, Precis. Eng. 46 (2016) 34–47. doi:10.1016/j.precisioneng.2016.06.001.

[27] X. Zhou, K. Li, D. Zhang, X. Liu, J. Ma, W. Liu, Z. Shen, Textures formed in a CoCrMo alloy by selective laser melting, J. Alloys Compd. 631 (2015) 153–164. doi:10.1016/j.jallcom.2015.01.096.

[28] X. Zhou, X. Liu, D. Zhang, Z. Shen, W. Liu, Balling phenomena in selective laser melted tungsten, J. Mater. Process. Technol. 222 (2015) 33–42. doi:10.1016/j.jmatprotec.2015.02.032.

[29] C. Qiu, C. Panwisawas, M. Ward, H.C. Basoalto, J.W. Brooks, M.M. Attallah, On the role of melt flow into the surface structure and porosity development during selective laser melting, Acta Mater. 96 (2015) 72–79.

doi:10.1016/j.actamat.2015.06.004.

[30] D. Wang, S. Wu, F. Fu, S. Mai, Y. Yang, Y. Liu, C. Song, Mechanisms and characteristics of spatter generation in SLM processing and its effect on the properties, Mater. Des. 117 (2017) 121–130. doi:10.1016/j.matdes.2016.12.060.

[31] C. Zhao, K. Fezzaa, R.W. Cunningham, H. Wen, F. De Carlo, L. Chen, A.D. Rollett, T. Sun, Real-time monitoring of laser powder bed fusion process using high-speed X-ray imaging and diffraction, Sci. Rep. 7 (2017) 1–11. doi:10.1038/s41598-017-03761-2.

[32] P. Bidare, I. Bitharas, R.M. Ward, M.M. Attallah, A.J. Moore, Fluid and particle dynamics in laser powder bed fusion, Acta Mater. 142 (2018) 107–120. doi:10.1016/j.actamat.2017.09.051.

[33] M.J. Matthews, G. Guss, S.A. Khairallah, A.M. Rubenchik, P.J. Depond, W.E. King, Denudation of metal powder layers in laser powder bed fusion processes, Acta Mater. 114 (2016) 33–42. doi:10.1016/j.actamat.2016.05.017.

[34] P.C. Collins, D.A. Brice, P. Samimi, I. Ghamarian, H.L. Fraser, Microstructural Control of Additively Manufactured Metallic Materials, Annu. Rev. Mater. Res. 46 (2016) 63–91. doi:10.1146/annurev-matsci-070115-031816.

[35] ASTM E112 - 13 - Standard Test Methods for Determining Average Grain Size, (2013). doi:10.1520/E0112.

[36] K. Darvish, Z.W. Chen, M.A.L. Phan, T. Pasang, Selective laser melting of Co-29Cr-6Mo alloy with laser power 180–360 W: Cellular growth, intercellular spacing and the related thermal condition, Mater. Charact. 135 (2018) 183–191. doi:10.1016/j.matchar.2017.11.042.

[37] B. Zhang, Y. Li, Q. Bai, Defect Formation Mechanisms in Selective Laser Melting: A Review, Chinese J. Mech. Eng. 30 (2017) 515–527. doi:10.1007/s10033-017-0121-5.

[38] T. DebRoy, H.L. Wei, J.S. Zuback, T. Mukherjee, J.W. Elmer, J.O. Milewski, A.M. Beese, A. Wilson-Heid, A. De, W. Zhang, Additive manufacturing of metallic components – Process, structure and properties, Prog. Mater. Sci. 92 (2018) 112–224. doi:10.1016/j.pmatsci.2017.10.001.

[39] R. Rai, J.W. Elmer, T.A. Palmer, T. DebRoy, Heat transfer and fluid flow during keyhole mode laser welding of tantalum, Ti–6Al–4V, 304L stainless steel and vanadium, J. Phys. D. Appl. Phys. 40 (2007) 5753–5766. doi:10.1088/0022-3727/40/18/037.

[40] W.E. King, H.D. Barth, V.M. Castillo, G.F. Gallegos, J.W. Gibbs, D.E. Hahn, C. Kamath, A.M. Rubenchik, Observation of keyhole-mode laser melting in laser powder-bed fusion additive manufacturing, J. Mater. Process. Technol. 214 (2014) 2915–2925. doi:10.1016/j.jmatprotec.2014.06.005.

[41] V.-P. Matilainen, H. Piili, A. Salminen, O. Nyrhilä, Preliminary Investigation of Keyhole Phenomena during Single Layer Fabrication in Laser Additive Manufacturing of Stainless Steel, Phys. Procedia. 78 (2015) 377–387. doi:10.1016/j.phpro.2015.11.052.

[42] I. Rosenthal, A. Stern, N. Frage, Strain rate sensitivity and fracture mechanism of AlSi10Mg parts produced by Selective Laser Melting, Mater. Sci. Eng. A. 682 (2017) 509–517. doi:10.1016/j.msea.2016.11.070.

[43] J. V. Giacchi, C.N. Morando, O. Fornaro, H.A. Palacio, Microstructural characterization of as-cast biocompatible Co-Cr-Mo alloys, Mater. Charact. 62 (2011) 53–61. doi:10.1016/j.matchar.2010.10.011.

[44] H.R. Kim, S.H. Jang, Y.K. Kim, J.S. Son, B.K. Min, K.H. Kim, T.Y. Kwon, Microstructures and mechanical properties of Co-Cr dental alloys fabricated by three CAD/CAM-based processing techniques, Materials (Basel). 9 (2016). doi:10.3390/MA9070596.

[45] S. Dadbakhsh, B. Vrancken, J.P. Kruth, J. Luyten, J. Van Humbeeck, Texture and anisotropy in selective laser melting of NiTi alloy, Mater. Sci. Eng. A. 650 (2016) 225–232. doi:10.1016/j.msea.2015.10.032.

[46] L. Thijs, K. Kempen, J.P. Kruth, J. Van Humbeeck, Fine-structured aluminium products with controllable texture by selective laser melting of pre-alloyed AlSi10Mg powder, Acta Mater. 61 (2013) 1809–1819. doi:10.1016/j.actamat.2012.11.052.

[47] L. Thijs, M.L. Montero Sistiaga, R. Wauthle, Q. Xie, J.P. Kruth, J. Van Humbeeck, Strong morphological and crystallographic texture and resulting yield strength anisotropy in selective laser melted tantalum, Acta Mater. 61 (2013) 4657–4668. doi:10.1016/j.actamat.2013.04.036.

[48] A. Molinari, The structural metastability of metallic alloys produced by Selective Laser Melting, La Metall. Ital. 1 (2017) 21–27.

[49] R. Narayan, ASM Handbook, Volume 23, Materials for Medical Devices, ASM International, 2012.

[50] S.M.J. Razavi, A. Avanzini, G. Cornacchia, L. Giorleo, F. Berto, Effect of heat treatment on fatigue behavior of as-built notched Co-Cr-Mo parts produced by Selective Laser Melting, Int. J. Fatigue. 142 (2021) 105926. doi:10.1016/j.ijfatigue.2020.105926.

[51] S.L. Sing, S. Huang, W.Y. Yeong, Effect of solution heat treatment on microstructure and mechanical properties of laser powder bed fusion produced cobalt-28chromium-6molybdenum, Mater. Sci. Eng. A. 769 (2020) 138511. doi:10.1016/j.msea.2019.138511.

[52] M. Béreš, C.C. Silva, P.W.C. Sarvezuk, L. Wu, L.H.M. Antunes, A.L. Jardini, A.L.M. Feitosa, J. Žilková, H.F.G. de Abreu, R.M. Filho, Mechanical and phase transformation behaviour of biomedical Co-Cr-Mo alloy fabricated by direct metal laser sintering, Mater. Sci. Eng. A. 714 (2018) 36–42. doi:10.1016/j.msea.2017.12.087.

[53] Y. Kajima, A. Takaichi, N. Kittikundecha, T. Nakamoto, T. Kimura, N. Nomura, A. Kawasaki, T. Hanawa, H. Takahashi, N. Wakabayashi, Effect of heat-treatment temperature on microstructures and mechanical properties of Co–Cr–Mo alloys fabricated by selective laser melting, Mater. Sci. Eng. A. 726 (2018) 21–31. doi:10.1016/j.msea.2018.04.048.

[54] R.N.J. Taylor, R.B. Waterhouse, A study of the ageing behaviour of a cobalt based implant alloy, J. Mater. Sci. 18 (1983) 3265–3280. doi:10.1007/BF00544151.

[55] ASTM G77 -17, Standard Test Method for Ranking Resistance of Materials to Sliding Wear Using Block-on-Ring Wear Test, (2017). doi:10.1520/G0077-17.

[56] J.A. Williams, R.S. Dwyer-Joyce, Contact Between Solid Surfaces, in: Mod. Tribol. Handb., CRC Press, 2001.

[57] H.K.D.H. Bhadeshia, Steels for bearings, Prog. Mater. Sci. 57 (2012) 268–435. doi:https://doi.org/10.1016/j.pmatsci.2011.06.002.

[58] E.P. Papadakis, C.A. Stickels, R.C. Innes, An ultrasonic technique for measuring the elastic constants of small samples, SAE Tech. Pap. 104 (1995) 830–837. doi:10.4271/950897.

[59] M.V. Mergulhão, C.E. Podestá, M.D.M. das Neves, Perspective of Additive Manufacturing Selective Laser Melting in Co-Cr-Mo Alloy in the Consolidation of Dental Prosthesis, in: C.E.P. and M.D.M. das N.E.-L.A. Dobrzański (Ed.), Biomater. Regen. Med., IntechOpen, Rijeka, 2018: p. Ch. 6. doi:10.5772/intechopen.69720.

[60] R. Pillar, S.D. Ramsay, Cobalt-base alloys, in: R.J. Narayan (Ed.), Mater. Med. Devices, ASM Interbational, 2012: pp. 211–222. doi:10.31399/asm.hb.v23.a0005669.

[61] J.H. Rao, Y. Zhang, K. Zhang, A. Huang, C.H.J. Davies, X. Wu, Multiple precipitation pathways in an Al-7Si-0.6Mg alloy fabricated by selective laser melting, Scr. Mater. 160 (2019) 66–69. doi:10.1016/j.scriptamat.2018.09.045.

[62] M. Zhang, Y. Yang, C. Song, Y. Bai, Z. Xiao, An investigation into the aging behavior of CoCrMo alloys fabricated by selective laser melting, J. Alloys Compd. 750 (2018) 878–886. doi:10.1016/j.jallcom.2018.04.054.

[63] ASTM F1537-20, Standard Specification for Wrought Cobalt-28Chromium-6Molybdenum Alloys for Surgical Implants (UNS R31537, UNS R31538, and UNS R31539), (2020). doi:10.1520/F1537-20.

[64] D.D. D'Lima, N. Steklov, B.J. Fregly, S.A. Banks, C.W. Colwell, In vivo contact stresses during activities of daily living after knee arthroplasty, J. Orthop. Res. 26 (2008) 1549–1555. doi:10.1002/jor.20670.

[65] A. Sharma, R.D. Komistek, C.S. Ranawat, D.A. Dennis, M.R. Mahfouz, In Vivo Contact Pressures in Total Knee Arthroplasty, J. Arthroplasty. 22 (2007) 404–416. doi:10.1016/j.arth.2006.07.008.

[66] E. Hornbogen, The role of fracture toughness in the wear of metals, Wear. 33 (1975) 251–259. doi:https://doi.org/10.1016/0043-1648(75)90280-X.

Chapter 4

LASER POWDER BED FUSION OF ALSI7MG ALLOYS
A LITERATURE REVIEW

4.1 Aluminum Silicon Magnesium casting alloys

Al-Si-Mg alloys belong to the family of Al-Si casting alloys and represent the 80-90% of commercially produced casting components. The most widely used Al-Si alloys have indeed a Si content in the range 7-10 wt.% that improves fluidity and castability, making Al-Si alloys suitable for different processes, such as sand, die, and permanent mold casting [1]. In the transportation field, that takes great advantages of the high weight-to-strength ratio of Al alloys, Al-Si-Mg are mainly used in the power train system [2]. Thanks to proper addition of Mg, these alloys are heat treatable, meaning that strengthening of the alloy is achievable by precipitation of fine coherent hard second phases (i.e. Mg_2Si) after a dedicated heat treatment, named solution treatment and aging. In the reason of their good castability and high mechanical strength after heat treatment, Al-Si-Mg alloys are typically used for structural castings, often requiring quite complex design. Among these alloys, the hypoeutectic Al-7Si-Mg ones are recommended for engine blocks, in the reason of high strength and elongation values at room temperature they can reach after heat treatment (T6). For these particular applications, they also exhibit an elevated thermal fatigue resistance, mainly ascribable to the low tendency to cracking in the plastic regime [2]. As can be appreciated in Table 4.1 that reports the nominal chemical composition of these alloys, with different Mg content, they also have a limited content of impurity. Since these alloys are usually obtained with secondary processes, and level of impurity can increase during recycling, the content of undesired elements (i.e. Fe) has to be carefully controlled. In the same

table, also the two principal standard designations are reported, according to the International Alloy Designation System (IADS) of the Aluminum Association [3,4] and to the EN 1780 standards [5–7], that comprises both a numerical and a chemical designation system. Hereafter, the chemical designation will be used to identify these alloys.

Table 4.1: Al-7Si-Mg alloys: designations, according to International Alloy Designation System (IADS) [3] and EURONORM (EN) [5–7] system, and nominal chemical composition according to EN 1706 [8] (when range is not specified, content of the element is to be intended as maximum acceptable).

Designation			***Element (wt.%)***								
IADS	***EN Chemical***	***EN Numerical***	***Al***	***Si***	***Mg***	***Mn***	***Fe***	***Cu***	***Ti***	***Zn***	***Other***
356.0	EN-AC AlSi7Mg0.3	EN-AC 42100	Bal.	6.5 – 7.5	0.25 – 0.35	0.10	0.19	0.05	0.25	0.07	0.10
357.0	EN-AC AlSi7Mg0.6	EN-AC 42200	Bal.	6.5 – 7.5	0.45 – 0.70	0.10	0.19	0.05	0.25	0.07	0.10

Two main families of AlSi7Mg alloys are defined, whose main difference relies in the percentage of Mg, accountable for the mechanical response of the alloys. AlSi7Mg0.6 alloy, indeed, in the reason of the high Mg content, can ensure greater mechanical strength. However, high amount of Mg promotes the formation of an undesired intermetallic compound (π-$Al_9FeMg_3Si_5$). In order to limit, or hinder, the formation of this compound, small amount of beryllium (0.04 – 0.07 wt.%) can be added. On the other hand, Be is associated to potential health issues (inhalation of beryllium fumes can cause acute or chronic berylliosis [1]), so a different solution has been found in limiting the Fe content up to 0.10 wt.%, as well as Be content up to 0.002 wt.%. As a consequence, variations of the nominal chemical composition of AlSi7Mg0.6 (357.0) alloy have been developed and seven different compositions (A357.0 to F357.0) have been so far listed in the Aluminum Association system [9].

When coming to innovative additive processes, AlSi7Mg alloys are one of the most commercially available Al alloys in forms of powders for AM applications, after the most widely used AlSi10Mg (360.0) alloy which has 0.45 wt% Mg. As shown in Figure 4.1 reporting the distribution of the academic research on LPBF of Al alloys in the recent years, the latter have yet been extensively investigated in the literature while quite limited researches have been carried out on AlSi7Mg alloys. However, by comparing mechanical properties of conventionally manufactured (sand or die casting) and heat treated (T6) parts, AlSi7Mg0.6 alloy is characterized by a better tensile response than AlSi10Mg, whose properties are R_m=290 MPa, $R_{p0.2}$=240 MPa, A%=2 and R_m=260 MPa, $R_{p0.2}$=220 MPa, A%=1 respectively [8]. In this view, the potential of LPBF could be more proficiently exploited by AlSi7Mg alloys, so, that is the reason why the AlSi7Mg0.6 alloy has been chosen as base material for the experimental investigations reported in the next section.

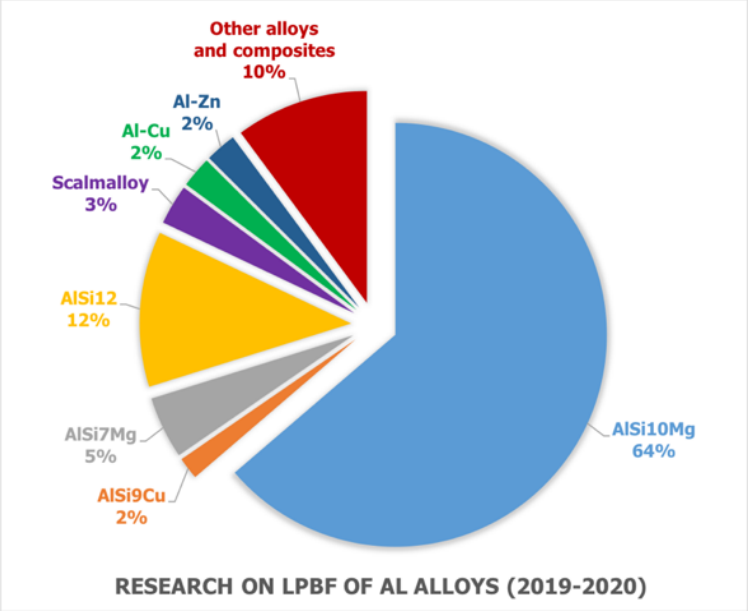

Figure 4.1: Published papers regarding laser-based powder bed fusion of aluminum alloys in the last years (Scopus®, accessed on September 2020)

4.2 Metallurgy of conventional cast AlSi7Mg alloys

As for all casting alloys, microstructure and thus mechanical properties of AlSi7Mg alloys are determined by:

- chemical composition;
- melt treatment and pouring;
- solidification conditions;
- eventual post-solidification densification treatment (e.g. Hot Isostatic Pressing, HIP);
- final heat treatment.

As these alloys are used for structural castings, the careful control of chemical composition is crucial. Ductility, for example, can be very high for these alloys, but it is strongly affected, besides the undesired presence of solidification defects, by impurity content as well as modification of the Al-Si eutectic. The role of each alloy element is synthetized in Table 4.2, where elements are classified in major, minor and impurity. Major elements define main properties of the alloy and both minor and impurity elements may affect castability, solidification, final properties and formation of second phases, that can be either desired or undesired.

Table 4.2: Alloy elements in AlSi7Mg, role and type (mayor, minor or impurity), adapted from [1].

Element	*Role*	*Type*
Si	Improves casting properties: fluidity, feeding and hot tear resistance.	Major
Mg	After aging treatment, forms Mg_2Si precipitates that improve strength and hardness.	Major
Ti	Refines grain structures, in particular if associated with B (TiB_2)	Minor
Fe	Forms insoluble and brittle phases that decrease ductility, such as β-needles $FeSiAl_5$ and α-phase $(Fe,Mn)_3Si_2Al_{15}$ (Chinese script).	Impurity
Mn	Changes the type of undesired Fe-phases, from β-needles to α scripts and reduces die soldering.	Impurity
Cu	If >0.05-0.1% can decrease corrosion resistance.	Impurity
Be	In the range 0.0005 – 0.002% (5 to 20 ppm) reduces oxidation losses and spinel inclusions. If >0.04% hinders the formation of undesired π-$Al_9FeMg_3Si_5$, however in percentage >0.002 is harmful for human health.	Minor
Na and Sr	Used as modifier of the Al-Si eutectic must be kept at very low concentration (100-300 ppm), since Na can form a thick oxide and Sr can cause porosity.	Minor

As already explained when discussing the rapid solidification occurring during LPBF process (Chapter 1), solidification conditions play a major role in defining microstructural features also in the case of conventional cast products. There are a number of casting processes (e.g. sand or die casting, lost foam, permanent mold casting [1]) and the discussion of each of them, and the respective resulting microstructure, is beyond the purpose of this dissertation. However, it should be mentioned that each casting process determines different fluid dynamics of molten material, cooling rates, heat extraction mechanism and they all govern defects formation during solidification (e.g. gas porosities, shrinkage cavities, oxide bi-film, cracks, etc..) and final microstructures (e.g. secondary dendrite arm spacing SDAS, grain size, size and distribution of the eutectic Silicon).

Nevertheless, as disclosed in Table 4.3, none of the conventional casting processes can reach the cooling rates estimated for LPBF, thus explaining the

principal reason why, even starting from the same chemical composition, additive and conventional processes result in very different microstructures.

Table 4.3: Typical cooling rates and Secondary Dendrite Arm Spacing (SDAS) for conventional casting processes (adapted from [10,11]) and additive Laser-based Powder Bed Fusion (LPBF).

Casting process	*Cooling rate [°C s^{-1}]*	*SDAS [µm]*
Dry sand	0.05 – 0.2	100 - 1000
Green sand	0.1 – 0.5	20 - 120
Permanent mold	0.3 – 1.0	20 - 70
Die casting	0.5 – 2.0	20 - 70
High-pressure die casting	50 - 500	5 - 15
LPBF	Approx. 10^6	-

4.2.1 Conventional as-cast microstructure

Al-Si-Mg alloys solidify in a dendritic structure and, as evidenced in Tab. 4.3, size of dendrites (quantified by the Secondary Dendrite Arm Spacing, SDAS) strictly depends on the solidification rate, thus on the casting process. SDAS has been positively related to mechanical properties [12,13], demonstrating that, in analogy with the well-known Hall-Petch relation, a low value of SDAS is beneficial in terms of all mechanical properties.

The equilibrium phase diagram of the Al-Si system, reported in Figure 4.2, presents a partial solid solubility and a eutectic reaction in correspondence of Si=12,6 wt.% that solidifies at 577 °C, while pure aluminum solidifies approx. at 658 °C. In particular, it can be noticed that solubility of Si in Al is rather limited, being 1.5 at.% at the eutectic temperature and approximately 0.05 at.% at 300 °C [14].

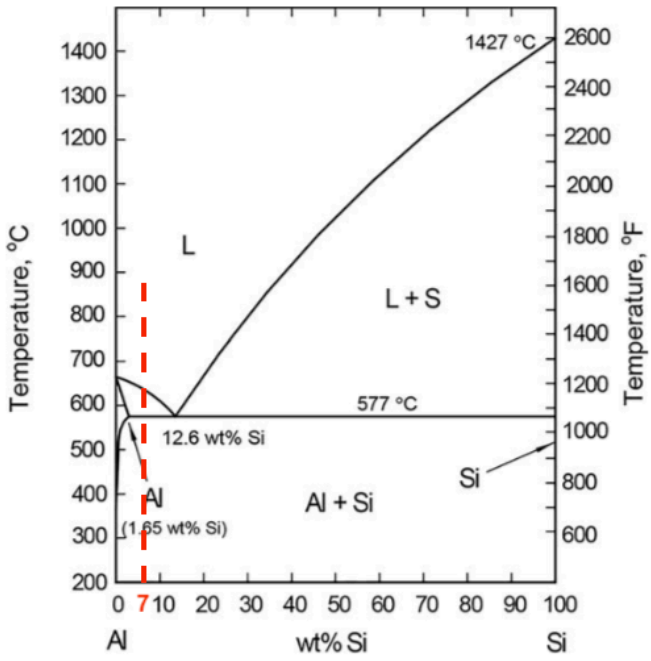

Figure 4.2: Al-Si phase diagram [15], the composition of the AlSi7Mg alloy is evidenced in the diagram by a red dotted line.

As a result, Si strongly segregates during solidification and the final microstructure consists of α-aluminum dendrites surrounded by the eutectic Al-Si phase (Figure 4.3a). Since eutectic Si solidifies in a brittle acicular or lamellar structure (Figure 4.3b), in order to improve strength of the alloy modification of the eutectic phase is usually performed by adding a small percentage (100-300 ppm) of Na or Sr in the melt. This addition changes the morphology of eutectic phase from acicular to a more convenient fibrous structure (Figure 4.3c).

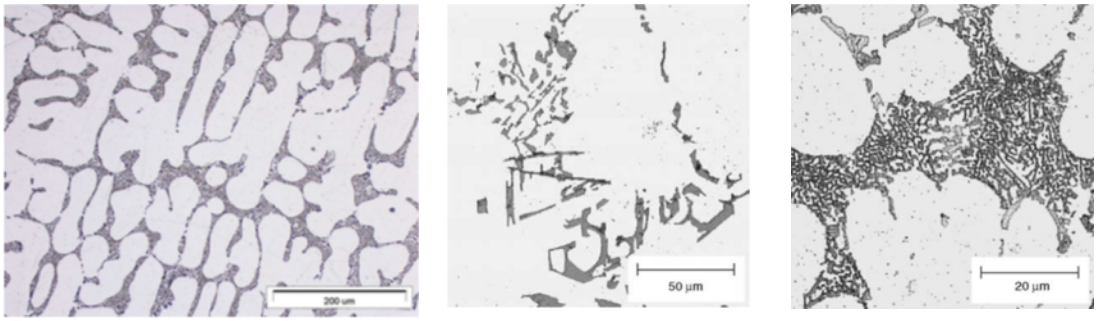

a b c

Figure 4.3: As-cast microstructure of AlSi7Mg alloys: a) general view where white α-aluminum dendrites surrounded by greyish eutectic phase can be appreciated [16], b) un-modified eutectic phase with acicular Si crystals, c) modified eutectic phase with a fibrous morphology [17].

In the reason of the presence Mg and impurity elements like Fe and Mn in the alloy, intermetallic compounds form during solidification, as a result of equilibrium and non-equilibrium transformations. Solid solubility of Fe in Al is very low, as a consequence Fe-based phases are the most common intermetallic compounds found in Al-Si alloys and have been extensively studied in the literature [18–22]. Due to their harmful effects on mechanical properties, especially for the alloy ductility and fatigue strength, they are undesired and several procedures have been developed in order to limit their effect, such as heat treatments, chemical and microstructural control [23]. Phase constituents and intermetallics of AlSi7Mg alloys are reported in Table 4.4. The amount of intermetallic compounds in the alloy is usually around 5 vol.% so, if not extracted from the matrix, they can be hardly detected by X-ray diffraction analyses (Figure 4.4). However, they can be easily recognized by conventional optical (Figure 4.5) and scanning electron (Figure 4.6) microscopy and are usually located in the interdendritic region.

Table 4.4: Phase constituents in the AlSi7Mg alloys (adapted from [23,24]).

Phase	*System, space group*	*Cell parameters [Å]*	*Morphology*	*Chemical composition [at.%]*	*Effect*
α-Al	Cubic (fcc)	a=4.0333	Dendrites	100 Al	
β-Si	Cubic, A4	a= 5.43054	Polyhedra, branched platelets, rods	100 Si	
α-Al(FeMnSi) **α-$Al_{15}(FeMn)_3Si_2$**	Cubic, Im3	a= 12.50	Polyhedra, Chinese Script	19.2 (FeMnCr), 7.7 Si	Reduces Machinability
β-Al_5FeSi	Monoclinic	a= 6.12 b= 6.12 c=41.48 α=91°	Needles	14.3 Fe, 14.3 Si	Deleterious, increases local stress (cracks initiator)
Mg_2Si	Cubic (fcc) Fm3m Hexagonal, β’	a= 6.351 a= 7.05 c=4.05	Fine Chinese Script, dispersed particles	66.6 Mg, 33.3 Si	Increases mechanical strength, decreases ductility
π-$Al_8Mg_3FeSi_2$	Hexagonal, P62m	a= 6.63 c=7.94	Chinese Script	14.3 Si, 21.4 Mg, 7.1 Fe	Decreases ductility
π-$Al_9FeMg_3Si_5$	Hexagonal, P62m		Chinese Script	48.9 Al 26.6 Si 14.9 Mg 8.6 Fe	Obtained after T6 treatment, less harmful than π-$Al_8Mg_3FeSi_2$

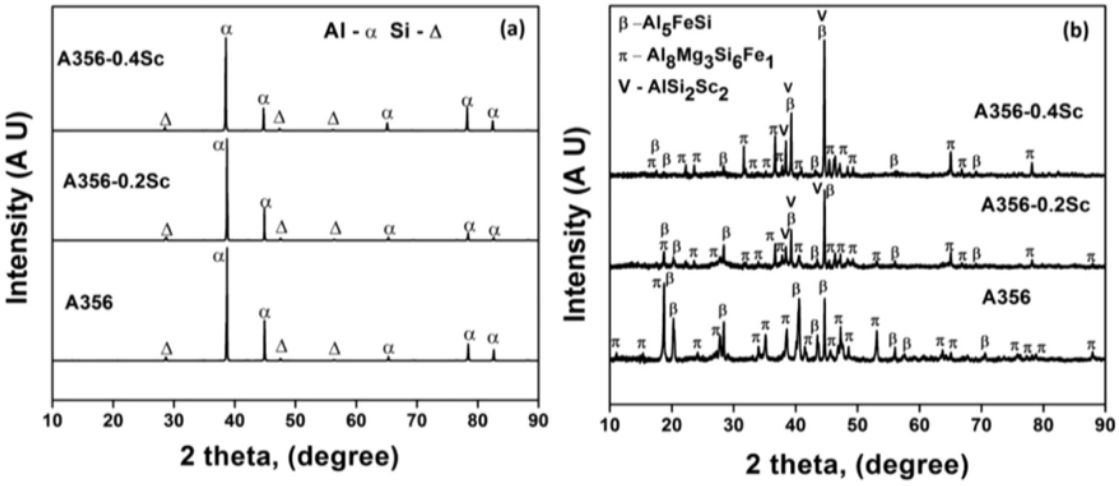

Figure 4.4: Examples of XRD pattern for modified and un-modified AlSi7Mg alloy: a) as-cast condition, b) extracted particles [25].

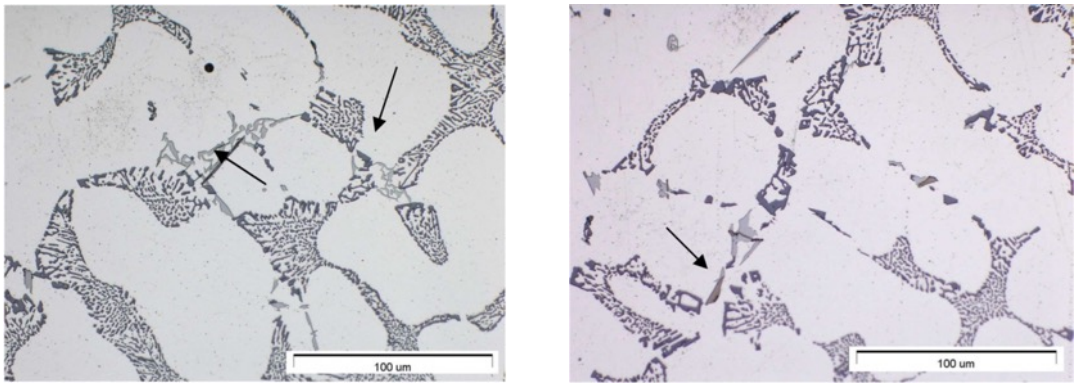

a b

Figure 4.5: Optical micrographs of as-cast microstructure of the AlSi7Mg0.6 alloy, showing intermetallic particles as indicated by arrows: a) Chinese-script and platelet morphologies, b) bulky precipitate [16].

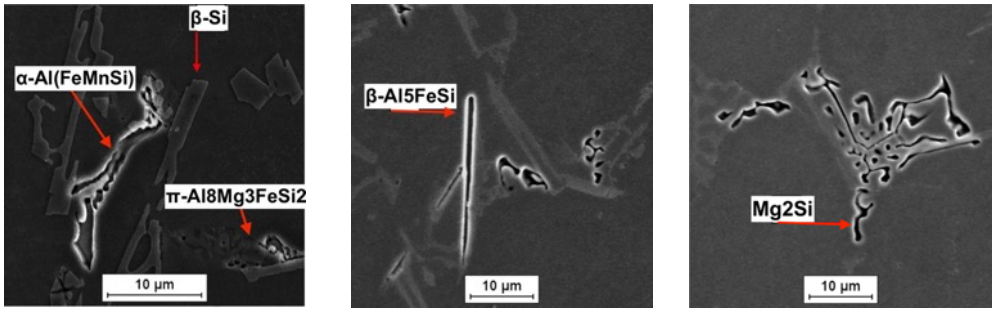

Figure 4.6: Scanning electron micrographs of AlSi7Mg0.6 alloy as-cast microstructure, showing intermetallic particles (adapted from [16]).

4.2.2 Solidification defects

In the final microstructure, typical solidification defects can be found, such as: interdendritic shrinkage, hot cracking, porosity and oxide inclusions [26]. Interdendritic shrinkage forms as a consequence of shrinkage during solidification and poor feeding of interdendritic regions. Hot cracking occurs in the last stages of solidification when the mushy region cannot withstand to imposed local stresses, thus forming intergranular cracks. Shrinkage and hot cracking are both related to the solidification range of the alloy but, for AlSi7Mg alloys, they do not represent a major concern. As showed by the phase diagram in Figure 4.2, where AlSi7Mg composition is marked by a red dotted line, they have a high amount of Si that increases the percentage of eutectic phase, thus reducing the solidification (or freezing) range, being 615 – 560 °C. A short solidification range reduces the probability to incur in hot cracking, while the large amount of eutectic phase promotes feeding of liquid phase, thus limiting shrinkage [15]. Porosity and oxides formation are rather a major concern for all aluminum alloys. The latter are due to the tendency of aluminum to easily react with oxygen, forming an oxide film (Al_2O_3) on the molten material, later incorporated in the bulk, leading to the so-called oxide bi-film (Figure 4.7a). Porosity (Figure 4.7b), on the other hand, can be mainly ascribed to the hydrogen content: hydrogen is the only gas that dissolves in liquid aluminum and, since the solubility of hydrogen in liquid aluminum is quite limited and strongly decreases during solidification, the most part of hydrogen tends to develops gas bubbles, thus forming spherical or elongated porosities with smooth surface [1,26]. Porosity is strictly related to oxides

formation; aluminum, indeed, tends to react with moisture present in the atmosphere and reduces water vapor (H_2O) in order to form Al_2O_3, thus it promotes the dissolution of hydrogen [17].

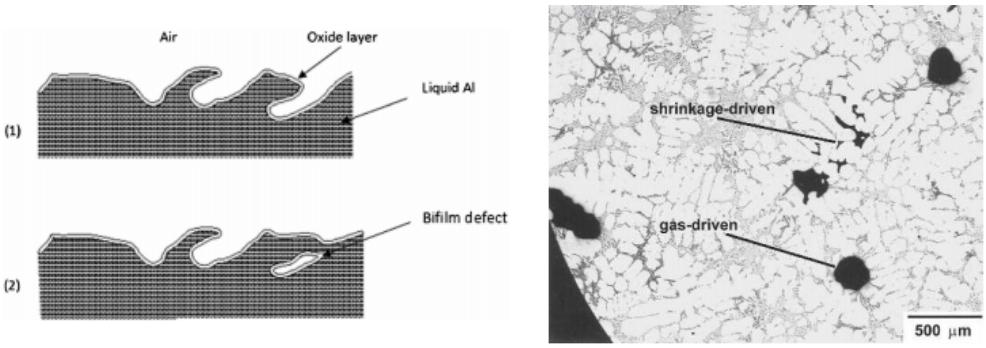

a b

Figure 4.7: Common defects in AlSi cast alloys: a) scheme of the process leading to oxide bi-film [27], b) interdendritic shrinkage cavities and gas porosities [28].

4.3 Heat treatment of conventional cast AlSi7Mg alloys

AlSi7Mg alloys achieve the highest mechanical properties after a well-defined full heat treatment designated as T6 temper, according to the definition given by ISO 2107 [29]. As already mentioned, the nanometric coherent Mg_2Si precipitates are responsible for the high mechanical strength obtained in T6 temper condition. The T6 heat treatment consists of three main stages, whose details are disclosed in Table 4.5:

- high-temperature solution treatment;
- quenching;
- artificial aging treatment.

Table 4.5: Specifications of T6 heat treatment for AlSi7Mg alloys, as reported by ASTM B917 [30].

		Solution treatment			***Artificial aging treatment***	
Alloy	***Final temper***	*Temperature [°C]*	*Time at temperature [h]*	***Quenching***	*Temperature [°C]*	*Time at temperature [h]*
AlSi7Mg0.3	T6	540 ± 5	6 to 12		155	3 to 5
AlSi7Mg0.6		540 ± 5	8		165	6 to 12

Solution treatment has the final purpose of release Mg in the aluminum matrix and during this treatment three key actions occur [31]: i) change in the morphology of eutectic Si particles, especially in case of un-modified alloys; ii) dissolution of coarse Mg_2Si particles formed during solidification; iii) homogenization of casting, by reducing elements segregation. Fe-based intermetallics are generally unaffected by conventional T6 treatment: at 540 °C α and β phases (Table 4.4) may undergo to some degree of spheroidization or fragmentation, but not to a phase transformation. However, according to some experimental evidences [22,32], when Mg=0.35-0.55 wt.%, the π to β phase transformation in Fe-based intermetallics may occur, leading to an additional release of Mg in the Al matrix and the dissolution of coarse script-like π-phases replaced by re-precipitated fine-scale platelets-like fine β-phases. In order to induce the precipitation of coherent Mg_2Si particles during the aging treatment, it is necessary firstly to retain the dissolved Mg in the Al matrix through a rapid quenching from the solution temperature, usually performed in hot water (<100 °C).

After quenching, a supersaturated Al solid solution (Al_{ss}) is formed and, in addition, the rapid cooling promotes a high density of vacancies in the crystal structure. Lastly, the artificial aging treatment stimulates the formation of fine precipitates, following a specific precipitation sequence:

$$Al_{ss} \rightarrow \text{GP Zones} \rightarrow \beta'' \rightarrow \beta' \rightarrow \beta\ (+Si)$$

Precipitation starts with the formation of fully coherent solute-rich clusters termed GP (Guinier-Preston) zones. GP zones are the first to homogeneously nucleate due to their coherency with the matrix and their atomic size. In this stage, vacancies play a major role in the nucleation of coherent precipitates by promoting diffusion and by relieving local strain in the lattice [33]. During aging, solute-rich clusters tend to transform and eventually evolve in an equilibrium phase (β) and excess free Si. However, before reaching the equilibrium phase, two metastable intermediate phases, also termed transition phases, exist. β'' is a coherent phase that strongly contributes to the strengthening of the alloy, while β' is a semi-coherent phase occurring in the first phase of softening. The qualitative trend in the alloy strength as a function of aging time and precipitates is given in Figure 4.8, while detailed information about phases that are developed during aging treatment is reported in Table 4.6. In the curve of Figure 4.8 two main conditions can be recognized: peak-aging, corresponding to the highest strength that can be reached, and an over-aging condition, where softening occurs. T6 heat treatment refers to the peak-aging condition. In more detail, according to Sha et al. [34], the precipitation sequence upon the peak-aged condition for the AlSi7Mg0.6 alloy can be expressed as:

$$Al_{ss} \rightarrow \text{solute clusters} \rightarrow \text{solute clusters} + \text{GP Zones} \rightarrow \text{solute clusters} + \text{GP Zones} + \beta''$$

It should be noted that aging effects and properties strictly depend on the Mg:Si ratio in the solid solution: an excess of Si (with respect to the stochiometric ratio Mg:Si=2 at% in Mg_2Si) can considerably change the kinetics of precipitation and phase composition. As can be derived from Table 4.6, Mg:Si ratio among aging phases is different: passing from GP-zones to β'', β', and finally β, the ratio increases; in other words, metastable phases are enriched in Si [35]. Ultimately, it is worth mentioning that any delay between quench and aging, termed pre-aging, should be avoided. Precipitation from Al_{ss}, in fact, occurs even at room temperature and, as many reported in the literature [31,34,36], pre-aging time affects the kinetics of precipitation and possibly final properties of the heat-treaded cast.

Table 4.6: Crystal structure, space groups and lattice parameters of phases occurring during aging of Al-Si-Mg alloys reported in the literature (adapted from [35,37,38]).

Phase	***Crystal Structure***	***Lattice parameters***			
		a [nm]	***b [nm]***	***c [nm]***	***γ or β [°]***
β”	Monoclinic	0.616	0.616	0.710	82 (γ)
Mg_5Si_6	C2/m	0.77	0.67	0.203	75 (γ)
$Mg_4Al_3Si_4$		1.516	0.405	0.674	105.3 (β)
β’	Hexagonal P63/m	0.705		0.405	
$Mg_{1.8}Si$		0.405		0.67	
		0.407		0.405	
		1.04		0.405	
		0.715		1.215	
	Orthorhombic	0.684	0.793	0.405	
		0.672	0.787	0.405	
β	Cubic	0.639			
Mg2Si	Fcc (CaF2)	0.6351			
Si	Cubic fcc	0.543			

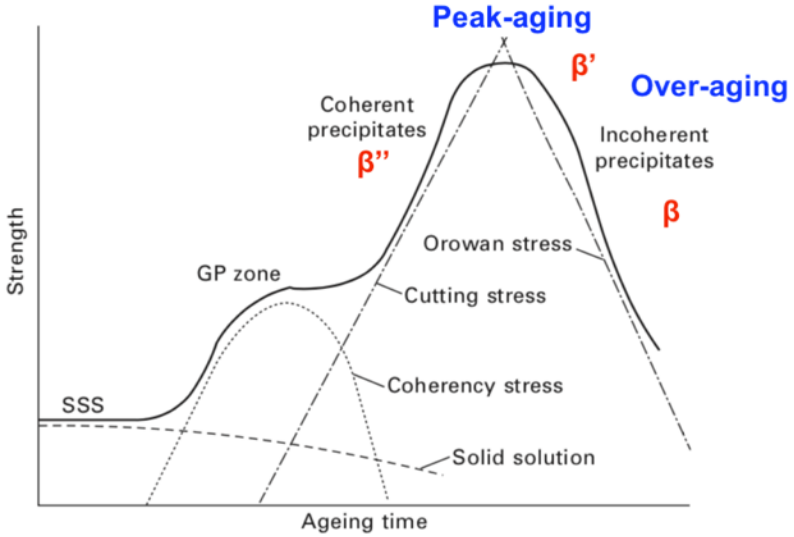

Figure 4.8: Qualitative trend of alloy strength as a function of aging time for an Al-Si-Mg alloy with details of precipitations stages and strengthening mechanisms (adapted from [39]).

4.4 Mechanical properties of conventional cast AlSi7Mg alloys

Minimum mechanical requirements for the AlSi7Mg alloys, in terms of hardness and tensile properties, are reported in Table 4.7. As discussed in the previous sections, these alloys are usually employed in the T6 condition, however, as a reference, in the same table also the properties of the as-cast (F condition) alloy are reported.

Tensile properties depend on both heat treatment and processing route. Indeed, as previously mentioned, mechanical properties are strictly related to SDAS values, which depends on the processing routes. As a result, sand castings, that are characterized by a higher SDAS value, exhibit lower mechanical properties than permanent mold castings. The influence ascribable to the manufacturing process is considered in the requirements given by standards, that establish lower criteria for acceptability in case of sand castings, especially in terms of ultimate strength and elongation. While in the as-cast condition data for AlSi7Mg0.3 and AlSi7Mg0.6 alloys are comparable, after heat treatment AlSi7Mg0.6 exhibits higher mechanical properties. This outcome, as mentioned in the previous section,

is ascribable to the higher Mg:Si ratio of the latter that leads to a more positive response to aging. Indeed, by comparing data of as-cast and heat-treated components, the strengthening effect of the heat treatment is quite evident. Yield strength is more than doubled for both sand and permanent mold castings, and ultimate strength is almost doubled. On the other hand, ductility of the alloy is not negatively affected by heat treatment that results in a good combination of high strength and elongation.

Table 4.7: Mechanical properties (minimum requirements) of AlSi7Mg alloys at room temperature as function of processing route and condition (F stands for as-fabricated, T6 for heat treated) [8,9,40].

Alloy	*Route*	*Condition*	*Hardness*	*Tensile properties*			
			HB	***E [GPa]***	***Ys [MPa]***	***UTS [MPa]***	***A%***
AlSi7Mg0.3	Sand casting	F	50	-	70-80	130-140	2-2,5
		T6	70-75	-	165-190	225-230	2-3.5
	Permanent mold casting	F	55	72.4	80-90	150-170	2,5-3
		T6	75-90	-	185-210	260-290	4-5
AlSi7Mg0.6	Sand Casting	F	50	71.7	90	170	2,5-5
		T6	85	-	210-250	250-315	1-3
	Permanent mold casting	F	55	71.7	90-100	170-190	2,5-6
		T6	100	-	240-290	320-360	3-5

It should be also mentioned that higher mechanical properties than the ones reported in Table 4.6 can be obtained with a proper optimization of heat treatment, and also by recurring to HIP in order to reduce internal solidification defects. As an example, for the heat-treated AlSi7Mg0.6 HIP sand cast alloy the following mechanical properties were reached: UTS=339 MPa, Ys=257 MPa and A%=7.5 [13]. For the heat-treated AlSi7Mg0.3 gravity die cast, tensile properties lied in the ranges UTS=297-333 MPa, Ys=254-266 MPa and A%=1.5-9.3 [12].

4.5 General considerations on LPBF of Al alloys

As shown in Figure 4.9, aluminum alloys are the most studied metallic material for AM applications. The chart reports the trend in the metallic materials that have been subject of scientific researches ever published and indexed on Scopus® database, for all AM technologies from 1980 to 2020. Aluminum alloys cover more than 30% of scientific research, followed by steels (25%) and titanium alloys (21%).

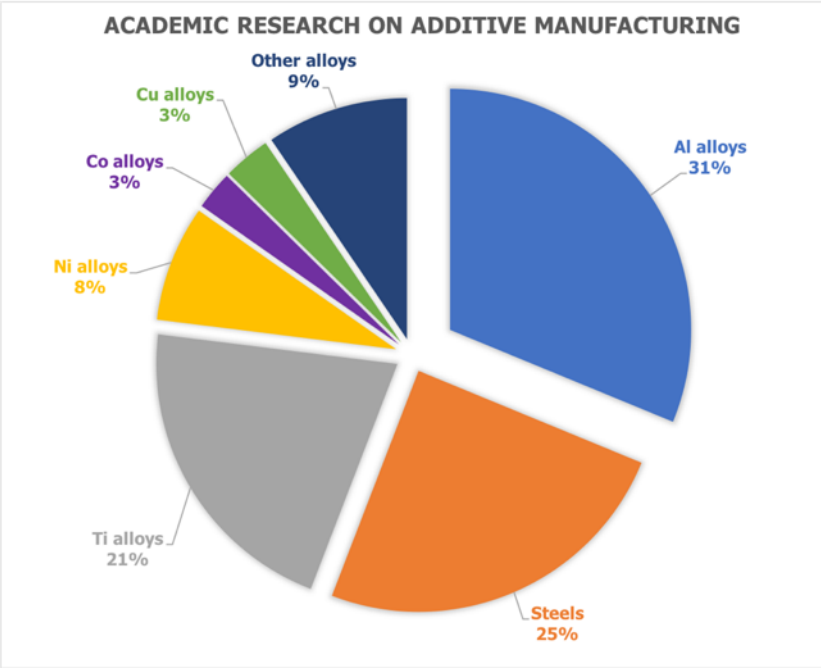

Figure 4.9: Trend in the scientific research of additively manufactured metallic materials, as indexed by Scopus® database (accessed on September 2020)

However, processing aluminum alloys can be quite challenging especially in case of LPBF. The reason mainly lies in the physical properties of aluminum that can be synthetized as follows [41]:

- Aluminum is characterized by a high laser reflectivity (91%) that leads to inefficiency of the process and the necessity of high laser power.
- Aluminum alloy powder is generally characterized by a low flowability and tends to adsorb moisture from the atmosphere, especially if not properly stored in a controlled environment. These aspects promote particles agglomeration and affect the proper spreading of a regular powder bed by means of the re-coater.
- Aluminum easily reacts with the oxygen present in the moisture or in the atmosphere, even in case of inert atmosphere with a controlled oxygen level as in the LPBF. Aluminum oxidizes easily and forms an oxide film on the melt pool that promotes the formation of metallurgical defects. In addition, also aluminum powder tends to oxidize and surface oxidation affect powder melting.
- Solubility of hydrogen in solid and liquid aluminum is very different, hydrogen derived from the reduction of H_2O of the moisture dissolves in the liquid aluminum and forms porosities when the liquid melt pool rapidly solidifies.
- Aluminum has a high thermal conductivity and a high thermal expansion coefficient. The high thermal conductivity leads to a lower heat accumulation during the process that can be responsible for cracks and porosities formation. In this view, platform pre-heating and high laser power are often required in order to obtain high-density parts. On the other hand, the high thermal expansion coefficient, along with a high solidification range, may promote high residual stress, cracks and deformations.
- Vaporization of low-melting alloy elements (such as Mg) can occur, thus leading to fluctuations in chemical composition.

As a consequence, not all aluminum alloys are suitable for LPBF technology. In order to obtain high-density and possibly crack-free parts, a narrowed solidification range and a good weldability are necessary. Therefore, among the commercially available aluminum alloys, the most widely used are the eutectic and near eutectic Al-Si cast alloys, namely AlSi12, AlSi10Mg and AlSi7Mg, as already evidenced by the chart in Figure 4.1. Among these alloys, as already mentioned, AlSi7Mg alloys are the most interesting for industrial applications in the reason of their good overall mechanical properties, especially after T6 heat treatment. It is however worth noticing that the aging treatment must be redesigned and tailored based on the peculiar microstructure resulting from LPBF.

4.6 Microstructure of as-built LPBF AlSi7Mg

In light of issues related to the LPBF of aluminum alloy reported in Section 4.5, a number of defects have been reported in the literature [41,42]. These defects were mainly related to: lacks of fusion and gas porosities, hot-cracking and residual stress, anisotropy, and poor surface quality. However, the studies hereafter discussed reported a near full-density (>99%) obtained after process optimization. As LPBF process is driven by a large number of process parameters and results can be strongly influenced by the feedstock material properties and the type of printing equipment utilized, literature optimized parameters will not be included in the present discussion. It should be mentioned, although, that the role of process parameters in the LPBF will be faced in the next chapter regarding experimental activities.

The microstructure of LPBF parts diverges substantially from conventionally cast counterparts, in the reason of the already discussed rapid solidification conditions. Due to rapid solidification conditions, the final microstructure consists of sub-micron sized primary α-Al surrounded by a fine fibrous network of eutectic Si. During the solidification of Al-Si alloys, indeed, primary α-Al cells grow epitaxially and Si is expelled into the liquid that finally solidifies as eutectic phase in correspondence of cells border (Figure 4.10)[43]. In addition, fast cooling rates extend the solubility of Si up to 5.4 wt.% [44], therefore, the actual amount of Si

ejected in the liquid phase is reduced. As a consequence, the supersaturation of Al cells with Si is promoted.

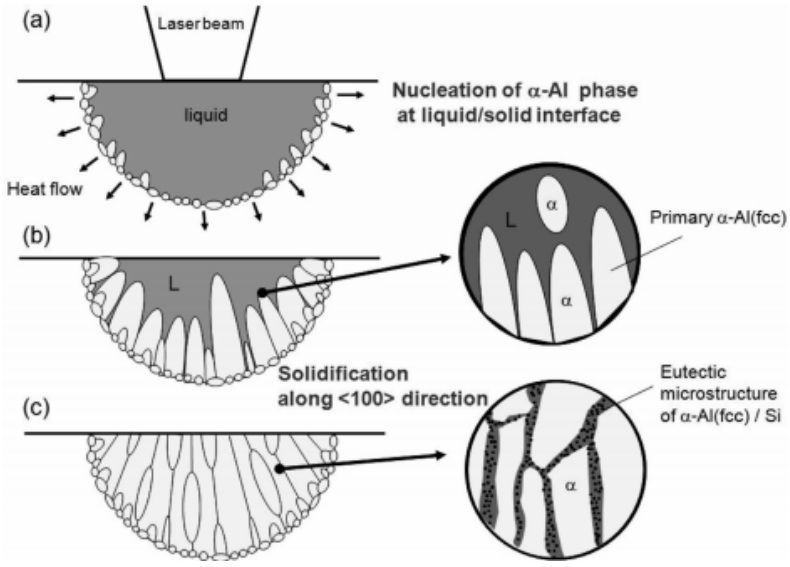

Figure 4.10: Schematic representation of solidification sequence for the LPBF AlSi10Mg alloy: a) melt pool formed by the laser beam, b) solidification of primary α-Al cells along <100> crystallographic direction, c) final microstructure [45].

The typical microstructure of the LPBF AlSi7Mg0.6 alloy, and more in general of the Al-Si alloys, is reported in Figures 4.11, and 4.12. Melt pools can be appreciated with low magnification optical microscopy (Figures 4.11a and 4.12a), where melt pool borders appear bluish and core is orange. The shape of melt pools changes according to samples extraction direction: it is elongated in case of section perpendicular to the building direction and semicircular in case of section parallel to the building direction. The peculiar fine cellular sub-structure can be appreciated only by means of high-magnification electron microscopy (Figures 4.11c,d,e and 4.12c,d,e). As a result of subsequent thermal cycles induced by the layer-wise process, cellular structure and in particular eutectic Si network have different morphology according to the location inside the melt pool [46]:

- Melt pool core (Figures 4.11c and 4.12c): this region experiences high solidification rates and it is marginally affected by subsequent scans, thus it is characterized by the finest microstructure and a continuous Si network.

- Melt pool borders (Figures 4.11d and 4.12d): this area is characterized by a coarser microstructure as they are formed by overlapping of consecutive laser scans and they experience lower solidification rates. An interrupted Si network can also be recognized.
- Heat Affected Zones (HAZs, Figures 4.11e and 4.12e): these regions are located just below melt pool borders, and more generally around the melt pools, and are characterized by a broken intercellular Si network, resulting from particles coarsening due to re-heating induced by the following scans.

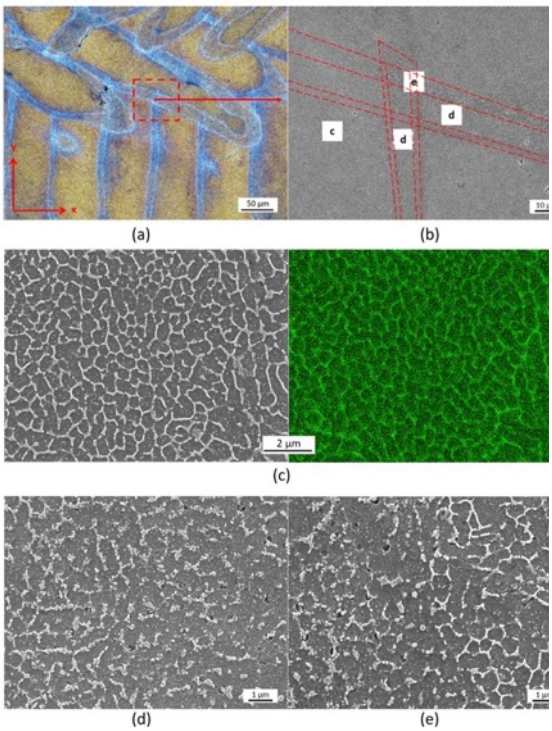

Figure 4.11: Micrographs of cross-section parallel to the working platform for the AlSI7Mg0.6 alloy: (a) optical, (b) low magnification SEM, (c) high magnification SEM of the melt pool core with EDS maps showing Si distribution in green color, (d) high magnification SEM of the melt pool border, (e) high magnification SEM of HAZ [47].

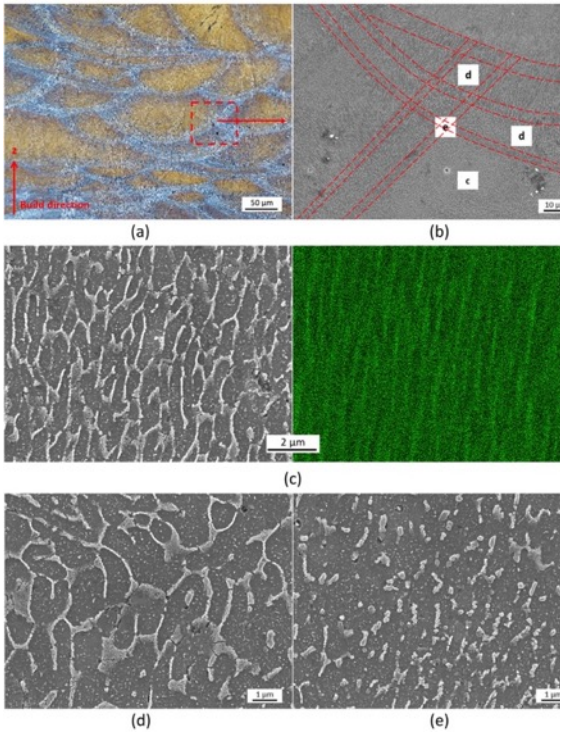

Figure 4.12: Micrographs of cross-section parallel to the building direction for the AlSI7Mg0.6 alloy: (a) optical, (b) low magnification SEM, (c) high magnification SEM of the melt pool core with EDS maps showing Si distribution in green color, (d) high magnification SEM of the melt pool border, (e) high magnification SEM of HAZ [47].

Therefore, as-built microstructure is nonhomogeneous and anisotropy in Al-Si alloys is mainly due to the Si segregations (Figure 4.13). In case of other additively

manufactured metallic materials, like stainless-steels, the main microstructural feature inducing anisotropy is related to the long epitaxial columnar grains crossing over layers (Figure 4.13b). For Al-Si alloys, instead, anisotropy is due to the different morphology of eutectic Si network and especially to Si segregations occurring in re-melted coarse regions (melt pool borders and HAZs, Figure 4.13a) [48].

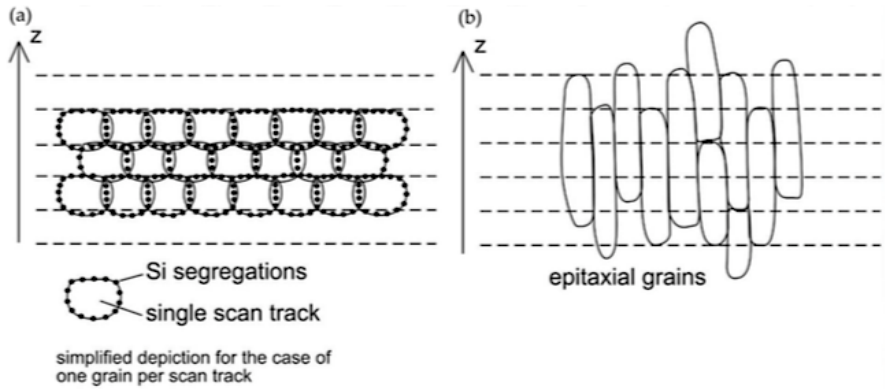

Figure 4.13: Schematic representation of microstructural features of additively manufactured: a) Al-Si alloys, b) stainless-steels [48].

The phases evidenced by X-ray diffraction analyses (XRD) of the as-built microstructure are Al, Si and Mg_2Si, as reported by the literature [47,49]. The presence of Fe-based intermetallic particles has not been evidenced either by XRD or metallographic analyses, presumably as a consequence of their low volume percentage and nanometric size. It is known, in fact, that rapid solidification usually contributes to reducing size of Fe-based and modifying the morphology of intermetallic particles [23,50,51].

4.7 Heat treatment of LPBF AlSi7Mg

The most part of the scientific research regarding the AlSi7Mg alloys processed by LPBF has been devoted to the AlSi7Mg0.6 one. Therefore, data concerning heat treatment and mechanical properties here reported is mainly related to the AlSi7Mg0.6 alloy. In particular, the current state of the art of the experimental

works focused on the heat treatment of this alloy is summarized, along with treatments conditions, in Table 4.8.

Four main post-process heat treatments were considered, that can be synthetized as follows:

- conventional T6 treatment;
- T6 treatment with a shortened solution treatment (0.25, 1, 2 h);
- direct aging from the as-built condition at the conventional aging temperature of 160-165 °C (T5 treatment);
- stress-relieving treatment performed at 300 °C x 2-3 h.

Table 4.8: Synthesis of heat treatment conditions applied in the literature to the LPBF AlSi7Mg0.6 alloy

	First stage			***Second stage***		
Treatment	***Temperature [°C]***	***Time [h]***	***Cooling***	***Temperature [°C]***	***Time [h]***	***Reference***
Stress-relief	270 - 300	2	-	-	-	[52–54]
Solution treatment	535	0.25 - 150	Water quenching	-	-	[44]
T6	535 - 540	1 - 12	Water quenching	160 – 180	3 - 10	[52,53,55–58]
Direct aging	160 - 170	4 - 6	-	-	-	[53,55–59]

When dealing with post-process heat treatment of LPBF Al-Si-Mg alloys, two main aspects should be considered [48,53,60]:

- Subsequent heat inputs due to the additive process can induce artificial aging while the part is being fabricated.

- Platform pre-heating, usually in the range 100-200 °C, promotes the precipitation of second phases, thus developing artificial aging and even over-aging in the as-built part.

As consequence, aging conditions of firstly-processed layers can be quite different from lastly solidified ones and several geometric and process parameters like size and shape of the part, time needed to complete the manufacturing process, affect the post-process heat treatment. Therefore, in the as-built conditions, besides grain refinements, other strengthening mechanisms are likely represented by both solid-solution strengthening due to the supersaturation of the Al matrix and precipitation hardening induced by aging induced by subsequent heat inputs [48].

4.7.1 Stress-relief Annealing

Microstructural analyses of the stress-relieved alloy (Figure 4.14) evidenced that no major changes from the as-built microstructure occurred: melt pools were still visible as well as the fine cellular microstructure embedded in the Si-eutectic network. However, many authors described the Si network as "blurred", suggesting a partial coalescence of Si-particles and possible coarsening, as a consequence of the diffusion of Si facilitated by high temperature exposure.

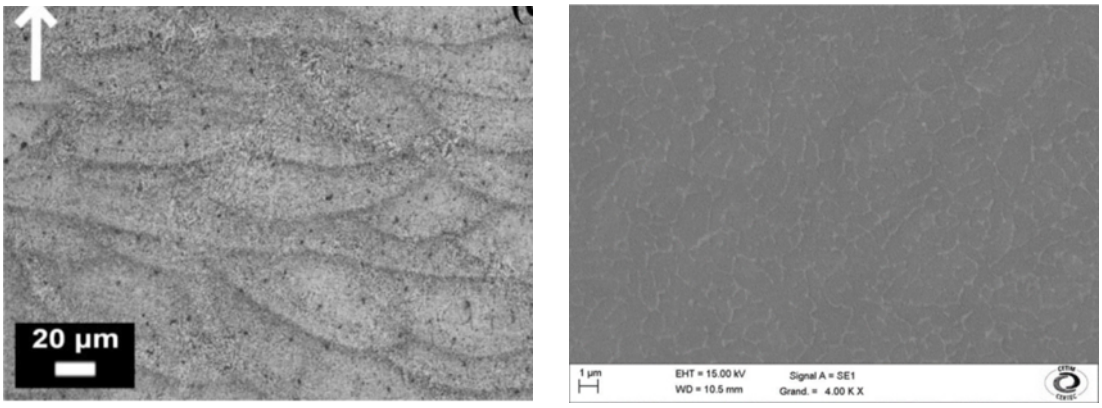

a b

Figure 4.14: Representative micrograph of stress-relieved AlSi7Mg0.6 alloy at: a) low magnification [52]; b) high magnification [53].

4.7.2 Direct Aging

Similarly to the case of stress-relieved alloy, the direct aging (T5 treatment) of the as-built alloy, performed in the literature at 160-170 °C, did not involve substantial modifications in the microstructure. For a long aging treatment (6h), authors reported that very fine Si-based particles precipitated along α-Al cells [54], but the Si-eutectic network was substantially unaffected by the treatment, leaving manufacturing tracks (i.e. melt pools borders) still clearly visible.

4.7.3 T6 treatment

As reported in Table 4.8, currently in the literature it has been investigated the solution treatment (535-540 °C for 0.25-150 h) eventually followed by water quenching and artificial aging (160-180 °C for 3-10 h).

After solution treatment at 540 °C, the microstructure drastically changed from the as-built condition. Peculiar features of the additively process, such as melt pools borders and fine cellular structure, disappeared. After solution treatment, the microstructure consisted of a homogeneous dispersion of almost-globular Si-particles in the α-Al matrix (Figure 4.15). During solution treatment, in fact, the supersaturated solid solution obtained by the rapid solidification during LPBF broke down and the solubility of Si from 5.4 wt.% fell down to a value of below 1.6 wt.%, that is the maximum value of Si solubility at the eutectic temperature, according to the equilibrium phase diagram [44,53]. It should be noticed that the anisotropy of the microstructure due to the Si segregation, differently arranged in the three main area (melt pools core, melt pool borders and HAZ) in the as-built microstructure, was strongly reduced. However, long-time holding at the solution temperature induced coarsening of Si-particles, as highlighted by Figure 4.15. Concurrently, an increase in the porosity content was also observed after solution treatment [53]. The observed porosities were mainly spherical and presumably related to the trapped gas inside melt pools during solidification that, due to the exposure at high temperature, expanded and formed typical gas porosities, similarly to the blistering phenomenon observed in the conventionally manufactured cast aluminum alloys [61].

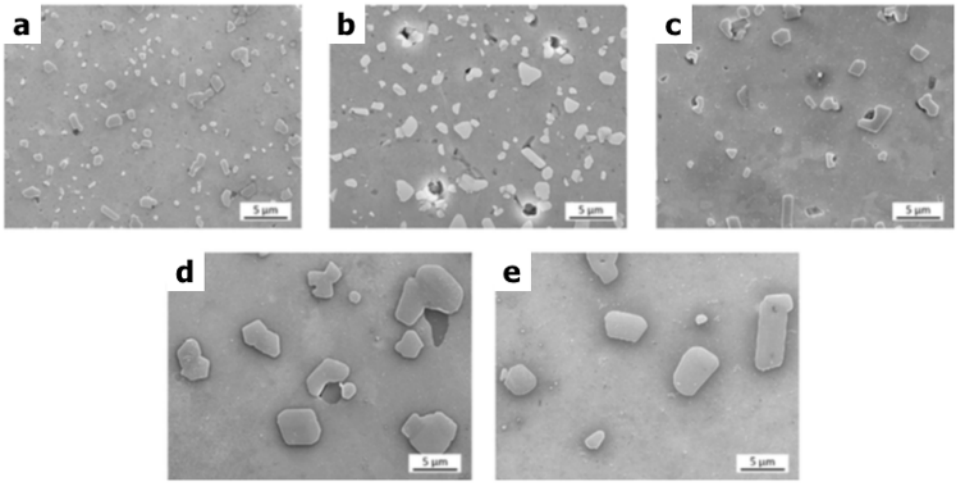

Figure 4.15: Microstructure evolution for the AlSi7Mg0.6 alloy subjected to solution treatment for: a) 0.25h; b) 1h; c) 4h ; d) 24h; e) 150h (adapted from [44]).

Aging treatment after solution and quenching was performed in the range 160-180 °C for 3-10 h holding time. After the complete T6 heat treatment, the presence of acicular needle-shaped Fe-base intermetallic compound (β-Al_5FeSi) has been highlighted by a few authors [53,56,58], as shown in Figure 4.16. The same were not evidenced in the as-built, direct aged or stress-relieved alloy, therefore it is possible to argue that coarsening of intermetallic particles occurred during high temperature solution treatment. Although Fe-intermetallics are known to be detrimental for the mechanical response of the cast alloy, the impact of these acicular and micrometric compounds on strength and ductility of the LPBF alloy still needs further investigations.

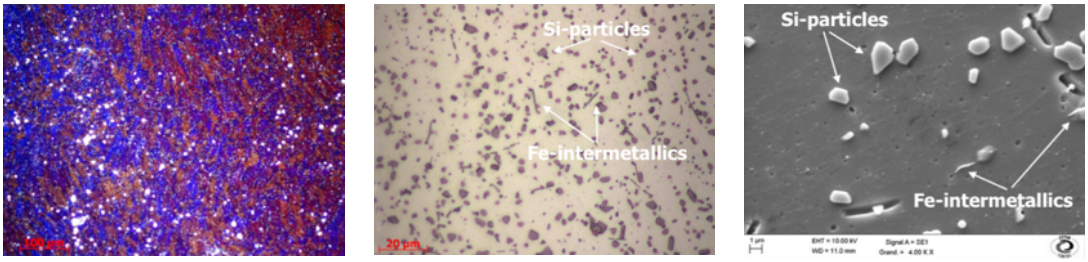

a b c

Figure 4.16: Low to high magnification microstructure for the AlSi70.6 LPBF alloy subjected to T6 heat treatment: a) polarized optical, b) bright field optical and c) SEM micrographs. Adapted from [53].

As will be discussed in the following section, direct aging of the as-built alloy and complete T6 treatment resulted in very different mechanical response. A first explanation can be found in the work of Rao et al. [62] who investigated the precipitation path of the direct aged (165 °C for 2 h) and T6 treated (solution treatment at 535 °C for 1 h followed by water quenching and aging at 165 °C for 6 h) AlSi7Mg0.6 LPBF alloy via TEM analyses. Based on their findings, the following considerations can be drawn:

- Precipitation sequence differed from direct aged and T6 alloy.
- Direct aging of the supersaturated LPBF as-built microstructure induced the precipitation of randomly oriented Si-particles, that were not observed in the as-built condition.
- Peak-aged T6 treated alloy (1h solution treatment) exhibited both β″ and β′ reinforcing phases, being β′ the predominating one, while the one expected in the peak-aged condition is only β″. With a longer solution treatment (8h), in the T6 peak aged condition only β″ phase was detected.

The precipitation of Si particles during direct aging can be explained by the extended Si solubility (5.4 wt.%) resulted from rapid solidification condition, that gives the necessary driving force to Si atoms cluster and precipitate. At the same time, giving the low Mg content (0.6 wt.%), clustering of Mg atoms is lower than Si, hindering the formation of Mg+Si particles (namely, β″).

After solution treatment, the supersaturation of Si is reduced and the precipitation sequence follows the one on the conventional cast alloys. However, in the peak-aged alloy the β′ phase was surprisingly the predominant phase. The premature appearance of β′ in the T6 peak-aged condition was related to a change in the kinetics of the transformation, by the reason of an increased vacancy concentration in the LPBF alloy. Vacancies, indeed, facilitate the diffusion of substitutional solutes in the Al matrix. According to their findings, the incremented vacancy concentration can be a consequence of the uniaxial tensile strains in the crystal lattice, due to residual stress, that may reduce the energy needed for the formation of vacancy. As a consequence, the nucleation of β′ is promoted in the LPBF alloy, explaining the presence of this phase in the peak-aged

condition in contrast to the cast alloy, for which β′ is mainly related to the over-aged condition. As will be discussed in the following Chapter regarding the experimental activities carried out on AlSi7Mg0.6 alloys, the occurrence of different precipitation behavior between direct aging and complete T6 treatment is also supported by XRD and thermal analyses (DTA and DSC).

4.8 Mechanical properties of LPBF AlSi7Mg

The current state of the art of the mechanical behavior, in terms of hardness and tensile properties, of the LPBF AlSi7Mg0.6 alloy is summarized in Table 4.9. Literature results have been organized as a function of temper condition (as-built, stress-relieved, T6 treated, and direct aged) and building platform pre-heating. When available, the direct comparison of different building directions was integrated, in order to highlight the anisotropy of the LPBF alloy.

By analyzing data in Table 4.9, a few general considerations can be derived:

- The as-built LPBF alloy is characterized by higher mechanical properties of T6 conventional treated cast alloy (whose treatments conditions and mechanical properties are reported in Tables 4.5 and 4.7 respectively). The difference can be ascribed to the grain refinement and solid solution strengthening peculiar of the LPBF alloy. In addition, the fine intercellular network due to alloy element segregation, mainly Si, acted as barrier to the dislocation movement, improving yield and ultimate strength. Mechanical properties were even higher in case of samples produced with platform pre-heating, thus confirming the above-mentioned aging induced during the process itself.
- The stress relieving treatment resulted in a decrease in hardness and strength, reaching values lower than the T6 heat-treated cast alloys. The drop can be attributed to coarsening of cells and more importantly to the partial diffusion of Si reducing the content of alloy elements in the matrix and thus the contribute due to solid solution strengthening. Consequently, the obstacle to dislocations movement are reduced, resulting in lower yield strength and improved ductility. Moreover, it should be considered that a

partial relieving of internal stress occurred, that could have affected the alloy strength.

- The highest mechanical properties were obtained after direct aging, that induced an increase in both yield and ultimate strength without considerably affecting the alloy ductility. The result can be related to the precipitation of very fine Si-particles inside Al cells, as observed by some authors, acting as obstacle to dislocation movement. In addition, in contrast to stress-relieving, aging treatment did not induce coarsening of the microstructure and a substantial release of internal stress.
- After T6 treatment, the intercellular network disappeared and strengthening is due to the presence of nanometric β′ and β″ precipitates. However, ultimate and yield strength were lower than as-built condition, while ductility is slightly promoted. Surprisingly, not appreciable differences between a long and a shortened solution treatment can be observed, even if microstructural analyses agreed in the occurrence of coarsening of Si-particles with increasing solution time.
- Mechanical properties of vertical (V) specimens, built perpendicularly to the platform, are generally lower than horizontal (H) ones, built parallelly to the platform. For the Al-Si alloys, as already mentioned, the anisotropy in the mechanical behavior is presumably related to the Si segregations. The position of layer boundaries, for which the Si network is coarser, with respect to the loading direction in the vertical specimens can be considered as a cause of the lower mechanical properties. After the T6 treatment, indeed, the homogenization of the microstructure is associated with a strong reduction in the anisotropy of the mechanical response.

Table 4.9: Summary of mechanical properties reported in the literature for the LPBF AlSi7Mg0.6 alloy as a function of temper condition and platform pre-heating (H and V samples had building direction respectively parallel and perpendicular to the platform). The acronym N.A. (not available) indicates that data was not reported in the manuscript

Condition	***Platform pre-heating*** **[°C]**	***Building direction***	***Hardness***	***Tensile properties***				***Reference***
				E [GPa]	**Ys [MPa]**	**UTS [MPa]**	**A% [-]**	
As-built	100	H	120 ±2 HV0.1	83 ±3	244 ±5	388 ±5	5.3 ±0.4	[52]
	150	H	112 HBW 5/250	N.A.	281	417	8.4	[53]
	150	V		N.A.	262	398	3.3	
	150	H	133 ±3 HV1	62 ±4	314 ±79	446 ±6	6.1 ±0.3	[58]
	150	V	129 ±8 HV1	62 ±2	282 ±19	435 ±18	3.0 ±1.0	
	N.A.	V	N.A.	71.1	240 ±40	406 ±19	9.9 ±3.9	[54]
	N.A.	H	102 HV0.3	N.A.	257 ±3	398 ±13	7.6 ±1.8	[56,59]
	N.A.	V	N.A.	N.A.	216 ±2	400 ±4	6.9 ±0.4	
Stress-relieved	100	H	81 ±1 HV0.1	76 ±2	190 ±5	289 ±6	8.3 ±1.2	[52]
	150	H	75 HBW 5/250	N.A.	150	257	16.8	[53]
	150	V		N.A.	152	266	11.5	
	N.A.	V	N.A.	75.7	139 ±2	234 ±2	19.5 ±1.2	[54]

T6 (8-12h solution)	100	H	116 ±1 HV0.1	84 ±3	250 ±10	308 ±12	5.2 ±0.2	[52]
	150	H	108 HBW 5/250	N.A.	295	350	10.1	[53]
	150	V		N.A.	280	318	3.0	
	150	H	95 ±6 HV1	58 ±17	239 ±10	293 ±17	6.3 ±3.0	[58]
	150	V	96 ±7 HV1	52 ±12	241 ±10	298 ±9	10.6 ±4.0	
T6 (0.25-1 h solution)	N.A.	H	113 HV0.3	N.A.	256 ±4	306 ±5	4.7 ±0.1	[56]
	150	H	100 ±6 HV1	49 ±12	227 ±23	317 ±19	6.9 ±1.0	[58]
	150	V	99 ±6 HV1	48 ±19	215 ±10	320 ±14	11.8 ±2.0	
Direct aging	150	H	126 HBW 5/250	N.A.	294	425	8.2	[53]
	150	V		N.A.	278	424	4.5	
	150	H	137 ±2 HV1	63 ±11	282 ±23	444 ±3	6.8 ±1.4	[58]
	150	V	136 ±3 HV1	65 ±2	261 ±8	431 ±16	3.2 ±0.9	
	N.A.	H	137 HV0.3	N.A.	309 ±3	411 ±10	4.8 ±0.8	[56,59]
	N.A.	V	N.A.	N.A.	282 ±1	411 ±21	4.1 ±0.4	
	N.A.	V	N.A.	74.0	278 ±15	430 ±5	6.2 ±1.1	[54]

The mechanical behavior was further studied by means of fracture surfaces analyses, whose representative literature results are reported in Figure 4.17. The fracture mode for the LPBF AlSi7Mg0.6 alloy is generally ductile, for all temper conditions, as can be noticed by the presence of fine micrometric dimples. Only in few cases [44,57], signs of fragile cleavage fracture were evidenced in conjunction with a general ductile behavior. Size of such dimples, after stress-relieving treatment, increased, as a consequence of coarsening occurred in the microstructure. Further increase in the dimples dimension occurred after T6 treatment and silicon particles could be found inside dimples showing a smooth and flat morphology, as a consequence of fragile fracture. In case of direct aged specimens, dimples were again micrometer-sized, as for the as-built condition. The difference in the size and morphology of dimples should be sought in the microstructural features of the alloy, since they nucleate from microstructural inhomogeneities. In fact, in case of T6 alloy dimples nucleated from Si-particles while for the as-built and direct aged conditions, where the cellular structure was still present, the absence of major inhomogeneities delayed the formation of dimples, thus resulting in higher mechanical properties.

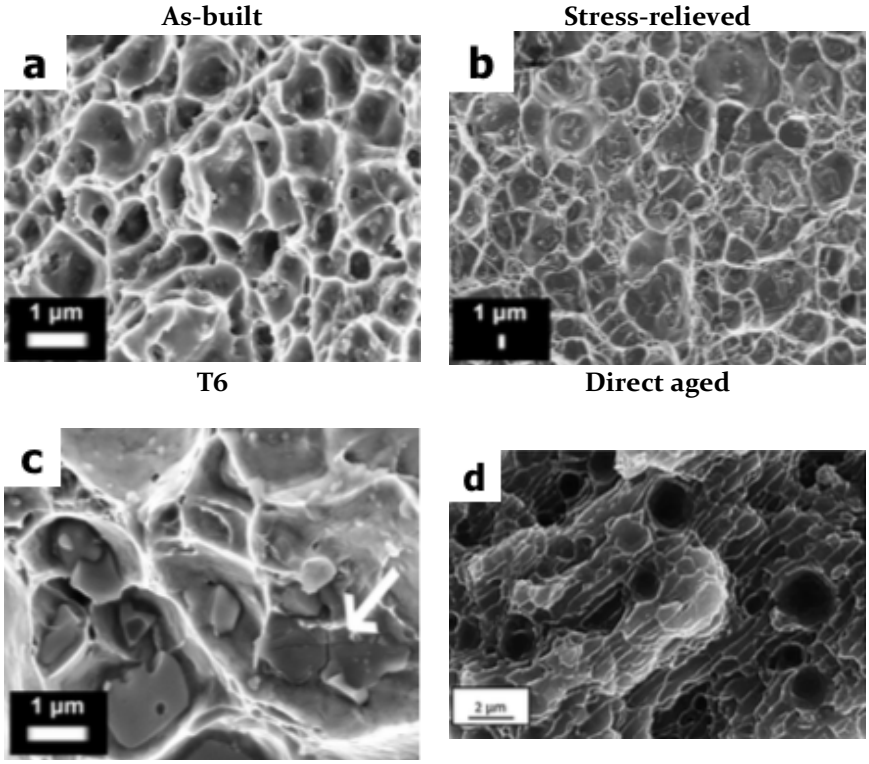

Figure 4.17: Fractographic analyses of samples subjected to tensile tests: a) as-built, b) stress-relieved, c) T6, d) Direct aged AlSi7Mg0.6 LPBF alloy (adapted from [52,56]).

References

[1] G. Sigworth, Aluminum Casting Alloys and Casting Processes, in: K. Anderson, J. Weritz, G. Kaufman (Eds.), Alum. Sci. Technol., ASM International, 2018. doi:10.31399/asm.hb.v02a.a0006524.

[2] Aluminium Automotive Manual, Eur. Alum. (n.d.). https://www.european-aluminium.eu/resource-hub/aluminium-automotive-manual/.

[3] ANSI H35.1/H35.1M, (2017).

[4] J.G. Kaufman, Aluminum Alloy and Temper Designation Systems of the Aluminum Association, in: Introd. to Alum. Alloy. Tempers, ASM International, 2000: pp. 9–22. doi:10.1361/iaat2000p009.

[5] EN 1780-1 Aluminium And Aluminium Alloys - Designation Of Alloyed Aluminium Ingots For Remelting, Master Alloys And Castings - Part 1: Numerical Designation System, (2005).

[6] EN 1780-2 Aluminium And Aluminium Alloys - Designation Of Alloyed Aluminium Ingots For Remelting, Master Alloys And Castings - Part 2: Chemical Symbol Based Designation System, (2002).

[7] EN 1780-3 Aluminium And Aluminium Alloys - Designation Of Alloyed Aluminium Ingots For Remelting, Master Alloys And Castings - Part 3: Writing Rules For Chemical Composition, (2002).

[8] EN 1706 Aluminium and aluminium alloys - Castings - Chemical composition and mechanical properties, (2020).

[9] K. Anderson, J. Weritz, J.G. Kaufman, eds., 357.0 and Variations A357.0 to F357.0*, in: Prop. Sel. Alum. Alloy., ASM International, 2019. doi:10.31399/asm.hb.v02b.a0006569.

[10] K. Sadayappan, A. Elsayed, Sand Casting of Aluminum Alloys, in: K. Anderson, J. Weritz, J.G. Kaufman (Eds.), Alum. Sci. Technol., ASM International, 2018. doi:10.31399/asm.hb.v02a.a0006533.

[11] S. Lampman, Permanent Mold Casting of Aluminum Alloys, in: K. Anderson, J. Weritz, J.G. Kaufman (Eds.), Alum. Sci. Technol., ASM International, 2018. doi:10.31399/asm.hb.v02a.a0006513.

[12] L. Ceschini, A. Morri, A. Morri, G. Pivetti, Predictive equations of the tensile properties based on alloy hardness and microstructure for an A356 gravity die cast cylinder head, Mater. Des. 32 (2011) 1367–1375. doi:10.1016/j.matdes.2010.09.014.

[13] L. Ceschini, A. Morri, A. Morri, A. Gamberini, S. Messieri, Correlation between ultimate tensile strength and solidification microstructure for the sand cast A357 aluminium alloy, Mater. Des. 30 (2009) 4525–4531. doi:10.1016/j.matdes.2009.05.012.

[14] J.L. Murray, A.J. McAlister, The AI-Si (Aluminum-Silicon) System, Bull. Alloy Phase Diagrams Vol. 5 (1984) 74–84.

[15] G. Sigworth, Solidification and Castability of Foundry Alloys, in: Alum. Sci. Technol. - ASM Handb. Vol. 2A, ASM International, 2018: pp. 165–174. doi:10.31399/asm.hb.v02a.a0006496.

[16] B. Dybowski, B. Adamczyk-Cieślak, K. Rodak, I. Bednarczyk, A. Kiełbus, J. Mizera,

The microstructure of AlSi7Mg alloy in as cast condition, Solid State Phenom. 229 (2015) 3–10. doi:10.4028/www.scientific.net/SSP.229.3.

[17] D.M. Stefanescu, R. Ruxanda, Solidification Structures of Aluminum Alloys, in: G.F. Vander Voort (Ed.), Metallogr. Microstruct., ASM International, 2004. doi:10.31399/asm.hb.v09.a0003727.

[18] L. Ceschini, I. Boromei, A. Morri, S. Seifeddine, I.L. Svensson, Effect of Fe content and microstructural features on the tensile and fatigue properties of the Al–Si10–Cu2 alloy, Mater. Des. 36 (2012) 522–528. doi:https://doi.org/10.1016/j.matdes.2011.11.047.

[19] X. Cao, J. Campbell, Morphology of β-Al5FeSi phase in Al-Si cast alloys, Mater. Trans. 47 (2006) 1303–1312. doi:10.2320/matertrans.47.1303.

[20] C.M. Dinnis, J.A. Taylor, A.K. Dahle, As-cast morphology of iron-intermetallics in Al-Si foundry alloys, Scr. Mater. 53 (2005) 955–958. doi:10.1016/j.scriptamat.2005.06.028.

[21] K. Chanyathunyaroj, U. Patakham, S. Kou, C. Limmaneevichitr, Microstructural evolution of iron-rich intermetallic compounds in scandium modified Al-7Si-0.3Mg alloys, J. Alloys Compd. 692 (2017) 865–875. doi:10.1016/j.jallcom.2016.09.132.

[22] J.A. Taylor, Iron-Containing Intermetallic Phases in Al-Si Based Casting Alloys, Procedia Mater. Sci. 1 (2012) 19–33. doi:10.1016/j.mspro.2012.06.004.

[23] W.S. Ebhota, T.-C. Jen, Intermetallics Formation and Their Effect on Mechanical Properties of Al-Si-X Alloys, in: Intermet. Compd. - Form. Appl., InTech Open, 2016: p. 13. doi:10.5772/intechopen.73188.

[24] M. Warmuzek, Metallographic Techniques for Aluminum and Its Alloys, in: G.F. Vander Voort (Ed.), Metallogr. Microstruct., ASM International, 2004: pp. 711–751. doi:10.31399/asm.hb.v09.a0003769.

[25] S.L. Pramod, Ravikirana, A.K.P. Rao, B.S. Murty, S.R. Bakshi, Effect of Sc addition and T6 aging treatment on the microstructure modification and mechanical properties of A356 alloy, Mater. Sci. Eng. A. 674 (2016) 438–450. doi:10.1016/j.msea.2016.08.022.

[26] E. Fiorese, F. Bonollo, G. Timelli, L. Arnberg, E. Gariboldi, New Classification of Defects and Imperfections for Aluminum Alloy Castings, Int. J. Met. 9 (2015) 55–66. doi:10.1007/BF03355602.

[27] M.A. El-Sayed, H. Hassanin, K. Essa, Bifilm defects and porosity in Al cast alloys, Int. J. Adv. Manuf. Technol. 86 (2016) 1173–1179. doi:10.1007/s00170-015-8240-6.

[28] Q.G. Wang, P.N. Crepeau, C.J. Davidson, J.R. Griffiths, Oxide films, pores and the fatigue lives of cast aluminum alloys, Metall. Mater. Trans. B. 37 (2006) 887–895. doi:10.1007/BF02735010.

[29] ISO 2107 Aluminium and aluminium alloys - Wrought products - Temper designations, (2007).

[30] ASTM B917 / B917M-12, Standard Practice for Heat Treatment of Aluminum-Alloy Castings from All Processes, (2012). doi:10.1520/B0917_B0917M-12.

[31] G. Sigworth, Heat Treatment of Aluminum Alloy Castings, ASM Handbook, in: K. Anderson, J. Weritz, J.G. Kaufman (Eds.), Alum. Sci. Technol., ASM International, 2018. doi:10.31399/asm.hb.v02a.a0006507.

[32] Q.G. Wang, C.J. Davidson, Solidification and precipitation behaviour of Al-Si-Mg casting alloys, J. Mater. Sci. 36 (2001) 739–750.

[33] M. Epler, Structures by Precipitation from Solid Solution, in: G.F. Vander Voort (Ed.), Metallogr. Microstruct., ASM International, 2004: pp. 134–139. doi:10.31399/asm.hb.v09.a0003731.

[34] G. Sha, H. Möller, W.E. Stumpf, J.H. Xia, G. Govender, S.P. Ringer, Solute nanostructures and their strengthening effects in Al–7Si–0.6Mg alloy F357, Acta Mater. 60 (2012) 692–701. doi:https://doi.org/10.1016/j.actamat.2011.10.029.

[35] L. Katgerman, D. Eskin, Hardening, annealing, and Aging, in: G.E. Totten, S. Mackenzie (Eds.), Handb. Aluminum, Vol.1 Phys. Metall. Process., CRC Press, 2003: pp. 278–280.

[36] L. Ceschini, A. Morri, A. Morri, Effects of the delay between quenching and aging on hardness and tensile properties of A356 aluminum alloy, J. Mater. Eng. Perform. 22 (2013) 200–205. doi:10.1007/s11665-012-0208-1.

[37] R. Vissers, M.A. van Huis, J. Jansen, H.W. Zandbergen, C.D. Marioara, S.J. Andersen, The crystal structure of the β′ phase in Al–Mg–Si alloys, Acta Mater. 55 (2007) 3815–3823. doi:https://doi.org/10.1016/j.actamat.2007.02.032.

[38] P.H. Ninive, A. Strandlie, S. Gulbrandsen-Dahl, W. Lefebvre, C.D. Marioara, S.J. Andersen, J. Friis, R. Holmestad, O.M. Løvvik, Detailed atomistic insight into the β″ phase in Al–Mg–Si alloys, Acta Mater. 69 (2014) 126–134. doi:https://doi.org/10.1016/j.actamat.2014.01.052.

[39] A.P. Mouritz, Strengthening of metal alloys, in: Introd. to Aerosp. Mater., 2012: pp. 57–90. doi:10.1533/9780857095152.57.

[40] K. Anderson, J. Weritz, J.G. Kaufman, eds., 356.0 and A356.0, in: Prop. Sel. Alum. Alloy., ASM International, 2019. doi:10.31399/asm.hb.v02b.a0006568.

[41] J. Zhang, B. Song, Q. Wei, D. Bourell, Y. Shi, A review of selective laser melting of aluminum alloys: Processing, microstructure, property and developing trends, J. Mater. Sci. Technol. 35 (2019) 270–284. doi:10.1016/j.jmst.2018.09.004.

[42] C. Galy, E. Le Guen, E. Lacoste, C. Arvieu, Main defects observed in aluminum alloy parts produced by SLM: From causes to consequences, Addit. Manuf. 22 (2018) 165–175. doi:10.1016/j.addma.2018.05.005.

[43] K.G. Prashanth, J. Eckert, Formation of metastable cellular microstructures in selective laser melted alloys, J. Alloys Compd. 707 (2017) 27–34. doi:10.1016/j.jallcom.2016.12.209.

[44] J.H. Rao, Y. Zhang, X. Fang, Y. Chen, X. Wu, C.H.J. Davies, The origins for tensile properties of selective laser melted aluminium alloy A357, Addit. Manuf. 17 (2017) 113–122. doi:10.1016/j.addma.2017.08.007.

[45] N. Takata, H. Kodaira, K. Sekizawa, Microstructure and mechanical properties of Al–10Si–0.4Mg alloy fabricated by selective laser melting, J. Japan Inst. Light Met. 67 (2017) 582–588. doi:10.2464/jilm.67.582.

[46] L. Thijs, K. Kempen, J.P. Kruth, J. Van Humbeeck, Fine-structured aluminium products with controllable texture by selective laser melting of pre-alloyed AlSi10Mg powder, Acta Mater. 61 (2013) 1809–1819. doi:10.1016/j.actamat.2012.11.052.

[47] H. Rao, S. Giet, K. Yang, X. Wu, C.H.J. Davies, The influence of processing

parameters on aluminium alloy A357 manufactured by Selective Laser Melting, Mater. Des. 109 (2016) 334–346. doi:10.1016/j.matdes.2016.07.009.

[48] L. Hitzler, S. Hafenstein, F.M. Martin, H. Clemens, E. Sert, A. Öchsner, M. Merkel, E. Werner, Heat treatments and critical quenching rates in additively manufactured Al-Si-Mg alloys, Materials. 13 (2020). doi:10.3390/ma13030720.

[49] M. Wang, B. Song, Q. Wei, Y. Zhang, Y. Shi, Effects of annealing on the microstructure and mechanical properties of selective laser melted AlSi7Mg alloy, Mater. Sci. Eng. A. 739 (2019) 463–472. doi:10.1016/j.msea.2018.10.047.

[50] R. CHEN, Y. SHI, Q. XU, B. LIU, Effect of cooling rate on solidification parameters and microstructure of Al-7Si-0.3Mg-0.15Fe alloy, Trans. Nonferrous Met. Soc. China. 24 (2014) 1645–1652. doi:https://doi.org/10.1016/S1003-6326(14)63236-2.

[51] J. Santos, A.E.W. Jarfors, A.K. Dahle, Formation of Iron-Rich Intermetallic Phases in Al-7Si-Mg: Influence of Cooling Rate and Strontium Modification, Metall. Mater. Trans. A. 50 (2019) 4148–4165. doi:10.1007/s11661-019-05343-5.

[52] F. Trevisan, F. Calignano, M. Lorusso, J. Pakkanen, E.P. Ambrosio, L. Mariangela, M. Pavese, D. Manfredi, P. Fino, Effects of heat treatments on A357 alloy produced by selective laser melting, World PM 2016 Congr. Exhib. (2016).

[53] A. Mauduit, H. Gransac, P. Auguste, S. Pillot, A. Diószegi, Study of AlSi7Mg0.6 Alloy by Selective Laser Melting: Mechanical Properties, Microstructure, Heat Treatment, J. Cast. Mater. Eng. 3 (2019) 1. doi:10.7494/jcme.2019.3.1.1.

[54] P. Van Cauwenbergh, A. Beckers, L. Thijs, B. Van Hooreweder, K. Vanmeensel, Heat treatment optimization via thermo-physical characterization of AlSi7Mg and AlSi10Mg manufactured by laser powder bed fusion (LPBF), Euro PM 2018 Congr. Exhib. (2020) 1–7.

[55] R. Casati, M.H. Nasab, V. Tirelli, M. Vedani, Effect of different heat treatment routes on microstructure and mechanical properties of AlSi7Mg, AlSi10Mg and Al-Mg-Zr-Sc alloys produced by selective laser melting, Euro PM 2018 Congr. Exhib. (2020).

[56] R. Casati, M. Vedani, Aging Response of an A357 Al Alloy Processed by Selective Laser Melting, Adv. Eng. Mater. 21 (2019) 1800406. doi:https://doi.org/10.1002/adem.201800406.

[57] J.H. Rao, Y. Zhang, K. Zhang, X. Wu, A. Huang, Selective laser melted Al-7Si-0.6Mg alloy with in-situ precipitation via platform heating for residual strain removal, Mater. Des. 182 (2019) 108005. doi:10.1016/j.matdes.2019.108005.

[58] J.C. Pereira, E. Gil, L. Solaberrieta, M. San Sebastián, Y. Bilbao, P.P. Rodríguez, Comparison of AlSi7Mg0.6 alloy obtained by selective laser melting and investment casting processes: Microstructure and mechanical properties in as-built/as-cast and heat-treated conditions, Mater. Sci. Eng. A. 778 (2020) 139124. doi:10.1016/j.msea.2020.139124.

[59] J.T. Oliveira de Menezes, E.M. Castrodeza, R. Casati, Effect of build orientation on fracture and tensile behavior of A357 Al alloy processed by Selective Laser Melting, Mater. Sci. Eng. A. 766 (2019) 138392. doi:10.1016/j.msea.2019.138392.

[60] R. Casati, M.H. Nasab, M. Coduri, V. Tirelli, M. Vedani, Effects of platform pre-heating and thermal-treatment strategies on properties of alsi10mg alloy processed by selective laser melting, Metals (Basel). 8 (2018) 954. doi:10.3390/met8110954.

[61] H. Toda, P.C. Qu, S. Ito, K. Shimizu, K. Uesugi, A. Takeuchi, Y. Suzuki, M. Kobayashi, Formation behaviour of blister in cast aluminium alloy, Int. J. Cast Met. Res. 27 (2014) 369–377. doi:10.1179/1743133614Y.0000000123.

[62] J.H. Rao, Y. Zhang, K. Zhang, A. Huang, C.H.J. Davies, X. Wu, Multiple precipitation pathways in an Al-7Si-0.6Mg alloy fabricated by selective laser melting, Scr. Mater. 160 (2019) 66–69. doi:10.1016/j.scriptamat.2018.09.045.

Chapter 5

LASER POWDER BED FUSION OF ALSI7MG0.6 ALLOY

EXPERIMENTAL ANALYSES

Foreword

The present Chapter synthetizes experimental activities carried out during the PhD research project on the AlSi7Mg0.6 alloy processed by Laser-based Powder Bed Fusion (LPBF). The main novelty aspect of the present work is related to the comprehensive analyses of the whole manufacturing process, thus considering both LPBF process optimization and post-process heat treatments assessment. Emphasis was given to the intimate relation between process, microstructure and properties. First, two different batches of feedstock powder were characterized and compared in term of properties of produced samples. Then, post-process heat treatments were deeply investigated and an innovative shortened T6 treatment proposed. Finally, the assessment of final mechanical properties was carried out, and mechanical behavior related to microstructural features.

Therefore, the present Chapter was focused on three main topics:

- Definition of the effect of feedstock powder and process parameters in the densification process of the alloy.
- Optimization of post-process heat treatment, with a specific focus on the relief of residual stress induced by the process.
- Assessment of the mechanical response of the peak-aged alloy, by comparison with the as-built alloy.

The Chapter is mainly based on the following papers, which I have co—authored as corresponding and first author:

- "*Effects of powders and process parameters on density and hardness of A357 aluminum alloy fabricated by selective laser melting*" by L. Tonelli, E. Liverani, G. Valli, A. Fortunato and L. Ceschini published in *The International Journal of Advanced Manufacturing Technology (vol.106:371–383, 2020)* and licensed by Springer Nature on September 28, 2020 (license number 4917510729401).

- The pre-print "*Role of direct aging and solution treatment on hardness, microstructure and residual stress of the A357 (AlSi7Mg0.6) alloy produced by powder bed fusion*" by L. Tonelli, E. Liverani, A. Morri and L. Ceschini currently unpublished and under review.

5.1 Process optimization: role of feedstock powder and process parameters

This section contains selected parts of the published paper "*Effects of powders and process parameters on density and hardness of A357 aluminum alloy fabricated by selective laser melting*" (license number 4917510729401 by Springer Nature). The published version of the paper can be accessed by the following link https://doi.org/10.1007/s00170-019-04641-x

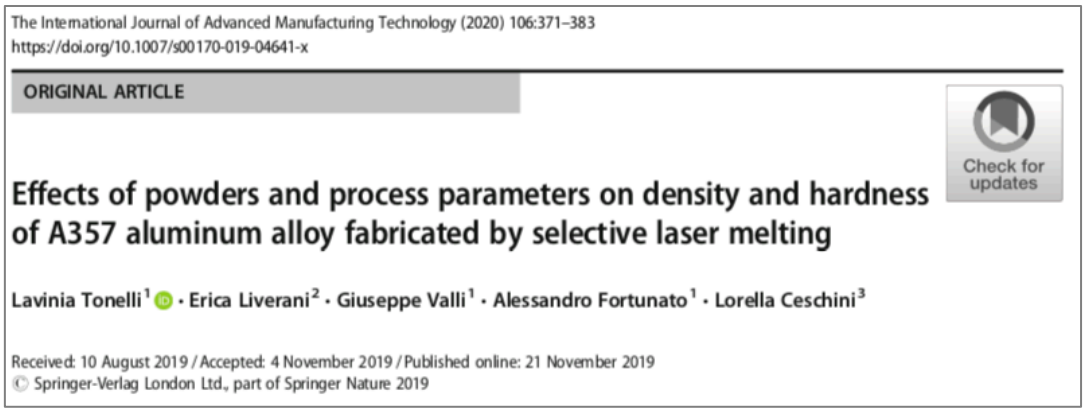

5.1.1 Aim and Scope

On the basis of the importance of feedstock material properties and proper stocking conditions, especially in case of aluminum reactive powder, the work dealt with the relationship between powder properties, powder pre-treatments, and process parameters on the fabrication of aluminum LPBF samples. The presence of porosity in LPBF builds, indeed, is not always caused only by un-optimized process parameters, but can also be related to the presence of porosities in the initial batch of powder due atomization gas entrapment [1]. Moreover, defects in LPBF components can result from non-spherical geometry and from the presence of attached "satellites" on main powder grains that compromise both the flowability and the packing capacity of the powder bed, compromising the deposition of the layer [2]. It should also be considered that in case of reactive materials such as aluminum, powder surface tends to react with oxygen to form a passivation aluminum oxide layer that absorbs humidity. A large number of fine particles increases the surface area in contact with air and thus the amount of

adsorbed water, which compromises the powder flow [3]. According to Hebert [4], the metallurgy of powder bed fusion technologies is strongly influenced by the feedstock quality: water absorption, formation of oxides and hydroxides layers can negatively affect not only the powder flowability, but also the melting and solidification processes. As a consequence, feedstock powder is strongly influenced by the storage and handling conditions and they are not always maintained in a controlled humidity and temperature environment. Therefore, the storage condition must be examined and possible solutions to re-establish the as-received properties of powders must be carried out. In this view, two different virgin A357 (AlSi7Mg0.6) powders were considered, nominally with the same chemical composition and supplied by the same manufacturer, but obtained with different gas atomization processes. On both powders, the effect of two preliminary drying treatments to eliminate the adsorbed humidity as a consequence of an uncontrolled storage was evaluated. LPBF samples were fabricated by using the two powders, subjected to the different pre-treatments, and by varying the process parameters, in order to correlate final properties of samples to both the process conditions and the quality of the powder feedstock. In particular, the authors have analyzed the mutual effects of the described factors as follows:

- influence of pre-treatment on powder morphology;
- influence of powder morphology (axis major and aspect ratio) on samples density and hardness;
- influence of pre-treatment temperature and soaking time on samples density and hardness;
- influence of process parameters (laser power and scan speed) on final samples density, hardness, and defects.

5.1.2 Experimental Procedure

Two different A357 (AlSi7Mg0.6) gas atomized powders were considered for the production of LPBF samples. Both powders, namely Powder L and Powder H, were produced by the same supplier (LPW Carpenter Additive, Carpenter Technology Corporation, USA) adopting two different processes, whose details cannot be

disclosed since they represent industrial sensitive information. Chemical composition and powder properties, given by the supplier, are reported in Table 5.1 and Table 5.2. Based on the provided data, powders mainly differ in the Mg and N content, higher in Powder H than Powder L, and in flowability and apparent density that could be provided only in case of Powder H.

Table 5.1: Chemical composition (wt.%) of powders, given by the supplier [5]

	Al	**Si**	**Mg**	**Fe**	**Cu**	**Mn**	**Ti**	**Zn**	**O**	**N**	**Other**
Powder L	Bal.	6.96	0.49	0.10	0.01	< 0.01	0.09	< 0.01	0.1	< 0.001	< 0.15
Powder H	Bal.	6.90	0.55	0.09	< 0.05	< 0.01	0.09	< 0.01	0.1	<0.2	< 0.1

Table 5.2: Powders properties, given by the supplier [5]

	Laser Size Diffraction [µm] (ASTM B822)			**Sieve Analysis (wt.%)**	**Carney Flow [s/75g]** (ASTM B213)	**Apparent Density [g/cm³]** (ASTM B212)
	DV(10)	DV(50)	DV(90)	+ 63 µm	-	-
Powder L	19.8	40.4	73.2	0	-	-
Powder H	26.0	40.0	62.0	0	38.25	1.3

In order to reduce the adsorbed humidity, both powder H and L were subjected to drying pre-treatments and two different conditions were considered: a high temperature drying and a low temperature one. The first one consisted of heating up to 200 °C and soaking for 1 h, the second one of heating up to 60 °C and soaking for 3 h. In both cases the heat treatment was carried out in a muffle furnace, in ambient atmosphere, using a heating ramp of 100 °C/h and an air cooling.

A total of four set of LPBF samples were realized, in order to compare both Powder L and H and both drying pre-treatments. LPBF samples were fabricated using the MYSINT100 RM manufactured by SISMA, in a nitrogen environment with a residual oxygen content of 0.1 vol.%. Samples (10 x 10 x 15 mm^3 blocks) were built perpendicularly to the platform adopting the process parameter disclosed in

Table 5.3; a roto-translating 3 x 3 mm^2 chessboard was used for scanning the bulk volume of each sample.

Table 5.3: Process parameters adopted for the fabrication of LPBF samples

Hatch spacing [mm]	Layer thickness [mm]	Laser Power [W]	Scan velocity [mm/s]	Energy density [J/mm^3]
0.07	0.02	70	500; 700; 900; 1200	100 – 41.7
		90	500; 700; 900; 1200	128.6 – 53.6
		110	500; 700; 900; 1200	157.1 – 65.5
		130	500; 700; 900; 1200	185.7 – 77.4
		150	500; 700; 900; 1200	214.3 – 89.3
		170	500; 700; 900; 1200	242.9 – 101.2

Powder characterization was carried out both in the as-received condition and after drying pre-treatments. Free surfaces of powders were analyzed by means of a Scanning Electron Microscopy with Energy Dispersive X-Ray Spectroscopy (SEM-EDS, Zeiss EVO 50), while powders cross-sections were analyzed with both optical microscopy (OM, Zeiss Imager A1) and SEM. On SEM micrographs of free powders, particles dimensional and geometric characterization was carried out via image analysis, using the ImageJ open source software. X-ray Diffraction (XRD, PANalytical Expert PRO with Xcelerator detector) was used to determine phase composition. A Cu-Kα radiation source (λ = 0.15406 nm) was adopted and θ - 2θ scans were carried out from 20 to 140°, with a 0.017° step size and a 25 s dwell time, operating at 40 kV and 40 mA.

Density of the produced samples was measured with an analytical balance (0.0001 g precision), following the Archimedes principle. Brinell hardness measurements (HBW 2.5/62.5, hence referred to as HB10 where 10 stands for the force/diameter ratio [6]), were performed on as-built samples within 12 h from the end of the process. Topography of top surfaces was characterized by means of 3D-Digital Microscopy (Hirox KH-7700). Chemical composition was determined by glow discharge optical emission spectroscopy (GDOES, GDA-650 Spectrum Analytik GmbH), while phase composition was evaluated by XRD, under the same operating conditions used for the powders.

Metallographic analyses were carried out on sections extracted from the direction parallel (longitudinal) and perpendicular (transverse) to the building one. They were prepared following standard metallographic procedures and chemically etched with Keller's reagent (20 s immersion at room temperature) [7] before the observation via OM and SEM-EDS microscope. Porosity measurements and defects dimensional characterization were performed using the ImageJ software.

5.1.3 Results and Discussion

POWDERS PROPERTIES

Representative SEM micrographs of the as-received L and H powders are shown in Figure 5.1. As can be noticed from Figure 5.1a,b, particles of powder H were generally more spherical than powder L, for which elongated particles were more frequent. In the case of powder H, several small and almost perfectly spherical particles could be found; the same did not apply to powder L. In addition, surface morphology of both set of powders was irregular and numerous satellites and collapsed particles can be found on the surfaces. The analysis of powders cross-section in Figure 5.1c,f, showed that they were characterized by a dendritic phase and they were mainly defect-free, even if in few cases typical solidification defects such as gas porosities, interdendritic shrinkages and possibly bi-film oxides were detected [8].

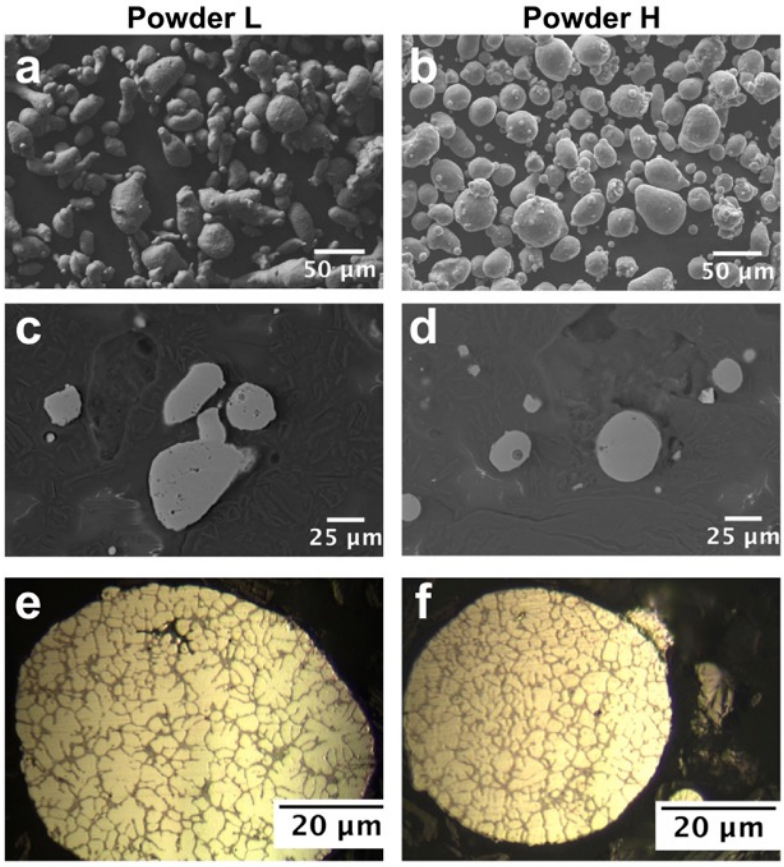

Figure 5.1: Representative micrographs of as-received powders: a) SEM free powders and c), e) SEM and OM powders cross-sections for powder L, b) SEM free powders and d), f) SEM and OM powders cross-sections for powder H.

Results of geometrical characterization of powder particles, in terms of major axis and aspect ratio, are reported in Figure 5.2. These two geometric parameters were chosen to characterize the powders since major axis quantifies the maximum dimension while the aspect ratio determines the roundness of the particles, being the ratio between the major and the minor axis. The size distribution of both powder L and H, ranging from 5 to 80 µm, is asymmetric and a positive skewness can be recognized, meaning that the size of the majority of particles lies at low values. In particular, in the as-received condition almost 40% of powders L and H had a major axis below 25 µm. Moreover, if only small powders with a size up to 10 µm are considered, the percentage is 8.5 for powder L and 30.8 for powder H, showing that the latter had a consistent amount of small particles. The percentage of particles with dimensions greater than 45 µm was, however, similar for both powders, being 13.1 for powder L and 12.4 for powder H. By comparing the results

obtained by image analysis and the ones given by the supplier and retrieved by laser diffraction (Table 5.2), it appears that the analysis performed via laser diffraction slightly overestimated the size of powder particles. The apparent loss of small particles after pre-treatment observed especially in case of powder H can be explained in the reason of the cohesion forces [9–11]. For small particles, indeed, the cohesive forces are able to agglomerate powders and this phenomenon is accentuated if the temperature rises. When the particles size increases, the ratio between the weight of a single particle and the cohesive force acting on it increases, making the forces unable to stabilize the cohesion between powder particles.

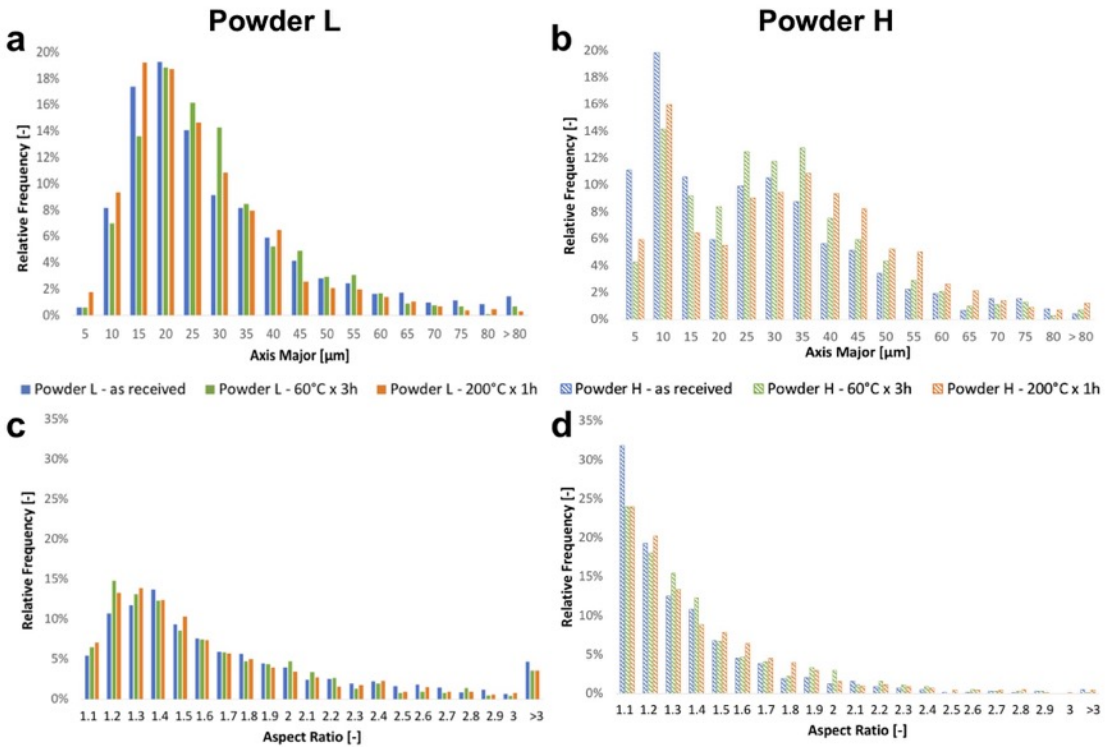

Figure 5.2: Results of particles dimensional and geometric analysis in terms of axis major and aspect ratio for: powder L (a) and (c), powder H (b) and (d).

Furthermore, the geometric analysis confirmed that particles belonging to powder H were significantly more spherical than powder L. Indeed, 31.8% of particles of powder H exhibited an aspect ratio from 1 to 1.1, thus almost perfectly spherical, with respect to 5.4% for powder L. By focusing on particles with the aspect ratio up to 1.5, the percentage raise up to 77.3 for powder H and only 47.4 in case of powder L. It is worth mentioning that a non-negligible number of powder L

particles, 4.7% of the total, had an aspect ratio greater than 3, meaning that almost 5% of powder L was made of strongly elongated particles. Pre-heating treatments seems not to have affected the shape of powders, since only small differences occurred in the measurements, ascribable to experimental variance.

Results of XRD phase analyses are reported in Figure 5.3. On XRD spectra, Al is the main phase detected (ICDD:4-0787), but also minor peaks of silicon (ICDD:27-1402) and alumina could be recognized. In particular, the peak located at 25.4° is consistent with α-Al_2O_3 phase (ICDD:46-1212) [12]. By focusing on the range between 20 and 30° (Figure 5.3b), it can be noticed that the α-Al2O3 peak was detected neither in powder L nor H after the treatment at 60 °C for 3 h, while it was found in the as-received powder and also after the drying treatment at 200 °C for 1 h. Superficial oxidation is indeed a known issue concerning AM powders. In a recent study carried out on different materials [13], XPS analyses showed the presence of a thin layer of oxide on the surface of powders in the as-received condition, even if produced with advanced technologies such as VIGA and plasma atomization. Given the tendency of aluminum to react with oxygen and to form aluminum oxide, as well as the high surface-to-volume ratio in the case of micron-sized powder particles, it is reasonable that aluminum oxide was detected by XRD analyses. As widely reported in the literature, aluminum powder tends to naturally form a thin oxide layer even at low temperature, such as room temperature [14–17]. However, the layer formed at room temperature is usually amorphous, thus it should not have been detected by XRD analyses as a well-defined peak. The amorphous layer, by increasing temperature, evolve in crystalline γ-Al_2O_3 and later in α-Al_2O_3 [16,17]. Therefore, the observed oxidation in the as-received condition is likely related to the high-temperature stages of gas atomization process. The growth of α-Al_2O_3 is usually related to induced tension stresses that lead to the formation of porosity and cracks in the film [16]. Moreover, experimental observation demonstrated that oxide can be wrinkled, thus presenting detachment at the solid/oxide interface [18–20]. After the heat treatment at 60 °C for 3 h the peak of α-Al_2O_3 phase disappeared. Basing on the above, it can be argued that the brittle and presumably cracked alumina surface layer experienced thermal shock that promoted spalling. It should be mentioned, in fact, that aluminum thermal expansion coefficient is considerably higher than those of aluminum oxide (10

times higher in case of γ-Al_2O_3 [16]). The α-Al_2O_3 phase was observed again after the heat treatment at 200 °C: it is possible that aluminum oxide still experienced thermal shock but the higher temperature promoted the formation of a new oxide layer or the oxidation of Al exposed as a consequence of spalling. This temperature can be sufficient to activate an oxidation process, in fact, literature data report the transition from amorphous to crystalline γ-Al_2O_3 at about 200 °C [21,22]. In fact, by comparing the integrated diffraction intensity of the Al (111) peak located at 38.5° and the one of α-Al_2O_3 (012) peak located at 25.4°, it can be argued that after the heat treatment aluminum oxide phase raised for both powders. The increase was more consistent in case of powder H, for which the Al_2O_3/Al ratio raised from 0.038 in the as-received condition to 0.058 after the 200 °C for 1 h treatment. The phenomenon is possibly related to the higher percentage of small and spherical particles in powder H. The raise for powder L, instead, was more limited, passing from Al_2O_3/Al=0.031 to 0.037.

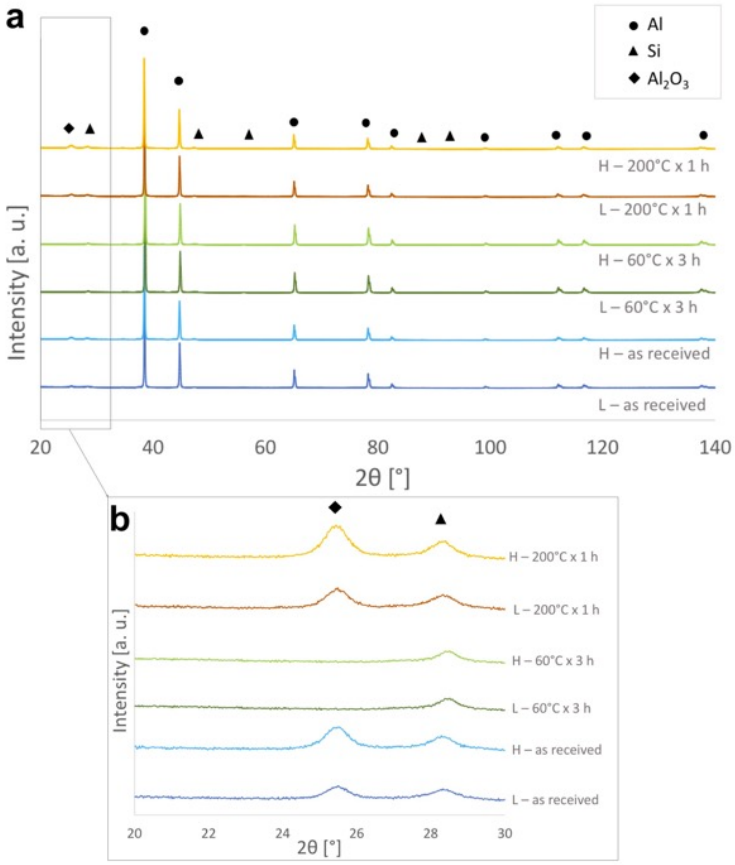

Figure 5.3: XRD spectra acquired for powder L and H in the as-received and pre-treated conditions: a) general view of the whole spectra, b) detail of the range 20°< 2θ <30°.

EFFECT OF LPBF PROCESS PARAMETERS

Density and hardness of LPBF samples, as a function of laser power and scanning velocities, are reported in Figure 5.4, where both powders and pre-treatment are also compared. Density of samples strictly depends on laser power: for powder H the relation between power and density was almost linear and, by increasing the power, the density of LPBF samples increased accordingly (Figure 5.4a-b). Powder L, instead, presented a threshold value of 110 W, since only in case of laser power beyond 110 W, the density increased linearly with the power. It should be mentioned that, due to the low absorptivity of aluminum, most of the irradiance of the laser beam is reflected. However, the total efficiency of the process can be improved by the multiple scattering phenomena occurring among powder particles [23], enhanced by spherical particles. The result can hence be related to the powder morphology discussed in the previous section. Samples obtained with powder H, being more spherical than powder L, always exhibited higher density, even for values of laser power lower than 110 W, at which powder L exhibited the poorest density. It can be assumed that elongated particles, which are more numerous in powder L, negatively affected the multiple scattering between particles and did not actively contribute to improve the efficiency of the process, especially at low laser power.

In addition, the greater flowability of powder H with respect to powder L (Table 5.2), that is strongly related with the sphericity of particles [24], has likely promoted the spreading of an even and compacted layer during the process, increasing density of final samples. This consideration agrees with the results obtained in relation to the higher density of the samples realized from powder H, compared to those printed with L. The influence of scanning velocity is evident in case of powder H where, for a given laser power, the lowest scanning velocity resulted in samples with maximum density. At high scanning velocities, indeed, spattering and denudation phenomena are accentuated [25,26], therefore it is probable that, for a given laser power, samples processed with the highest scanning velocity had a major content of porosities. Samples obtained from powder L, instead, were more influenced by powder pre-treatment than scanning velocity. More generally, in terms of density all H and L samples benefited from the powder heat-treatment carried out at 60 °C. As discussed before, powders treated at 200

°C are presumably covered by an oxide layer. Thus, in order to melt the powder particles higher power is necessary, with respect to the powder dried at 60 °C, where the oxide layer is not present.

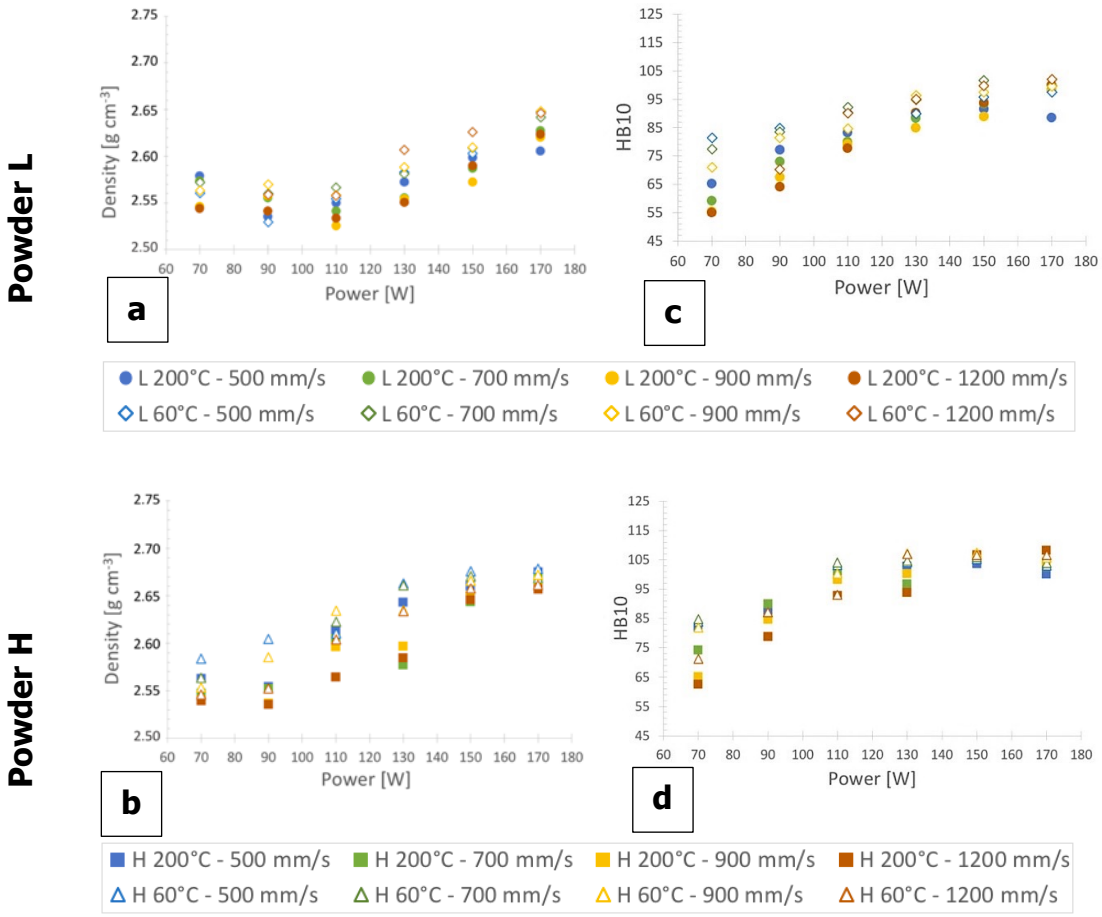

Figure 5.4: Results of: a), b) density and c), d) hardness measurements as a function of laser power, scanning velocities and powder pre-treatment for sample produced with powders L and H respectively.

As for density, also hardness of LPBF samples was strongly related to the applied laser power: by increasing the power the hardness increases, for both powder H and L (Figure 5.4c,d). The lowest hardness measured was approx. 50-60 HB10 in case of low-density samples while, for samples with the highest density, a maximum of approx. 103 and 108 HB10 was obtained for powder L and H, respectively. It is worth mentioning that high-density LPBF as-built samples

reached hardness values comparable and even higher than the conventional AlSi7Mg0.6 heat-treated cast alloy [27]. The result confirms that the LPBF process itself succeeds, in the reason of the fine and supersaturated resulting microstructure [28], in obtaining a hardness comparable and even higher than the conventional heat-treated alloy.

As high energy density can lead to metal vaporization, the chemical composition of LPBF samples was evaluated with GD-OES in case of samples processed with the highest energy density (Table 5.4), that exhibited also the highest density. By comparing the results with the requirements for the AlSi7Mg0.6 alloy given by EN 1706 [29] standard, it can be argued that chemical composition of samples obtained with powder H complies with the standard. On the other hand, the Mg content of powder L samples is slightly lower than the one required for the AlSi7Mg0.6 alloy.

Table 5.4: Chemical composition, measured by GD-OES, of samples produced with the highest volume energy density (P=170W, v=500 mm/s, E=242.9 J mm^{-3}) for both L and H powder and pre-treatments.

Powder	***Pre-Treatment***	***Element (wt.%)***					
		Al	***Si***	***Mg***	***Ti***	***Fe***	***Zn***
L	60 °C x 3 h	92.445	6.842	0.429	0.103	0.071	0.072
L	200 °C x 1 h	92.236	6.902	0.410	0.108	0.099	0.083
H	60 °C x 3 h	92.397	6.687	0.565	0.150	0.085	0.069
H	200 °C x 1 h	92.356	6.795	0.571	0.123	0.049	0.066

Phase composition of LPBF samples, as measured by XRD analyses, is reported in Figure 5.5 for representative samples processed with a constant scanning speed of 900 mm s^{-1} and a power of 70 and 150 W and with powder subjected to the high temperature pre-treatment (200 °C for 1 h). In the spectra, regardless the type of powder, no trace of Al_2O_3 was evidenced. The only appreciable phases were, in fact, Al and Si.

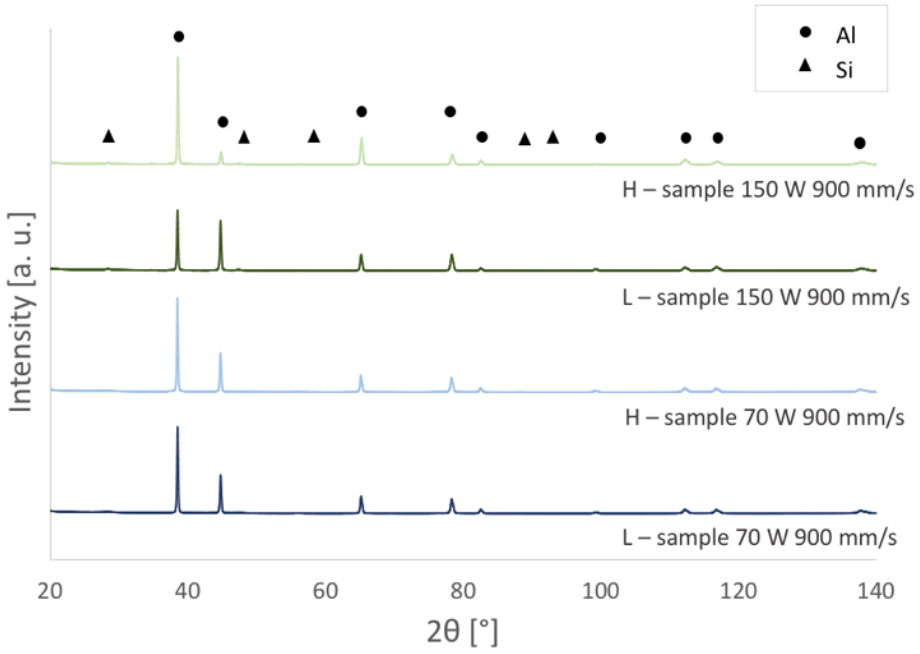

Figure 5.5: XRD spectra for LPBF samples produced with powder L and H (pre-treated at 200°C for 1 h) with a scanning velocity of 900 mm/s and laser power of 70 and 150 W, in the as-built conditions.

MICROSTRUCTURAL DEFECTS CHARACTERIZATION

The maximum density obtained in the present study was still lower than the reference value for the conventional cast AlSi7Mg0.6 alloy, being 2.68 g cm^{-3} [27]. A maximum relative density of 98% and 99% was reached using powder L and H, respectively. Therefore, microstructural discontinuities were presumably present in the high-density samples. As a first assessment, the measurement of the total area occupied by porosities was performed via image analysis on metallographic cross-sections, whose results are reported in Table 5.5 and confirm that porosity percentage is higher for powder L. In addition, results showed that samples with the lowest porosity content were processed with the highest energy density (170 W, 500 mm s^{-1}) and adopting the 60 °C heat-treatment for powders.

Table 5.5: Results of image analysis measurements performed on metallographic cross-sections of LPBF samples

Sample	*Powder Pre-treatment*	*Powder*	*Porosity area on cross section [%]*	*Presence of spatters in the inspected areas [%]*	*Mean spatters diameter [µm]*
170 W-500 mm s^{-1}	60 °C x 3 h	L	1.75	73.3	399 ± 112
		H	0.90	20.0	427 ± 75
170 W-500 mm s^{-1}	200 °C x 1 h	L	4.97	66.7	424 ± 112
		H	1.07	40.0	382 ± 98
170 W-1200 mm s^{-1}	60 °C x 3 h	L	2.05	80.0	247 ± 105
		H	2.30	40.0	382 ± 98
170 W-1200 mm s^{-1}	200 °C x 1 h	L	3.72	86.7	249 ± 121
		H	2.61	46.7	290 ± 50

However, densities obtained via image analysis are lower than those measured following the Archimedes principle, so, a deeper investigation was carried out by comparing morphological and microstructural features. As evidenced on Figure 5.6, on the cross-section of samples, large material discontinuities, with dimensions greater than 200 µm, were found (Figure 5.6a,c). These discontinuities consisted of a round area with a coarser microstructure with respect of the regular microstructure that surrounded the defect, with a cavity lying beneath, possibly related to the spattering phenomena. As already reported by other researchers [30], who investigated morphological aspects of A357 alloy processed by LPBF, spattering, balling and un-melted powder particles can be found on the surfaces. Un-melted particles and spatters can be distinguished by their microstructure since cooling rates of powders are higher than spatters. In the present study, the majority of powders particles have been proved to be smaller than 60 µm, so it is unlikely that these defects might be related to un-melted particles. In their work [30], authors showed spatters with dimension greater than 200 µm with consistent gas porosity content.

With the aim to correlate the defects observed on cross-sections with spatters generation, morphological and microstructural features were compared. As regards morphological features, 3D maps of samples top surfaces were acquired with the 3D digital microscope, for high-density samples processed with laser power 170 W and scanning velocity 1200 mm s^{-1} (Figure 5.6b,d), that revealed the presence on the surfaces of large spatters with a maximum height of about 270 μm. Top surfaces were chosen for the analysis since they represent the last processed layer. On the metallographic cross-sections, a fixed number of zones were investigated on each sample and for every zone it was recorded the presence, or the absence, of spatters to determine the percentage of spatters identified on the cross-section. Furthermore, for each defect identified as spatter, the quantification of dimension was determined via image analysis. The results of the above described spatters analysis, also reported in Table 5.5, demonstrated that a larger extent of such defects was found on samples obtained with powder L than powder H, by a factor of about two. In addition, by comparing the dimensions measured by image analysis with the morphological investigation in Figure 5.6b,d, spatters were positively related to the microstructural defects detected on-cross sections. Spatters in the dimension of approximately 200 μm, that are generated during the LPBF process and consist of molten material ejected by the melt pool, can negatively affect the deposition and the melting of the subsequent layer, as illustrated by Wang et al. [31], therefore they can generate microstructural defects. It is worth noting that, both in case of powder L and H, by increasing the scanning velocity the amount of spatters defects on cross-section increased accordingly, but their dimension decreased.

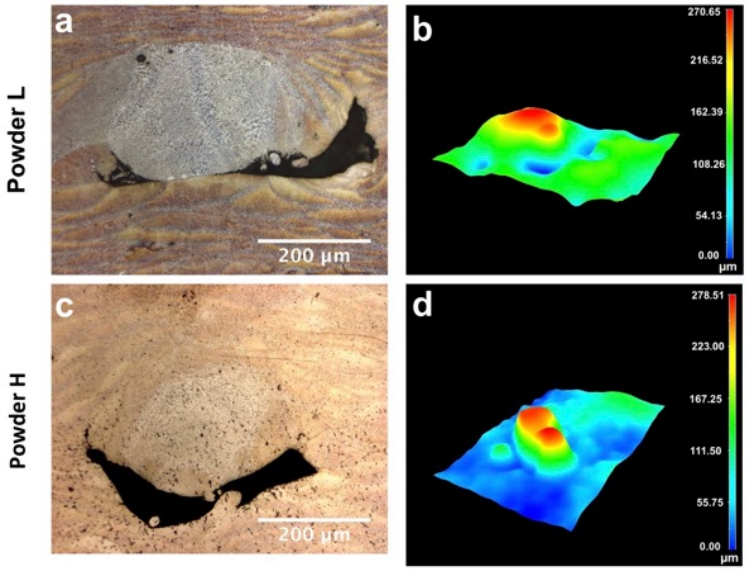

Figure 5.6: Results of spatters analysis: a) and c) optical micrograph of sample cross-section showing a spatters defect for powder L and H respectively; b) and d) 3D maps of top surfaces of a representative sample for powder L and H respectively.

Spatter defects were finally analyzed with the aid of SEM-EDS: as disclosed in Figure 5.7, spatters defects had high content of spherical gas porosities with dimension lower than 10 µm. In the large cavity underlying the spatter, melted and semi-melted material can be found and the EDS analysis evidenced the presence of elevated concentrations of oxygen in the cavity (Spectra 2,3,4) with respect to the reference material (Spectrum 1).

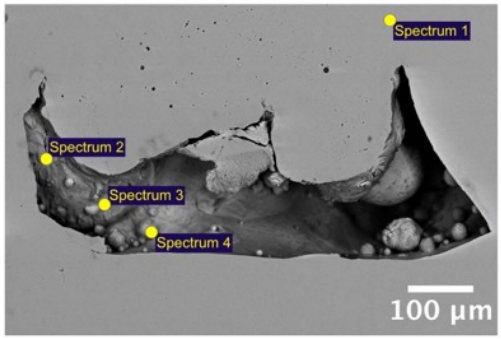

	Element (wt.%)			
	Al	Si	Mg	O
Spectrum 1	90.98	7.38	0.34	1.30
Spectrum 2	60.49	3.21	1.94	34.36
Spectrum 3	78.84	5.37	0.00	15.79
Spectrum 3	82.27	7.10	0.37	10.26

Figure 5.7: Results of SEM-EDS analysis performed on a spatter defect detected on sample cross-section

5.1.4 Conclusions

Experiments have been carried out with the aim of investigating the effect of the powder conditions in terms of size, morphology and pre-treatment on the properties of the final LPBF samples. To this purpose, two different batches of AlSi7Mg0.6 gas atomized powder were characterized and compared. Density, hardness and microstructural defects of samples produced by LPBF have been analyzed with regard to the feedstock material. Based on the outcomes of the present work, the following conclusions can be drawn:

- High energy density was necessary to reduce porosity and increase hardness in the processed samples.
- For the same process parameters, powder with a higher percentage of spherical particles (as powder H) allowed to obtain samples with the highest densities, probably by reason of the enhanced flowability of the powder.
- Powder drying pre-treatment, both at 60 °C for 3 h and 200 °C for 1 h, did not directly affect the morphology of particles but it probably promoted the aggregation phenomena of smaller particles and that facilitated the smaller powders to become satellites of the larger ones.
- Powder pre-treated at 60 °C resulted in samples with higher density and hardness if compared to the analogue ones obtained from powder pre-treated at 200 °C. The result is presumably related to the presence of an aluminum oxide layer on the surface of powder pre-treated at the higher temperature, as evidenced by XRD analyses.
- High scanning speeds promoted the formation of spattering, identified by the presence of large microstructural discontinuities; however, the average dimension of such discontinuities was greater in the case of low scanning speed. Spherical powders reduced the spattering phenomenon.

5.2 Heat treatment optimization

This section contains selected parts of the pre-print of the currently unpublished paper "*Role of direct aging and solution treatment on hardness, microstructure and residual stress of the A357 (AlSi7Mg0.6) alloy produced by powder bed fusion"* by L. Tonelli, E. Liverani, A. Morri and L. Ceschini.

5.2.1 Aim and Scope

The response to heat treatment for the LPBF AlSi7Mg0.6 alloy was investigated. Specifically, the present study was aimed at systematically studying the effect of different heat-treatments on microstructure, hardness and residual stress of the alloy produced with no platform pre-heating. Based on the state of the art discussed in Chapter 4, two specific heat treatment conditions were considered: direct aging and a modified T6 treatment. A short solution treatment (10 minutes), in particular, was chosen in order to limit microstructural coarsening and increase in the porosity content evidenced by previous literature works [32–34]. Aging curves at four different temperatures have been obtained starting from both as-built and solution treated samples, with the aim to define the peak-aging treatment conditions for the direct aged and solution treated alloy. As residual stress represents one of the major concerns in the additively manufactured parts, in order to assess the effect of the investigated treatments on residual stress, results have also been compared to the stress relieving treatment. Raman spectroscopy was used to measure and compare residual stress. For comparison purposes, the same analyses were also carried out on the conventional sand cast AlSi7Mg0.6 alloy, in view of highlighting microstructural features peculiar of the additive process.

5.2.2 Experimental Procedure

Following the work described in Section 5.1, samples were produced with the so-called powder H, pre-treated at 60 °C for 3 h, and by setting process parameters reported in Table 5.6. Blocks 10x10x20 mm^3 were fabricated with the SISMA MySint 100 RM metal 3D printer on an aluminum platform without pre-heating and by adopting a perpendicular building direction, with respect to the platform. All samples were produced in a single batch in order to assure that were subjected to the same thermal cycle. After the building process, samples were stored at -20 °C to avoid undesired natural pre-aging [35]. Conventional sand cast samples, investigated as a reference, were extracted from engine blocks. Chemical compositions of cast and LPBF samples were determined by Glow Discharge Optical Emission Spectroscopy (GDOES, GDA-650 Spectrum Analytik GmbH). Results complied to requirements given by the EN 1706 [29] standard for the AlSi7Mg0.6 alloy regardless different processing routes.

Table 5.6: Process parameters adopted for production of LPBF AlSi7Mg0.6 samples for heat treatment investigation

Power [W]	***Layer thickness [mm]***	***Hatch distance [mm]***	***Scanning velocity [mm/s]***	***Scanning pattern***	***Shielding gas***
170	0.02	0.07	500	3x3 mm roto-translating chessboard	N_2

The investigated heat treatment designations and conditions, in terms of temperature and holding time, are reported in Table 5.7. In order to determine the peak-aging condition, LPBF alloy and conventionally sand cast alloy were subjected to artificial aging (AA) to obtain aging curves. Aging curves, indeed, display the evolution of hardness (HV_1, [36]) as a function of holding time at the

specific temperature, and the peak-aging is represented by the time-temperature conditions resulting in the highest hardness. Before artificial aging, cast samples underwent the conventional long-term (12 h) solution treatment (ST), followed by quenching in water at 60 °C (WQ). LPBF samples were instead subjected to artificial aging both in the as-built state and after a short-term (10 min) ST followed by WQ. Four aging temperatures were investigated: 150, 170, 190 and 210 °C for a total holding time of 28 h. Cast and LPBF samples that underwent ST+WQ+AA are identified as T6, while LPBF samples that were submitted to direct artificial aging in the as-built condition are identified by AA. Stress relieving (SR) treatment usually applied to aluminum LPBF parts was also performed at three different temperatures (100, 200 and 300 °C) for a fixed time of 2 h. SR samples were employed as a reference for the assessment of residual stress relief.

Table 5.7: Designations and conditions of investigated heat treatments

Samples	***Stress Relieving (SR)***		***Solution Treatment (ST)***		***Quenching (WQ)***	***Artificial Aging (AA)***	
	T [°C]	*t [h]*	*T [°C]*	*t [h]*		*T [°C]*	*t [h]*
Cast T6	-		540	12	Warm water (60°C)	150 170 190 210	0 - 28
LPBF T6	-		540	0.17	Warm water (60°C)	150 170 190 210	0 - 28
LPBF AA	-		-		-	150 170 190 210	0 – 28
LPBF SR	100 200 300	2	-		-	-	-

Samples were subjected to microstructural characterization by means of Optical (OM, Reichert MEF3), Scanning Electron (SEM, Zeiss Evo 50), and Field Emission

Gun Scanning Electron (FEG-SEM, Tescan Mira3) microscopes, both equipped with Energy Dispersive X-ray Spectroscopy (EDS). Before the analyses, samples were polished up to 1 μm polycrystalline diamond suspension and etched with 20 s immersion in Keller's reagent (2.5 mL HNO_3, 1.5 mL HCl, 1.0 mL HF and 95 mL distilled water). Residual stress was evaluated by measuring the shift of the Si peak obtained by μRaman spectroscopy on polished surfaces, as already proposed by other researchers for the same alloy [34,37] and as commonly used for Si-based products [38–40]. At least five spectra per condition were randomly acquired; each spectrum consisted of 10 accumulations with 10 s dwell time at ambient condition. Spectra were recorded by means of a Renishaw InVia micro-spectrometer equipped with a Leica DMLM microscope using a 50 mW Ar^+ laser source (wavelength: 514.5 nm). Thermal analyses were carried out using a differential thermal analyzer (DTA, Rheometric Scientific STA 1500) on LPBF as-built, LPBF ST+WQ and cast ST+WQ samples. Specimens of about 30 mg mass were heated in the temperature range 30-550 °C with a heating rate of 15 °C min^{-1} under Ar atmosphere. DTA curves were then elaborated with RSI Orchestrator software to determine the onset and peak temperatures. Phase composition was determined by X-ray diffraction (XRD, PANalytical Expert PRO with Xcelerator detector) with CuKα (λ = 0.15406 nm) radiation. θ - 2θ scans were carried out in the range 20-90° with 0.017° step size and 10 s dwell time. XRD spectra were then processed with the Xpert Highscore Plus software for phase identification and peak analysis.

5.2.3 Results and Discussion

AGING RESPONSE

Aging curves, obtained by measuring the hardness evolution as a function of holding time at the different aging temperatures, are reported in Figure 5.8. In case of direct artificial aging (Figure 5.8a), all the investigated temperatures up to 3 h soaking time induced strengthening in the LPBF as-built alloy. Peak-aging condition was found at 170 °C x 1 h, producing a 17% increase in hardness if compared to the as-built condition (from 117 HV_1 to 136 HV_1). For longer holding

time, higher temperatures (in the range 170-210 °C) induced softening of the alloy, probably due to overaging caused by coarsening, while at the lowest temperature (150 °C) a second hardness peak was found. However, since it corresponds to 24 h soaking time, in view of preserving time and cost-efficiency of the whole process, this condition was no further investigated. Nevertheless, it is worth mentioning that this a valuable result in case of long-term LPBF process carried out on pre-heated platform at the usual temperature of 150 °C. Aging curves of the LPBF and cast alloy subjected to ST+WQ are reported in Figure 5.8b,c. After ST+WQ the hardness of LPBF alloy dropped to 82 HV_1, comparable to the ST+WQ cast alloy, and it was more sensitive to aging treatment (Figure 5.8b). The highest tested temperature (210 °C) led to a substantial hardness loss, while a short treatment (about 2 h) at 190 °C induced a limited hardness increase (from 82 to 120 HV_1). A more significant strengthening was instead obtained with aging at 150 and 170 °C, with an outstanding 60% increase in hardness (130 HV_1) in the peak aging condition found for 4 h at 150 °C. In case of conventional cast alloy (Figure 5.8c) the most favorable peak aging condition was found with heating at 190 °C x 4 h, that led to a 46% increase in hardness compared to ST+WQ condition (from 80HV_1 to 117 HV_1). This condition indeed returned a hardness value comparable to the aging condition advised by ASTM B917 (170 °C x 10-12 h), but with a much shorter treatment time.

As concerns the effect of stress relief treatment on hardness, it should be noticed that stress-relieving at 100 °C (SR100) did not affect the hardness of the as-built alloy (117 HV_1). The medium temperature (SR200) treatment slightly increased the hardness up to 120 HV_1, as also confirmed by the 210 °C aging curve (Figure 5.8a). High temperature stress relieving (SR300), instead, caused a significant hardness drop to approximately 84 HV_1, comparable to the solution treated and quenched cast and LPBF alloys.

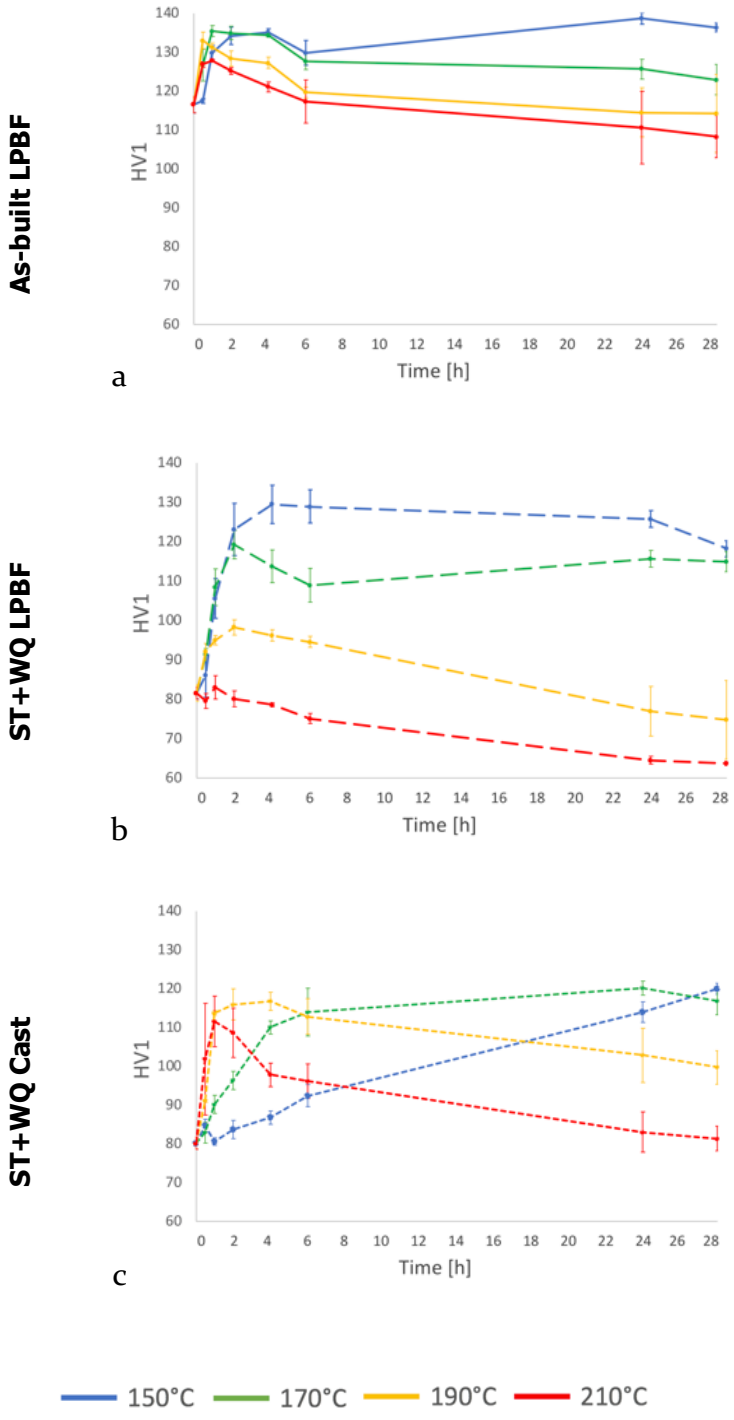

Figure 5.8: Aging curves for: a) as-built LPBF, b) ST+WQ LPBF, c) ST+WQ cast AlSi7Mg0.6 alloy.

Thermal analyses (DTA) were carried out to investigate the reason behind the different response to aging treatment displayed by aging curves. DTA curves obtained for the LPBF as-built alloy, the LPBF alloy solution treated and water

quenched (ST+WQ) and the cast alloy solution treated and water quenched (ST+WQ) are compared in Figure 5.9. Five exothermic peaks, identified by letters A, B, C, D and E, could be detected on the investigated samples, with the only exception of LPBF ST+WQ alloy for which peak A was not clearly identifiable.

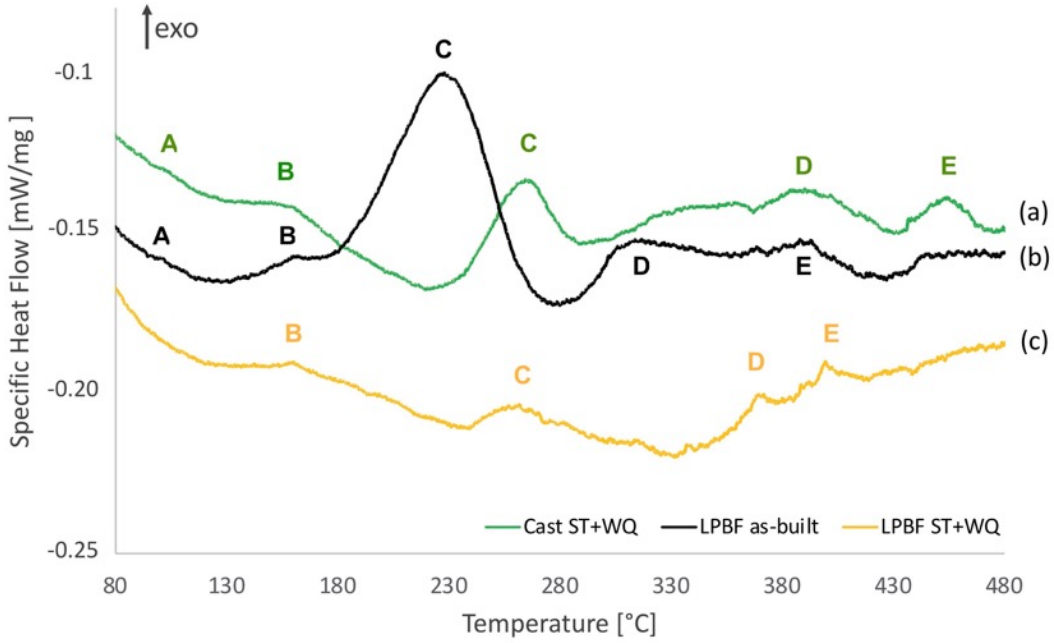

Figure 5.9: DTA analyses of: a) Cast ST+WQ; b) LPBF as-built; c) LPBF ST+WQ samples. Letters A, B, C, D and E identify exothermic peaks.

Exothermic peaks correspond to the phase precipitations and transformations occurring in the range 90-450 °C. Most of the literature regarding the conventional cast alloy [41–44] fixes the formation of GP zones at about 100 °C, thus corresponding to peak A. However, the attribution of the remaining peaks is quite debated in the literature. Several authors [41–43] agree in the attribution of the peak at about 200-250 °C (peak C) to the precipitation of β″ coherent and strengthening phase, while peak D may correspond to both the β″ to β′ transformation and the precipitation of Si, and peak E to the final transformation into the equilibrium incoherent β (Mg_2Si) phase. It should be noticed that none of the aforementioned references evidenced a peak in the range of 150 °C (termed B

in Figure 5.9) that has indeed been found on DTA curves of all investigated samples. According to [44], who still investigated AlSi7Mg cast alloys, the precipitation of β" is anticipated at about 150 °C and peak in the range of 220-250 °C (C) is attributed to the precipitation of β′, while the following peak (D) to the precipitation of Si. In the case of the LPBF AlSi7Mg0.6 alloy, Casati and Vedani [32] associated peak C to the β′′ phase, peak D to β′ and the last one located close to 350 °C (E) to the Si precipitation. Moving to the LPBF AlSi10Mg alloy, that follows the same precipitation path of the AlSi7Mg alloy, Marola et al. [45] attributed the peak C to the precipitation of Si from the supersaturated solid solution, and the peak D to the precipitation of Mg_2Si. For the same alloy, instead, Fiocchi et al. [46] identified the peak C as Mg_2Si precipitation and the following peak D to the Si precipitation.

It is worth noticing that in the present investigation peak C prevailed for all samples and the area under that peak, that corresponds to the enthalpy of the transformation, in case of LPBF as-built sample is much higher if compared to solution-treated samples (92.9 J g^{-1} for LPBF as-built, 24.4 and 6.5 J g^{-1} for Cast ST+WQ and LPBF ST+WQ respectively). Moreover, it should be noticed that all peaks, unless A and B, in the LPBF as-built alloy are moved to lower temperatures with respect to both cast ad LPBF solution-treated alloy. Based on supersaturation of the LPBF alloy (Si solubility is extended up to 5.4% [34]) and on the work carried out by Rao et al. [47], it is plausible that peak C is rather related to the precipitation of Si from the solid solution than precipitation of precipitation of β′ or β′′ phases. This assumption will be also supported by microstructural analyses reported later in this section.

XRD spectra showing phase composition of the AlSi7Mg0.6 alloy in the investigated conditions are reported in Figure 5.10. Major peaks identified for all spectra belong to Al (ICDD: 4-0787) and Si (ICDD: 27-1402) phases. It should be noticed that in case of cast samples a preferred crystallographic orientation was evidenced by the prevalence of Al (200) at 44.7° and Al (222) at 82.4° peaks. As-cast samples were extracted from a sand cast engine block, this is presumably related to the specific region of samples extraction. In view of this, for the sake of a proper comparison, the XRD spectra were acquired on cast samples extracted from the same region of the engine block. A detail of the most intense Si peak, Si

(111), is given in the inset: in LPBF as-built and direct aged (AA) samples the peak was almost negligible while after solution treatment, as well as in cast samples, was well defined, suggesting the occurrence of Si precipitation during solution treatment. Low peaks in the range of 35 - 40° can be possibly attributed to Mg_5Si_6 phase (ICDD: 1-088-1207), Al_8Fe_2Si intermetallic phase (ICDD: 20-0030), and Mg_2Si (ICDD: 35-0773). In case of Mg_2Si, the peak located at approximately 40° was chosen to compare the occurrence of precipitation among samples. For the LPBF alloy, the peaks corresponding to Mg_2Si and Fe-based intermetallics became appreciable only after solution treatment, while the peak attributed to Mg_5Si_6 was much less prominent in the cast alloy, especially after T6 treatment. However, the presence of such peak, attributed to the β″ (Mg_5Si_6) phase, is independent from heat-treatments condition and thus it seems mainly related to the LPBF process and, for this reason, it was not further investigated in the present work. As regards Fe-based intermetallics, literature results showed, indeed, that coarsening of intermetallic particles might occur even after a short (1-2 h) solution treatment. Intermetallic compound (presumably β-Al_5FeSi) became visible as acicular particles at both optical and scanning electron analyses [32,33]. However, metallographic analyses carried out in the present work did not evidenced the presence of Fe-based compounds, possibly as a consequence of the very short solution treatment that hindered intermetallic coarsening.

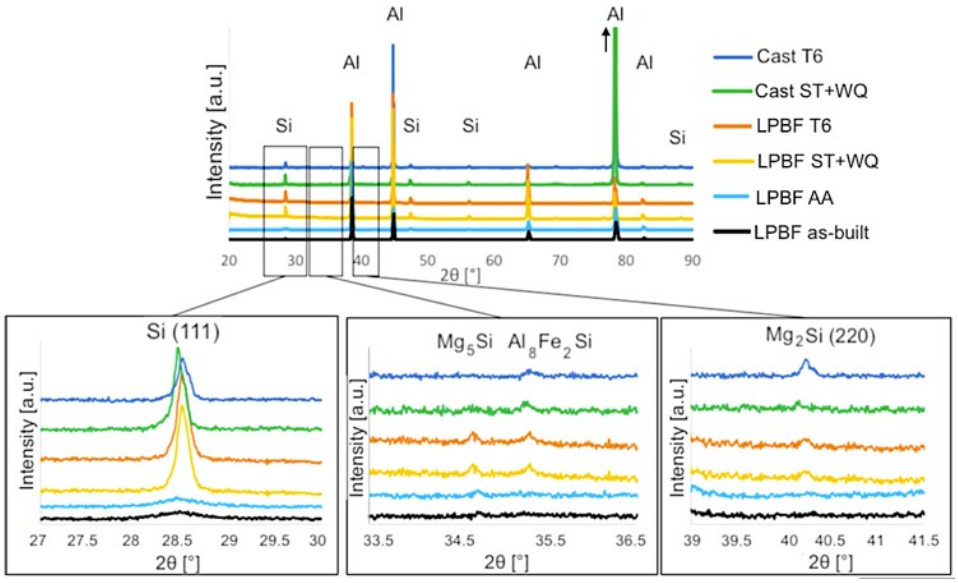

Figure 5.10: XRD analyses of as-built, ST+WQ and T6 peak-aged alloys: global view and details of lower peaks in the range 27-30°, 33.5-36.5°, 39-41.5°.

Al lattice parameter was calculated from XRD spectra and displayed as a function of lattice planes in Figure 5.11. The reference value for the lattice parameter of Al is 4.0494 Å (ICDD: 4-0787). LPBF samples in as-built and artificially aged conditions exhibited significantly lower lattice parameters, quite stable for all lattice planes. Cast and LPBF samples in T6 and ST+WQ state, instead, displayed comparable lattice parameters that increased to values close to the nominal one. Since the atomic radius of Si is lower than the one of Al, a shrink aluminum lattice implies that a large part of Si is retained in the solid solution in the LPBF as-built alloy. Results also suggest that some of the retained Si was released after the direct aging treatment and it was almost completely ejected after solution treatment and quenching. Similar results for the Al-Si-Mg alloys produced by LPBF were also reported by other authors [45,48]. In particular, according to Rao et al. [48], Si super-solubility is strictly related to the crystallographic-dependent residual strain in the Al matrix, thus a possible way to reduce the strain is to induce the precipitation of Si-rich particles.

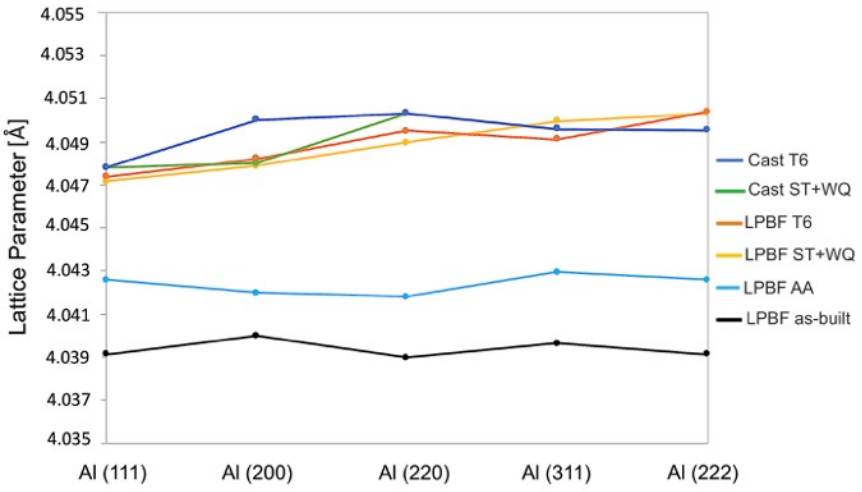

Figure 5.11: Lattice parameter calculated for the aluminum phase from XRD spectra, as a function of lattice planes.

RESIDUAL STRESS

Residual stress was evaluated by the characterization of the frequency of Si as measured via Raman analyses, as unstressed Si displays a Raman frequency at 520 cm^{-1} [49–51]. Mechanical stress can shift the peak to lower values (in case of tensile stress) and higher values (in case of compressive stress) [52], therefore Raman

spectroscopy is commonly used to determine internal residual stress in different Si-based components [38–40].

Raman spectra were collected for cast and LPBF heat-treated samples and were compared to the LPBF as-built condition and to the reference value of unstressed Si (Table 5.8). In the LPBF as-built alloy, Si-peak is located to a significant lower value (approximately 512 cm^{-1}) than reference, suggesting an internal tensile stress state. As regards stress-relieving (SR) treatments, results showed that the SR performed at 100°C (SR 100) did not affect the internal stress state while SR 200 and SR 300 succeeded in relieving some of the residual stress, since the Si-peak increased up to about 518 cm^{-1}. As regards strengthening treatments, direct aging of the LPBF as-built alloy had a little effect on reducing tensile stress, hence, a longer soaking time was taken under consideration. According to 170 °C aging curve (Figure 5.8) the peak hardness was maintained even for longer treatment, therefore, with the aim to induce a more significant relieving of internal stress, artificial aging treatment at 170 °C x 4 h was performed. However, both AA treatments resulted in a comparable value of Raman frequency of Si, settled at about 515 cm^{-1}, suggesting that temperature more than time has a significant effect in stress relieving. Conversely, ST+WQ treatments succeeded to completely release the internal tensile stress since the measured shift of the Si is about 521 cm^{-1}. This outcome was disclosed for both LPBF and conventional cast alloy. Finally, the complete T6 treatment for the LPBF alloy produced a complete relaxation of internal stress since the Si-peak is comparable to the unstressed reference value of 520 cm^{-1}.

Table 5.8: Average Raman shift of the Si-peak measured for all investigated samples, compared with reference value for unstressed Si [36–38].

Sample	*Condition*	*Si Raman Shift [cm^{-1}]*
LPBF as-built	as-built	512.2 ± 0.9
LPBF SR 100	SR (100°C x 120 min)	511.9 ± 0.8
LPBF SR 200	SR (200°C x 120 min)	517.3 ± 0.9
LPBF SR 300	SR (300°C x 120 min)	518.3 ± 0.1
LPBF ST+WQ	ST (540°C x 10 min) +WQ	521.2 ± 1.5
LPBF T6 (peak-aged)	ST+WQ+AA (150°C x 4 h)	520.5 ± 0.8
LPBF AA (peak-aged)	AA (170°C x 1h)	515.1 ± 0.1
	AA (170°C x 4h)	514.1 ± 0.9
Cast ST+WQ	ST (540°C x 720 min) +WQ	520.8 ± 0.9
Cast T6 (peak-aged)	ST+WQ+AA (190°C x 4 h)	517.8 ± 2.3
Reference		520

MICROSTRUCTURE

Metallographic analyses of the LPBF alloys are reported in Figure 5.12, where stress relieved (SR 300) and solution treated (ST+WQ) microstructures are compared to the as-built one. As reported in the [53,54], the as-built sample is dominated by a hierarchical microstructure that comprised a layered structure due to subsequent solidified melt pools, resolved at low magnification optical analyses (Figure 5.12a), and a cellular sub-structure inside melt pools that can be appreciated only at higher magnifications (Figure 5.12b). Such cellular structure is composed by a fine and continuous network of eutectic Si surrounding the Al-α phase (Figure 5.12c). During the extremely rapid solidification imposed by LPBF, epitaxial growth of the primary Al-α phase occurs and, as a consequence, columnar

grains crossing-over layers can be appreciated in the high magnification optical analyses (Figure 5.12b). After SR300 treatment, coarsening of the microstructure occurred, even if the layered structure and melt pools border could still be appreciated by optical analyses (Figure 5.12d,e). SEM microscopy (Figure 5.12f) revealed an interrupted Si network and the coalescence of small globular Si particles. The brief exposure (10 minutes) at solution temperature (540°C) resulted in a significant modification of the microstructure. Melt pool borders were no longer appreciable (Figure 5.12g,h), the fine Si-rich network broke-up and very fine, for the most sub-micron sized, globular particles were formed (Figure 5.12i).

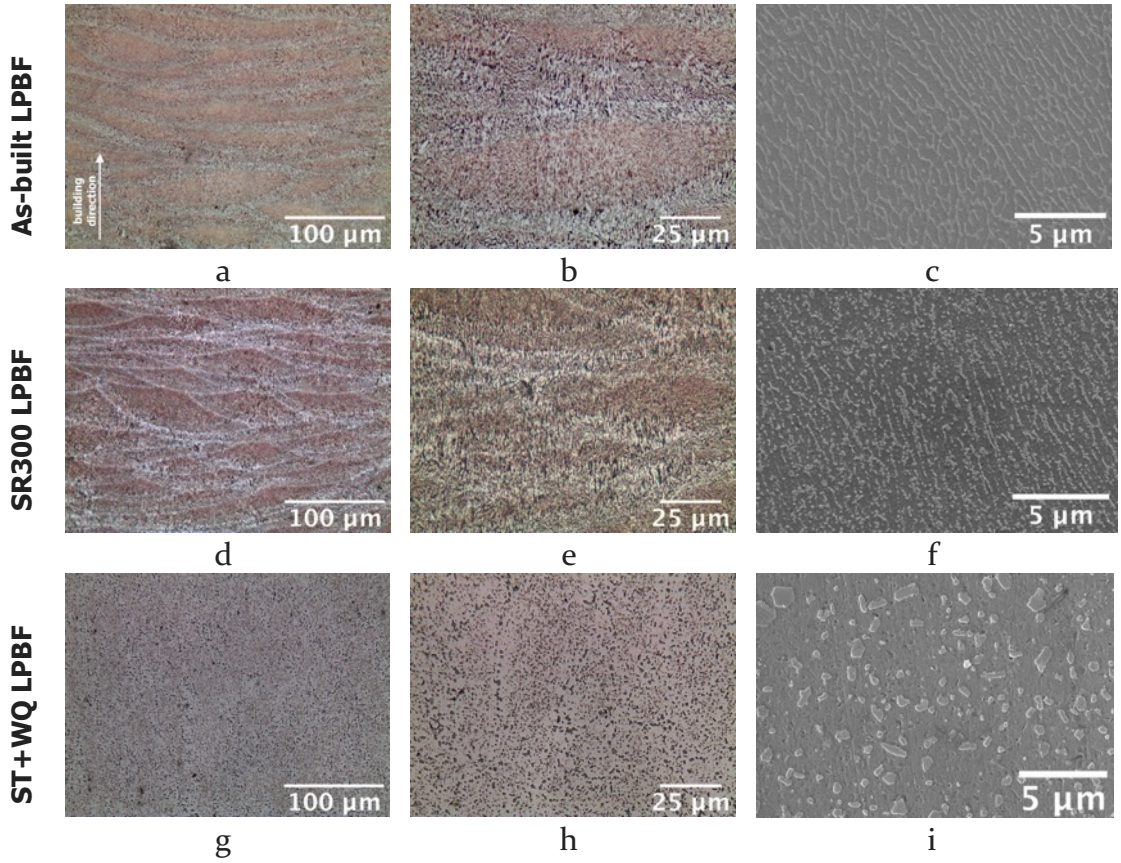

Figure 5.12: Metallographic analyses on LPBF as-built (a-c), SR 300 (d-f) and ST+WQ (g-h) samples

FEG-SEM EDS maps (Figure 5.13) were performed to evaluate the distribution of the alloy elements in the in the as-built samples and after solution treatment. Results confirmed that in the as-built state Si was retained in the supersaturated

solid solution and, after solution treatment, Si segregated into the above-mentioned globular particles.

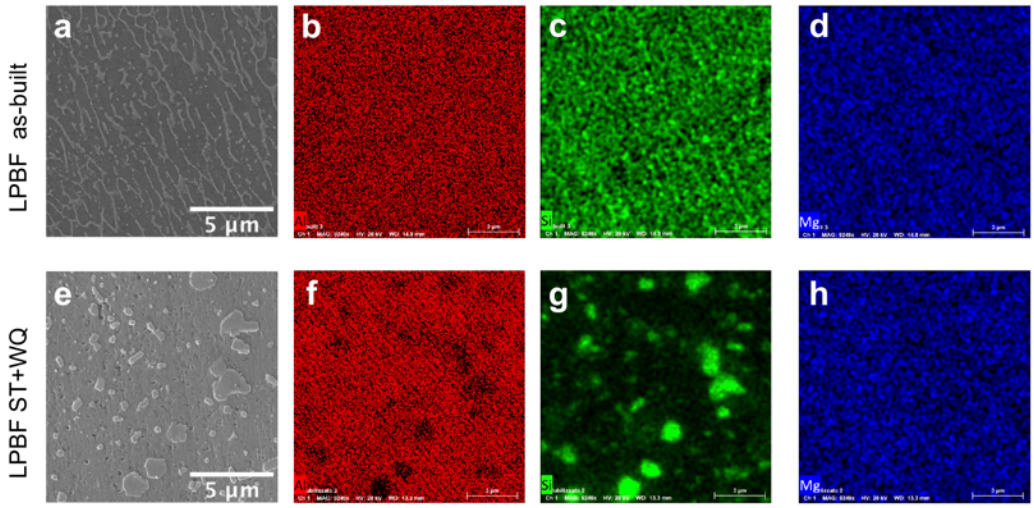

Figure 5.13: FEG-SEM EDS maps of as-built (a) and ST+WQ (e) LPBF samples showing concentration of: b) and f) aluminum; c) and g) silicon; d) and h) magnesium.

5.2.4 Conclusions

The present work was focused at assessing the role of heat treatment on microstructure, hardness and residual stress of the AlSi7Mg0.6 alloy produced by laser powder bed fusion (LPBF). Stress relieving, direct aging and complete modified T6 treatment were investigated and, as a reference, also the conventional sand-cast alloy was considered. Based on the results, the following conclusions can be drawn:

- Stress relieving treatment applied to the LPBF as-built alloy produced a drop in the hardness value and was not sufficient to completely release residual stress.
- Direct aging of LPBF as-built alloy resulted in strengthening the alloy and also succeeded in a partial relief of internal stress.
- The optimized T6 treatment (solution treatment at 540 °C for 10 min + aging at 150 °C for 4 h) was able to return hardness values comparable to

the direct aging treatment but it succeeded also in completely relieving internal stress.

- With respect to the conventional sand-cast T6 alloy, both treatments resulted in higher hardness values in the peak-aging condition.
- Microstructural results suggested that, in the reason of the supersaturated solid solution derived from the LPBF process, different precipitation phenomena were involved in case of direct aging and T6 treatments of the LPBF alloy. Direct aging induced partial precipitation of Si from the Al matrix while after solution treatment most part of Si segregated into fine globular particles. In T6 alloy, strengthening was induced by second phases precipitated during aging.

5.3 Assessment of tensile properties in the peak-aged condition

5.3.1 Aim and scope

As a final analysis of the heat treatment response of the LPBF AlSi7Mg0.6 alloy, tensile tests were carried out on the as-built and heat-treated conditions. The aim was to compare tensile properties of the as-built material with the optimized peak-aged conditions (AA and T6), as resulted from Section 5.2. Prior to the fabrication of samples for tensile tests, LPBF process parameters were further optimized in order to obtain a relative density higher than 99.5%. Fracture surfaces were then characterized by means of FEG-SEM and the discussion of the fracture behavior was also supported by a full microstructural characterization of tensile samples.

5.3.2 Experimental procedure

Tensile samples were built on an aluminum platform without pre-heating using the SISMA MySint 100 RM metal 3D printer and adopting the parameters reported in Table 5.8, that were able to optimize samples density up to 99.5%. Gas atomized

AlSi7Mg0.6 powder, fully characterized in Section 5.1 and identified as powder H, was used after the pre-treatment carried out at 60 °C x 3 h in a muffle furnace in ambient atmosphere. A unique vertical building direction, thus perpendicular to the building platform, was chosen in order to assess the mechanical behavior of the direction characterized by the lowest mechanical properties in the reason of the anisotropy induced by LPBF process, as widely reported by literature data [33,55,56]. In this view, data obtained in this study will presumably represent the minimum threshold value for the as-built, AA and T6-treated alloy.

Table 5.8: Process parameters adopted for production of LPBF AlSi7Mg0.6 tensile samples

Power [W]	***Layer thickness [mm]***	***Hatch distance [mm]***	***Scanning velocity [mm/s]***	***Scanning pattern***	***Shielding gas***
175	0.02	0.08	500	3x3 mm roto-translating chessboard	N_2

Round cross-section tensile specimens (5 mm diameter) with a parallel length of 28 mm and an original gauge length of 25 mm were machined from LPBF near-net-shape samples, as shown in Figure 5.14. Tests were conducted at room temperature following the EN ISO 6892 standard [57]. Tensile tests were performed on a screw tensile testing machine, equipped with a resistance furnace, a 20-kN load cell and a clip-on extensometer. Tests were conducted in displacement control mode, with a crosshead speed of 0.007 mm s^{-1} according to ASTM E8 [58].

Heat treatment conditions applied to tensile samples are synthetized in Table 5.9 and, based on the findings discussed in Section 5.2; only peak-aged conditions were considered. Hardness was also evaluated for all tested conditions via Brinell (HB10 [6]) measurements.

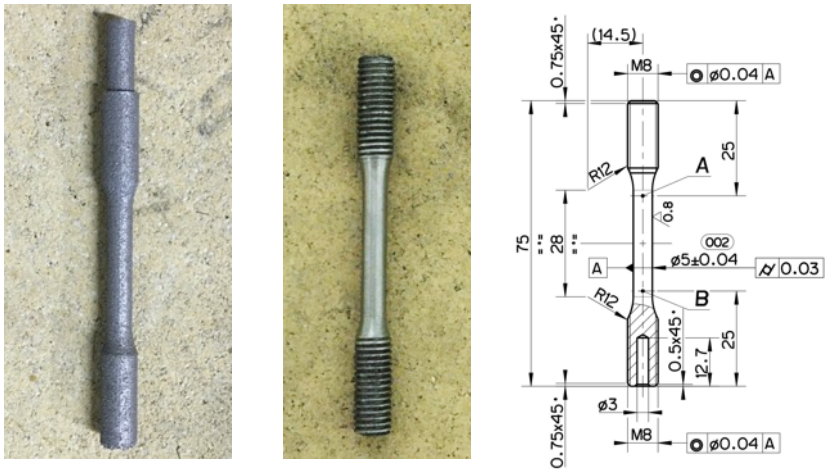

a b c

Figure 5.14: AlSi7Mg0.6 samples for tensile tests: a) as-fabricated via LPBF, b) machined, c) geometry and dimensions

Table 5.9: Designations and conditions of heat treatments applied to tensile samples

Samples	***Solution Treatment (ST)***		***Quenching (WQ)***	***Artificial Aging (AA)***	
	T [°C]	*t [h]*		*T [°C]*	*t [h]*
As-built	-	-	-	-	-
T6	540	0.17	Warm water (60°C)	150	4
AA		-	-	170	1

After tensile tests, fracture surfaces were analyzed by means of FEG-SEM (Tescan Mira 3) microscope to highlight fracture behavior. Microstructural analyses were also carried out on sections extracted from the grip region of tensile

samples. Sections underwent standard metallographic preparation up to chemical etching with Keller's reagent, as already reported in Sections 3.1.2 and 3.2.2. Microstructural analyses were performed via optical (Reichert MEF3) and FEG-SEM (Tescan Mira 3) microscopes.

5.3.3 Results and discussion

Results of tensile tests and hardness value are compared in Figure 5.15 while representative high and low magnification of fracture surfaces can be seen in Figure 5.16. The as-built LPBF alloy exhibited $R_{p0.2}$=216±5 MPa and, with reference to the literature results reported in Chapter 4 (Table 4.9), this value is comparable to samples fabricated in similar conditions (vertical building direction and no platform pre-heating), but it is about 30 % lower compared to literature results on sample built with platform pre-heating (100-150 °C), who reported value up to approximately 280 MPa. Based on literature review and experimental results discussed in the previous section, it is possible that samples built with platform pre-heating experienced artificial aging, that may justify the difference with respect to no-preheating condition here discussed. Similar considerations can be valid also for ultimate tensile strength that, for the present work, was set at R_m=394±6 MPa. Elongation was 5.2±0.7 and, considering standard deviation, it is comparable to the literature results obtained in similar conditions.

Direct aging (AA at 170 °C for 1 h) of the alloy increased both $R_{p0.2}$ and $R_{m,}$ that reached the highest values, 274±4 MPa and 422±10 MPa respectively, without a significant reduction in ductility (A%=4.6±1.2). Based on the results discussed in the previous section, it is plausible that the increase in strength of the alloy is related to the precipitation of nanometric Si particles that contribute to hinder dislocation movements. It is worth mentioning that mechanical properties in AA condition are comparable to the literature data obtained for vertical samples built with and without platform pre-heating.

The optimized T6 treatment (solution treatment at 540 °C for 1 h + water quenching + aging at 150 °C for 4 h) increased both $R_{p0.2}$ (249±8 MPa) and A% (9.7±1.9), with respect to the as-built alloy. On the other hand, it exhibited the lowest R_m (337±2 MPa). By comparing with the literature work of Pereira et al. [56]

who still performed a T6 treatment optimized on the peculiar AM microstructure, thus comprising of a short solution treatment (0.25 h at 540 °C), both yield and ultimate tensile strength are slightly higher, the increase was 16% and 5%, respectively.

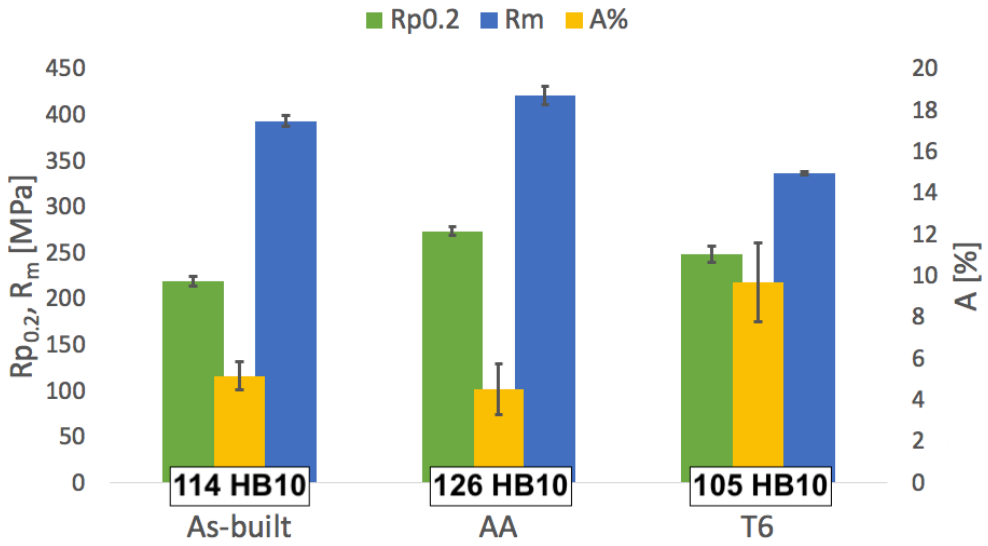

Figure 5.15: Results of tensile tests performed on the as-built and heat-treated LPBF AlSi7Mg0.6 alloy in terms of proof stress ($Rp_{0.2}$), ultimate tensile strength (R_m), and elongation (A%). Average hardness values (HB10) are also reported.

Fracture surfaces were analyzed via electron microscopy with the aim to identify the fracture mechanisms that led to samples failure (Figure 5.16). From low magnifications micrographs (Figures 5.16a,b,c) a few porosity defects can be identified on surfaces (highlighted by white arrows) that have presumably affected the ultimate tensile strength of samples. In fact, in case of heat treatable Al alloys ultimate strength and elongation are remarkably influenced by defects while yield strength is substantially unaffected by the presence of porosity, as reported by [35,59]. All tested conditions exhibited a ductile fracture mode, as confirmed by high magnification analyses (Figures 5.16d-i) in which very fine dimples can be recognized. Dimples denote a ductile fracture and are formed as a consequence of material yielding. They usually nucleate in correspondence of material discontinuities, like Si particles in T6 samples. In fact, fractured Si particles were found inside dimples in the T6 alloy (Figure 5.16i). On the basis of flat surfaces of broken Si particles, it can be inferred that brittle fracture mechanism occurred for

them, as also observed by Trevisan et al. [60]. Very small particles could be found also inside dimples of AA samples (Figure 5.16h), confirming that precipitation of Si from supersaturated solution, discussed in Section 5.2, occurred. The finest dimples were observed for the as-built alloys and, as will be later discussed, this outcome is likely correlated to the finest cellular microstructure observed in this alloy condition. On fracture surface of as-built alloy, no evidence of particles inside dimples was found (Figure 5.16g), while cellular structure is still recognizable, as also observed by Casati and Vedani [32]. The absence of microstructural inhomogeneities delayed dimples nucleation and hindered their growth, as also confirmed by the overall fine dimples dimension (approx. 1 μm in case of as-built alloy). These outcomes are also supported by the previously discussed tensile results in which both as-built and AA samples showed greater ultimate tensile strength and hardening than T6 samples.

Microstructural analyses are reported in Figure 5.17. With respect to the microstructural analyses discussed in Section 5.2, it is worth noticing that the modification of process parameters did not result in a marked change in the microstructure. By comparison to the as-built alloy, AA preserved the structure formed by consequent solidified melt pool, indeed, as observed in the previous section, higher temperatures are needed in order to delete laser traces. However, at high magnification the cellular structure of AA samples appears less defined and coarser than as-built ones. In some regions it is also slightly fragmentated. Finally, the T6 treatments deleted any trace of the manufacturing process and homogenized the microstructure, resulting in a fine distribution of globular Si particles in the aluminum matrix. In order to correlate microstructural features to mechanical behavior, further microstructural aimed at characterize shape, distribution and dimensions of Si network and Si particles, as well as average grains dimensions, are currently carried out.

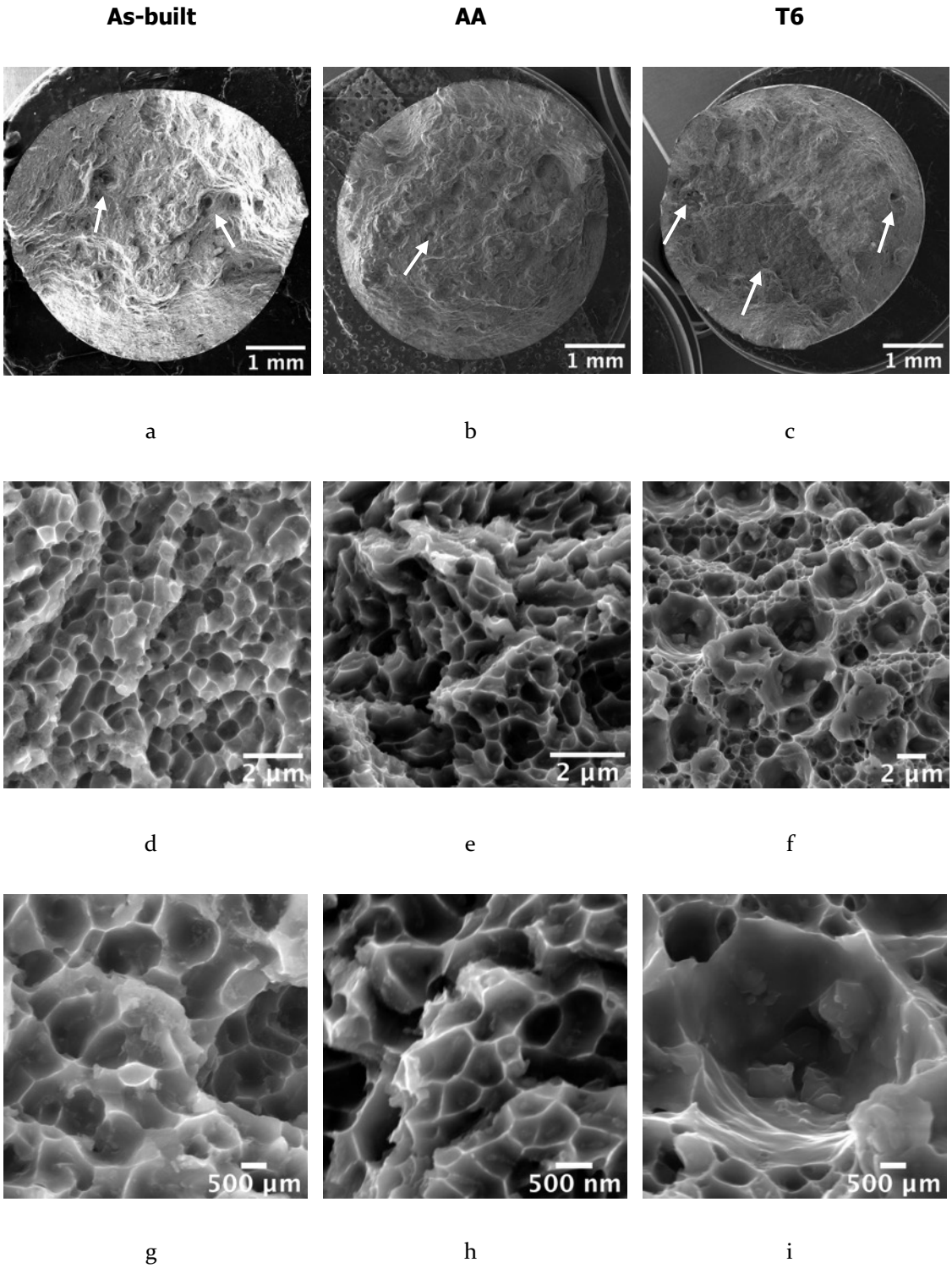

Figure 5.16: Fractographic micrographs of: a), d), g) as-built; b), e), h) AA; c), f), i) T6 representative samples. White arrows in a), b), c) highlight defects on fracture surface.

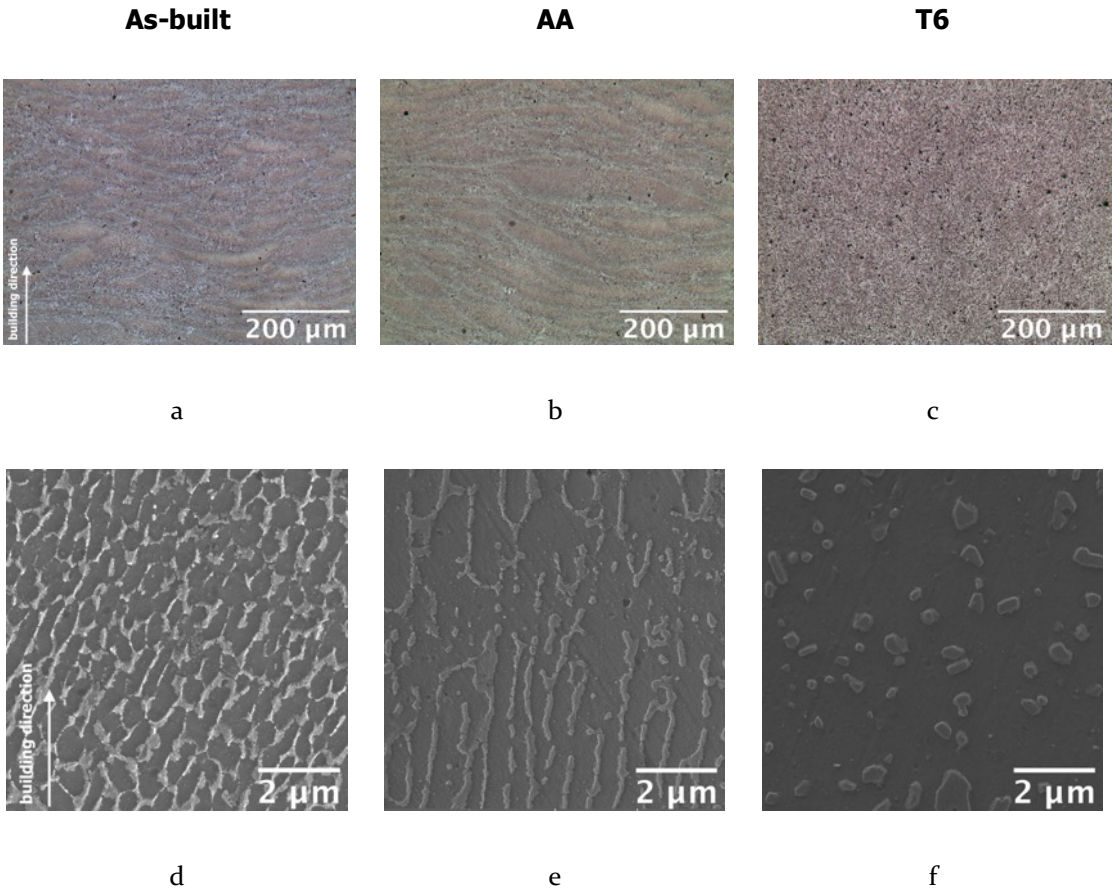

Figure 5.17: Microstructural analyses of: a) and d) as-built, b) and e) AA, c) and f) T6 representative samples.

5.3.4 Conclusions

The present work was aimed at characterizing the tensile properties of the AlSi7Mg0.6 LPBF alloy in the as-built, direct aged and T6 heat-treated in the peak-aging condition. Tensile results were discussed on the basis of both fractographic and microstructural analyses, and the following conclusions can be drawn:

- As-built alloy exhibited a good compromise between mechanical strength and ductility. A further increase in the mechanical strength can be obtained after direct aging (170 °C for 1 h) with a little reduction in ductility.
- T6 optimized treatment (540 °C for 10 minutes + quenching and aging at 150 °C for 4 h) results in homogenizing the microstructure and, with respect to the as-built alloy, it almost doubled the ductility and increased the yield stress. However, T6 exhibited the lowest ultimate tensile strength.
- All conditions exhibited a ductile fracture, with very fine dimples formed on fracture surfaces as a result of the very fine microstructure observed by metallographic characterization. The low ultimate strength showed by T6 samples was confirmed by the presence of Si particles inside dimples, coarser than the ones observed on AA samples.
- Further analyses are currently ongoing with the aim to better highlight the relation between microstructural features and mechanical response.

References

[1] I.E. Anderson, E.M.H. White, R. Dehoff, Feedstock powder processing research needs for additive manufacturing development, Curr. Opin. Solid State Mater. Sci. 22 (2018) 8–15. doi:https://doi.org/10.1016/j.cossms.2018.01.002.

[2] J.H. Tan, W.L.E. Wong, K.W. Dalgarno, An overview of powder granulometry on feedstock and part performance in the selective laser melting process, Addit. Manuf. 18 (2017) 228–255. doi:10.1016/j.addma.2017.10.011.

[3] J.A. Muñiz-lerma, A. Nommeots-nomm, K.E. Waters, M. Brochu, A Comprehensive Approach to Powder Feedstock Characterization for Powder Bed Fusion Additive Manufacturing : A Case Study on AlSi7Mg, Materials (Basel). 11 (2018) 1–15. doi:10.3390/ma11122386.

[4] R.J. Hebert, Viewpoint: metallurgical aspects of powder bed metal additive manufacturing, J. Mater. Sci. 51 (2016) 1165–1175. doi:10.1007/s10853-015-9479-x.

[5] Carpenter Technology, (n.d.). www.carpenteradditive.com.

[6] ASTM E10 Standard Test Method for Brinell Hardness of Metallic Materials, (2018). doi:10.1520/E0010-18.

[7] M. Warmuzek, Metallographic Techniques for Aluminum and Its Alloys, in: G.F. Vander Voort (Ed.), Metallogr. Microstruct., ASM International, 2004: pp. 711–751. doi:10.31399/asm.hb.v09.a0003769.

[8] E. Fiorese, F. Bonollo, G. Timelli, L. Arnberg, E. Gariboldi, New Classification of Defects and Imperfections for Aluminum Alloy Castings, Int. J. Met. 9 (2015) 55–66. doi:10.1007/BF03355602.

[9] N.P. Karapatis, A sub-process approach of selective laser sintering, (2002) 210. doi:10.5075/epfl-thesis-2506.

[10] R. Baitimerov, P. Lykov, D. Zherebtsov, L. Radionova, A. Shultc, K.G. Prashanth, Influence of Powder Characteristics on Processability of AlSi12 Alloy Fabricated by Selective Laser Melting, Mater. . 11 (2018). doi:10.3390/ma11050742.

[11] G. Yablokova, M. Speirs, J. Van Humbeeck, J.-P. Kruth, J. Schrooten, R. Cloots, F. Boschini, G. Lumay, J. Luyten, Rheological behavior of β-Ti and NiTi powders produced by atomization for SLM production of open porous orthopedic implants, Powder Technol. 283 (2015) 199–209. doi:https://doi.org/10.1016/j.powtec.2015.05.015.

[12] S. Lamouri, M. Hamidouche, N. Bouaouadja, H. Belhouchet, V. Garnier, G. Fantozzi, J.F. Trelkat, Control of the γ-alumina to α -alumina phase transformation for an optimized alumina densification, Boletín La Soc. Española Cerámica y Vidr. 6 (2016) 47–54. doi:10.1016/j.bsecv.2016.10.001.

[13] E. Hryha, R. Shvab, H. Gruber, A. Leicht, L. Nyborg, E. Hryha, R. Shvab, H. Gruber, A. Leicht, L. Nyborg, Surface Oxide State on Metal Powder and its Changes during Additive Manufacturing : an Overview, La Metall. Ital. (2018) 34–39.

[14] F.P. Fehlner, Low-temperature oxidation, Philos. Mag. B Phys. Condens. Matter; Stat. Mech. Electron. Opt. Magn. Prop. 55 (1987) 633–636. doi:10.1080/13642818708218369.

[15] N. Eisenreich, H. Fietzek, M. Del Mar Juez-Lorenzo, V. Kolarik, A. Koleczko, V.

Weiser, On the mechanism of low temperature oxidation for aluminum particles down to the nano-scale, Propellants, Explos. Pyrotech. 29 (2004) 137–145. doi:10.1002/prep.200400045.

[16] S. Hasani, M. Panjepour, M. Shamanian, The oxidation mechanism of pure aluminum powder particles, Oxid. Met. 78 (2012) 179–195. doi:10.1007/s11085-012-9299-1.

[17] M.A. Trunov, M. Schoenitz, X. Zhu, E.L. Dreizin, Effect of polymorphic phase transformations in Al2O3 film on oxidation kinetics of aluminum powders, Combust. Flame. 140 (2005) 310–318. doi:10.1016/j.combustflame.2004.10.010.

[18] Z.G. Yang, P.Y. Hou, Wrinkling behavior of alumina scales formed during isothermal oxidation of Fe-Al binary alloys, Mater. Sci. Eng. A. 391 (2005) 1–9. doi:10.1016/j.msea.2004.05.016.

[19] V.K. Tolpygo, D.R. Clarke, Wrinkling of α-alumina films grown by oxidation - II. Oxide separation and failure, Acta Mater. 46 (1998) 5167–5174. doi:10.1016/S1359-6454(98)00134-7.

[20] Z. Suo, Wrinkling of the oxide scale on an aluminum-containing alloy at high temperatures, J. Mech. Phys. Solids. 43 (1995) 829–846. doi:10.1016/0022-5096(95)00014-A.

[21] A. Bianconi, R.Z. Bachrach, S.B.M. Hagstrom, S.A. Flodström, Al-Al2O3 interface study using surface soft-x-ray absorption and photoemission spectroscopy, Phys. Rev. B. 19 (1979) 2837–2843. doi:10.1103/PhysRevB.19.2837.

[22] G. Faraci, S. La Rosa, A.R. Pennisi, Y. Hwu, G. Margaritondo, Evidence for a new aluminum oxidation state, Phys. Rev. B. 47 (1993) 4052–4055. doi:10.1103/PhysRevB.47.4052.

[23] C.D. Boley, S.A. Khairallah, A.M. Rubenchik, Calculation of laser absorption by metal powders in additive manufacturing, Appl. Opt. 54 (2015) 2477–2482.

[24] S. Vock, B. Klöden, A. Kirchner, T. Weißgärber, B. Kieback, Powders for powder bed fusion : a review, Prog. Addit. Manuf. 0 (2019) 0. doi:10.1007/s40964-019-00078-6.

[25] P. Bidare, I. Bitharas, R.M. Ward, M.M. Attallah, A.J. Moore, Fluid and particle dynamics in laser powder bed fusion, Acta Mater. 142 (2018) 107–120. doi:10.1016/j.actamat.2017.09.051.

[26] M.J. Matthews, G. Guss, S.A. Khairallah, A.M. Rubenchik, P.J. Depond, W.E. King, Denudation of metal powder layers in laser powder bed fusion processes, Acta Mater. 114 (2016) 33–42. doi:10.1016/j.actamat.2016.05.017.

[27] G. Sigworth, Aluminum Casting Alloys and Casting Processes, in: K. Anderson, J. Weritz, G. Kaufman (Eds.), Alum. Sci. Technol., ASM International, 2018. doi:10.31399/asm.hb.v02a.a0006524.

[28] W.J. Sames, F.A. List, S. Pannala, R.R. Dehoff, S.S. Babu, The metallurgy and processing science of metal additive manufacturing, Int. Mater. Rev. 6608 (2016) 1–46. doi:10.1080/09506608.2015.1116649.

[29] EN 1706 Aluminium and aluminium alloys - Castings - Chemical composition and mechanical properties, (2020).

[30] M. Hamidi Nasab, D. Gastaldi, N. Lecis, M. Vedani, On Morphological Surface Features of the Parts Printed by Selective Laser Melting (SLM) On morphological

surface features of the parts printed by selective laser melting (SLM), Addit. Manuf. 24 (2018) 373–377. doi:10.1016/j.addma.2018.10.011.

[31] D. Wang, S. Wu, F. Fu, S. Mai, Y. Yang, Y. Liu, C. Song, Mechanisms and characteristics of spatter generation in SLM processing and its effect on the properties, Mater. Des. 117 (2017) 121–130. doi:10.1016/j.matdes.2016.12.060.

[32] R. Casati, M. Vedani, Aging Response of an A357 Al Alloy Processed by Selective Laser Melting, Adv. Eng. Mater. 21 (2019) 1800406. doi:https://doi.org/10.1002/adem.201800406.

[33] A. Mauduit, H. Gransac, P. Auguste, S. Pillot, A. Diószegi, Study of AlSi7Mg0.6 Alloy by Selective Laser Melting: Mechanical Properties, Microstructure, Heat Treatment, J. Cast. Mater. Eng. 3 (2019) 1. doi:10.7494/jcme.2019.3.1.1.

[34] J.H. Rao, Y. Zhang, X. Fang, Y. Chen, X. Wu, C.H.J. Davies, The origins for tensile properties of selective laser melted aluminium alloy A357, Addit. Manuf. 17 (2017) 113–122. doi:10.1016/j.addma.2017.08.007.

[35] L. Ceschini, A. Morri, A. Morri, Effects of the delay between quenching and aging on hardness and tensile properties of A356 aluminum alloy, J. Mater. Eng. Perform. 22 (2013) 200–205. doi:10.1007/s11665-012-0208-1.

[36] EN ISO 6507 Metallic materials – Vickers hardness test, (2018).

[37] M. Wang, B. Song, Q. Wei, Y. Zhang, Y. Shi, Effects of annealing on the microstructure and mechanical properties of selective laser melted AlSi7Mg alloy, Mater. Sci. Eng. A. 739 (2019) 463–472. doi:10.1016/j.msea.2018.10.047.

[38] T. Menold, E. Hadjixenophontos, R. Lawitzki, G. Schmitz, M. Ametowobla, Crystal defects in monocrystalline silicon induced by spot laser melting, J. Appl. Phys. 127 (2020). doi:10.1063/1.5142676.

[39] C. Song, L. Du, L. Qi, Y. Li, X. Li, Y. Li, Residual stress measurement in a metal microdevice by micro Raman spectroscopy, J. Micromechanics Microengineering. 27 (2017). doi:10.1088/1361-6439/aa8912.

[40] B. Matthey, T. Pirling, M. Herrmann, J. Schreiber, Determination of bulk residual stresses in superhard diamond-SiC materials, J. Eur. Ceram. Soc. 40 (2020) 1035–1042. doi:10.1016/j.jeurceramsoc.2019.11.055.

[41] Q.G. Wang, C.J. Davidson, Solidification and precipitation behaviour of Al-Si-Mg casting alloys, J. Mater. Sci. 36 (2001) 739–750.

[42] R. Chen, Q. Xu, H. Guo, Z. Xia, Q. Wu, B. Liu, Correlation of solidification microstructure refining scale, Mg composition and heat treatment conditions with mechanical properties in Al-7Si-Mg cast aluminum alloys, Mater. Sci. Eng. A. 685 (2017) 391–402. doi:10.1016/j.msea.2016.12.051.

[43] C. Garcia-Cordovilla, E. Lousi, Thermal Analysis of Aluminum Alloys, in: D.S. MacKenzie, G.E. Totten (Eds.), Anal. Charact. Aluminum, Steel, Superalloys, 1st ed., CRC Press, 2006: pp. 293–338.

[44] M. Massazza, G. Riontino, C. Riontino, A. Triggiani, E. Carà, Effect of Be on Phase Transformations in an A357-AlSiMg Alloy, Mater. Sci. Forum. 396–402 (2002) 965–970. doi:10.4028/www.scientific.net/MSF.396-402.965.

[45] S. Marola, D. Manfredi, G. Fiore, M.G. Poletti, M. Lombardi, P. Fino, L. Battezzati, A comparison of Selective Laser Melting with bulk rapid solidification of AlSi10Mg

alloy, J. Alloys Compd. 742 (2018) 271–279. doi:10.1016/j.jallcom.2018.01.309.

[46] C.A. Biffi, J. Fiocchi, A. Tuissi, Selective laser melting of AlSi10 Mg: Influence of process parameters on Mg2Si precipitation and Si spheroidization, J. Alloys Compd. 755 (2018) 100–107. doi:10.1016/j.jallcom.2018.04.298.

[47] J.H. Rao, Y. Zhang, K. Zhang, A. Huang, C.H.J. Davies, X. Wu, Multiple precipitation pathways in an Al-7Si-0.6Mg alloy fabricated by selective laser melting, Scr. Mater. 160 (2019) 66–69. doi:10.1016/j.scriptamat.2018.09.045.

[48] J.H. Rao, Y. Zhang, K. Zhang, X. Wu, A. Huang, Selective laser melted Al-7Si-0.6Mg alloy with in-situ precipitation via platform heating for residual strain removal, Mater. Des. 182 (2019) 108005. doi:10.1016/j.matdes.2019.108005.

[49] J.H. Parker, D.W. Feldman, M. Ashkin, Raman scattering by silicon and germanium, Phys. Rev. 155 (1967) 712–714. doi:10.1103/PhysRev.155.712.

[50] P.A. Temple, C.E. Hathaway, Multiphonon Raman spectrum of silicon, Phys. Rev. B. 7 (1973) 3685–3697. doi:10.1103/PhysRevB.7.3685.

[51] K. Uchinokura, T. Sekine, E. Matsuura, Raman scattering by silicon, Solid State Commun. 11 (1972) 47–49. doi:https://doi.org/10.1016/0038-1098(72)91127-1.

[52] G. Sarau, A. Bochmann, R. Lewandowska, S. Christiansen, From Micro– to Macro–Raman Spectroscopy: Solar Silicon for a Case Study, in: Adv. Asp. Spectrosc., InTech, 2012: pp. 221–246. doi:10.5772/48143.

[53] N.T. Aboulkhair, N.M. Everitt, I. Maskery, I. Ashcroft, C. Tuck, Selective laser melting of aluminum alloys, MRS Bull. 42 (2017) 311–319. doi:10.1557/mrs.2017.63.

[54] J. Zhang, B. Song, Q. Wei, D. Bourell, Y. Shi, A review of selective laser melting of aluminum alloys: Processing, microstructure, property and developing trends, J. Mater. Sci. Technol. 35 (2019) 270–284. doi:10.1016/j.jmst.2018.09.004.

[55] J.T. Oliveira de Menezes, E.M. Castrodeza, R. Casati, Effect of build orientation on fracture and tensile behavior of A357 Al alloy processed by Selective Laser Melting, Mater. Sci. Eng. A. 766 (2019) 138392. doi:10.1016/j.msea.2019.138392.

[56] J.C. Pereira, E. Gil, L. Solaberrieta, M. San Sebastián, Y. Bilbao, P.P. Rodríguez, Comparison of AlSi7Mg0.6 alloy obtained by selective laser melting and investment casting processes: Microstructure and mechanical properties in as-built/as-cast and heat-treated conditions, Mater. Sci. Eng. A. 778 (2020) 139124. doi:10.1016/j.msea.2020.139124.

[57] ISO 6892 Metallic materials - Tensile testing, (2019) 54.

[58] ASTM E8/E8M standard test methods for tension testing of metallic materials 1, (2015) 1–27. doi:10.1520/E0008.

[59] Q.G. Wang, Microstructural effects on the tensile and fracture behavior of aluminum casting alloys A356/357, Metall. Mater. Trans. A. 34 (2003) 2887–2899. doi:10.1007/s11661-003-0189-7.

[60] F. Trevisan, F. Calignano, M. Lorusso, J. Pakkanen, E.P. Ambrosio, L. Mariangela, M. Pavese, D. Manfredi, P. Fino, Effects of heat treatments on A357 alloy produced by selective laser melting, World PM 2016 Congr. Exhib. (2016).

Part B

Wire-and-Arc Additive Manufacturing

Chapter 6

WIRE-AND-ARC ADDITIVE MANUFACTURING OF AUSTENITIC STAINLESS-STEELS

A LITERATURE REVIEW

6.1 Austenitic stainless-steels

Stainless steels are Fe-Cr alloys with a low content of C (maximum 1.2 wt.%) and a minimum nominal Cr content of 11 wt.% that, by formation of a stable protective oxide passivation film (Cr_2O_3), protects the steel from corrosion. At this purpose, the passivation film, if damaged, will quickly reform on the surface in some oxygen is present [1]. Stainless steels are classified as a function of their crystal structure at room temperature into: ferritic (bcc), martensitic (bct), austenitic (fcc), and duplex (containing two different structures). If they can be reinforced via precipitation hardening, they are referred to as PH stainless steels. According to the American Iron and Steel Institute (AISI) designation, they are classified on account of their chemical composition.

On the basis of the Fe-Cr phase diagram (Figure 6.1a), the equilibrium phase at room temperature is ferrite. The austenite phase is limited to the so-called γ-loop at high temperature and for low percentage of Cr (below 13 wt.%). However, γ-loop can be extended with the addition of austenite stabilizers like C and mainly Ni (Figure 6.1a) up to the suppression of the γ→α transformation and the retention of metastable γ phase to room temperature, as for austenitic stainless steel that contain between 8 and 20 wt.% of Ni. C content, instead, has to be limited (usually between 0.02 – 0.08 wt.% and lower that 0.03 wt.% for low carbon grades, such as 304L and 316L) in order to avoid the phenomenon of sensitization due to the precipitation of Cr-rich carbides (mainly $(Fe,Cr)_{23}C_6$) between 500-800 °C that leads to Cr-depleted zones near grain boundaries and exposes the alloy to localized

intergranular corrosion [1,2]. If possible, in order to reduces sensitization and increase corrosion resistant, a solution treatment at temperatures higher than 1100 °C followed by a rapid cooling can be applied.

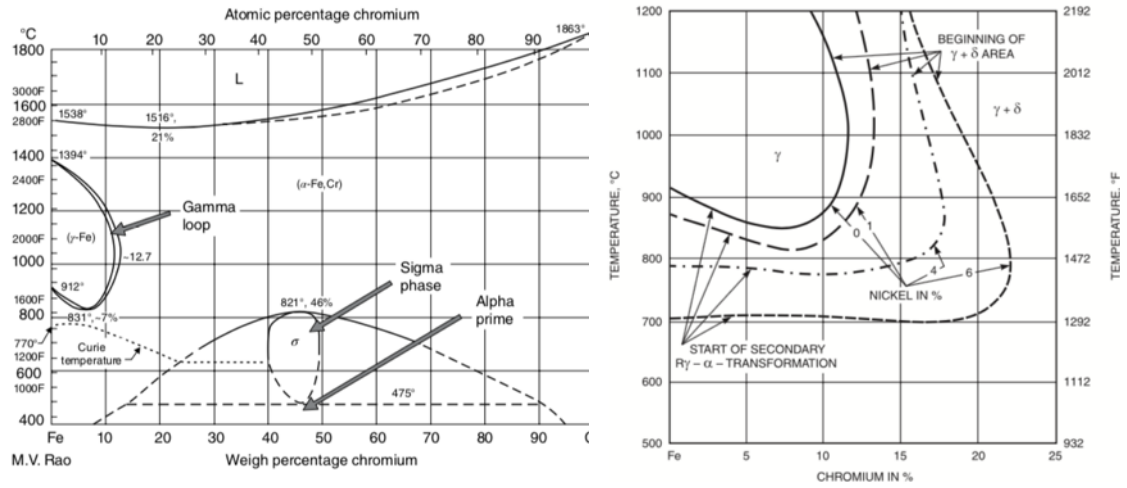

a b

Figure 6.1: Fe-Cr phase diagram (a); γ-loop extension as a function of Ni addition (b) [1,2]

It should be also noticed that, as showed by the Fe-Cr diagram, there is another equilibrium phase, called σ-phase. The σ-phase is a hard and brittle intermetallic phase (FeCr with 1:1 stoichiometric ratio) that precipitates from the ferrite phase during cooling and it is usually undesired in stainless steels because it reduces toughness and Cr content of the matrix. Its formation is quite sluggish and requires an extended permanence in the range 500-700 °C and a high Cr content (45-50 wt.%), thus it is an issue especially for ferritic and martensitic stainless-steels, but also for austenitic ones [1,2]. At temperature below 475 °C, the ferrite phase separates into the Cr-enriched α' brittle phase.

Austenitic stainless steels have a fully γ-fcc crystal structure at room temperature, even if some δ-ferrite can be retained, and they belong to the AISI 3XX (Cr-Ni) series. They have an overall Cr, Ni, Mn, Si content above 25 wt.%, along with Mo, Ti, N, Nb, and Cr generally higher than 16 wt.%. The effects of the mentioned alloy elements are summarized in Table 6.1.

Table 6.1: Role of major alloy elements in austenitic stainless steels [1]

Element	*Role*
Cr	Responsible for corrosion resistance of the alloy (forms the protective Cr_2O_3 oxide film) Tends to form $M_{23}C_6$ carbides Helps stabilizing ferrite
Ni	Stabilizes austenite
C	Forms carbides (detrimental for corrosion resistance) Helps stabilizing austenite
N	Increase strength and pitting corrosion resistance if added in the range 0.1-0.25wt.% Stabilizes austenite
Si	In concentration up to 1wt.% improves the fluidity of the molten metal and promotes deoxidation
Mn	Increases the solubility of N thus helps stabilizing austenite Forms with S stable manganese sulfides (MnS)
Mo	Improves pitting corrosion resistance Provides solid-solution strengthening Helps stabilizing ferrite
Ti, Nb	Form carbides Improve resistance to intergranular corrosion Helps stabilizing ferrite

Austenitic stainless steels are paramagnetic and have a good corrosion and oxidation resistance up to 650 °C. In addition, they are characterized by good strength, excellent ductility and toughness even at low temperature, making them suitable for cryogenic applications. They cannot be strengthened by heat

treatment, but can be hardened via coldworking [1]. They are used in a wide range of applications, including pressure vessels, kitchen equipment, medical devices and constructions.

6.2 Welding of austenitic stainless-steels

Austenitic stainless steels are considered very weldable. It should be considered that they have a high thermal expansion coefficient, a low thermal conductivity, and a high electrical resistivity; all these aspects affect the weldability of these alloys. They can be welded with several techniques, including resistance processes, and require a lower heat input than carbon steels. However, precautions have to be taken in order to avoid distortions due to thermal expansion and sensitization. Fully austenite stainless steels are also susceptible to solidification and liquation cracking, to the extent that a small content of δ-ferrite (in the range 5-10 wt.%) is desired in order to limit cracking tendency. The crack susceptibility of austenitic stainless steel as a function of the ratio between the equivalent content of Cr and Ni is reported in Figure 6.2. This ratio, as it will be better discussed in the next section, is related to the amount of δ-ferrite and determines the solidification modes of the fusion zone.

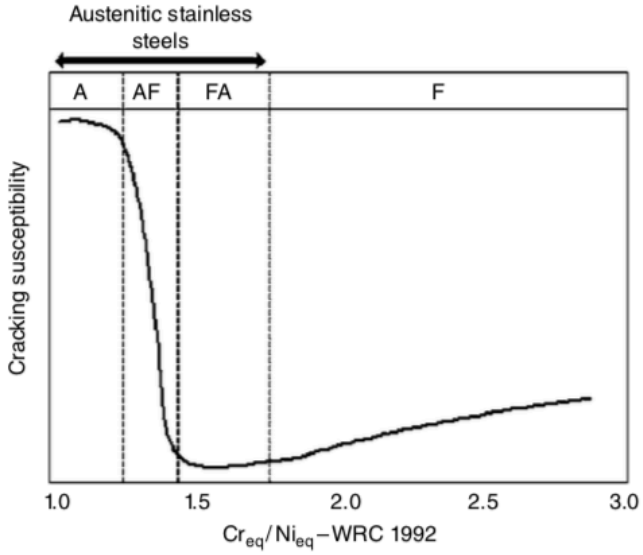

Figure 6.2: Solidification cracking susceptibility of stainless steels as a function of the ratio between the equivalent content of Cr and Ni [2]

If the fusion zone solidified as fully austenitic cracking might occur, thus a certain amount of δ-ferrite is usually preferred. The effect of δ-ferrite in solidification of the austenitic stainless steels fusion zones can be summarized as [1]:

- The presence of δ-ferrite reduces solidification range of the alloy.
- The coefficient of thermal expansion is lower for δ-ferrite than austenite, thus reducing tensile and compressive stress occurring during heating and cooling.
- Impurities, like P and S, have a higher solubility in δ-ferrite than austenite, so impurities that can act as cracks initiators are reduced.
- The difference in the interfacial energy between austenite and δ-ferrite prevents the formation of continuous liquid film due to segregation.
- The two-phase microstructure inhibits crack propagation.
- δ-ferrite is detrimental for corrosion resistance of the alloy as it generates Cr-depleted zones that can become susceptible for localize corrosion.

Solidification modes of austenitic stainless steels welds are represented in Figure 6.3.

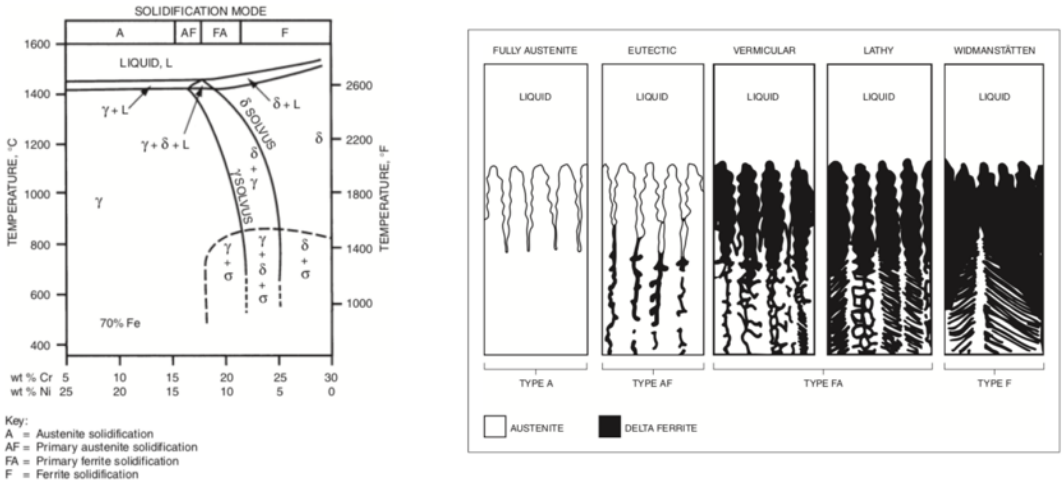

a b

Figure 6.3: Solidification modes in austenitic stainless steels: a) vertical section of ternary-phase diagram at approximately 70% Fe; b) relative morphologies [1].

Austenitic stainless steels with a high Ni-content, with composition on the left of the three-phase eutectic L+γ+δ, solidifies with a fully austenite microstructure (Type A in Figure 6.3b). With increasing Cr-content, moving to the right side of the phase diagram, solidification mode changes into austenite-ferrite (Type AF in Figure 6.3b) with δ-ferrite formed in the latest stage of the primary austenite solidification in the interdendritic regions as a result of eutectic reaction. For composition after the three-phase eutectic region, δ-ferrite becomes the primary phase. In ferrite-austenite solidification (Type FA in Figure 6.3b), δ-ferrite dendrites form at the beginning of the solidification, core of these dendrites is Cr-rich while outer regions are depleted in Cr. When reaching the δ+γ region, the outer portion of the dendrites transforms in austenite, leaving behind δ-ferrite in form of skeleton in correspondence of dendrites core, termed vermicular ferrite. Lathy ferrite is still a result of the FA solidification mode, but δ-ferrite assume the shape of laths or needles. A mixed lathy and vermicular microstructure is often observed. In Type F, the solidification develops completely as δ-ferrite and the solid-state transformation into austenite occurs at lower temperatures in Windmanstätten-like sideplates along ferrite-ferrite grain boundaries. This solidification mode is seldom observed in austenitic stainless-steels, being much more common in duplex stainless steels [1,3].

6.2.1 Prediction of ferrite content

A number of empirical relationships and constitutional diagrams have been developed with the aim to predict the content of δ-ferrite on the basis of the equivalent content of Cr (Cr_{eq}) and Ni (Ni_{eq}). Cr and Ni equivalency are calculated on the basis of specific relationships that consider ferrite and austenite stabilizer, respectively. Cr_{eq} and Ni_{eq} values are then used to determine ferrite content according to the constitutional diagrams. The most widespread are: the Schaeffler, the DeLong and the Welding Research Council (WRC) diagrams.

SCHAEFFLER DIAGRAM

Schaeffler diagram (Figure 6.4) was developed in 1942 and it is based on the following formula [1]:

$$Cr_{eq} = \%Cr + \%Mo + (1.5 \times \%Si) + (0.5 \times \%Nb)$$

$$Ni_{eq} = \%Ni + (0.5 \times \%Mn) + (30 \times \%C)$$

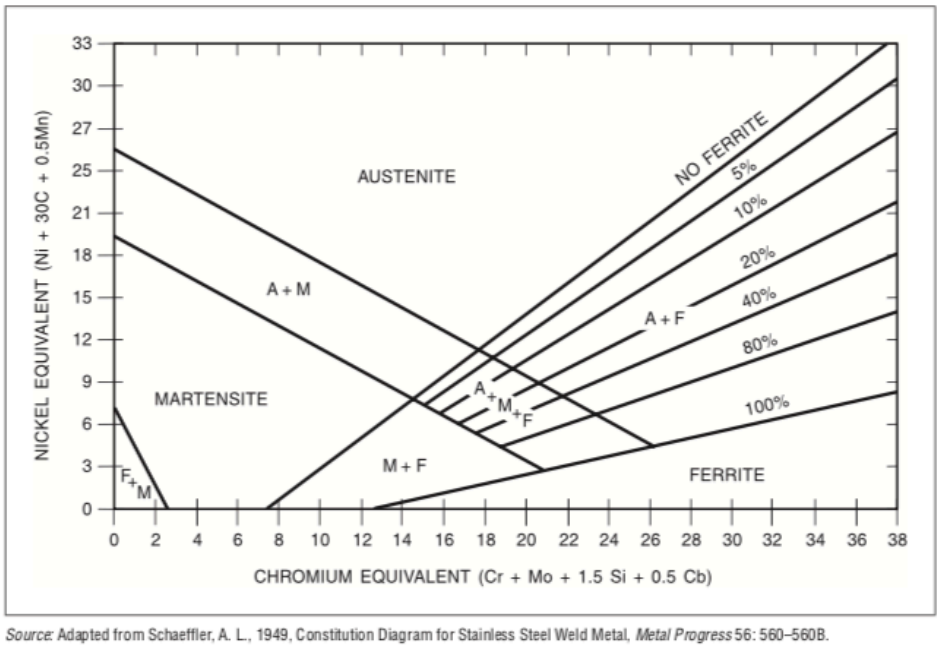

Source: Adapted from Schaeffler, A. L., 1949, Constitution Diagram for Stainless Steel Weld Metal, *Metal Progress* 56: 560–560B.

Figure 6.4: Schaeffler diagram for the prediction of ferrite content and solidification structure [1]

Schaeffler diagram returns the amount of δ-ferrite (vol.%), as well as solidification structure between martensite (M), ferrite (F), austenite (A) and multi-structures (M+F, F+M, A+M, A+F, A+M+F). It includes a wide range of chemical composition and, in the diagram, the volume percent of ferrite was determined by metallographic analyses.

DELONG DIAGRAM

DeLong et al. developed the diagram (Figure 6.5) in 1956 by reviewing the Schaeffler one and by including also nitrogen as austenite stabilizer. Cr and Ni equivalency are calculated as follows [1]:

$$Cr_{eq} = \%Cr + \%Mo + (1.5 \times \%Si) + (0.5 \times \%Nb)$$

$$Ni_{eq} = \%Ni + (0.5 \times \%Mn) + (30 \times \%C) + (30 \times \%N)$$

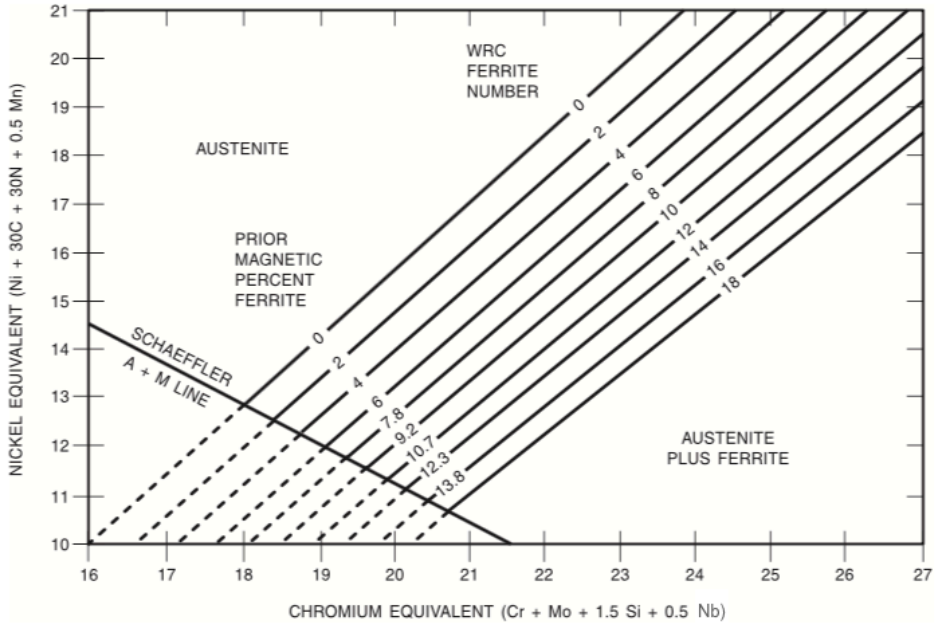

Figure 6.5: DeLong diagram for the prediction of ferrite content and solidification structure [1]

DeLong diagram still returns the amount of δ-ferrite (wt.%) and solidification structure between austenite, austenite plus ferrite, and austenite plus martensite. It also introduces the WRC ferrite number (FN), a standardized method to experimentally determine the amount of ferrite via magnetic measurements described in AWS A4.2M and ISO 8249. Up to a ferrite content of approximately 8 vol.%, FN and ferrite percentage coincide while, for values below this threshold, the two values significantly diverge. As for the WRC diagram that follows, it

includes a narrowed range of chemical composition with respect to the Schaeffler diagram.

WRC DIAGRAM

WRC diagram represents the evolution of DeLong diagram, it was firstly developed in 1988 and revised in 1992. Formula for the calculation of Cr_{eq} and Ni_{eq} were expanded in order to include also the composition of many duplex steels and the contribution of Si and Mn was deleted from formula as follows [1]:

$$Cr_{eq} = \%Cr + \%Mo + (0.7 \times \%Nb)$$

$$Ni_{eq} = \%Ni + (35 \times \%C) + (20 \times \%N) + (0.25 \times \%Cu)$$

In Figure 6.6 is reported the 1992 WRC diagram in which ferrite content is given only as a function of FN and the only solidification structures considered are: fully austenite, austenite-ferrite, ferrite-austenite and fully ferrite. This diagram was recognized as the most accurate to predict ferrite content in austenitic stainless steels.

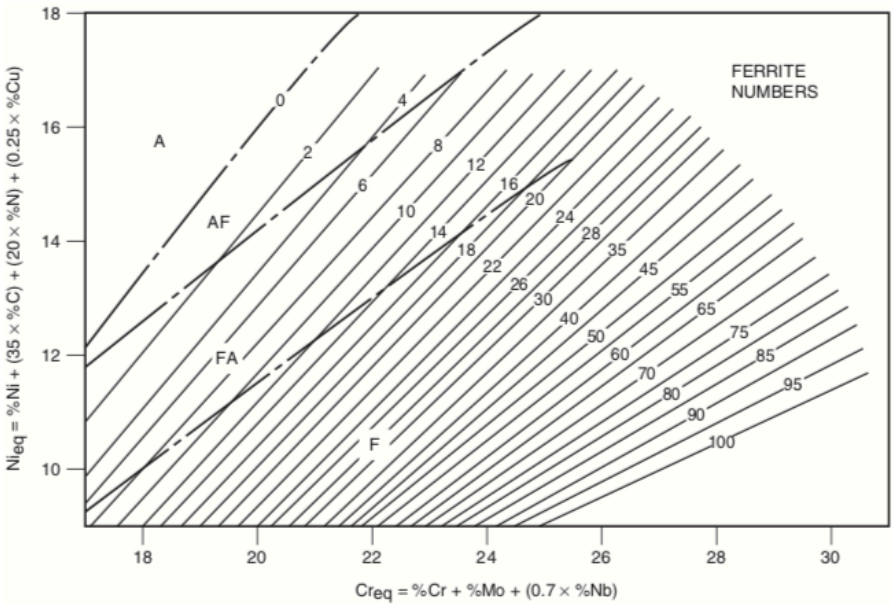

Figure 6.6: WRC 1992 diagram for the prediction of ferrite content and solidification structure in austenitic and duplex stainless steels [1]

6.3 WAAM of Stainless-steels

Wire-and-arc Additive Manufacturing has been successfully applied to stainless steels, specifically to: austenitic stainless steels grade 304L and mainly 316L [4–11], martensitic stainless steel grade 420 [12,13], precipitation-hardenable stainless steel 17-4 and 15-5 PH [14,15], duplex stainless steels [16].

Up to October 2020, approximately 60 papers have been indexed by the Scopus® database on the WAAM of stainless steels, all published between 2017-2020, demonstrating the growing interest on this topic. Most of literature works were focused on process optimization but few of them dealt with microstructure and process characterization, whose main results regarding austenitic stainless steel will be presented in the following sections.

6.3.1 Metallurgy of WAAM austenitic stainless-steels

Microstructure of WAAM austenitic stainless steels results from the continuous deposition of molten material that undergo rapid solidification and subsequent re-heating due to the deposition of the subsequent layer. Consequently, it is strongly related to thermal cycles occurring during the whole deposition process. As for the experimental material discussed in the following Chapter, literature works focused on the characterization of plates obtained by subsequent deposition of continuous single layers of molten material. Due to the more basic deposition strategy with respect to LPBF, by retrieving the scheme reported in Chapter 1 the hierarchical microstructure can be simplified as reported in Figure 6.7.

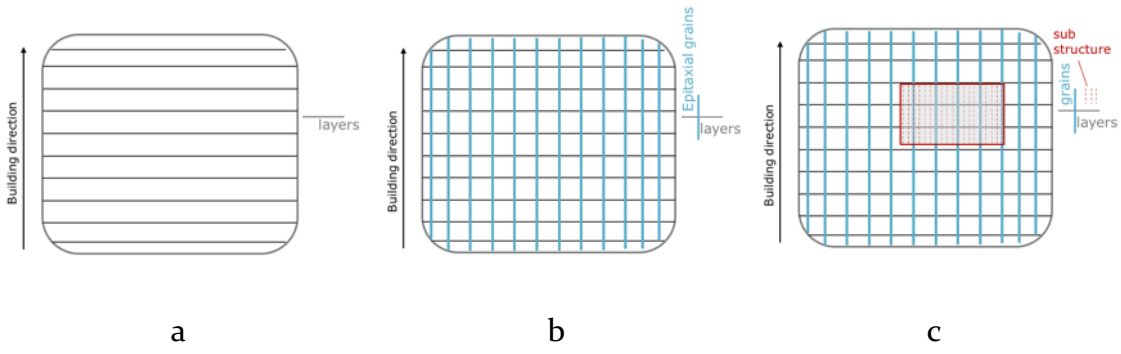

Figure 6.7: Schematic representation of the hierarchical microstructure WAAM plates: a) layers, b) epitaxial grains, c) fine sub-structure.

By observing the microstructure along the building direction, layers, epitaxial grains and columnar sub-structure inside grains can be defined. Typical semicircular melt pools can be found on transversal cross-section of plates, as will be showed in the following Chapter.

Microstructural analyses evidenced that microstructure was composed by large columnar grains crossing-over layers directed along the building direction, evidenced by macrostructural analyses (Figure 6.8a), and a finer columnar-dendrite sub-structure within columnar grains. As reported in Figure 6.8b, three main regions can be identified in each layer:

- the bottom area adjacent to the layer boundary in which cellular structure ca be recognized;
- the core of the layer in which microstructure develops as a fine columnar structure;
- the top of the layer, adjacent to the upper one, in which microstructure turn into coarse columnar structure with secondary dendrites.

For high energy input WAAM processes, like plasma arc welding (PAW), a transition in the grain morphology from columnar to equiaxed (CET) grains were evidenced as a function on increasing scanning speed, as a consequence of the G/R variation across the melt pool, as discussed in Chapter 1 [17].

Works reported both γ-austenite as primary phase, type AF solidification mode [8] for and δ-ferrite as primary phase, type FA solidification mode [18], according to the value of Ni and Cr equivalency for the specific alloy, AISI 316L and 304L respectively. Morphology of δ-ferrite was evidenced as skeletal, or vermicular, and lathy [18,19], but even Windmanstätten-like ferrite was evidenced in correspondence of the top region of the last deposited layer [18].

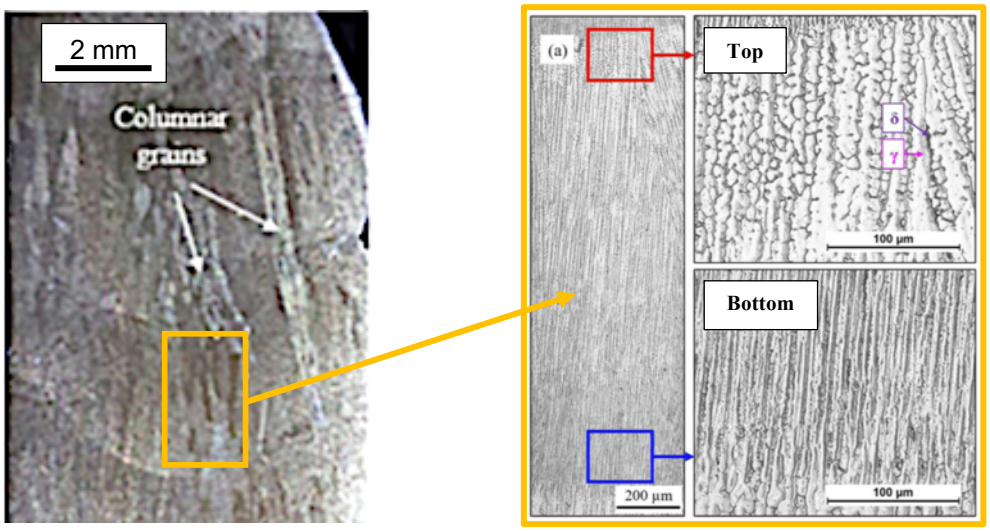

a b

Figure 6.7: Microstructural analyses on WAAM austenitic stainless steels: a) columnar grains crossing-over layers; b) microstructure inside the layer [8,18].

Epitaxial growth was evidenced by microstructural analyses performed along layer boundaries (Figure 6.8) and EBSD analyses (Figure 6.9). In particular, Wang et al. [8] and Gordon et al. [19] reported a preferential orientation along the <001> and <200> crystallographic direction for grains oriented along the building direction, respectively.

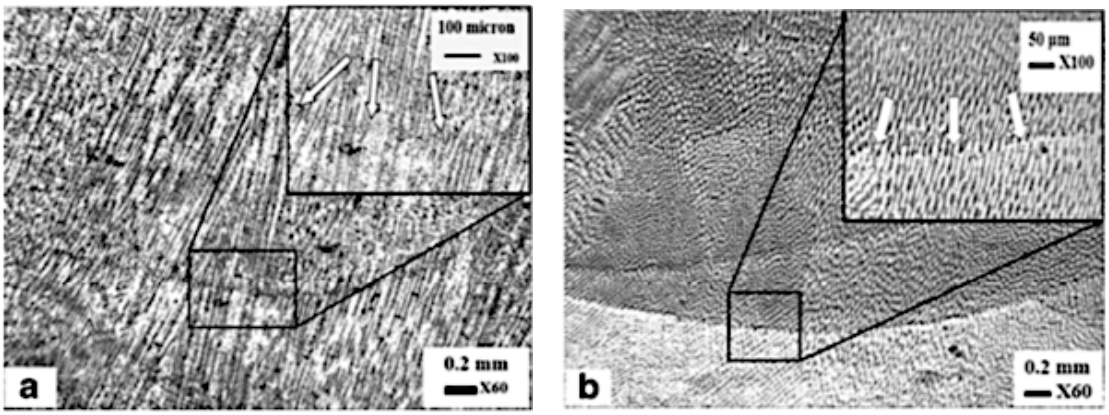

a b

Figure 6.8: Microstructural analyses on interlayer region of WAAM austenitic stainless steels [18]

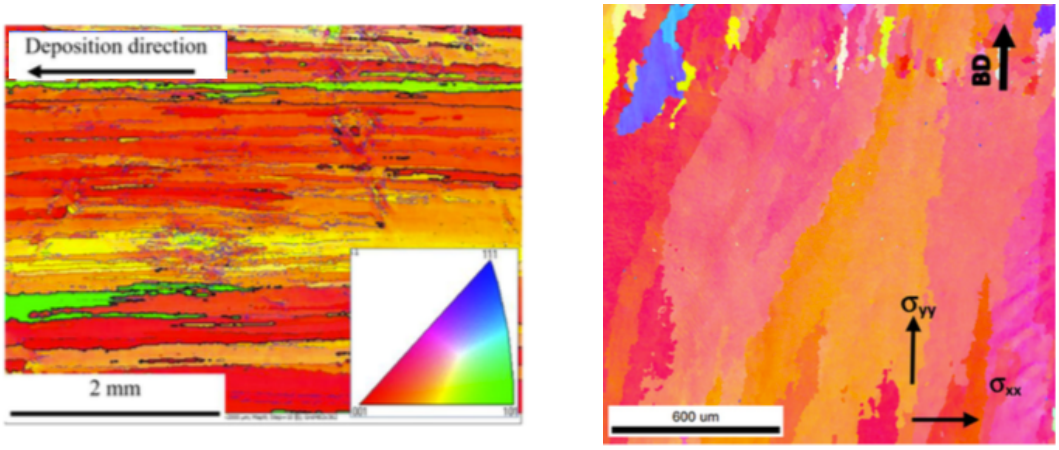

a b

Figure 6.9: EBSD analyses of WAAM austenitic stainless steels showing preferential texture along deposition direction: a) Wang et al. [8]; b) Gordon et al. [19].

Defects reported for the WAAM products are spattering and porosity, especially in case of GMAW as a consequence of the electric current acting directly on the wire feedstock. Furthermore, contamination of wire feedstock can be adsorbed into the melt pool causing porosity [17]. Residual stress has been reported to cause warpage, distortion and cracking. In case of stainless steels, internal stress is also strongly related to the solid-state phase transformation occurring during repeated thermal cycles [17].

6.3.2 Mechanical properties WAAM austenitic stainless-steel

Many of the aforementioned experimental works performed uniaxial tensile tests on specimens extracted from WAAM austenitic stainless steel plates in the longitudinal (L, parallel to the deposited layers) and transversal directions (T, perpendicular to the deposited layers), whose results are summarized in Table 6.2. Anisotropy in mechanical response was found, mainly ascribable to the epitaxial growth, as also discussed in Chapter 1 of the present dissertation. Difference in the

mechanical properties of longitudinal and transversal specimens was evidenced, especially if ultimate tensile strength is concerned. In GMAW processes, the longitudinal direction exhibited the higher ultimate tensile strength while in the GTAW transversal specimen was characterized by higher strength. It should be noticed that only one work reported the elastic modulus resulted from tensile tests on L and T directions and such value, between 132 and 139 GPa, was considerably lower than the reference value for the wrought conventional austenitic stainless steel (200 GPa [20]). The correlations between microstructure and mechanical properties will be addressed in the following Chapter regarding experimental activities carried out on the WAAM 304L austenitic stainless steel.

Table 6.2: Mechanical properties reported in the literature for the WAAM austenitic stainless steels (grade 304L and 316L) as a function of samples extraction direction

Alloy	**Process type**	**Specimen orientation**	**E [GPa]**	**$R_{p0.2}$ [MPa]**	**UTS [MPa]**	**$A_{\%}$ [%]**	**Reference**
316L	SpeedArc	L	-	418	550	-	[8]
304L	GMAW	L	139	296	524	/	[19]
		T	132	306	499	/	
304L	GTAW	L	/	231	622	88	[4]
		T	/	235	678	57	
304L	GMAW	L	/	356	612	/	[21]
		T	/	455	580	58	

References

[1] Stainless and heat-resistant steels, in: AWS Weld. Handb. - Vol. 4, American Welding Society (AWS), n.d.

[2] D.H. Philips, Welding engineering - An introduction, John Wiley & Sons, Chichester, West Sussex, 2016.

[3] S. Kou, Corrosion-resistant materials: Stainlees Steels, in: Weld. Metall., Second edi, John Wiley & Sons, Hoboken, New Jersey, 2003: pp. 431–454.

[4] L. Ji, J. Lu, C. Liu, C. Jing, H. Fan, S. Ma, Microstructure and mechanical properties of 304L steel fabricated by arc additive manufacturing, MATEC Web Conf. 128 (2017). doi:10.1051/matecconf/201712803006.

[5] H. KITANO, T. NAKAMURA, Distortion reduction of parts made by wire and arc additive manufacturing technique using low transformation temperature welding materials, Q. J. JAPAN Weld. Soc. 36 (2018) 31–38. doi:10.2207/qjjws.36.31.

[6] P. Baldissera, C. Delprete, Deep cryogenic treatment of AISI 302 stainless steel: Part II - Fatigue and corrosion, Mater. Des. 31 (2010) 4731–4737. doi:10.1016/j.matdes.2010.05.015.

[7] J.W. Elmer, G. Gibbs, The effect of atmosphere on the composition of wire arc additive manufactured metal components, Sci. Technol. Weld. Join. 24 (2019) 367–374. doi:10.1080/13621718.2019.1605473.

[8] L. Wang, J. Xue, Q. Wang, Correlation between arc mode, microstructure, and mechanical properties during wire arc additive manufacturing of 316L stainless steel, Mater. Sci. Eng. A. 751 (2019) 183–190. doi:https://doi.org/10.1016/j.msea.2019.02.078.

[9] X. Zhang, Q. Zhou, K. Wang, Y. Peng, J. Ding, J. Kong, S. Williams, Study on microstructure and tensile properties of high nitrogen Cr-Mn steel processed by CMT wire and arc additive manufacturing, Mater. Des. 166 (2019) 107611. doi:10.1016/j.matdes.2019.107611.

[10] W. Wu, J. Xue, L. Wang, Z. Zhang, Y. Hu, C. Dong, Forming process, microstructure, and mechanical properties of thin-walled 316L stainless steel using speed-cold-welding additive manufacturing, Metals (Basel). 9 (2019). doi:10.3390/met9010109.

[11] N. Rodriguez, L. Vázquez, I. Huarte, E. Arruti, I. Tabernero, P. Alvarez, Wire and arc additive manufacturing: a comparison between CMT and TopTIG processes applied to stainless steel, Weld. World. 62 (2018) 1083–1096. doi:10.1007/s40194-018-0606-6.

[12] J. Lunde, M. Kazemipour, S. Salahi, A. Nasiri, Microstructure and Mechanical Properties of AISI 420 Stainless Steel Produced by Wire Arc Additive Manufacturing, in: TMS 2020 149th Annu. Meet. Exhib. Suppl. Proc., Springer, 2020. doi:https://doi.org/10.1007/978-3-030-36296-6_39.

[13] M. Kazemipour, J.H. Lunde, S. Salahi, A. Nasiri, On the Microstructure and Corrosion Behavior of Wire Arc Additively Manufactured AISI 420 Stainless Steel, in: TMS 2020 149th Annu. Meet. Exhib. Suppl. Proc., Springer, 2020. doi:https://doi.org/10.1007/978-3-030-36296-6_41.

[14] A. Caballero, J. Ding, S. Ganguly, S. Williams, Wire + Arc Additive Manufacture of

17-4 PH stainless steel: Effect of different processing conditions on microstructure, hardness, and tensile strength, J. Mater. Process. Technol. 268 (2019) 54–62. doi:https://doi.org/10.1016/j.jmatprotec.2019.01.007.

[15] C. Guo, R. Hu, F. Chen, Microstructure and performances for 15-5 PH stainless steel fabricated through the wire-arc additive manufacturing technology, Mater. Technol. (2020) 1–12. doi:10.1080/10667857.2020.1800296.

[16] J. Stützer, T. Totzauer, B. Wittig, M. Zinke, S. Jüttner, GMAW Cold Wire Technology for Adjusting the Ferrite–Austenite Ratio of Wire and Arc Additive Manufactured Duplex Stainless Steel Components, Met. . 9 (2019). doi:10.3390/met9050564.

[17] W. Jin, C. Zhang, S. Jin, Y. Tian, D. Wellmann, W. Liu, Wire arc additive manufacturing of stainless steels: A review, Appl. Sci. 10 (2020). doi:10.3390/app10051563.

[18] O. Yilmaz, A.A. Ugla, Microstructure characterization of SS308LSi components manufactured by GTAW-based additive manufacturing: shaped metal deposition using pulsed current arc, Int. J. Adv. Manuf. Technol. 89 (2017) 13–25. doi:10.1007/s00170-016-9053-y.

[19] J. V. Gordon, C. V. Haden, H.F. Nied, R.P. Vinci, D.G. Harlow, Fatigue crack growth anisotropy, texture and residual stress in austenitic steel made by wire and arc additive manufacturing, Mater. Sci. Eng. A. 724 (2018) 431–438. doi:10.1016/j.msea.2018.03.075.

[20] S.D. Washko, G. Aggen, Wrought Stainless Steels, in: Prop. Sel. Irons, Steels, High-Performance Alloy., ASM International, 1990. doi:10.31399/asm.hb.v01.a0001046.

[21] C. V. Haden, G. Zeng, F.M. Carter, C. Ruhl, B.A. Krick, D.G. Harlow, Wire and arc additive manufactured steel: Tensile and wear properties, Addit. Manuf. 16 (2017) 115–123. doi:10.1016/j.addma.2017.05.010.

Chapter 7

WIRE-AND-ARC ADDITIVE MANUFACTURING OF AISI 304L AUSTENITIC STAINLESS-STEELS
EXPERIMENTAL ANALYSES

Foreword

The present Chapter synthetizes experimental activities carried out on AISI 304L stainless steels plates produced by Wire-and-Arc Additive Manufacturing during the PhD course. Experimental analyses were aimed at characterizing microstructural and mechanical properties of WAAM plates, by underlining the relation between microstructural features and properties, also considering anisotropy. With reference to the state of the art discussed in the previous Chapter, the main novelty of the present work lies in the analyses of the direction at 45° to the deposited layers and, more importantly, on the investigation of the evidenced anisotropic elastic behavior.

Therefore, the work was focused on two main topics:

- Mechanical and microstructural characterization of samples extracted from WAAM plates along three different orientations (longitudinal, transversal and diagonal with respect to the deposition layer).
- Focus on the role of the preferred texture formed by the additive process in determining the elastic modulus.

The Chapter is mainly based on the following papers, which I have co—authored:

- "*Tensile properties and microstructural features of 304L austenitic stainless steel produced by Wire-and-Arc Additive Manufacturing*" by V. Laghi, M. Palermo, L. Tonelli, G. Gasparini, L. Ceschini and T. Trombetti published in *The International Journal of Advanced Manufacturing Technology (vol. 106(9-10), pp. 3693-3705)* and licensed by Springer Nature on September 22, 2020 (license number 4914321484415).
- "*Influence of inter-layer cooling on microstructure and mechanical properties of wire arc additive manufactured 304L austenitic stainless steel*" by L. Tonelli, R. Sola, V. Laghi, M. Palermo, T. Trombetti and L. Ceschini, pre-print currently unpublished.
- *"Orthotropic elastic model for Wire-and-Arc Additively Manufactured stainless steel"* by V. Laghi, L. Tonelli, M. Palermo, M. Bruggi, R. Sola, L. Ceschini and T. Trombetti, pre-print currently under review.

7.1 Mechanical and Microstructural characterization

This section contains selected parts of the published paper: "*Tensile properties and microstructural features of 304L austenitic stainless steel produced by Wire-and-Arc Additive Manufacturing*" (license number 4914321484415 by Springer Nature). The published version of the paper can be accessed by the following link: https://doi.org/10.1007/s00170-019-04868-8.

The International Journal of Advanced Manufacturing Technology
https://doi.org/10.1007/s00170-019-04868-8

ORIGINAL ARTICLE

Check for updates

Tensile properties and microstructural features of 304L austenitic stainless steel produced by wire-and-arc additive manufacturing

Vittoria Laghi[1] · Michele Palermo[1] · Lavinia Tonelli[2] · Giada Gasparini[1] · Lorella Ceschini[1] · Tomaso Trombetti[1]

Received: 3 October 2019 / Accepted: 19 December 2019

This section contains also selected parts of the unpublished paper: "*Influence of inter-layer cooling on microstructure and mechanical properties of wire arc additive manufactured 304L austenitic stainless steel*".

7.1.1 Aim and scope

Among the different metal 3D printing strategies, Wire-and-Arc Additive Manufacturing (WAAM) technique allows high deposition rates, resulting to be more suitable to realize large-scale structural components and to guarantee lower costs compared to other AM techniques for metals [1–3]. Although much research effort has been devoted to assess Powder Based Fusion (PBF) and powder-based Direct Energy Deposition (DED) of metallic materials [4–6], nowadays there is limited amount of research work concerning the influence of WAAM process parameters on the metallic materials properties [7,8]. Among WAAM processed steels, the available literature reports limited data about maraging steel [9], 2Cr13 martensitic stainless steel [10], 316L [11–13] and 304L [14–16] austenitic stainless

steels, as well as 2209 duplex stainless steel [17]. These works suggested the presence of microstructural anisotropy induced by the process. However, very few studies emphasized the effect of the specific microstructural features induced by the process on mechanical behavior [8,9]. In light of the above, the focus of the present work is to investigate the influence of elements orientation on the tensile properties of WAAM plates produced using a commercial austenitic ER 308L Si wire, through both mechanical and microstructural characterization.

7.1.2 Experimental procedure

Specimens for the experimental tests were cut from plates (380 x 380 x 4 mm^3) that have been realized at MX3D facilities [18] by using GMAW-WAAM and a commercially available ER 308L Si austenitic stainless steel wire, supplied by *Oerlikon* [19]. A total of ten plates were provided, processed with the same process parameters (reported in Table 7.1), but five of them were processed adopting an interlayer cooling system, consisting of a flow of compressed dry air, while the other five without any control of cooling, leading to uncontrolled cooling conditions. Active cooling is usually adopted to increase deposition rate [20]. An interlayer cooling strategy, in fact, limits the delay between successive depositions, necessary to promote heat dissipations and control the inter-layer temperature that, if too high, may lead to unstable melt pools. Actually, long idle time can lead to an unprofitable total production time and consequently limit the high depositions rates, which are one of the main features of this additive process. Consequently, analyses were also conducted to assess the effect of the active cooling on plates properties and microstructure. Hereafter, specimens processed with active cooling will be referred to as A (active cooling) specimens, while those without cooling system will be identified as U (uncontrolled cooling).

In order to evaluate possible microstructural and mechanical anisotropy induced by the process, the tested specimens have been cut from the plates following three main orientations with respect to the deposition layer (according to the scheme reported in Figure 7.1): (i) longitudinal (L), i.e. parallel to the deposition layer; transversal (T), i.e. perpendicular to the deposition layer; (iii) diagonal (D), i.e. at 45° with reference to the deposition layer.

Table 7.1: Process parameters for WAAM of plates (Courtesy of MX3D [18]).

Process parameters	***Details***	***Value***
Deposition power	Current	100 - 140 A
	Arc voltage	18 - 21 V
Speed	Welding speed	15 - 30 mm s^{-1}
	Wire feed rate	4 - 8 m min^{-1}
	Deposit rate	0.5 - 2 kg h^{-1}
Distance and angle	Layer height	0.5 - 2 mm
	Electrode to layer angle	90°
Wire	Wire grade	ER308LSi
	Wire diameter	1 mm
Shielding gas	Shield gas type	98% Ar, 2%CO_2
	Shield gas flow rate	10-20 L min^{-1}

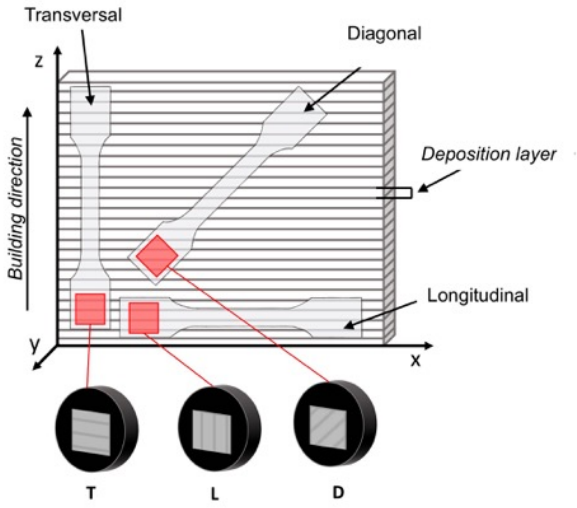

Figure 7.1: Orientation of the tensile specimens cut from WAAM plates with respect to the deposition layer and scheme of extraction of the metallographic samples for the microstructural characterization

Specimen for tensile tests were shaped according to ISO 6892-1 [21] (Figure 7.2) and their surface was polished by mechanical milling, reducing the final thickness to an average value of 2.5 to 3 mm, starting from the nominal 4 mm thickness of the plates. The inherent as-printed surface would have indeed affected the proper determination of the cross-sectional area.

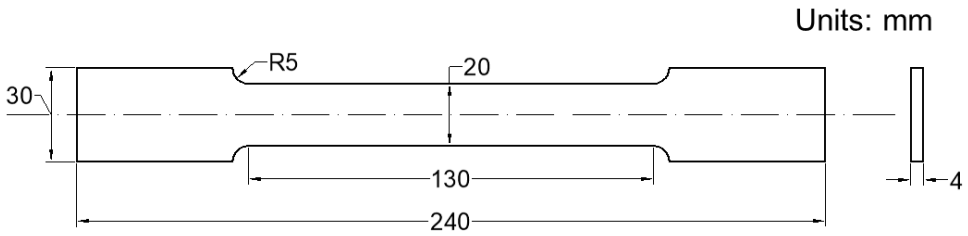

Figure 7.2: Geometry and dimensions (mm) of the flat tensile specimens according to ISO 6892-1 [21]

Images of the specimens before and after milling are shown in Figure 7.3a,b. Surface topography images obtained by 3D-Digital Microscopy (Hirox KH-7700), before and after polishing, are compared in Figure 7.3c,d. As can be noticed from 3D reconstructions, the as-printed surface is characterized by a consistent waviness, due to the layer-by-layer deposition strategy. After the milling process, the waviness was removed and the roughness significantly reduced, thus allowing to consider the surface substantially flat. The most significant surface roughness parameters of the polished specimen have been measured with stylus profilometry (Hommelwerke T200, 5 µm tip radius) and resulted equal to Ra=0.53±0.06 µm and Rz=5±0.12 µm.

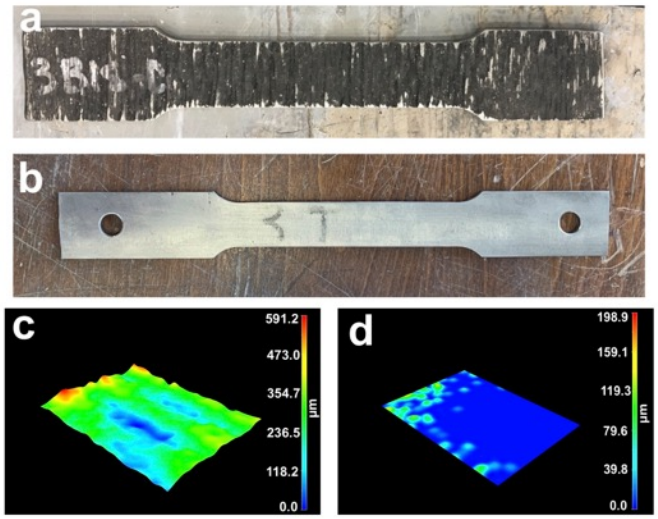

Figure 7.3: Tensile specimen cut from WAAM plates: (a) as-printed and (b) after milling; surface topography obtained with 3D-Digital Microscopy of the specimen (c) as-printed and (b) after milling

Tensile tests have been performed according to ISO 6892-1 [21] on a Universal testing machine of 500 kN load capacity. The specimens have been tested in displacement-control at a loading speed of 2 MPa s^{-1}. Two types of monitoring systems have been adopted: a linear deformometer of nominal dimension of 50 mm, to detect the linear deformation of the specimens up to yielding, and an optical-based system referred to as Digital Image Correlation (DIC), to acquire the full strain field during the whole test until failure. Before testing, the dimensions of the specimens have been measured by means of a digital caliper, in order to obtain the true values of cross-sectional area. A total number of 10 measures over the entire gauge length were measured and then averaged for each specimen. Elastic Modulus (E), 0.2% proof stress ($Rp_{0.2}$), ultimate tensile strength (UTS) and elongation to failure ($A_{\%}$) were evaluated from the engineering stress-strain curves. After the tensile tests, specimens fracture surfaces were analysed both at low magnification by 3D-digital microscopy and at higher magnification with SEM-EDS to investigate the specific failure mechanisms. Standard Vickers microhardness HV0.1 (100 g load and 15 s dwell time) measurements were carried out in the interlayer regions of U and A metallographic samples according to the test method described in ISO 6507 standard [22], with the aim to highlight local variations induced by the active cooling system.

The chemical composition of WAAM plates has been checked by Glow Discharge Optical Emission Spectroscopy (GDOES: GDA-650, Spectruma Analytik GmbH, Hof, Germany), with a sputtered burnt spot of 4 mm diameter. To relate the mechanical behavior with the specific microstructural features induced by the WAAM process, microstructure was investigated out by means of 3D-Digital Microscopy (Hirox KH-7700), Reflected Light Optical Microscopy (RLOM) and Scanning Electron Microscopy (SEM) equipped with energy dispersive X-ray spectroscopy (EDS). Samples for microstructural characterization have been cut from grip regions of L, T and D tensile specimens, according to the scheme shown in Figure 7.1. Samples were mounted in a phenolic resin, grounded with silicon carbide papers up to 1200 grits and finally polished according to ASTM E3 standard [23] up to 1 μm polycrystalline diamond suspension to obtain a mirror finish. Chemical etching with 20 s immersion in the Vilella's reagent (1 g picric acid, 5 mL hydrochloric acid and 100 mL ethanol [24]) was performed to highlight

microstructure. In addition, a specific colour etching was applied to highlight the presence of δ-ferrite phase, following the procedure described in [25].

7.1.3 Results and Discussion

COMPOSITION AND MICROSTRUCTURE

GD-OES compositional analysis was performed on A and U printed plates and results are reported in Table 7.2, where the composition of the feedstock wire is reported as well. Since type ER 308LSi is the common filler wire used in the conventional welding processes of austenitic stainless steel 304L, results of WAAM plates were also compared to the 304L (UNS-S-30403), whose chemical composition is still reported for an easy reference in Table 7.2. From the comparison, it can be inferred that the composition of WAAM samples meets the requirements of UNS-S-30403 for an AISI 304L chromium-nickel austenitic stainless steel. So, hereafter all results on the WAAM samples will be compared to the properties of 304L stainless steel.

Table 7.2: Results of the GD-OES composition analyses (wt.%) performed on the WAAM samples compared to the nominal chemical composition of the wire (given by the supplier) and 304L (UNS-S-30403) austenitic stainless steels according to ASTM A276 [26] respectively.

	Element (wt.%)											
	C	***Cr***	***Ni***	***Mn***	***Si***	***Co***	***V***	***Mo***	***Cu***	***P***	***S***	***Fe***
Wire	0.02	20	10	1.8	0.85	-	-	0.2	-	<0.025	<0.020	Bal.
WAAM A	0.01	19.5	9.6	1.7	0.6	0.5	0.11	0.02	0.02	0.022	0.011	Bal.
WAAM U	0.02	19.6	10.3	1.7	0.6	0.1	0.08	0.17	0.08	0.024	0.001	Bal.
304L	<0.03	18.0-20.0	8.0-12.0	<2.0	<1.0	-	-	-	-	<0.045	<0.03	Bal.

Values of Cr_{eq} and Ni_{eq} were calculated according to the Schaeffler and DeLong equations and compared to the respective diagrams, as reported in Figure 7.4. Both A and U should contain approximately 10-13 vol.% of δ-ferrite; in the next sections presence of δ-ferrite will be confirmed also by XRD analyses. According to the

phase diagram reported in Figure 7.5, type A+F solidification mode should be expected.

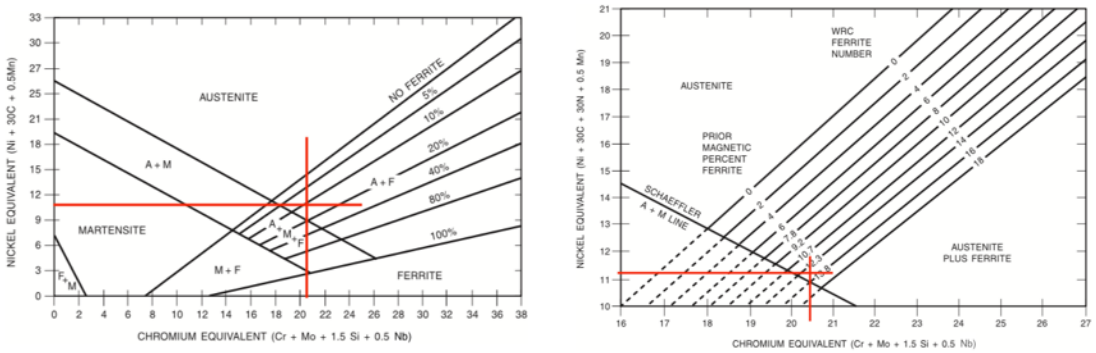

a b

Figure 7.4: a) Schaeffler and b) DeLong diagrams for the prediction of ferrite content and solidification structure; red lines indicate average Cr_{eq} and Ni_{eq} of WAAM plates as obtained from GD-OES measurements (adapted from [27]).

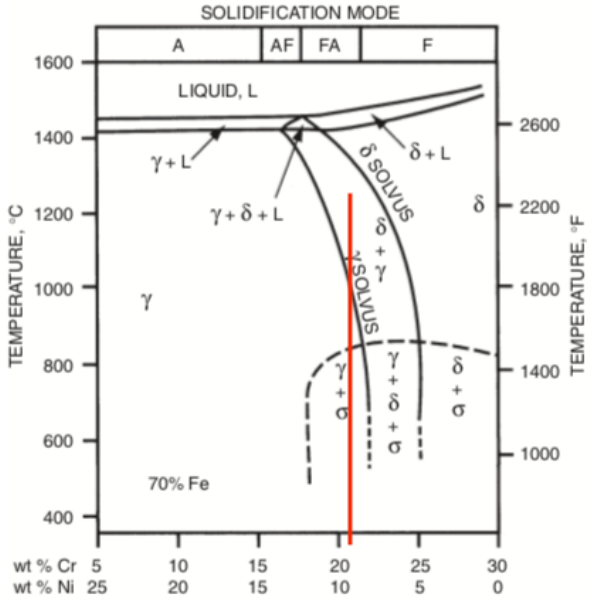

Figure 7.5: Vertical section of ternary-phase diagram at approximately 70% Fe where average composition of WAAM plates is evidence by red line [27].

Figure 7.6 shows the typical microstructure of WAAM processed 304L, obtained by 3D digital microscopy at relatively low magnification on metallographic samples extracted from the grip regions of T (Figure 7.6a), L (Figure 7.6b) and D (Figure 7.6c) tensile specimens, according to the scheme in Figure 7.1. No macroscopic defect (e.g. cracks, porosity, or lack of fusion) was evidenced by metallographic analyses in the majority of the as-printed samples between any two adjacent layers. Thus, the process resulted in mainly defect-free plates with a dense structure. The low magnification optical images in Figure 7.6 clearly show the typical hierarchical microstructure of additively manufactured parts, as discussed in Chapter 1, induced by the layer-by-layer process and the rapid solidification of the molten material. In the micrographs, deposition layers (approx. 1.5 mm) are highlighted by red lines, columnar grains (approx. 500 µm wide) by yellow lines and the fine columnar sub-structure within grains by green lines. Deposition layers are perpendicular, parallel and 45° oriented to loading direction in specimens T, L and D, respectively. The three-dimensional microstructure of samples can be seen in the reconstructions in Figure 7.7, that qualitatively report the orientation of melt pools and deposited layer along the three main sections of tensile specimens (xz, xy and yz planes). From three-dimensional micrographs, it is evident that fabrication of plates occurred as subsequent deposition of single layers of molten material, following unidirectional deposition strategy. Thus, each layer represents a solidified melt pool, whose typical semicircular shape can be recognized in transversal cross-sections (i.e. yz and xy planes).

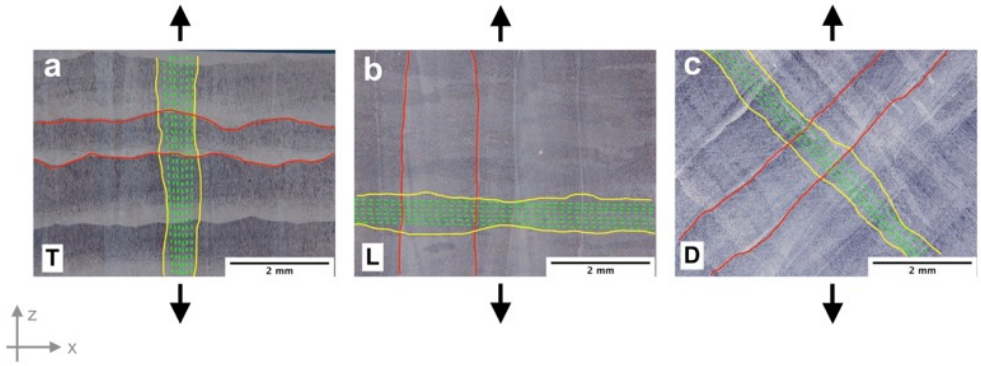

Figure 7.6: Representative low magnification 3D Digital micrographs of: a) transverse, b) longitudinal and c) diagonal tensile samples (Figure 7.1), where deposition layer, epitaxial grain growth and columnar sub-structure directions are highlighted by red, yellow and green lines, respectively; black arrows indicates the loading direction.

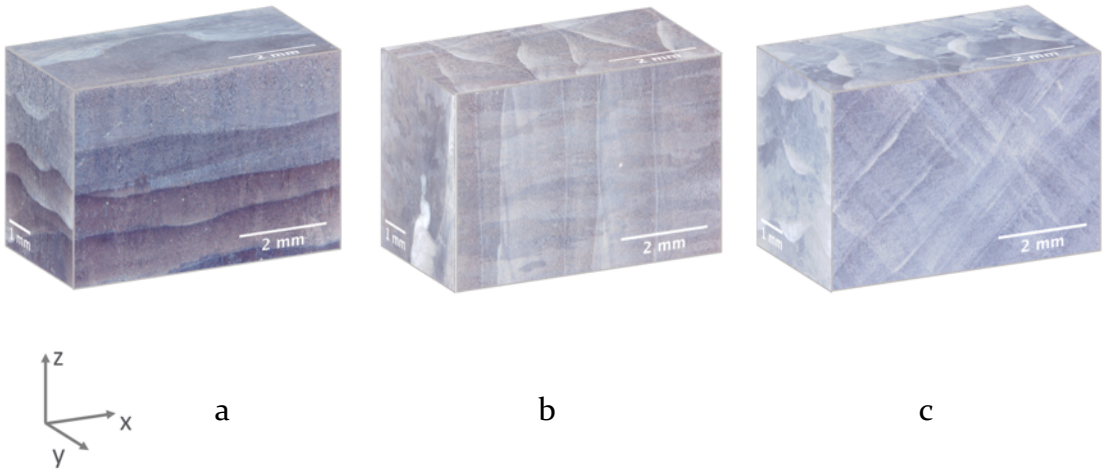

Figure 7.7: Three-dimensional microstructural reconstructions for: a) transverse, b) longitudinal and c) diagonal tensile samples

From the micrographs in Figures 7.6 and 7.7 it can also be appreciated that the macro morphology throughout the X-Z plane of the WAAM plate is dominated by columnar grains formed by epitaxial growth, with a preferential texture along the building direction (Z axis in Figure 7.1), perpendicular to the bottom substrate up to the top section. The extension of the grains across several deposition layers, has already been encountered in other studies concerning WAAM processes [11,28]. Indeed, such morphology is strictly dependent on the specific nature of WAAM technology, that essentially consists of an additive multi-pass welding process in which, during each deposition, the upper part of the former layer is re-melted. When solidification occurs, the grains follow an epitaxial growth with direction perpendicular to the solid/liquid interface, according to the maximum temperature gradient [29], as evidenced by Figure 7.8. In this figure, details of grains across layers are given in bright field and polarized light optical micrographs. High magnifications analyses of the interlayer region, with furthers detail of microstructure within epitaxial grains, are reported in Figure 7.9. As already reported by [30], the structure inside layers changes from the bottom to the top. A finer structure can be found in the bottom of the upper layer where cellular structure grows from the fusion line and develops in a columnar structure

while, in the upper part of the bottom layer, adjacent to the fusion line, a coarser columnar-dendritic structure can be found. To highlight this feature, the interlayer region is shown in Figures 7.9a,b, where a coarser columnar-dendritic sub-structure below the layer boundary and a finer columnar sub-structure above the boundary were revealed. Additional information regarding the columnar structure can be obtained by Figure 7.9c in which, due to the specific color etching, the presence of δ-ferrite was revealed by white regions. As previously described, solidification microstructure of austenitic stainless-steel welds is related to the composition of the alloy and, for the case studied, the welds should solidify with the γ-austenite being the primary or leading phase and the δ-ferrite located in the interdendritic spaces (Figures 7.4 and 7.5). This assumption is supported by microstructural results in Figure 7.9 where δ-ferrite was revealed inside the fine columnar-dendritic sub-structure developed during the WAAM process. It should be noticed that, despite the different cooling conditions, both U and A samples exhibited the same microstructural features at both low and high magnification analyses.

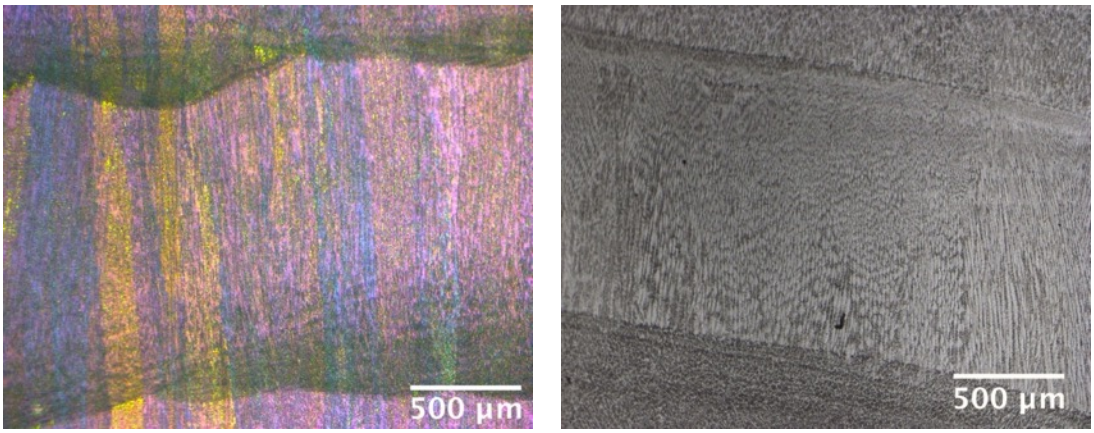

a b

Figure 7.8: Epitaxy across layers in the 304L WAAM plates: a) polarized light, b) bright field optical analyses.

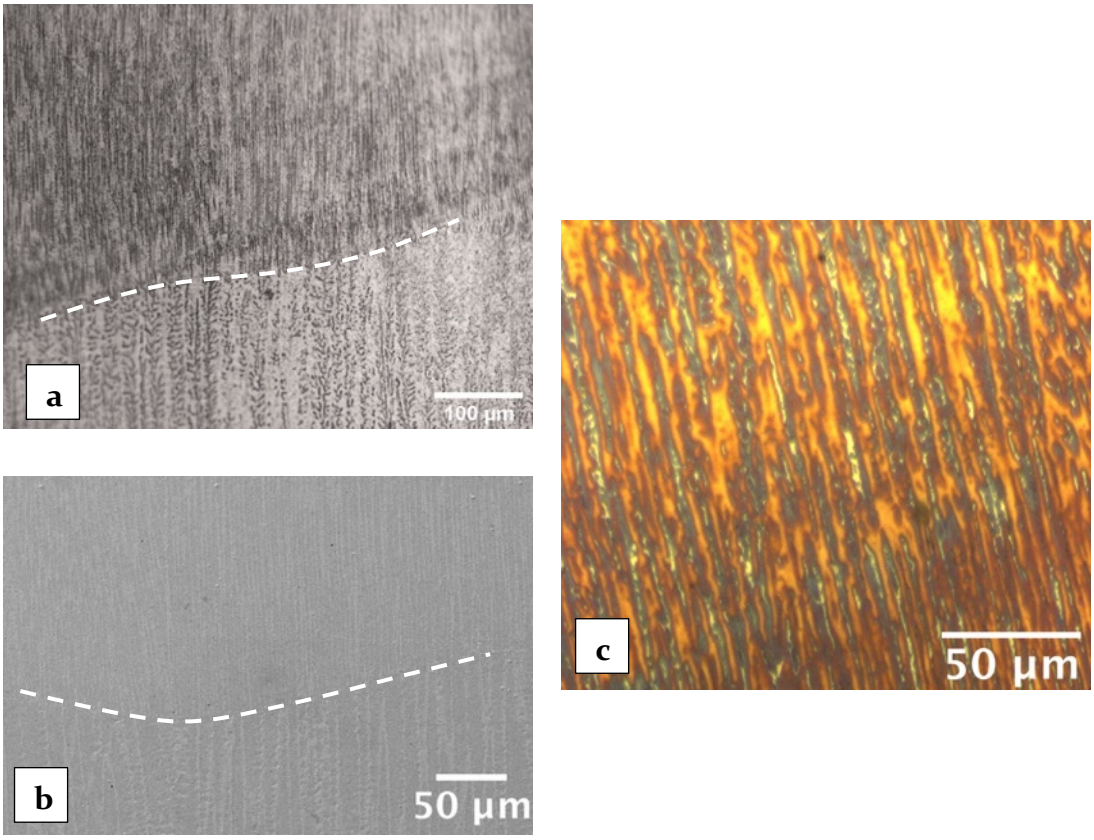

Figure 7.9: Detail of the columnar sub-structure in the 304L WAAM plates: a) and b) optical and SEM analyses of the interlayer region (white dashed line indicate layer boundary), c) δ-ferrite inside columnar structures evidenced by white zones.

As a consequence, the highly-oriented microstructure changes their morphology according to the different orientation considered by reference to the building direction. This aspect was already shown by low magnification micrographs in Figure 7.7. However, in order to highlight the anisotropy in the microstructure higher magnification analyses on xy, xz and yz planes of T, L and D specimens are reported in Figure 7.10. As showed by micrographs, microstructural features changed according to the considered planes: layers and interlayer boundaries (i.e. melt pool borders) are differently oriented along on xy, xz and yz planes and, consequently, also epitaxial grains and columnar sub-structure. Grains and sub-structure, in fact, appeared elongated on xz planes (Figure 7.10a-c) on all samples but, when different directions are considered, both grains and sub-structure appeared more equiaxed (e.g. Figure 7.10d,f,h,i).

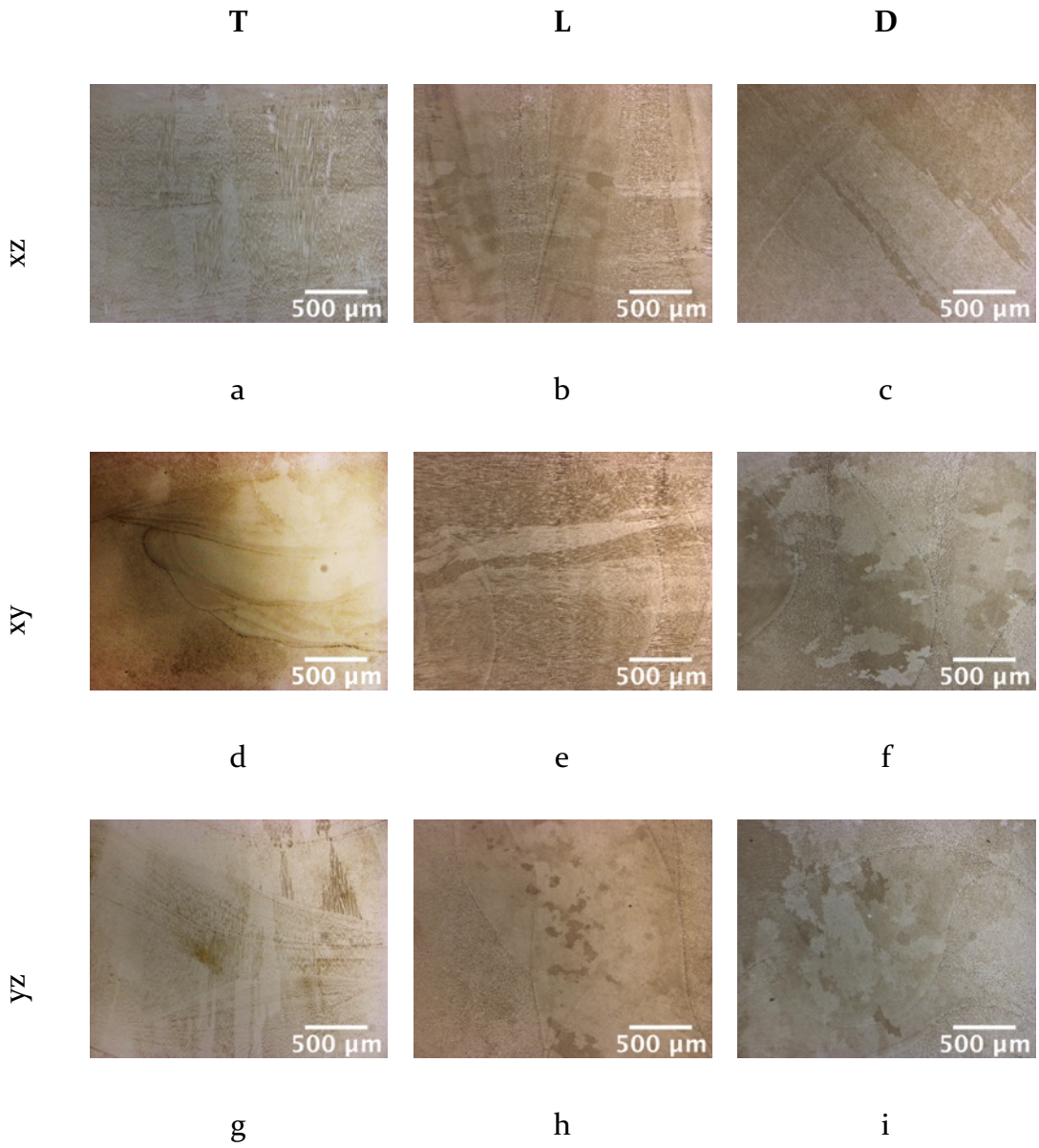

Figure 7.10: Representative OM micrographs showing anisotropy in the microstructural features of: a), d), g) transverse, b), e), h) longitudinal and c), f), i) diagonal tensile samples on xz, xy and yz planes as defined in Figure 7.7.

MECHANICAL CHARACTERIZATION

Results of tensile tests are reported in Figure 7.11 for both U and A specimens and for the three investigated orientations. Trends in mechanical properties for both U and A specimens are comparable and, by considering the standard deviations, also results are comparable. This outcome supports the above-discussed microstructural analyses and suggests that intercooling does not affect final properties of WAAM plates. A not negligible anisotropy in the mechanical behavior was instead found, with respect to specimen orientation. Specimens L and T exhibited similar mechanical properties, both in terms of 0.2% proof stress (about 350 MPa), ultimate tensile strength (in the range 510-580 MPa) and elongation to failure (20-34% with a high deviation). On the other hand, specimens D showed slightly higher tensile properties, with a 0.2% proof strength of about 400 MPa, an ultimate tensile strength higher than 580 MPa and 24-27% of elongation. Noteworthy is the influence of the specimen orientation in the values of Youngs modulus, much higher for specimens D (average value of 230 GPa) with respect to specimens L (average value of 130 GPa) and T (average value of 105 GPa).

Similar influence of specimens orientation in tensile results in terms Young modulus was reported by [31]. Although it has to be mentioned that the experiments were conducted on 316L stainless steel realized with LPBF process, thus the different orientations in [31] refer to different building directions, while in the present case L, T and D orientations refer to different extraction directions from the plate.

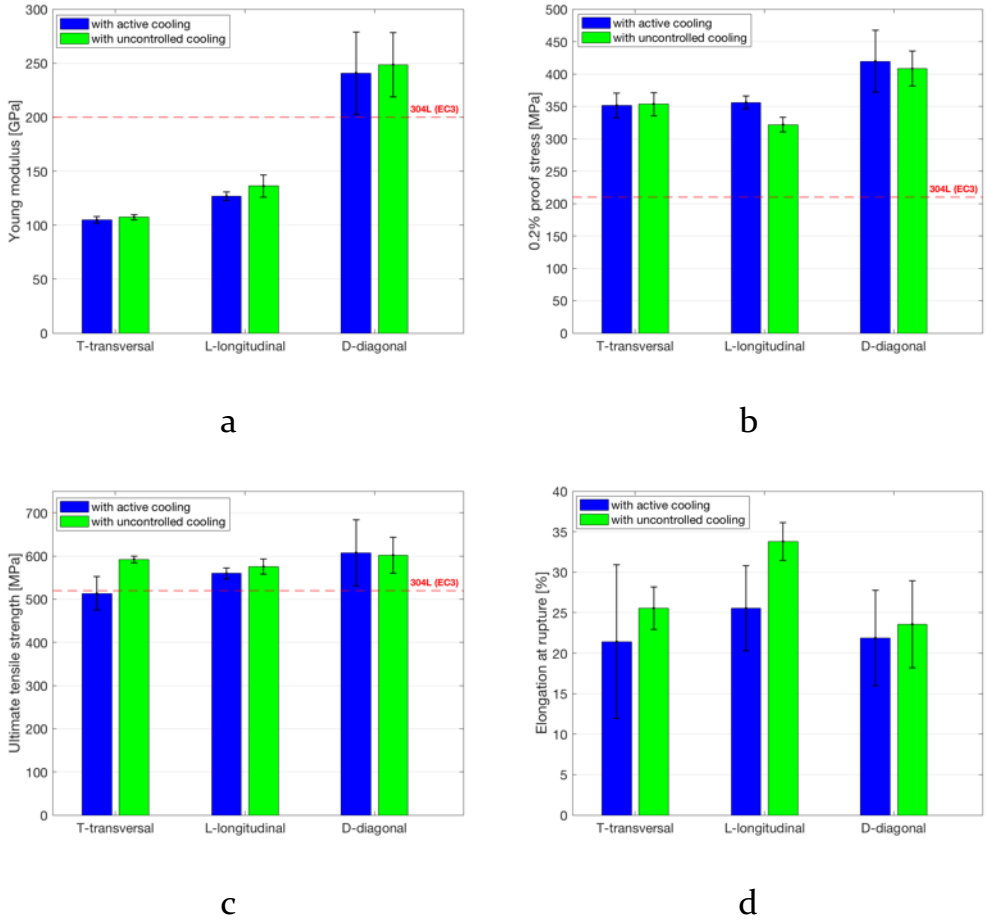

Figure 7.11: Results of the tensile tests on transversal, longitudinal and diagonal 304L WAAM specimens (see Figure 7.1): (a) Young modulus; (b) 0.2% proof stress; (c) ultimate tensile strength; (d) elongation to failure. In the diagram, reference values for the standard 304L according to Eurocode are also reported in red dashed lines

The observed anisotropy in the mechanical behavior of WAAM specimens might be related to the different grain orientations, with respect to the loading direction, as schematically shown in Figure 7.6. It is well known that under uniaxial tensile loading, plastic deformation of metals preferentially occurs along slip planes oriented at 45° with respect to the loading direction, where shear stress reaches the maximum value [32]. Hindering dislocation slip, which is responsible for plastic deformation, by proper strengthening mechanisms, allows increasing metals tensile strength. Several studies demonstrate that grain refinement is the most effective strengthening mechanisms, besides solid solution, in AM parts, enhancing both strength and toughness, due to the high solidification rates

induced by the process [33]. In the hierarchical microstructure typical of additively manufactured parts, the first obstacle to dislocation slip is the fine columnar sub-structure (few micrometers in case of present WAAM plates). The observed anisotropy in the tensile properties of WAAM 304L stainless steel samples should be likely related to the different orientations of this fine columnar sub-structure among T, L and D specimens, schematically shown in Figure 7.6. The superior tensile properties in terms of yield and ultimate tensile strength observed in D samples can be related to the highest density of cells boundaries along the main slip direction oriented at 45° to the tensile loading. It is worth noting that specimens D also exhibited the highest elastic modulus, clearly related to crystallographic and mechanical fibering, that are widely reported as the main reasons for the elastic anisotropy of metals [32,34] and will be discussed in the following sections. By comparing the results of the present study with the international standard building codes [35–37], it can be noted that 0.2% proof stress of the WAAM processed 304L steel is higher than the standard requested for the standard material, while the ultimate tensile strength is comparable. The strong difference is represented by the value of the Young modulus, as already discussed, higher for the D specimens while consistently lower than the one required by the standards in the case of L and T specimens.

Representative images of the tensile fracture surfaces, obtained by multi-focus microscopy at relatively low magnification, are shown in Figure 7.12, highlighting that no macroscopic defects were present in the majority of the tested samples. High magnification analyses were also carried out by SEM-EDS to better highlight specific microstructural features of the failure (Figure 7.13) and evidenced the presence of very small dimples, about 1 μm in size, in all the tested specimens, independently from specimen orientation, typical of a ductile failure. The fineness of the dimples (few micrometers in case of present WAAM plates) is clearly related to the corresponding very fine sub-structure induced by the WAAM process in the stainless steel.

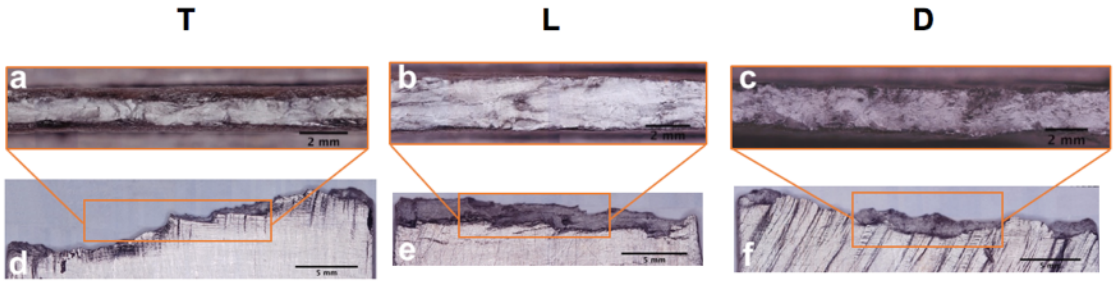

Figure 7.12 Low magnification micrographs obtained by 3D multifocus microscopy of the top and lateral view of the fracture region: a) and d) transversal, b) and e) longitudinal, c) and f) diagonal tensile samples

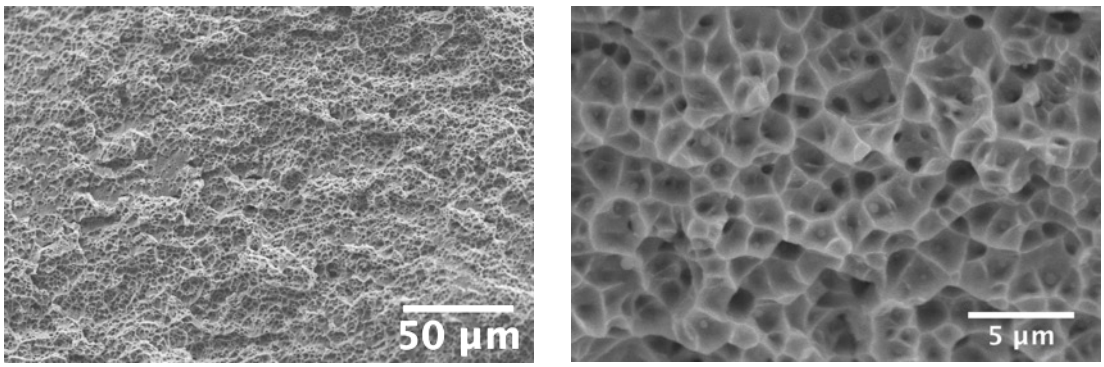

a b

Figure 7.13: SEM analyses of fracture surfaces of 304L WAAM specimens: representative low magnification (a) and high magnification (b) micrographs.

Vickers microhardness measurements (HV0.1) have been performed on metallographic L, T and D samples, and the results are reported in Figure 7.14. With the aim to assess the effect of the active cooling on the microstructure, micro-hardness was evaluated in the inter-layer region of samples, distinguishing the coarse columnar-dendritic structure at the top of the bottom layer from the fine cellular structure at the basis of the upper layer and the layer boundary. All samples exhibited a comparable value of hardness of approximately 250$HV_{0.1}$ and, by condidering standard deviation of experimental results, no difference can be evidenced either according to different inter-layer areas or cooling conditions. This outcome agrees with previously discussed microstructural analyses as well as tensile test results.

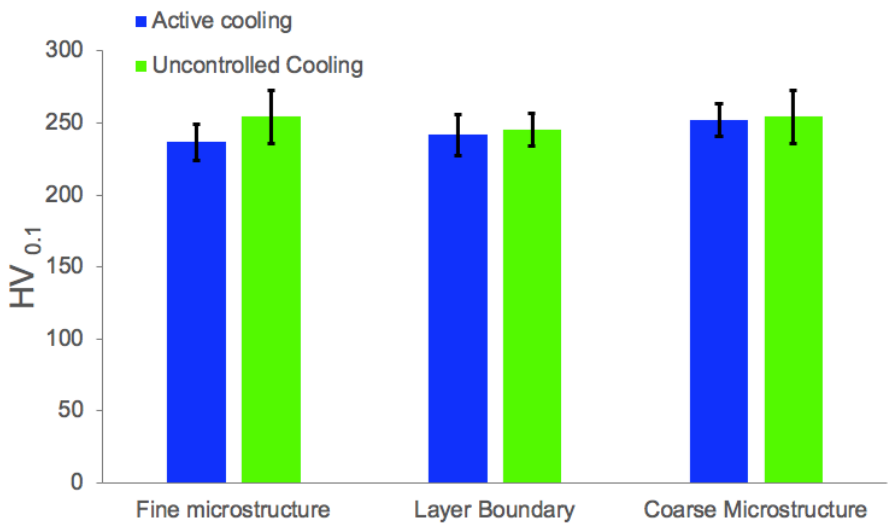

Figure 7.14: Micro-hardness (HV0.1) measurements carried out in the inter-layer regions of L, T and D samples extracted from AISI 304L WAAM plates processed with and without active cooling system.

7.1.4 Conclusions

Results of the experimental campaign aimed at characterizing static mechanical properties (Young modulus, yield and ultimate tensile strength, elongation to failure, hardness), chemical composition and microstructure of Wire-and-Arc Additive Manufacturing (WAAM) plates produced by ER308LSi wire are reported. The main goal is to draw some considerations on the effect of the forced cooling applied to each deposited layer on microstructure and related mechanical properties, and also on the potential anisotropic mechanical behavior induced by the specific microstructural feature induced by the WAAM properties. The following conclusions can be drawn:

- Chemical analysis showed that the printed material might be considered as a 304L stainless steel.
- Specimens for microstructural and mechanical characterization have been cut from 304L plates, with different orientations with respect to the

deposition layer: transversal direction (T), longitudinal direction (L), and diagonal direction (D).

- Microstructural analyses at different magnifications revealed a substantially defect-free, full-dense material, characterized by a hierarchical microstructure, typical of additively manufactured parts, structured in: deposition layers, epitaxial grains crossing over layers and a fine columnar sub-structure inside the epitaxial grains.
- Anisotropy in the tensile properties was observed, with the highest properties measured in D specimens. This behavior was related to the highest density of sub-structure boundaries hindering dislocation slip, that preferentially occurs at 45° with respect to the tensile loading direction. All the investigated samples showed a ductile failure mode, characterized by very small dimples on the fracture surfaces.
- No significant influence due to the forced cooling applied to each deposited layer was evidenced in microstructural, tensile and hardness analyses.
- Strong anisotropy in the Young modulus was also evidenced. This aspect will be further addressed in the following section.

7.2 Focus on elastic modulus

This section contains selected parts of the unpublished paper: "*Orthotropic elastic model for Wire-and-Arc Additively Manufactured stainless steel*", aimed at correlate the anisotropy evidenced in the Young modulus with the crystallographic texture.

7.2.1 Aim and scope

Giving the outcomes discussed in the previous section, further analyses were carried out by X-ray diffraction in order to highlight the correlation between microstructure and the marked anisotropy evidenced in the elastic modulus. The

previously presented microstructural analyses showed epitaxial columnar grains strongly oriented along the maximum thermal gradient. Thus, presumably, the microstructure is dominated by a preferential crystallographic orientation, as also evidenced by other authors [30,38]. Based on the intrinsic elastic anisotropy of the austenitic stainless steel crystal structure [39,40], the aim was to verify the presence of a preferred texture in WAAM L, T and D specimens and eventually correlate it to the elastic modulus obtained via tensile tests. It is well known, in fact, that the fcc-cubic crystal structure of stainless steels is anisotropic and its elastic modulus varies in the range of 101-297 GPa on the basis of the crystal direction, being <111> the stiffest direction and <100> the least stiff one [41]. For the conventional polycrystalline material, with no preferred orientation, the average value of 190-200 GPa is commonly adopted.

7.2.2 Experimental procedure

X-Ray diffraction (XRD: X'Pert PRO diffractometer, PANAlytical, Almelo, NL) was used to determine phase composition of T, L and D representative WAAM samples. Spectra were acquired with a Ni-filtered Cu-Kα radiation source in the range $40° < 2\theta < 100°$, with a step size of 0.02° and 120 s/step dwell time, using a 1D array of solid-state detector (X'Celerator PANAlytical). Acquired spectra were elaborated with HighScorePlus software (PANAlytical) for phase identification and peaks characterization, texture coefficients were then obtained following the procedure described by [42,43]. On polished and etched surface of a representative D metallographic specimen, EBSD analyses were also carried out using the Nova NanoSEM 450 device, which was equipped with a QC-200 i (Bruker) EBSD system featuring an e–Flash1000 detector. Samples, placed at an inclination of 70° with respect to the electron beam axis, were scanned at 15 kV acceleration voltage under low-vacuum (40 Pa) conditions in order to avoid charging drift of their non-conductive surfaces.

7.2.3 Results and discussion

Previously reported microstructural analyses evidenced the occurrence of epitaxial growth developed during the rapid solidification of each deposited layer all along the WAAM process. Accordingly, grain growth of each newly deposited layer followed the crystallographic orientation of the previously solidified one, resulting in a preferred texture. Therefore, crystal structure was analyzed with XRD, whose results are reported in Figure 7.15 for a set of representative samples. XRD spectra (Figure 7.15a) showed that, for all samples, the predominant phase was austenite (γ) with minor traces of delta-ferrite (δ), as already evidenced by the previous microstructure characterization.

The reference pattern for austenite (ICDD 33-0379) is characterized by five peaks corresponding to (111), (200), (220), (311), (222) crystallographic planes. However, as can be noticed by the XRD results for the investigated WAAM samples, none of the spectra exhibited the (222) austenite peak located at approximately 95.96° and, more importantly, samples showed different peaks characterized also by different intensities, suggesting the occurrence of a varied preferred orientation. Specifically, T, L and D directions showed two, four and three austenite peaks respectively. With the aim of quantifying such preferred crystallographic orientation, texture coefficients (TC) for the dominant γ-austenite phase were calculated. The results are reported in Figure 7.15b. If no preferred orientation exists, TC is equal to 1 for all crystallographic planes, while in case that one or more orientations prevail, TC assumes value higher than 1 for the dominant orientations. Data reported in Figure 7.15b show that T direction is dominated by (200) orientation, while for L directions (200) and (220) are more predominant.

It should be noticed that (111) peak was not revealed on T sample and was almost negligible for L one, while it prevails on D direction. From the results of the analysis of texture coefficients it can be inferred that a relationship between the Young modulus obtained with tensile tests and the preferred crystallographic orientation among samples exists. In particular, the dominant orientation of the stiffest direction D (E≃250 GPa) differs consistently from both L and T ones, which showed instead a much lower Young modulus, approximately 140 GPa and 110 GPa respectively.

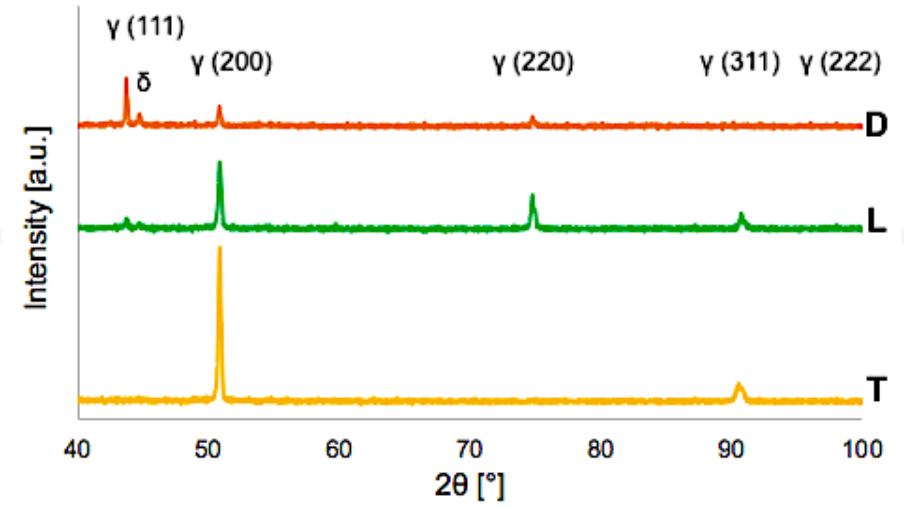

a

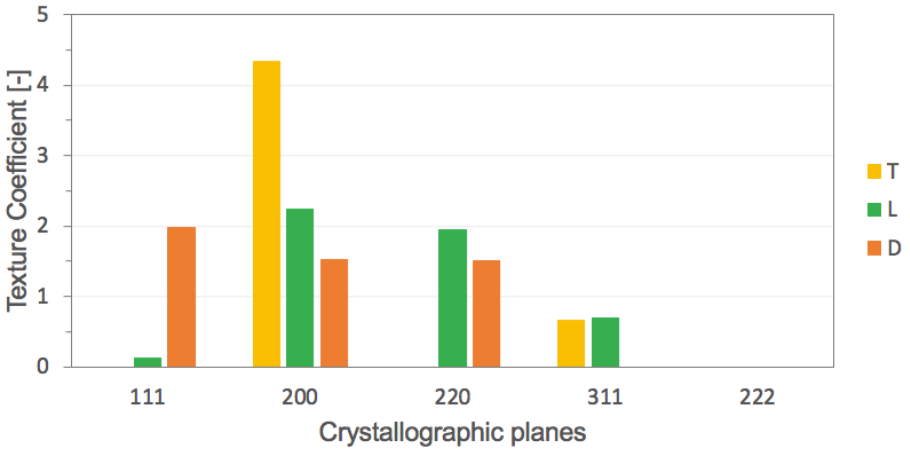

b

Figure 7.15: Results of XRD analyses: a) XRD spectra showing phase composition for transversal (T), longitudinal (L) and diagonal (D) specimens; b) texture coefficients for γ-austenite phase derived from spectra

The presence of a marked crystallographic preferential orientation in the γ-austenite phase was also confirmed by EBSD analyses. According to the inverse pole figures (IPF) and maps reported in Figure 7.16 for sample D, a texture oriented along the <111> crystallographic direction exists. This outcome further supports the above discussion, relating the highest stiffness exhibited by D direction with the stiffest crystallographic direction of the fcc stainless steel lattice structure.

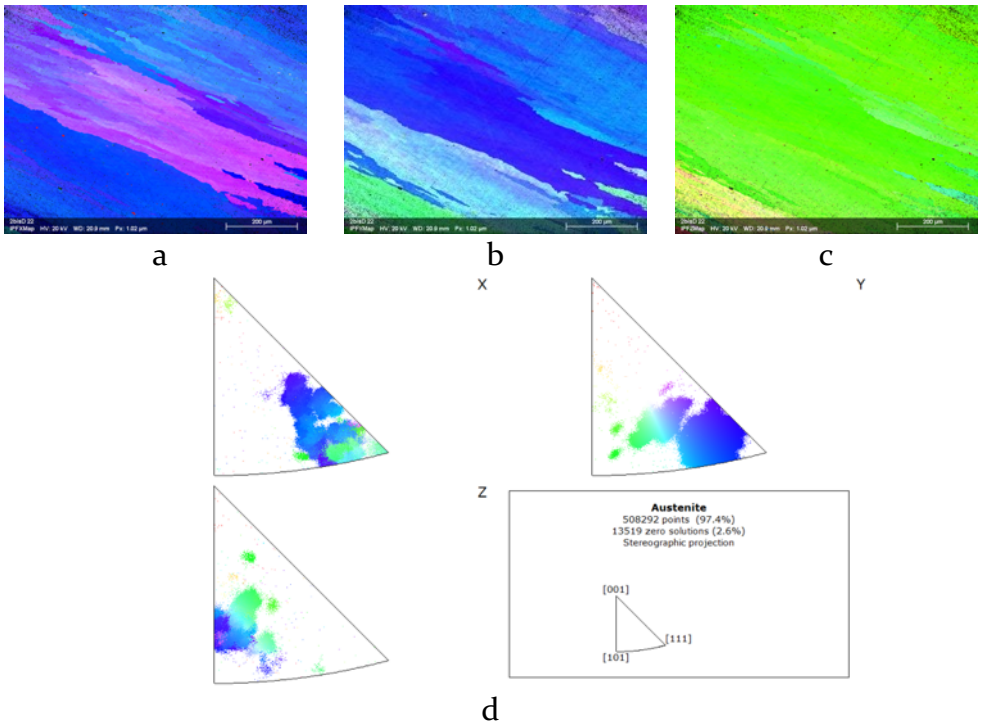

Figure 7.16: Inverse pole figures (IPF) from EBSD analyses for a representative D sample: a) IPFx map; b) IPFy map; c) IPFz map; d) relative IPF

7.2.4 Conclusions

The present work was aimed at highlighting the relationship between the peculiar microstructure induced by the WAAM process to the elastic properties, specifically the elastic modulus, along the directions parallel (L), perpendicular (T) and diagonal (D) with respect to the deposition layers of WAAM AISI 304L austenitic stainless-steel plates using X-ray diffraction and EBSD analyses. Based on the results, the following conclusions can be outlined:

- Analyses of texture coefficients, obtained via XRD analyses, confirmed the presence of crystallographic texture. Texture was different among L, T and D specimens. In particular, for T specimens, who exhibited the lowest elastic modulus (approx. 110 GPa), a predominance of (200) crystallographic plane was observed. For D specimens, whose modulus was approx. 250 GPa, the (111) plane was predominant, as also confirmed by EBSD analyses.
- Given the intrinsic anisotropy of the fcc crystal structure of austenitic stainless steels, whose elastic modulus ranges from 101-297 GPa on the basis of the crystal direction, a correlation between texture induced by WAAM processes and elastic modulus was found.

References

[1] K. V. Wong, A. Hernandez, A Review of Additive Manufacturing, ISRN Mech. Eng. 2012 (2012) 1–10. doi:10.5402/2012/208760.

[2] S.W. Williams, F. Martina, A.C. Addison, J. Ding, G. Pardal, P. Colegrove, Wire + Arc additive manufacturing, Mater. Sci. Technol. (United Kingdom). 32 (2016) 641–647. doi:10.1179/1743284715Y.0000000073.

[3] A. Uziel, Looking at large-scale, arc-based Additive Manufacturing, Weld. J. 4 (2016).

[4] C. Buchanan, V.P. Matilainen, A. Salminen, L. Gardner, Structural performance of additive manufactured metallic material and cross-sections, J. Constr. Steel Res. 136 (2017) 35–48. doi:10.1016/j.jcsr.2017.05.002.

[5] T. DebRoy, H.L. Wei, J.S. Zuback, T. Mukherjee, J.W. Elmer, J.O. Milewski, A.M. Beese, A. Wilson-Heid, A. De, W. Zhang, Additive manufacturing of metallic components – Process, structure and properties, Prog. Mater. Sci. 92 (2018) 112–224. doi:10.1016/j.pmatsci.2017.10.001.

[6] Y. Zhang, L. Wu, X. Guo, S. Kane, Y. Deng, Y. Jung, J. Lee, J. Zhang, Additive Manufacturing of Metallic Materials : A Review, J. Mater. Eng. Perform. 27 (2018) 1–13. doi:10.1007/s11665-017-2747-y.

[7] I.S. Kim, K.J. Son, Y.S. Yang, P.K.D.V. Yaragada, Sensitivity analysis for process parameters in GMA welding processes using a factorial design method, Int. J. Mach. Tools Manuf. 43 (2003) 763–769. doi:10.1016/S0890-6955(03)00054-3.

[8] M. Dinovitzer, X. Chen, J. Laliberte, X. Huang, H. Frei, Effect of wire and arc additive manufacturing (WAAM) process parameters on bead geometry and microstructure, Addit. Manuf. 26 (2019) 138–146. doi:10.1016/j.addma.2018.12.013.

[9] X. Xu, S. Ganguly, J. Ding, S. Guo, S. Williams, F. Martina, Microstructural evolution and mechanical properties of maraging steel produced by wire + arc additive manufacture process, Mater. Charact. 143 (2018) 152–162. doi:10.1016/j.matchar.2017.12.002.

[10] J. Ge, J. Lin, Y. Chen, Y. Lei, H. Fu, Characterization of wire arc additive manufacturing 2Cr13 part: Process stability, microstructural evolution, and tensile properties, J. Alloys Compd. 748 (2018) 911–921. doi:10.1016/j.jallcom.2018.03.222.

[11] J. V. Gordon, C. V. Haden, H.F. Nied, R.P. Vinci, D.G. Harlow, Fatigue crack growth anisotropy, texture and residual stress in austenitic steel made by wire and arc additive manufacturing, Mater. Sci. Eng. A. 724 (2018) 431–438. doi:10.1016/j.msea.2018.03.075.

[12] W. Wu, J. Xue, L. Wang, Z. Zhang, Y. Hu, C. Dong, Forming process, microstructure, and mechanical properties of thin-walled 316L stainless steel using speed-cold-welding additive manufacturing, Metals (Basel). 9 (2019). doi:10.3390/met9010109.

[13] N. Rodriguez, L. Vázquez, I. Huarte, E. Arruti, I. Tabernero, P. Alvarez, Wire and arc additive manufacturing: a comparison between CMT and TopTIG processes applied to stainless steel, Weld. World. 62 (2018) 1083–1096. doi:10.1007/s40194-018-0606-6.

[14] L. Ji, J. Lu, C. Liu, C. Jing, H. Fan, S. Ma, Microstructure and mechanical properties

of 304L steel fabricated by arc additive manufacturing, MATEC Web Conf. 128 (2017). doi:10.1051/matecconf/201712803006.

[15] C. V. Haden, G. Zeng, F.M. Carter, C. Ruhl, B.A. Krick, D.G. Harlow, Wire and arc additive manufactured steel: Tensile and wear properties, Addit. Manuf. 16 (2017) 115–123. doi:10.1016/j.addma.2017.05.010.

[16] L. Gardner, P. Kyvelou, C. Buchanan, TESTING OF WIRE AND ARC ADDITIVELY MANUFACTURED TUBULAR SECTIONS, (2019) 978–981. doi:10.3850/978-981-11-0745-0.

[17] F. Hejripour, F. Binesh, M. Hebel, D.K. Aidun, Thermal modeling and characterization of wire arc additive manufactured duplex stainless steel, J. Mater. Process. Technol. 272 (2019) 58–71. doi:10.1016/j.jmatprotec.2019.05.003.

[18] MX3D Webpage, (n.d.).

[19] Oerlikon, (n.d.).

[20] U. Reisgen, R. Sharma, S. Mann, L. Oster, Increasing the manufacturing efficiency of WAAM by advanced cooling strategies, Weld. World. 64 (2020) 1409–1416. doi:10.1007/s40194-020-00930-2.

[21] ISO 6892 Metallic materials - Tensile testing, (2019) 54.

[22] EN ISO 6507 Metallic materials – Vickers hardness test, (2018).

[23] ASTM International, E3 Preparation of Metallographic Specimens, Annu. B. ASTM Stand. 11 (2017) 1–17. doi:10.1520/E0003-11R17.1.

[24] G.F. Vander Voort, G.M. Lucas, E.P. Manilova, Metallography and microstructures of stainless steels and maraging steels, Mater. Park. OH ASM Int. (2004) 670–700.

[25] D.W. Hetzner, Etching stainless steels for delta ferrite, Adv. Mater. Process. 165 (2007) 33–34.

[26] ASTM A276-16, Standard Specification for Stainless Steel Bars and Shapes, ASTM Int. (2016) 1–8. doi:10.1520/A0276.

[27] Stainless and heat-resistant steels, in: AWS Weld. Handb. - Vol. 4, American Welding Society (AWS), n.d.

[28] X. Xu, G. Mi, Y. Luo, P. Jiang, X. Shao, C. Wang, Morphologies, microstructures, and mechanical properties of samples produced using laser metal deposition with 316 L stainless steel wire, Opt. Lasers Eng. 94 (2017) 1–11. doi:10.1016/j.optlaseng.2017.02.008.

[29] W.J. Sames, F.A. List, S. Pannala, R.R. Dehoff, S.S. Babu, The metallurgy and processing science of metal additive manufacturing, Int. Mater. Rev. 6608 (2016) 1–46. doi:10.1080/09506608.2015.1116649.

[30] L. Wang, J. Xue, Q. Wang, Correlation between arc mode, microstructure, and mechanical properties during wire arc additive manufacturing of 316L stainless steel, Mater. Sci. Eng. A. 751 (2019) 183–190. doi:https://doi.org/10.1016/j.msea.2019.02.078.

[31] L. Hitzler, J. Hirsch, B. Heine, M. Merkel, W. Hall, A. Öchsner, On the anisotropic mechanical properties of selective laser-melted stainless steel, Materials (Basel). 10 (2017). doi:10.3390/ma10101136.

[32] G.E. Dieter, D.J. Bacon, Mechanical metallurgy, McGraw-hill, 1986.

[33] E.W. Hovig, A.S. Azar, F. Grytten, K. Sørby, E. Andreassen, Determination of anisotropic mechanical properties for materials processed by laser powder bed fusion, Adv. Mater. Sci. Eng. 2018 (2018). doi:10.1155/2018/7650303.

[34] T.H. Courtney, Mechanical behavior of materials, Waveland Press, 2005.

[35] EN 1993 1-4: Eurocode 3: Design of steel structures, part 1-4: General rules, supplementary rules for stainless steel, (2015).

[36] AS/NZS 4673: Cold-formed stainless steel structures, (2001).

[37] SEI/ASCE 08-02: Specification for the design of cold-formed stainless steel structural members, (1991).

[38] P. Kyvelou, H. Slack, D.D. Mountanou, M.A. Wadee, T. Ben Britton, C. Buchanan, L. Gardner, Mechanical and microstructural testing of wire and arc additively manufactured sheet material, Mater. Des. 192 (2020) 108675. doi:10.1016/J.MATDES.2020.108675.

[39] H.M. Ledbetter, Monocrystal-Polycrystal Elastic Constants of a Stainless Steel, Phys. Status Solidi. 85 (1984) 89–96. doi:10.1002/pssa.2210850111.

[40] H.M. Ledbetter, Predicted monocrystal elastic constants of 304-type stainless steel, Phys. B+C. 128 (1985) 1–4. doi:https://doi.org/10.1016/0378-4363(85)90076-2.

[41] B. Hutchinson, Critical assessment 16: Anisotropy in metals, Mater. Sci. Technol. (United Kingdom). 31 (2015) 1393–1401. doi:10.1179/1743284715Y.0000000118.

[42] P. Saikia, A. Joseph, R. Rane, B.K. Saikia, S. Mukherjee, Role of substrate and deposition conditions on the texture evolution of titanium nitride thin film on bare and plasma-nitrided high-speed steel, J. Theor. Appl. Phys. 7 (2013) 66. doi:10.1186/2251-7235-7-66.

[43] M. Liu, H. Liu, D. Wang, B. Liu, Y. Shi, F. Li, Y. Gong, L. Li, L. Li, W. Zhang, Effect of nanodiamond concentration and the current density of the electrolyte on the texture and mechanical properties of Ni/Nanodiamond composite coatings produced by electrodeposition, Materials (Basel). 12 (2019). doi:10.3390/ma12071105.

Chapter 8

WIRE-AND-ARC ADDITIVE MANUFACTURING OF ALUMINUM ALLOYS

A LITERATURE REVIEW

8.1 Aluminum Magnesium wrought alloys

The Al-Mg wrought alloys belong, according to the IADS designation system, to the 5xxx series in which Mg content is in the range 0.8 – 5 wt.%. Al-Mg alloys are non-heat treatable, thus they cannot be strengthened by solution treatment and aging, as for others Al alloys such as the Al-Si-Mg ones discussed in Chapters 4 and 5. Consequently, strengthening of these alloys is achieved via solid solution and cold working. As reported in Figure 8.1, Mg is indeed quite effective as solid solution hardener and, among the non-heat-treatable aluminum wrought alloys, the 5xxx series are characterized by the highest ultimate tensile strength, ranging from 125 to 435 MPa depending on the temper condition (O annealed or H strain hardened) [1].

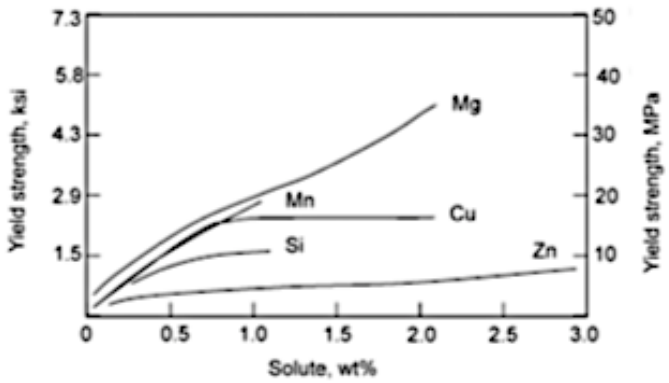

Figure 8.1: Effect of main alloying elements in solid solution strengthening of pure aluminum in the annealed condition [1]

Al-Mg alloys also exhibit a high toughness, even at cryogenic temperatures. Main applications of this series include: cryogenic tanks, pressure vessels, automotive components, cans, crane ad streetlight parts. By reason of their good corrosion resistance, even in salt water conditions, they are also widely used in the shipbuilding industries [1]. However, in case of alloys with a high Mg content, the formation of continuous β-Mg_3Al_2 precipitates at grain boundaries, occurring in heavily cold-worked exposed to temperatures from 120 to 200 °C, must be avoided as it can lead to intergranular corrosion.

Alloys of the 5xxx series are difficult and expensive to extrude and, consequently, they are commercialized in form of plates and sheets obtained via cold working. Nevertheless, they are also characterized by a good weldability, as will be later discussed [2].

8.1.1 Welding of non-heat-treatable aluminum wrought alloys

Joining of wrought aluminum parts (sheets, plates, rods, bars, extrusions, ecc…) can be obtained by welding, especially fusion welding, as aluminum alloys are characterized by a good weldability. However, a few issues have to be addressed [1]:

- Oxide formation
- Hydrogen solubility
- Cracking sensitivity
- Electrical Conductivity
- Thermal conductivity
- Thermal expansion

Many of the issues listed above have been already examined in Chapter 4 when discussing the LPBF of aluminum alloys, since aspects like oxides formation, high hydrogen solubility and thermal conductivity represents major concerns for this

material. The natural thin oxide film that forms on the surface of aluminum has to be removed before welding, as: i) melting temperature of aluminum oxide is approx. 2050 °C (while pure aluminum undergoes melting at 660 °C); ii) oxides fragments can be entrapped in the weld and affect ductility or promote porosity and crack formation; iii) since the oxide is an electrical insulator it can prevent arc initiation for electrical arc-based processes. As hydrogen dissolves very rapidly in molten aluminum and has almost no solubility at the solid state (Figure 8.2), any potential source of hydrogen has to be carefully avoided, such as: moisture and lubricants of the filler wire, moisture in the shielding gas or any potential water leaks in the equipment. The natural aluminum oxide is thin and porous but, if it adsorbs water (hydrated oxide), might grow in thickness and acts as potential source for porosity formation [2]. Alloys of the 5xxx series are the most prone to form a hydrated oxide on the surface of the filler wire or base metal, thus particular attention has to be paid to storing the material in a controlled atmosphere [1].

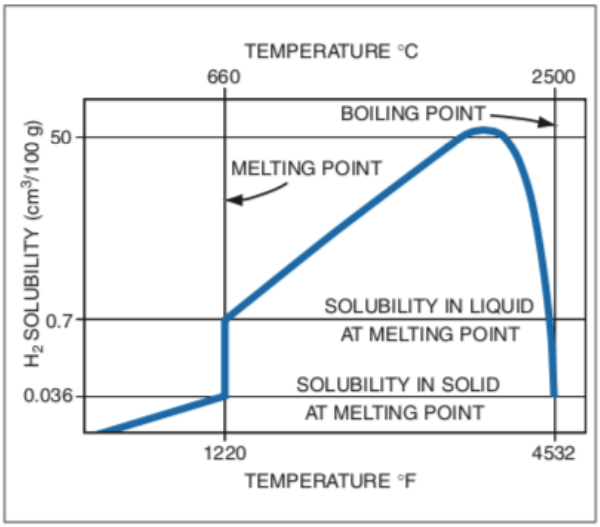

Figure 8.2: Hydrogen solubility in aluminum [2]

Aluminum has a high thermal conductivity and requires high heat input to undergo melting, even if the melting temperature is lower than other material, like steels. It is also characterized by a high thermal expansion that can results in warping, distortions and deformations if the welding process is not properly

designed. On the other hands, the high electrical conductivity favors the arc-based welding processes.

Attention must be paid also to crack sensitivity of aluminum alloys, strongly influenced by the solidification range, beside grain size. Cracking developed during welding of aluminum alloys are hot cracking that, as already reported in Chapter 4, occurs at the last stages of solidification when mushy region cannot withstand to the imposed local stresses, thus forming intergranular cracks. The alloy chemical composition defines the solidification ranges and so determines the cracking sensitivity. Accordingly, crack sensitivity curves (Figure 8.3) have been developed in order to estimate the tendency of the alloy to incur cracking formation. Based on these curves, the proper filler wire can be chosen with the aim to reduce cracking sensitivity, especially for those alloys with a high cracking sensitivity, as Al-Cu (2xxx series) alloys. In case of Al-Mg alloys, cracking sensitivity becomes negligible if Mg content is higher than 5 wt.%.

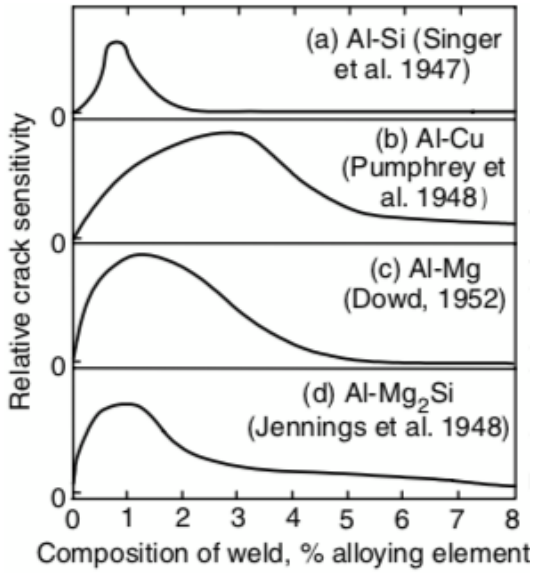

Figure 8.3: Cracking sensitivity of aluminum alloys as a function of alloy elements content [3]

Cracking sensitivity can be strongly reduced by adopting the proper combination of base metal and filler wire, as shown in Figure 8.4. Table 8.1 reports the advisable filler wire to be adopted for non-heat-treatable alloys.

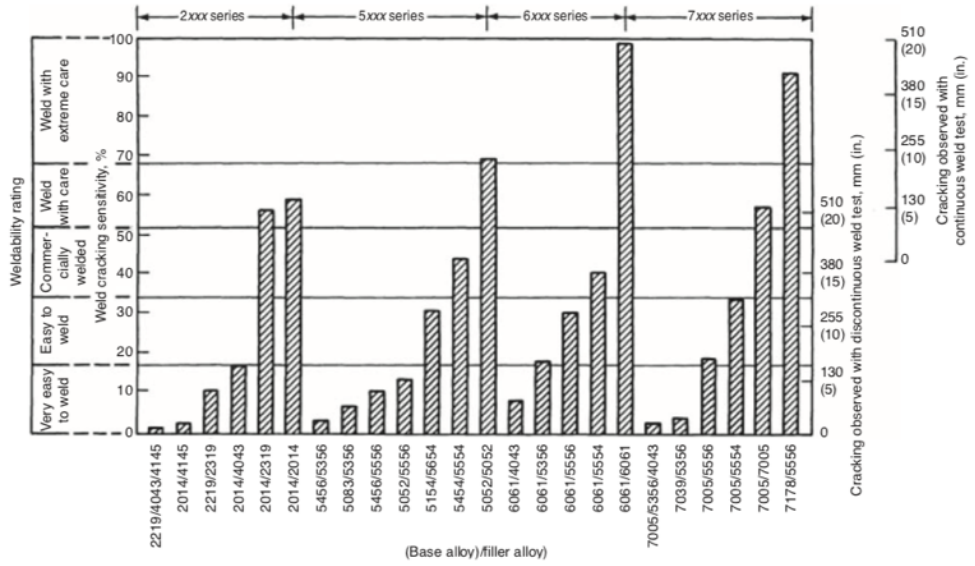

Figure 8.4: Selection of base metal/filler wire to avoid or limit cracking formation [4]

Table 8.1: Guidelines for alloy-filler selection for non-heat-treatable alloys [4]

Base metal	***Filler wire***
1xxx (pure Al)	1xxx (pure Al) or 4xxx (Al-Si)
3xxx (Al-Mn)	1xxx (pure Al) or 4xxx (Al-Si)
5xxx (Al-Mg, low Mg)	5xxx (Al-Mg) or 4xxx (Al-Si)
5xxx (Al-Mg, high Mg)	5xxx (Al-Mg)

8.1.2 The AlMg4.5Mn alloy

The experimental activity, described in the following chapter, focused on the Al-4.5Mg alloy (AA 5083 according to IADS) used in the WAAM process. This is a moderate-strength weldable alloy developed in 1950s specifically to shipbuilding applications but it is currently widely used also in the automotive field [5]. The nominal chemical composition is reported in Table 8.2 while typical mechanical properties at various temperature for the O temper condition, similar to those of welds, are summarized in Table 8.3.

Table 8.2: Al-4.5Mg-Mn alloy: designations, according to International Alloy Designation System (IADS) [6] and EURONORM (EN) [7–9] system, and nominal chemical composition according to [5].

Designation			***Element (wt.%)***									
IADS	***EN Chemical***	***EN Numerical***	***Al***	***Si***	***Mg***	***Mn***	***Fe***	***Cu***	***Ti***	***Zn***	***Cr***	***Other***
5083	EN-AW Al4.5MgMn	EN-AW 5083	Bal.	0.4 max	4 – 4.9	0.4 – 1.0	0.4 max	0.1 max	0.15 max	0.25	0.05-0.25	0.15

Table 8.3: Typical mechanical properties at various temperature for the Al4.5MgMn annealed alloy [5].

Temperature [°C]	***Tensile properties***		
	Ys [MPa]	***UTS [MPa]***	***A%***
-195	405	165	36
-80	295	145	30
-30	290	145	27
25	290	145	25
100	275	145	36
150	215	130	50
205	150	115	60
260	115	75	80
315	75	50	110
370	41	29	130

As already mentioned, this alloy is characterized by a good corrosion resistance, that makes it suitable for marine applications, but it can be susceptible to stress-corrosion cracking.

8.2 WAAM of Aluminum alloys

The scientific research of WAAM applied to aluminum alloys in confined to the last two-three years, and was primarily focused on the 2xxx (such as 2319, 2219, 2024, 2050 alloys) [10–14] and 5xxx (5083, 5183, 5087, 5356) series [15–20]. As a consequence of the afore-mentioned issues in welding of aluminum alloys, also WAAM is quite challenging [21]. As depicted in Figure 8.5, porosity is a severe problem in WAAM aluminum components, followed by deformations, residual stress, cracks and oxidation. Surface quality and delamination represent, instead, minor concerns.

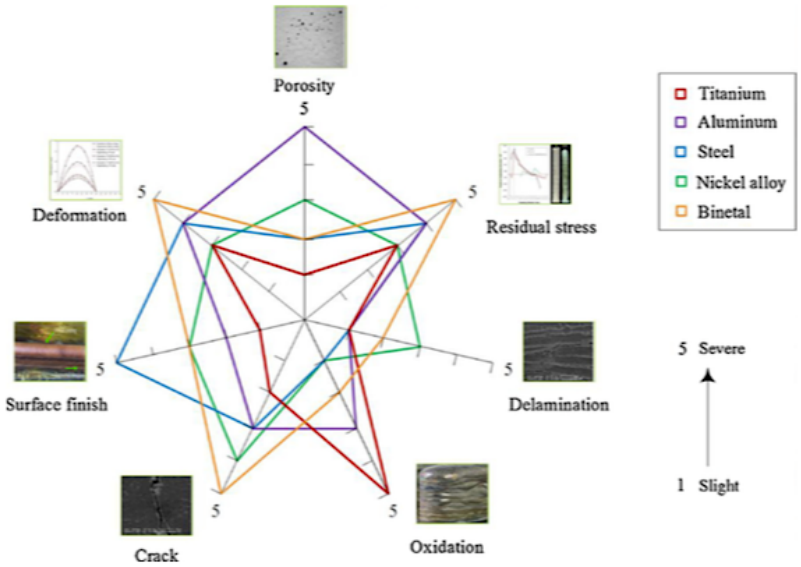

Figure 8.5: Defects encountered in the WAAM of several materials [22]

As highlighted by the topical review by S. Thapliyal [21], advanced processes like interlayer rolling or Cold Metal Transfer (CMT) technology might be adopted in order to limit the extent of defects and improve the quality of WAAM parts.

The deformation induced by inter layer rolling promotes the reduction of porosity and such reduction is a function of the applied pressure. Gu et al. [23] verified that a 45 kN load applied between layers was sufficient to eliminate the porosity content in both AA2319 and AA5087 alloys. The effect of the interlayer rolling in pore reduction and grain refinement can be appreciated from microstructural analyses reported in Figures 8.6 and 8.7.

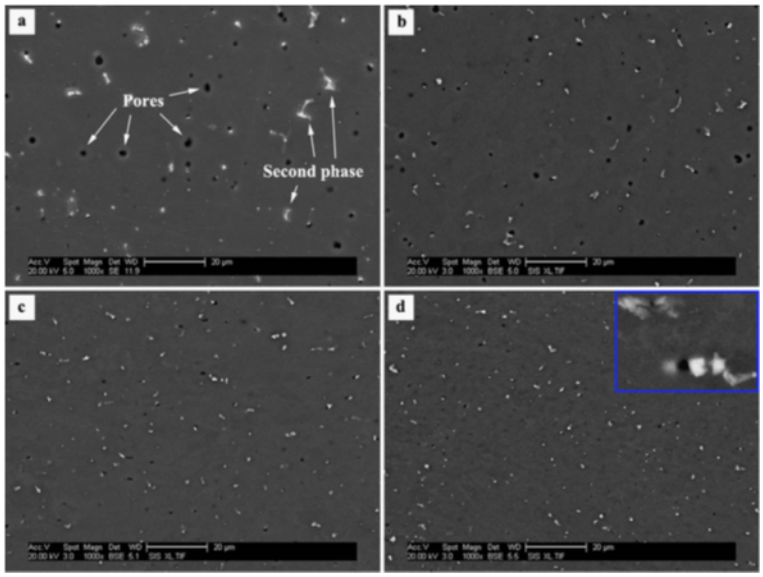

Figure 8.6: SEM micrographs for WAAM 5087 alloy in the as-deposited condition (a) and after interlayer rolling at 15 kN (b), 30 kN (c), 45 kN (d) [23].

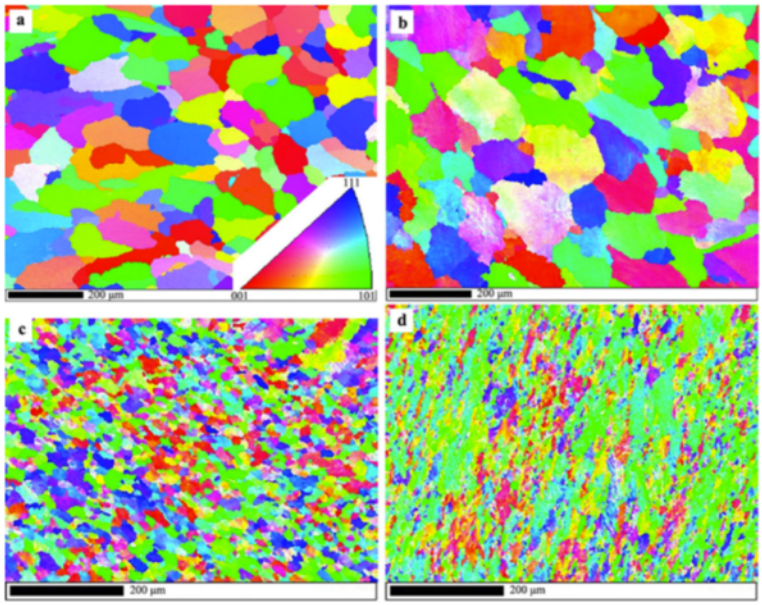

Figure 8.7: EBSD analyses for WAAM 5087 alloy in the as-deposited condition (a) and after interlayer rolling at 15 kN (b), 30 kN (c), 45 kN (d) [23].

However, the application of a dedicated interlayer rolling can be easily applied for simple geometries while, for complex structure, resorting to this technology may become less convenient.

CMT is instead a variation of the GMAW process, patented by Fronius Ldt, in which both heat input and spatter ejection are controlled and minimized. A lower heat input, indeed, leads to lower peak temperatures and lower hydrogen dissolution, thus gas entrapment and porosity are reduced. Another variation of the CMT process is the pulse advance mode (CMT-PADV), that results in fine grain structures and pores elimination [21,24]. Furthermore, another variation of CMT called variable polarity cold metal transfer (VP-CMT) resulted, for the Al-6Mg alloy, in obtaining equiaxed grains (Figure 8.8) and a tensile strength of 333 MPa [18], comparable to the conventional wrought alloy. This unprecedented result is quite encouraging as one of major drawbacks of WAAM is related to the low achievable mechanical properties with respect to the wrought counterparts [21,24,25].

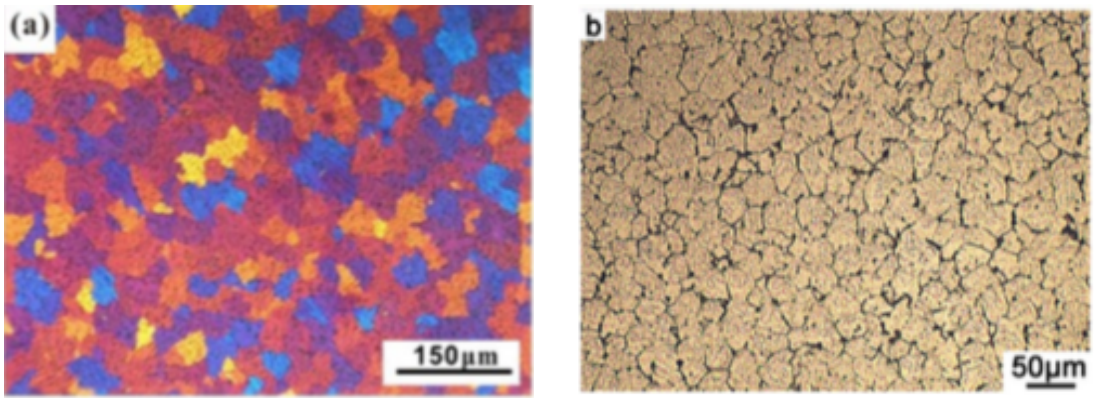

Figure 8.8: Equiaxed grain formed in the CMT of the: a) AA5183 and b) Al6Mg alloy [18,26].

When present, pores and cracks tend to lie in the interlayer region, as shown in Figure 8.9.

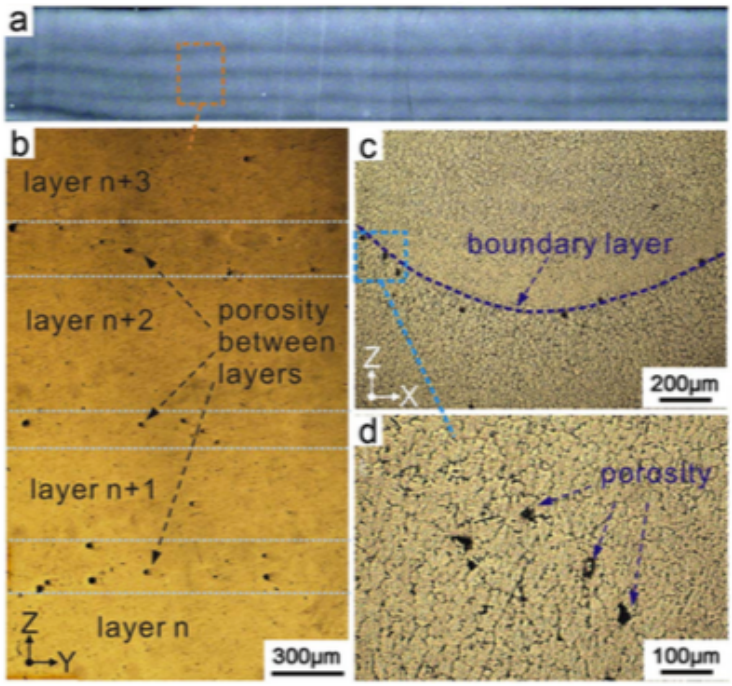

Figure 8.9: Microstructural analyses of Al6Mg alloy showing defects in the interlayer regions: a) macrographs of the deposited plate, b) low magnification optical micrograph, c) high magnification optical micrograph on the interlayer region, d) detail of porosity on layer boundary [18]

Mechanical properties reported in the literature for the WAAM Al-Mg alloys are synthetized in Table 8.4, as a function of process type and specimen extraction direction with respect to the deposited layers, being longitudinal if extracted parallelly to the layers, and transversal if extracted perpendicularly. As can be noticed from the table, different process parameters and alloys were adopted in the literature works, thus a direct comparison is hardly achievable. However, as a general consideration, no marked anisotropy was found when the longitudinal and transversal orientations were considered, even if the transversal direction was always characterized by a slightly lower ultimate tensile strength. By comparing the AA5183 alloy processed by GMAW and CMT, it can be noticed that analogous results were reported, proving that even if CMT is often recommended for the WAAM of aluminum alloys, comparable results can also be obtained with the conventional GMAW process. On the contrary, by focusing on the AA5987 alloys, the GTAW process resulted in poor mechanical properties, especially if compared to the same alloy processed with CMT.

Table 8.4: Literature review of mechanical properties for the WAAM Al-Mg alloys

Process type	Alloy	Specimen orientation	E [GPa]	$R_{po.2}$ [MPa]	UTS [MPa]	A% [%]	Reference
GMAW	5183	L	73	145	293	/	[17]
CMT-PADV + interlayer rolling	5087	L	/	142	291	22.4	[16]
CMT Pulse	5356	L	/	115	268	28	[17]
		T	/	115	254	17	
CMT	5183	L	/	/	293	/	[15]
		T	/	/	281	/	
VP GTAW	5087	L	/	77	176	11	[27]
		T	/	77	170	11	
VP CMT	Al6Mg	L	/	/	315	/	[18]
		T	/	/	265	/	

References

[1] J.G. Kaufman, Properties and Applications of Wrought aluminum alloys, in: K. Anderson, J. Weritz, J.G. Kaufman (Eds.), Prop. Sel. Alum. Alloy., ASM International, 2019. doi:10.31399/asm.hb.v02b.a0006543.

[2] Aluminum and Aluminum Alloys, in: AWS Weld. Handb. - Vol. 4, American Welding Society (AWS), n.d.

[3] J.N. DuPont, Fundamentals of Weld Solidification, in: T. Lienert, T. Siewert, S. Babu, V. Acoff (Eds.), Weld. Fundam. Process., ASM International, 2011. doi:10.31399/asm.hb.v06a.a0005609.

[4] P. Berube, Weldability of Aluminum Alloys, in: K. Anderson, J. Weritz, J.G. Kaufman (Eds.), Alum. Sci. Technol., ASM International, 2018. doi:10.31399/asm.hb.v02a.a0006510.

[5] K. Anderson, J. Weritz, J.G. Kaufman, eds., 5083: Moderate-Strength Weldable Alloy, in: Prop. Sel. Alum. Alloy., ASM International, 2019. doi:10.31399/asm.hb.v02b.a0006697.

[6] ANSI H35.1/H35.1M, (2017).

[7] EN 1780-2 Aluminium And Aluminium Alloys - Designation Of Alloyed Aluminium Ingots For Remelting, Master Alloys And Castings - Part 2: Chemical Symbol Based Designation System, (2002).

[8] EN 1780-1 Aluminium And Aluminium Alloys - Designation Of Alloyed Aluminium Ingots For Remelting, Master Alloys And Castings - Part 1: Numerical Designation System, (2005).

[9] EN 1780-3 Aluminium And Aluminium Alloys - Designation Of Alloyed Aluminium Ingots For Remelting, Master Alloys And Castings - Part 3: Writing Rules For Chemical Composition, (2002).

[10] X. Fang, L. Zhang, G. Chen, K. Huang, F. Xue, L. Wang, J. Zhao, B. Lu, Microstructure evolution of wire-arc additively manufactured 2319 aluminum alloy with interlayer hammering, Mater. Sci. Eng. A. 800 (2021) 140168. doi:https://doi.org/10.1016/j.msea.2020.140168.

[11] J. Gu, M. Gao, S. Yang, J. Bai, J. Ding, X. Fang, Pore formation and evolution in wire + arc additively manufactured 2319 Al alloy, Addit. Manuf. 30 (2019) 100900. doi:https://doi.org/10.1016/j.addma.2019.100900.

[12] G. Liu, J. Xiong, External filler wire based GMA-AM process of 2219 aluminum alloy, Mater. Manuf. Process. 35 (2020) 1268–1277. doi:10.1080/10426914.2020.1779936.

[13] Z. Qi, B. Cong, B. Qi, G. Zhao, J. Ding, Properties of wire + arc additively manufactured 2024 aluminum alloy with different solution treatment temperature, Mater. Lett. 230 (2018) 275–278. doi:https://doi.org/10.1016/j.matlet.2018.07.144.

[14] Y. Zhou, X. Lin, N. Kang, W. Huang, J. Wang, Z. Wang, Influence of travel speed on microstructure and mechanical properties of wire + arc additively manufactured 2219 aluminum alloy, J. Mater. Sci. Technol. 37 (2020) 143–153. doi:https://doi.org/10.1016/j.jmst.2019.06.016.

[15] X. Fang, L. Zhang, G. Chen, X. Dang, K. Huang, L. Wang, B. Lu, Correlations between microstructure characteristics and mechanical properties in 5183

aluminium alloy fabricated by wire-arc additive manufacturing with different arc modes, Materials (Basel). 11 (2018). doi:10.3390/ma11112075.

[16] J. Gu, X. Wang, J. Bai, J. Ding, S. Williams, Y. Zhai, K. Liu, Deformation microstructures and strengthening mechanisms for the wire+arc additively manufactured Al-Mg4.5Mn alloy with inter-layer rolling, Mater. Sci. Eng. A. 712 (2018) 292–301. doi:10.1016/j.msea.2017.11.113.

[17] A. Horgar, H. Fostervoll, B. Nyhus, X. Ren, M. Eriksson, O.M. Akselsen, Additive manufacturing using WAAM with AA5183 wire, J. Mater. Process. Technol. (2018). doi:10.1016/j.jmatprotec.2018.04.014.

[18] C. Zhang, Y. Li, M. Gao, X. Zeng, Wire arc additive manufacturing of Al-6Mg alloy using variable polarity cold metal transfer arc as power source, Mater. Sci. Eng. A. 711 (2018) 415–423. doi:10.1016/j.msea.2017.11.084.

[19] X. Zhang, Q. Zhou, K. Wang, Y. Peng, J. Ding, J. Kong, S. Williams, Study on microstructure and tensile properties of high nitrogen Cr-Mn steel processed by CMT wire and arc additive manufacturing, Mater. Des. 166 (2019) 107611. doi:10.1016/j.matdes.2019.107611.

[20] K. Oyama, S. Diplas, M. M'hamdi, A.E. Gunnæs, A.S. Azar, Heat source management in wire-arc additive manufacturing process for Al-Mg and Al-Si alloys, Addit. Manuf. 26 (2019) 180–192. doi:10.1016/j.addma.2019.01.007.

[21] S. Thapliyal, Challenges associated with the wire arc additive manufacturing (WAAM) of aluminum alloys, Mater. Res. Express. 6 (2019) 112006. doi:10.1088/2053-1591/ab4dd4.

[22] B. Wu, Z. Pan, D. Ding, D. Cuiuri, H. Li, J. Xu, J. Norrish, A review of the wire arc additive manufacturing of metals: properties, defects and quality improvement, J. Manuf. Process. (2018). doi:10.1016/j.jmapro.2018.08.001.

[23] J. Gu, J. Ding, S.W. Williams, H. Gu, J. Bai, Y. Zhai, P. Ma, The strengthening effect of inter-layer cold working and post-deposition heat treatment on the additively manufactured Al–6.3Cu alloy, Mater. Sci. Eng. A. 651 (2016) 18–26. doi:https://doi.org/10.1016/j.msea.2015.10.101.

[24] T.A. Rodrigues, V. Duarte, R.M. Miranda, T.G. Santos, J.P. Oliveira, Current status and perspectives on wire and arc additive manufacturing (WAAM), Materials (Basel). 12 (2019). doi:10.3390/ma12071121.

[25] K.S. Derekar, A review of wire arc additive manufacturing and advances in wire arc additive manufacturing of aluminium, Mater. Sci. Technol. (United Kingdom). 34 (2018) 895–916. doi:10.1080/02670836.2018.1455012.

[26] B. Zhang, L. Zhang, C. Wang, Z. Wang, Q. Gao, Microstructure and properties of Al alloy ER5183 deposited by variable polarity cold metal transfer, J. Mater. Process. Technol. 267 (2019) 167–176. doi:10.1016/j.jmatprotec.2018.12.011.

[27] Z. Qi, B. Qi, B. Cong, R. Zhang, Microstructure and mechanical properties of wire + arc additively manufactured Al-Mg-Si aluminum alloy, Mater. Lett. 233 (2018) 348–350. doi:10.1016/j.matlet.2018.09.048.

Chapter 9

WIRE-AND-ARC ADDITIVE MANUFACTURING OF ALMG4.5MN ALLOY

EXPERIMENTAL ANALYSES

Foreword

The present Chapter synthetizes the experimental activities carried out during the PhD course on AlMg4.5Mn plates produced by Wire-and-Arc Additive Manufacturing (WAAM). The work focused on the morphological, microstructural and mechanical characterization of samples extracted from WAAM plates along three different orientations (longitudinal, transversal and diagonal with respect to the deposition layer). Experimental analyses aimed at correlate microstructure and mechanical properties. In particular, the investigation of the diagonal direction (45° to the deposition layers) represents the main novelty of the present work, by reference to the state of art reported in the previous Chapter.

The Chapter contains selected parts from the following paper, currently under review, which I have co—authored as first and corresponding author:

"*AA5083 (Al-Mg) plates produced by Wire-and-Arc Additive Manufacturing: effect of specimen orientation on microstructure and tensile properties*" by L. Tonelli, V. Laghi, M. Palermo, T. Trombetti, L. Ceschini.

9.1 Microstructural, morphological and mechanical characterization

9.1.1 Aim and scope

Wide research effort has been recently devoted to GMAW and GTAW-based WAAM processes for aluminum alloys [1], also focusing on wrought Al-Mg alloys of the 5000 series [2–7]. Aluminum alloys are highly appreciated by several industrial sectors for their high strength-to-weight ratio, very long in-service life, low maintenance, and contribution to the energy performance of buildings [8]. The low elastic modulus could be a main limit in the use of Al alloys, but it is well-known that the global stiffness of structural elements can be improved by a proper design of cross-sections characterized by high moment of inertia. This can be achieved by the use of complex-shaped extrudates, often made of the 6000 aluminum alloys series since the use of the 5000 series alloys is limited by their low extrudability. In this view, the WAAM process would help realizing optimized cross-section members of the 5000 series to guarantee a superior stiffness with a minimum amount of material, also gaining the advantage of the superior corrosion resistance of this series with regard to the 6000 one [9]. Up to date, the research work on WAAM of 5000 series Al alloys (5083, 5183, 5087, 5356) has been focused on: (i) tensile behavior [2,3,5,10]; (ii) microstructural defects [1–4] and (iii) possible anisotropic mechanical behavior induced by the process [7,9,10,15]. Regarding tensile properties, literature results report an almost isotropic tensile behavior [2,10,11]. On the contrary, tests carried out on stainless steel WAAM plates, as reported in the previous Chapters, showed a highly anisotropic behavior. Moreover, to the best of the authors knowledge, for Al alloys of the 5000 series there are no data currently available on the tensile behavior of specimens extracted at 45° to the deposition layer.

Based on the above, the focus of the present study is to investigate the influence orientation to the of deposition layer on the tensile properties of AA5183 aluminum plates produced by GMAW-WAAM. Tensile tests have been carried out on specimens extracted from WAAM plates considering three orientations, being perpendicular (90°), parallel (0°) and diagonal (45°) to the deposited layers, to

investigate possible anisotropic behavior. Results of tensile tests are correlated with the results of extensive microstructural and fractographical analyses, aimed at relating the new production process to the specific induced microstructural features and consequently to the final mechanical properties and failure mechanisms.

9.1.2 Experimental procedure

WAAM aluminum plates (380x380x4 mm^3) were manufactured and supplied by the Dutch company MX3D [15]. Commercially available aluminum AlMg4.5Mn0.7 welding wire (ER 5183 according to AWS A5.10 designation [16]) supplied by Oerlikon [17] was used as feedstock material. GMAW-based process with a standard pulse signal was adopted to build the aluminum plates and the main process parameters are reported in Table 9.1. According to the scheme in Figure 9.1, plates were built in the vertical (z) direction by overlapping individual layers of metallic material. Chemical composition of WAAM plates was checked by means of quantitative analysis carried out by Glow Discharge Optical Emission Spectroscopy (GDOES, Spectruma Analytik GDA-650).

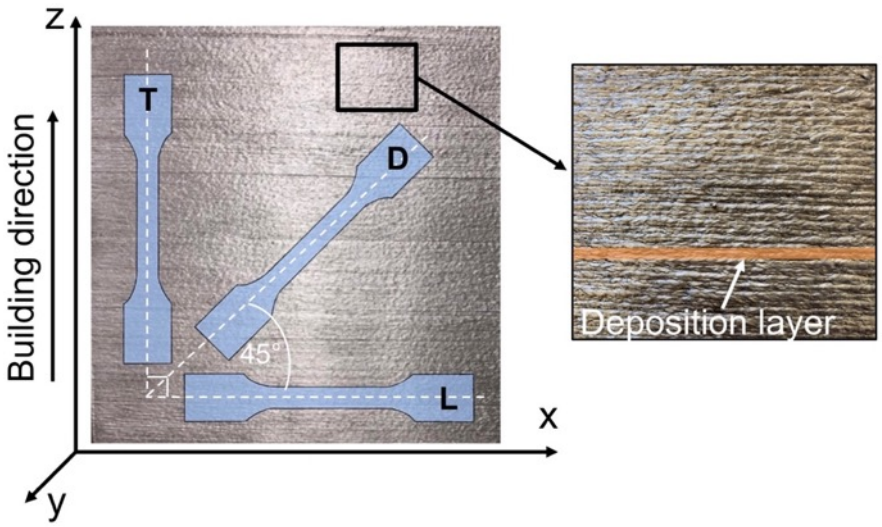

Figure 9.1: Picture of an aluminum WAAM plate with the schematic representation of samples extraction directions, according to the building direction (z axis) and deposition layer (x axis); in the inset a detail of inherent surface.

Table 9.1: Process parameters used for WAAM aluminum plates deposition (Courtesy of MX3D [15]).

Process parameters	***Details***	***Value***
Deposition power	Current	30 - 50 A
	Arc voltage	14 - 15 V
Speed	Welding speed	12 - 15 mm s^{-1}
	Wire feed rate	2 - 3 m min^{-1}
	Deposit rate	0.5 - 2 kg h^{-1}
Distance and angle	Layer height	0.5 - 2 mm
	Electrode to layer angle	90°
Wire	Wire grade	ER 5183
	Wire diameter	1.2 mm
Shield gas	Shield gas type	100% Ar
	Shield gas flow rate	10-20 L min^{-1}

Mechanical characterization of WAAM plates consisted of tensile and hardness tests. Flat dog-bone tensile specimens were machined from the WAAM plates considering three main directions, with respect to the deposition layer, as represented in Figure 9.1: longitudinal (L), transversal (T), and diagonal (D) thus being parallel, perpendicular and inclined at 45° to the layer, respectively. Tensile tests were performed at room temperature, according to ISO 6892-1 [18] on a Metrocom universal testing machine of 500 kN load capacity under displacement-control with loading rate of 2 MPa s^{-1}. Strain up to the yield point was measured by a Linear Variable Displacement Transducer (LVDT) of 50 mm gauge length. Geometry and dimensions of tensile specimens were chosen according to ISO 6892-1 [18] (gauge length of 160 mm, gauge width of 20 mm and nominal thickness of 4 mm according to ASTM E8/E8M-16a standard [19]) and the as-built surface roughness of the WAAM plates was preserved. Four specimens for each extraction direction (L, T and D) were tested. Before testing, gauge length dimensions of each specimen were measured by means of a digital caliper. Given the inherent surface roughness of the specimens due to the printing process (Figure 9.1), the values of cross-sectional area and thickness were taken from volume equivalency, by means of the Archimedes' principle, according to previous literature work on as-built

WAAM specimens [12,13]. Elastic Modulus (*E*), yield stress (calculated as 0.2% proof stress) (*YS*), ultimate tensile strength (*UTS*) and elongation to failure ($A_{\%}$) were evaluated. Vickers hardness tests HV_1 (1 kg load, 15 s dwell time) were carried out on samples extracted from the grip region of tensile specimens [20].

Surface topography of WAAM plates was analyzed by means of a 3D-Digital Microscope (Hirox KH-7700) with the aim of characterizing morphological features peculiar of the aluminum WAAM plates. Waviness and roughness profiles, and related parameters (R_a, R_z), were evaluated according to the EN ISO 4287 standard [21] by means of a stylus profilometer (Hommelwerke T2000, 5 μm tip radius).

Phase composition was determined by X-ray diffraction (XRD, PANalytical Expert PRO with Xcelerator detector) operating at 40 kV and 40 mA. For XRD analysis, Cu-Kα (λ = 0.15406 nm) was used as radiation source and scans were carried out from 20 to 90° (θ - 2θ), with a 0.01° step size and a 10 s dwell time.

A comprehensive macro and microstructural characterization was performed via Optical Microscopy (OM) and Field Emission Gun Scanning Electron Microscopy equipped with an Energy Dispersive X-ray Spectroscope (FEG-SEM EDS), using both secondary and back-scattered electrons. According to the scheme reported in Figure 9.2, samples for microstructural analyses were extracted from grip regions of L, D and T tensile specimens and the three principal cross-sections (lying on x-z, x-y and z-y planes) were considered. Standard grinding and polishing procedures (ASTM E3 [22]) were used for preparing metallographic samples and, in order to reveal specific microstructural features, chemical etching was carried out via 30 s immersion in the Keller's reagent (2.5 mL HNO3, 1.5 mL HCl, 1.0 mL HF and 95 mL distilled water [23]).

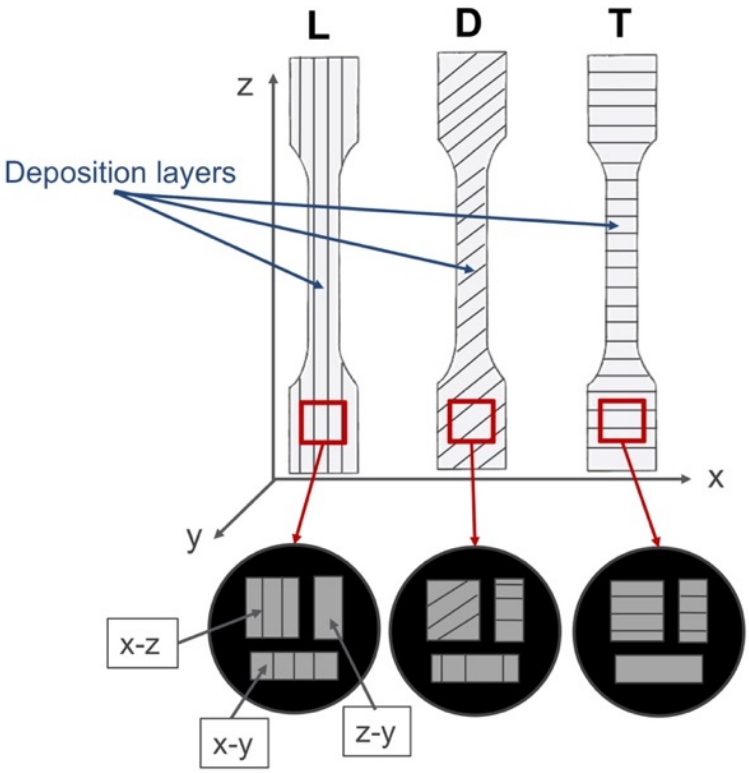

Figure 9.2: Samples for microstructural analyses: schematic representation of samples extraction directions from L, D and T WAAM tensile specimens.

Fracture surfaces of the tensile specimens were firstly inspected by 3D-Digital microscopy and then by FEG SEM-EDS microscopy, for both a general and more detailed characterization. In order to investigate the crack path, samples extracted close to the fracture surfaces were also subjected to metallographic preparation, as described above, and then analysed by OM and FEG-SEM.

9.1.3 Results and discussion

CHEMICAL COMPOSITION

Results of chemical composition analysis, carried out by GD-OES, are reported in Table 9.2 and compared to the nominal composition of the ER5183 feedstock wire, as provided by the supplier [17], and to the nominal composition of AA5083 alloy [9], of which the ER5183 wire is the common filler material. Results show that,

with respect to the feedstock wire, WAAM plates exhibited a higher content of the main alloy element (Mg) and a lower presence of Mn, however these values fall within the range of AA5083. It is worth noticing also that no trace of Si, nominally present in the wire and in the AA5083 alloy, was detected on WAAM plates.

Table 9.2: Chemical composition of WAAM aluminum plates (mean value and standard deviation) measured by GD-OES, compared to the nominal composition of the feedstock wire ER5183 [17] and AA5083 alloy [9]. Where a specific range is not reported, value has to be considered as maximum admissible content.

	Elements (wt. %)								
	Al	***Mg***	***Mn***	***Fe***	***Zn***	***Ti***	***Cr***	***Si***	***Cu***
WAAM plates	Bal.	4.876 ±0.047	0.614 ±0.013	0.097 ±0.003	0.032 ±0.002	0.086 ±0.003	0.042 ±0.001	-	-
Wire	Bal.	4.5	0.8	0.1	-	0.1	0.1	0.3	0.1
AA5083	Bal.	4.0 – 4.9	0.4 – 1.0	0.4	0.25	0.15	0.05 – 0.25	0.4	0.1

SURFACE MORPHOLOGY

As concerning morphological characterization, it can be inferred that the surface of WAAM plates is typically characterized by a high roughness and a marked waviness, inherent of the process itself that consists of subsequent deposition of thick (1 to 2 mm) layers of molten material [24]. Evidence can be found in the representative waviness profile measured by a stylus profilometer along the building direction (z axis) on the surface of WAAM plates (Figure 9.3a), where it is possible to recognize a cyclic repetition of peaks and valleys, consistent with the layer deposition thickness (0.5 - 2 mm, Table 9.1), being the maximum distance between the highest peak and the lowest valley (total height of waviness profile) equal to 357 µm. The corresponding roughness profile is reported in Figure 9.3b and revealed a poor surface finishing, characterized by typical surface roughness parameters R_a= 21 µm and R_z = 94 µm. The high surface roughness can be ascribable to the deposition process, consisting of the subsequent formation of melt pools, as highlighted by 3D digital micrographs reported in Figure 9.4. As for the AISI 304L described in Chapter 7, plates were fabricated by deposition of single

layers of molten material. However, in this case solidified melt pools are visible as due to the pulse signal adopted in order to control heat input, resulting in droplets detachment. Figure 9.4a shows the typical surface of WAAM plates, where both the deposition layers (whose boundaries are highlighted by yellow dashed lines) and melt pools (highlighted by red dashed lines) can be recognized. In some cases, typical defects of conventional welding process, also reported for WAAM components, were detected on plates surfaces (x-z plane) [24,25]. For example, Figure 9.4b shows a collapsed melt pool, while spatters, consisting of metal droplets ejected from the liquid pool and then solidified in spherical shape, can be appreciated in Figure 9.4c.

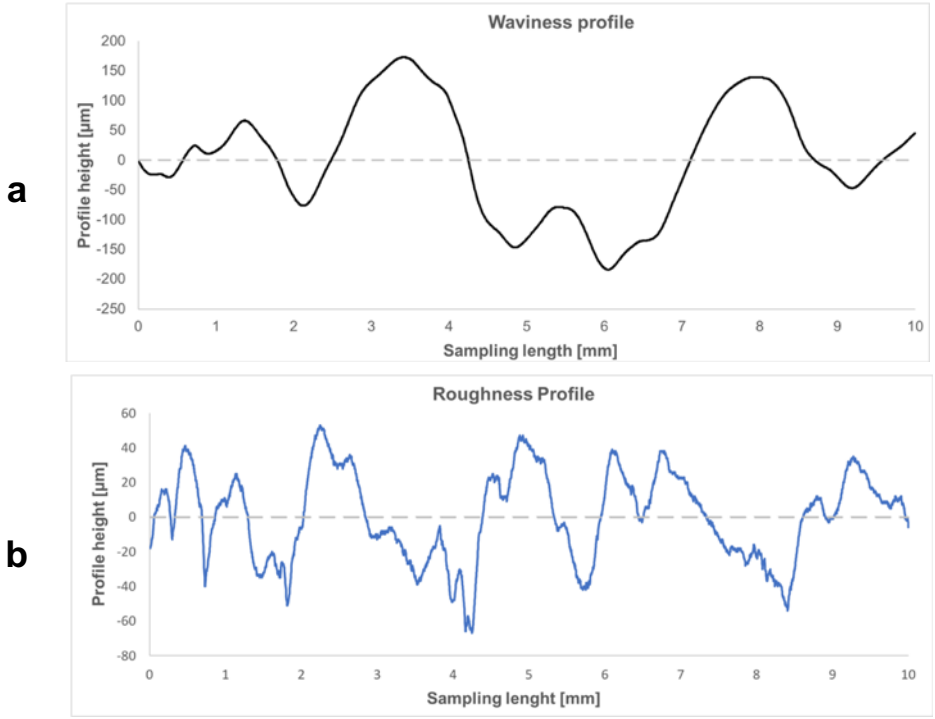

Figure 9.3: Profilometric analyses of WAAM plates surface: a) representative waviness profile along building direction (z axis), b) corresponding roughness profile.

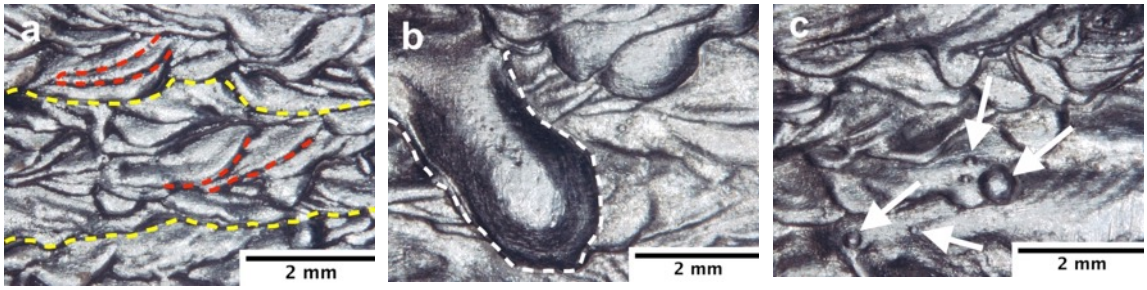

Figure 9.4: 3D digital micrographs of WAAM plates surface (x-z plane): a) regular surface where dashed yellow lines highlight deposition layers boundaries while red ones highlight melt pools boundaries, b) collapsed melt pool underlined by white dashed line, c) spatters, indicated by white arrows

PHASE COMPOSITION

Results of X-Ray diffraction analyses performed on L, D and T samples are reported in Figure 9.5. In the general view of spectra (Figure 9.5a), only the α-Al phase can be appreciated. By focusing on the low intensities, in the range of 2θ = 20-60° (Figure 9.5b), for all three directions, few small peaks can be recognized, that can be attributed to second phases, i.e. intermetallic compounds. In Al-Mg-Mn alloys, main intermetallic compounds are Mg-rich and Fe-rich [26–28] such as Al_3Mg_2, Al_5Mg_8, and $Al_6(Fe,Mn)$. Similar spectra were presented by [29], who studied the effect of Fe and Mn addition to the Al-5Mg-Mn alloy solidified in near-rapid cooling conditions, and by [2] who investigated the AA5183 alloy processed by CMT WAAM. They evidenced the presence of $Al_6(Fe,Mn)$ and Al_5Mg_8 respectively and, based on their previous work and on FEG-SEM analyses, that will be later reported and discussed, low intensity peaks in Figure 9.5b can be reasonably attributed to these intermetallic compounds.

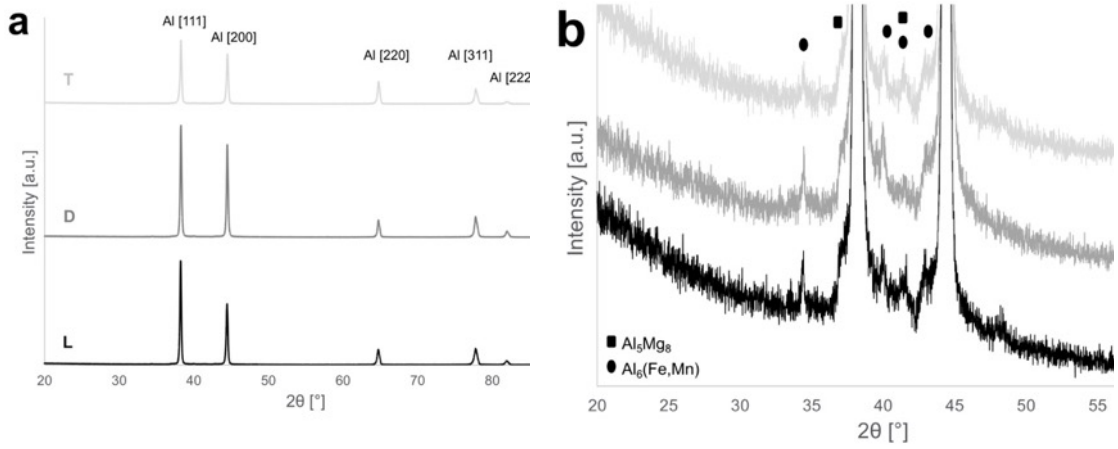

Figure 9.5: XRD analysis: a) whole spectra and b) detail of low peaks in the 20-60° portion for longitudinal (L), diagonal (D) and transversal (T) samples.

MICROSTRUCTURE

Microstructure of L, D and T samples were firstly studied by light microscopy (OM) along three main planes, in accordance with Figure 9.2, thus allowing assembling the three-dimensional reconstructions shown in Figure 9.6, while higher magnification analyses are reported in Figure 9.7. As it can be noticed particularly from Figure 9.6, microstructural features such as layer boundaries (yellow dashed lines) and melt pool boundaries (red dashed lines) were differently oriented with respect to the tensile test direction (black arrows) in L, D and T samples and this should lead to a different mechanical response. Extensive macro (greater than 100 μm) and micro porosity (of about a few of tens of microns) were detected in all samples and along all considered planes, as also noticeable by detailed analyses in Figure 9.7. Macro and micro porosity were mainly located in correspondence of interlayer regions and melt pool borders, as showed in Figure 9.8a. Porosity located in the region adjacent to layer boundaries was also found by other researchers in Al-Mg alloys processed by WAAM [2–5,11] and it is considered one of the major issues in processing aluminum alloys with this technology [30,31]. Such porosities are commonly spherical in shape, as in the present study, thus suggesting gas entrapment, ascribable to shielding gas and especially to hydrogen content, whose solubility in solid aluminum is much smaller than that in the molten state [30,32]. The hydrogen content probably derived from surface

contamination of the feedstock wire, such as moisture that reacted with molten aluminum during the process [31]. Microcracks in the interlayer region were also evidenced (Figure 9.8b), arranged in the area subjected to re-heating by the deposition of the subsequent layer. Intergranular cracks were already reported in the literature by Horgar et al. [4] for the WAAM processed AA5183 and they were attributed to the hot cracking phenomenon. It is well known that hot cracking is mainly related to the alloy composition that indirectly refers to the amount of eutectic present at solidification and, for this reason, this is the main welding problem of the AA5083 alloy, not readily eliminated by simple change in welding procedures [33,34]. Some studies [35,36] evidenced the positive effect of titanium (Ti)-boron (B), scandium (Sc), erbium (Er) and zirconium (Zr) additions on mitigating the hot cracking tendency, due to the induced grain refinement. However, WAAM process, in the reason of high cooling rate, yet results in a very fine microstructure, thus microcracks are presumably mainly related to porosity content. As shown in Figure 9.8b, indeed, cracks tend to connect micro-porosities present in the interlayer region.

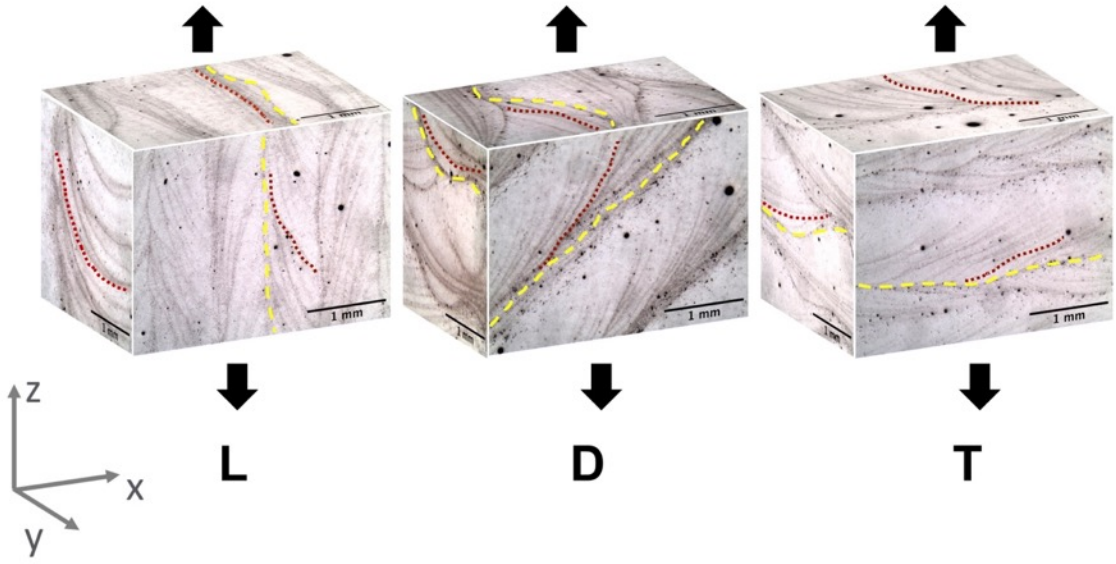

Figure 9.6: 3D microstructural reconstructions by optical micrographs of longitudinal (L), diagonal (D) and transversal (T) samples. Black arrows indicate tensile direction, yellow dashed lines highlight layer boundaries and red dashed lines highlight melt pool boundaries.

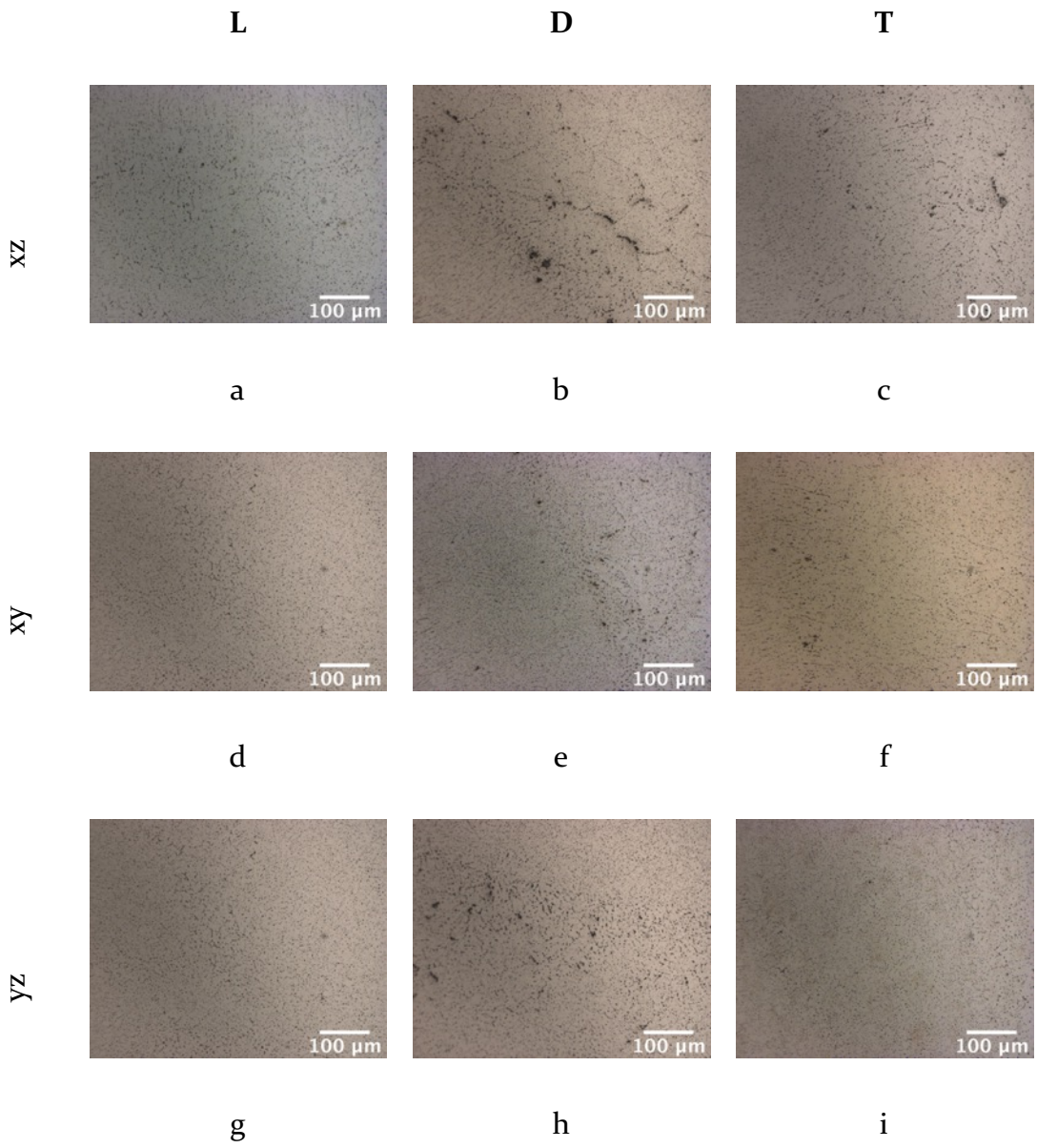

Figure 9.7: Representative OM high magnification micrographs showing microstructure of: a), d), g) longitudinal, b), e), h) diagonal and c), f), i) transverse tensile samples on xz, xy and yz planes as defined in Figure 9.6.

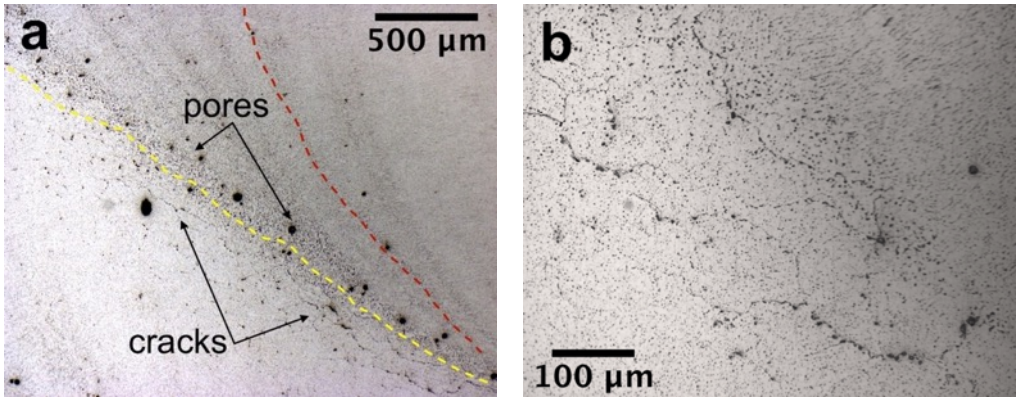

Figure 9.8: Micrographs of a representative samples showing: a) porosity and cracks in the interlayer region (yellow dashed line identifies layer boundary, red dashed line indicates a melt pool boundary), b) detail of cracks.

The analysis at the optical microscope revealed the presence of two main phases: a light one, being the primary α-Al phase, and a dark one corresponding to secondary phases, such as intermetallic compounds (Figure 9.9a). Second phases were already detected by XRD analyses (Figure 9.5) and attributed to Fe- and Mg-rich intermetallic phases. In the reason of the high cooling rate that material experiences during WAAM process [24,37], these secondary phases were extremely fine [29] and, in addition, they were uniformly distributed in the Al matrix, as already observed by [2]. FEG-SEM analyses (Figure 9.9b) evidenced the presence of two different types of intermetallic compounds, that have been further investigated by EDS spectroscopy (Figure 9.9c,d). In accordance with XRD results, grey equiaxed particles (Figure 9.9c) mainly contain Al, Mg and Mn and thus were consistent with the Al_5Mg_8 phase, while bright vermicular particles (Figure 9.9d), in the reason of the presence of Fe, could be identified as Al_6(MnFe). It should be noticed that Si was no detected by the mass spectrometric analysis, while EDS revealed a small amount of Si in correspondence of some intermetallic compounds. A possible explanation is that the Si, present in a very low content, segregated in these secondary phases.

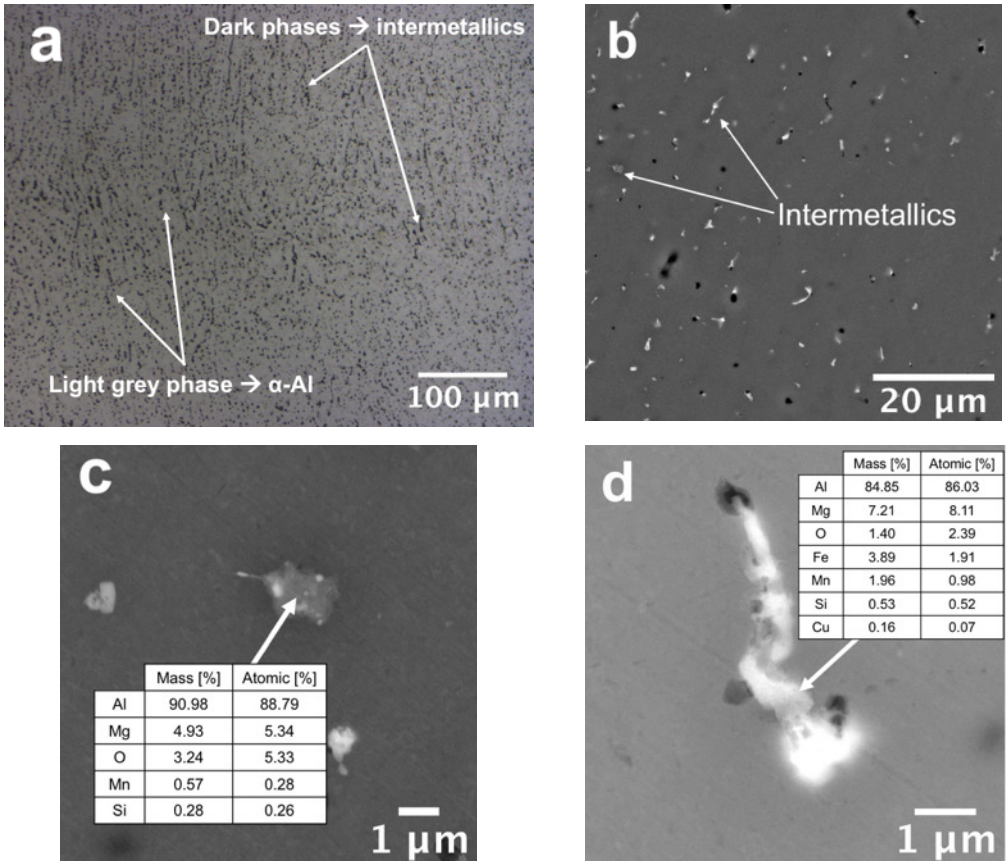

Figure 9.9: Microstructural analyses: a) optical micrographs of an interlayer region, b) FEG-SEM micrographs showing the two different types of intermetallic compounds (indicated by white arrows), c) and d) FEG-SEM EDS analysis of intermetallic compounds.

HARDNESS

Vickers hardness measurements HV_1 were performed on metallographic samples and, by referring to Figure 9.2, they were conducted on the three sections considered (x-z, z-y and x-y plane) with the aim of determining the overall hardness of samples. Hardness values were in the range 79 – 84 HV_1 and, by considering standard deviations, they were comparable for all samples (Table 9.3). The resulting hardness is consistent and even higher than values reported in literature for similar alloys processed by WAAM [3,4] and nominal value reported for conventional AA5083-O sheets, equal to 75 HB (that can be conventionally compared to 75 HV) [9]. Following the Hall-Petch relationship, the increase in hardness is mainly due to the very fine microstructure resulting from WAAM process.

Table 9.3: Hardness measurements carried out on samples: average values and standard deviations

Sample	HV_1
L	84 ± 4
D	81 ± 3
T	79 ± 4
average	81 ± 2

TENSILE TESTS

Figure 9.10 shows the whole stress-strain curves for specimens L (Figure 9.10a), T (Figure 9.10b) and D (Figure 9.10c). The curves showed in general a quite uniform stress-strain behavior within each specimen orientation, also evidenced in the low standard deviations presented in Figure 9.11. All directions presented a first elastic segment, followed by a post-yielding hardening behavior. It is worth noticing that all three orientations evidenced the phenomenon of serrated yielding or serrated flow, also known as the Portevin-Le Chatelier (PLC) effect, as evidenced also by curves reported by [9] for the same WAAM processed AA5083 alloy. This phenomenon is due to plastic deformation instability and can be observed in the stress-strain curves of many metal alloys as repetitive steps, called yielding teeth or serrated yielding [38]. The PLC effect is associated to diffusion of solute atoms occurring at higher rate than speeds of dislocations and is a well-known issue concerning Al-Mg alloys as well as the 5083 alloy [39–41], but it has also been associated to preferential crystallographic orientations [42]. This suggests that the serrated yielding observed in the stress-strain curves of the WAAM specimens is an intrinsic property of the specific alloy but can be also related to the additive process.

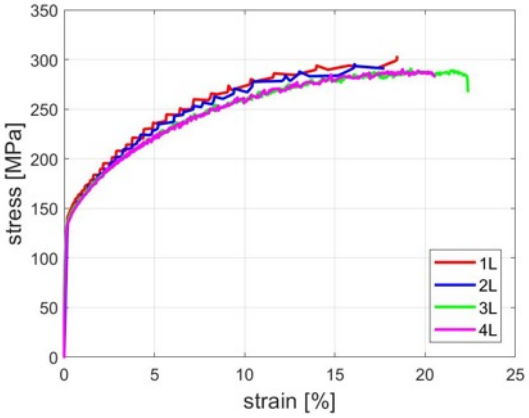

a

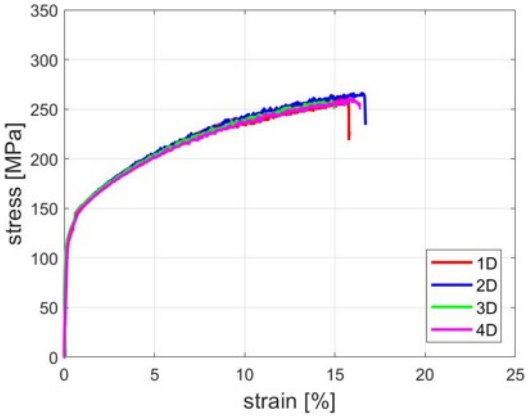

b

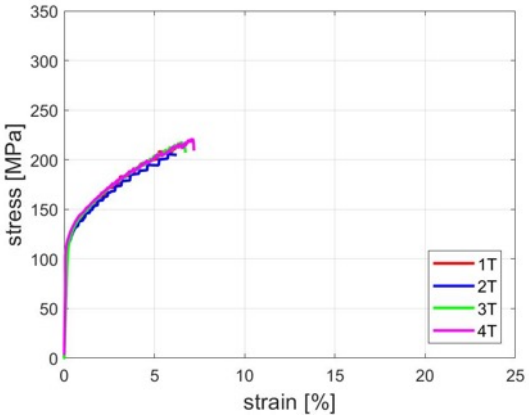

c

Figure 9.10: Stress-strain curves for tensile tests: a) longitudinal (L); b) diagonal D; c) transversal (T) specimens.

The histograms in Figure 9.11 provide a comparison of the average properties of three different orientations tested for each tensile property investigated. In particular, the trends showed a marked anisotropic behavior mainly for both ultimate tensile strength and elongation to failure values (Figures 9.11c and d), for which in both cases the highest values were for orientation L (295±5 MPa and 20±2%) and the lowest for T (215±6 MPa and 7±1%). A similar trend can be observed for yield stress (Figures 9.11b), although the difference among the three orientations was slightly lower. Young's modulus values presented instead a different trend, since specimens L and T exhibited similar values (80-86 GPa) while specimens D showed the lowest one (66 GPa). However, by taking into account the high standard deviations registered for specimens D and L, the values can be considered almost comparable for all directions. The different mechanical response of the three orientations will be explained when analyzing the results of fracture surfaces characterization, reported in the next section.

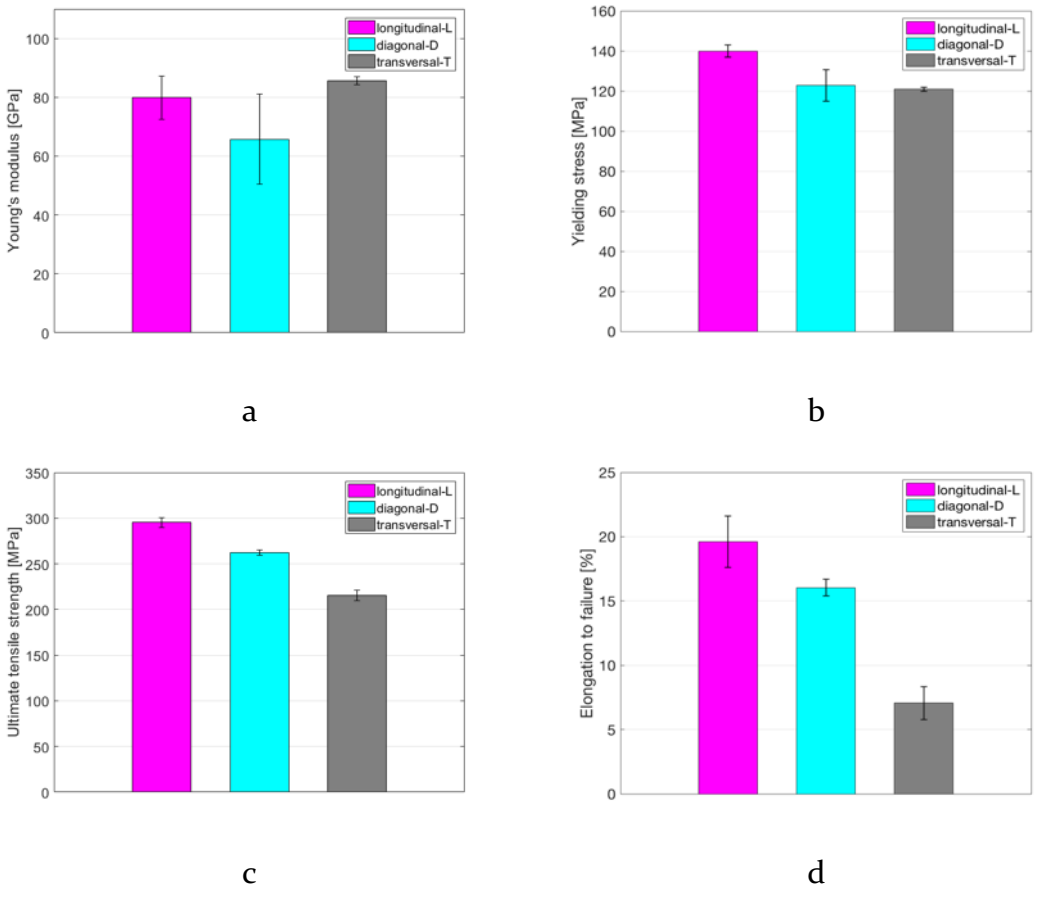

Figure 9.11: Results of the tensile tests on longitudinal (L), diagonal (D) and transversal (T) specimens

By comparing the results of the present study with the outcomes of previous experiments on similar WAAM processed aluminum alloys reported in Chapter 8 (Table 8.4), it can be noticed that in general yield stress and ultimate tensile strength values are in line with the results of the present work. However, higher elongation to failure for specimens T were presented in literature with respect to those obtained in the present campaign.

It is worth noting that the values of tensile strength and elongation measured on L specimens were higher than those reported for the conventionally manufactured thin (1.2 - 6.3 mm) sheets of the 5083-O alloy, being 275 MPa and 16 % respectively [14].

FRACTURE SURFACES

In order to study the main fracture mechanisms occurred during tensile tests, fracture regions have been investigated both at low and high magnification. Low magnification analyses of the lateral view of the fracture regions (Figure 9.12 a,b,c) suggested that, in case of D and T samples, fracture occurred along layer boundaries, while in case of L samples fracture crossed-over the layers. The same was confirmed by metallographic analyses carried out on polished sections of fracture surfaces (Figure 9.12 d,e,f), where it can be clearly appreciated that fracture path followed the boundary between two consecutive layers for samples D and T.

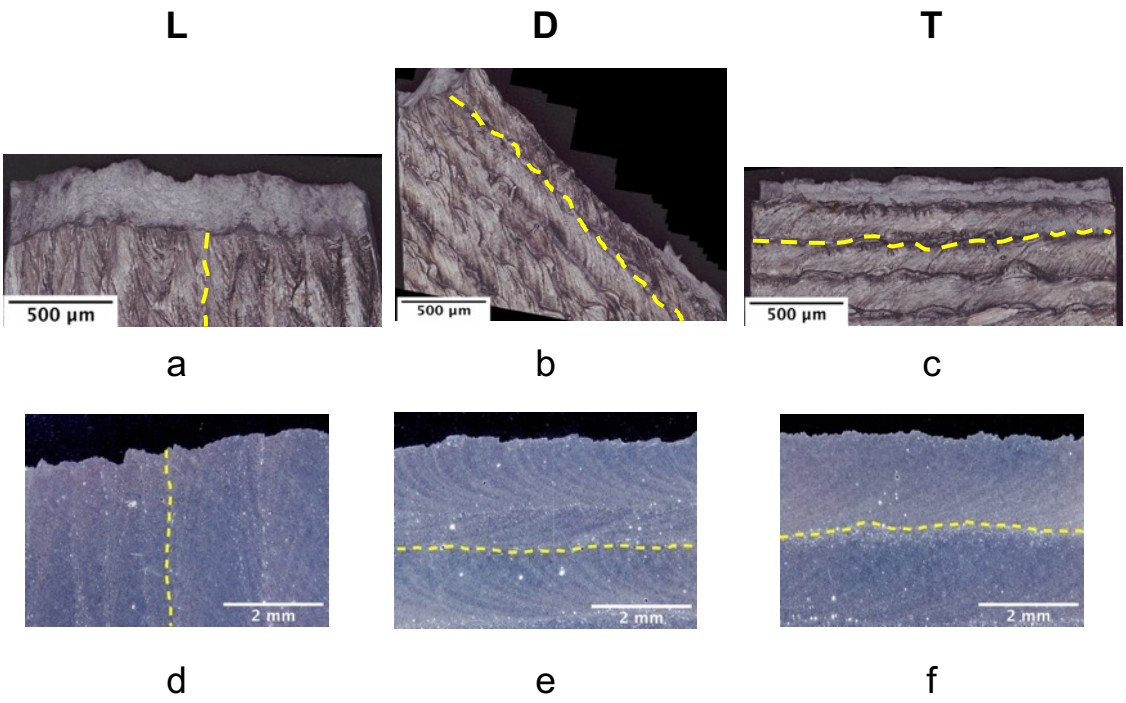

Figure 9.12: 3D digital analyses of fracture region (x-z plane): a), b), c) lateral view for sample L, D and T respectively; d), e), f) corresponding metallographic cross-sections. Deposition layers are defined by yellow dashed lines

Further analyses of fracture surfaces were carried out by means of FEG-SEM in order to deeply investigate their morphology. The general view of fracture surfaces (Figure 9.13 a,b,c) showed extensive porosity, in particular in case of samples T where pores strongly prevailed. This result confirmed that fracture in T and D samples occurred along layer boundaries where the majority of porosity lied, according to the previously discussed microstructural results. For samples L, instead, fracture occurred perpendicularly with respect to the deposition layer, so it crossed-over all the layers. However, pores could still be identified on L fracture surfaces, belonging to the interlayer regions of each layer. The shape of pores on L and T surfaces was almost spherical (Figure 9.13d,f), while on D surfaces it was quite elongated (Figure 9.13e). The dimensions of these defects in some case reached 100 µm, but in most cases they lied in the range size 10-50 µm. During tensile tests, and more in general when a load is applied, microcracks can generate from pores and eventually result in macrocracks, thus reducing the overall mechanical strength of the material [2]. So, if defects are unfavorably aligned with

respect to the direction of the applied load, i.e. perpendicularly to the tensile load, they can be detrimental for the mechanical strength of the component. With reference to the mechanical tests results (Figure 9.11), samples T showed indeed the lowest mechanical properties, in particular in terms of ultimate strength and elongation, while L ones the highest. Thus, it could be inferred that the orientation of the deposition layer, that determines also the orientation of defects (pores and cracks) with respect to the tensile direction (Figure 9.6), played an important role in determining the mechanical response of WAAM aluminum parts. Based on these results, in accordance with the outcomes reported in literature, it is preferable to align the deposition layer with the tensile direction, as for sample L. Mechanical properties of D samples ranged in between those of L and T ones, so this suggests that orienting the layer at 45° to the tensile direction is preferable than 90°.

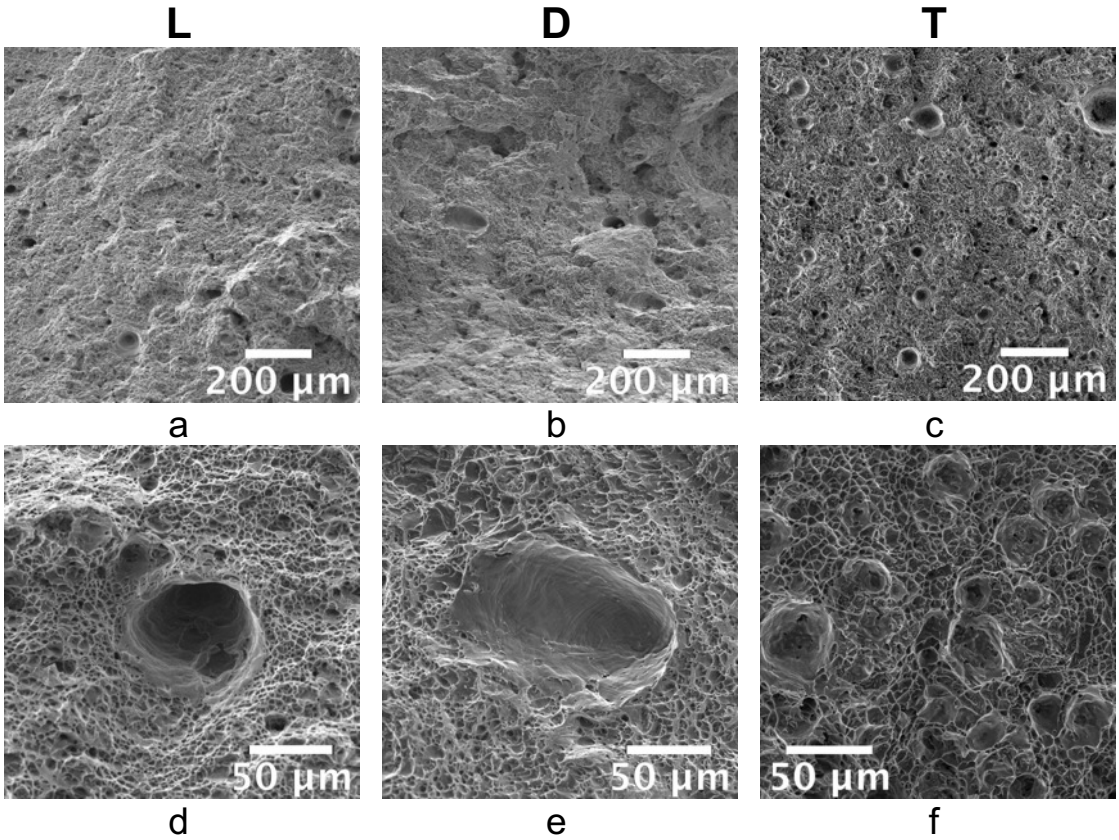

Figure 9.13: FEG-SEM analyses of fracture surfaces (x-y plane): a), b), c) low magnification micrographs for samples L, D and T; d), e), f) corresponding high magnification details of surfaces

Observation of fracture surfaces at higher magnification evidenced the presence of dimples in all tested samples, typical of a ductile fracture (Figure 9.14). Dimples were very fine (lower than 10 μm) and equiaxed on samples L (Figure 9.14a), coarser but still equiaxed on T samples (Figure 9.14b), while slightly elongated on D samples, probably due to the effect of shear stresses (Figure 9.14c). FEG-SEM EDS analysis revealed the presence, inside dimples, of two types of very small particles (about 1 μm), Mg-rich and Fe-rich respectively (Figure 9.14d,e), consistent with the intermetallic compounds evidenced by microstructural characterization.

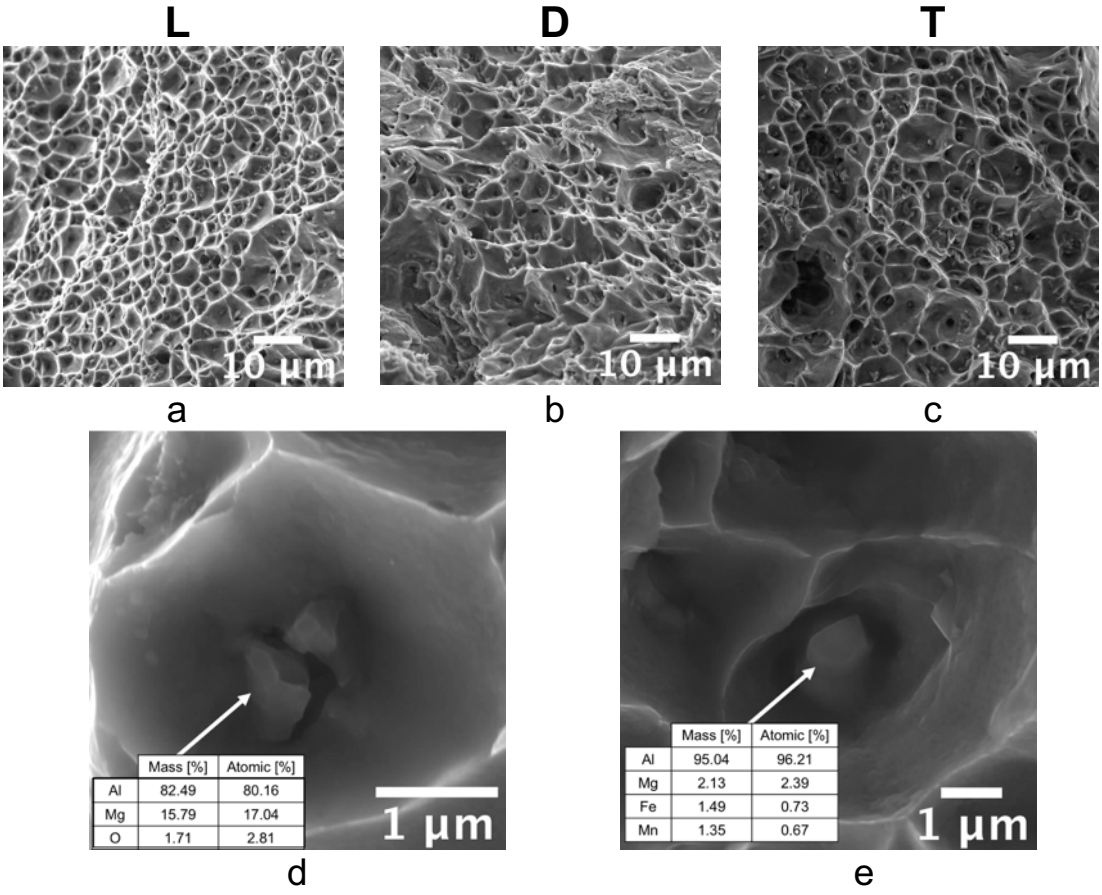

Figure 9.14: High magnification FEG-SEM analyses of fracture surfaces: a), b), c) dimples morphology for samples L, D and T; d) and e) semiquantitative FEG-SEM EDS analyses of particles inside of dimples

9.1.4 Conclusions

In the present work, the assessment of morphological, mechanical and microstructural features of aluminum plates produced by Wire-and-Arc Additive Manufacturing (WAAM) using an ER5183 wire was carried out. Aiming to a comprehensive characterization of WAAM plates, all the analyses were performed on specimens extracted along the parallel (L), diagonal (D) and perpendicular (T) directions, with respect to the deposition layer. Based on experimental results, the following conclusions can be drawn:

- Chemical composition of WAAM plates complied with the standards for 5083 aluminum alloy.
- The deposition process resulted in a layered structure comprised of successive solidified melt pools and the final microstructure was composed by α-Al phase and fine Fe and Mg-based intermetallic particles, homogeneously distributed in the aluminum matrix.
- Microstructural discontinuities (gas porosity and microcracks) were evidenced by microstructural analyses, especially located in the interlayer regions of all specimens. A consistent porosity was also evidenced on all fracture surfaces and, reasonably, it was the main responsible for the tensile response of the WAAM specimens.
- Results of tensile tests evidenced an anisotropic behavior, according to L, D and T orientation, especially in terms of ultimate strength and elongation. L direction exhibited the highest tensile properties (with ultimate strength and elongation comparable to the wrought 5083 alloy), while T direction was characterized by the lowest mechanical properties.
- The anisotropic tensile behavior was related to the alignment of the deposition layer with respect to the tensile direction, taking into account that microstructural discontinuities were mainly found in the interlayer area. Indeed, specimens T, whose layers are perpendicular to the loading direction, exhibited the lowest mechanical properties while L specimens, whose layers are parallel, the highest ones.

References

[1] K.S. Derekar, A review of wire arc additive manufacturing and advances in wire arc additive manufacturing of aluminium, Mater. Sci. Technol. (United Kingdom). 34 (2018) 895–916. doi:10.1080/02670836.2018.1455012.

[2] X. Fang, L. Zhang, G. Chen, X. Dang, K. Huang, L. Wang, B. Lu, Correlations between microstructure characteristics and mechanical properties in 5183 aluminium alloy fabricated by wire-arc additive manufacturing with different arc modes, Materials (Basel). 11 (2018). doi:10.3390/ma11112075.

[3] J. Gu, X. Wang, J. Bai, J. Ding, S. Williams, Y. Zhai, K. Liu, Deformation microstructures and strengthening mechanisms for the wire+arc additively manufactured Al-Mg4.5Mn alloy with inter-layer rolling, Mater. Sci. Eng. A. 712 (2018) 292–301. doi:10.1016/j.msea.2017.11.113.

[4] A. Horgar, H. Fostervoll, B. Nyhus, X. Ren, M. Eriksson, O.M. Akselsen, Additive manufacturing using WAAM with AA5183 wire, J. Mater. Process. Technol. (2018). doi:10.1016/j.jmatprotec.2018.04.014.

[5] C. Zhang, Y. Li, M. Gao, X. Zeng, Wire arc additive manufacturing of Al-6Mg alloy using variable polarity cold metal transfer arc as power source, Mater. Sci. Eng. A. 711 (2018) 415–423. doi:10.1016/j.msea.2017.11.084.

[6] X. Zhang, Q. Zhou, K. Wang, Y. Peng, J. Ding, J. Kong, S. Williams, Study on microstructure and tensile properties of high nitrogen Cr-Mn steel processed by CMT wire and arc additive manufacturing, Mater. Des. 166 (2019) 107611. doi:10.1016/j.matdes.2019.107611.

[7] K. Oyama, S. Diplas, M. M'hamdi, A.E. Gunnæs, A.S. Azar, Heat source management in wire-arc additive manufacturing process for Al-Mg and Al-Si alloys, Addit. Manuf. 26 (2019) 180–192. doi:10.1016/j.addma.2019.01.007.

[8] D. Kosteas, Sustainability, Durability and Structural Advantages as Leverage in Promoting Aluminium Structures, Key Eng. Mater. 710 (2016) 13–21. doi:10.4028/www.scientific.net/KEM.710.13.

[9] K. Anderson, J. Weritz, J.G. Kaufman, eds., Properties and Selection of Aluminum Alloys, (2019). doi:10.31399/asm.hb.v02b.9781627082105.

[10] Z. Qi, B. Qi, B. Cong, R. Zhang, Microstructure and mechanical properties of wire + arc additively manufactured Al-Mg-Si aluminum alloy, Mater. Lett. 233 (2018) 348–350. doi:10.1016/j.matlet.2018.09.048.

[11] M. Köhler, S. Fiebig, J. Hensel, K. Dilger, Wire and arc additive manufacturing of aluminum components, Metals (Basel). 9 (2019) 1–9. doi:10.3390/met9050608.

[12] P. Kyvelou, H. Slack, D.D. Mountanou, M.A. Wadee, T. Ben Britton, C. Buchanan, L. Gardner, Mechanical and microstructural testing of wire and arc additively manufactured sheet material, Mater. Des. 192 (2020) 108675. doi:10.1016/J.MATDES.2020.108675.

[13] V. Laghi, M. Palermo, G. Gasparini, V.A. Girelli, T. Trombetti, Experimental results for structural design of Wire-and-Arc Additive Manufactured stainless steel members, 2019.

[14] V. Laghi, M. Palermo, L. Tonelli, G. Gasparini, L. Ceschini, T. Trombetti, Tensile properties and microstructural features of 304L austenitic stainless steel produced by wire-and-arc additive manufacturing, Int. J. Adv. Manuf. Technol. (2020) 3693–3705. doi:10.1007/s00170-019-04868-8.

[15] MX3D Webpage, (https://mx3d.com/).

[16] AWS, A5.10 Specification for Bare Aluminum and Aluminum-Alloy Welding Electrodes and Rods, 1999 (1999) 31.

[17] Oerlikon, (https://www.oerlikon-welding.com/).

[18] ISO 6892 Metallic materials - Tensile testing, (2019) 54.

[19] ASTM E8/E8M standard test methods for tension testing of metallic materials 1, (2015) 1–27. doi:10.1520/E0008.

[20] EN ISO 6507 Metallic materials – Vickers hardness test, (2018).

[21] EN ISO 4287 Geometrical Product Specifications (GPS) - Surface texture: Profile method - Terms, definitions and surface texture parameters, (2009).

[22] ASTM International, E3 Preparation of Metallographic Specimens, Annu. B. ASTM Stand. 11 (2017) 1–17. doi:10.1520/E0003-11R17.1.

[23] G.F. Vander Voort, G.M. Lucas, E.P. Manilova, Metallography and microstructures of stainless steels and maraging steels, Mater. Park. OH ASM Int. (2004) 670–700.

[24] T.A. Rodrigues, V. Duarte, R.M. Miranda, T.G. Santos, J.P. Oliveira, Current status and perspectives on wire and arc additive manufacturing (WAAM), Materials (Basel). 12 (2019). doi:10.3390/ma12071121.

[25] G.E. Dieter, D.J. Bacon, Mechanical metallurgy, McGraw-hill, 1986.

[26] K.A. Yasakau, M.L. Zheludkevich, S. V. Lamaka, M.G.S. Ferreira, Role of intermetallic phases in localized corrosion of AA5083, Electrochim. Acta. 52 (2007) 7651–7659. doi:10.1016/J.ELECTACTA.2006.12.072.

[27] Q. Ran, Aluminium – Magnesium – Manganese Ternary Alloy Phase Diagram, in: ASM Alloy Phase Diagr. Cent., 2007: pp. 142–149.

[28] J.E. Hatch, Aluminum: Properties and Physical Metallurgy, Aluminum Association Inc. and ASM International, 1984.

[29] Y. Liu, G. Huang, Y. Sun, L. Zhang, Z. Huang, J. Wang, C. Liu, Effect of Mn and Fe on the Formation of Fe- and Mn-Rich Intermetallics in Al-5Mg-Mn Alloys Solidified Under Near-Rapid Cooling, Mater. (Basel, Switzerland). 9 (2016) 88. doi:10.3390/ma9020088.

[30] S. Thapliyal, Challenges associated with the wire arc additive manufacturing (WAAM) of aluminum alloys, Mater. Res. Express. 6 (2019) 112006. doi:10.1088/2053-1591/ab4dd4.

[31] B. Wu, Z. Pan, D. Ding, D. Cuiuri, H. Li, J. Xu, J. Norrish, A review of the wire arc additive manufacturing of metals: properties, defects and quality improvement, J. Manuf. Process. (2018). doi:10.1016/j.jmapro.2018.08.001.

[32] D.E.J. Talbot, Effects of Hydrogen in Aluminium, Magnesium, Copper, and Their Alloys, Int. Metall. Rev. 20 (1975) 166–184. doi:10.1179/imtlr.1975.20.1.166.

[33] J.C. Lippold, E.F. Nippes, W.F. Savage, Investigation of Hot Cracking in 5083-0

Aluminum Alloy Weldments., Weld. J. (Miami, Fla). 56 (1977).

[34] R. LIU, Z. DONG, Y. PAN, Solidification crack susceptibility of aluminum alloy weld metals, Trans. Nonferrous Met. Soc. China. 16 (2006) 110–116. doi:10.1016/S1003-6326(06)60019-8.

[35] M.G. Mousavi, C.E. Cross, Ø. Grong, Effect of scandium and titanium–boron on grain refinement and hot cracking of aluminium alloy 7108, Sci. Technol. Weld. Join. 4 (1999) 381–388. doi:10.1179/136217199101538030.

[36] Z. Xu, Z. Zhao, G. Wang, C. Zhang, J. Cui, Microstructure and mechanical properties of the welding joint filled with microalloying 5183 aluminum welding wires, Int. J. Miner. Metall. Mater. 21 (2014) 577–582. doi:10.1007/s12613-014-0944-3.

[37] T. DebRoy, H.L. Wei, J.S. Zuback, T. Mukherjee, J.W. Elmer, J.O. Milewski, A.M. Beese, A. Wilson-Heid, A. De, W. Zhang, Additive manufacturing of metallic components – Process, structure and properties, Prog. Mater. Sci. 92 (2018) 112–224. doi:10.1016/j.pmatsci.2017.10.001.

[38] P. V. Trusov, E.A. Chechulina, Serrated yielding: Physical mechanisms, experimental dates, macrophenomenological models, PNRPU Mech. Bull. 2014 (2014) 186–232. doi:10.15593/perm.mech/2014.3.10.

[39] A. Yilmaz, The Portevin-Le Chatelier effect: A review of experimental findings, Sci. Technol. Adv. Mater. 12 (2011). doi:10.1088/1468-6996/12/6/063001.

[40] H. Sheikh, Investigation into Characteristics of Portevin-Le Chatelier Effect of an Al-Mg Alloy, J. Mater. Eng. Perform. 19 (2010) 1264–1267. doi:10.1007/s11665-010-9634-0.

[41] N. Fakhar, F. Fereshteh-Saniee, R. Mahmudi, Significant improvements in mechanical properties of AA5083 aluminum alloy using dual equal channel lateral extrusion, Trans. Nonferrous Met. Soc. China. 26 (2016) 3081–3090. doi:10.1016/S1003-6326(16)64440-0.

[42] Y.Z. Shen, K.H. Oh, D.N. Lee, The effect of texture on the Portevin-Le Chatelier effect in 2090 Al-Li alloy, Scr. Mater. 51 (2004) 285–289. doi:10.1016/j.scriptamat.2004.04.030.

Conclusions

In the complex framework of Additive Manufacturing (AM) of metallic components, the present research project was devoted to highlight the peculiar microstructural features resulting from AM and to investigate the relationship between process, microstructure and properties.

The work focused on two main AM processes, being Laser-based Powder Bed Fusion (LPBF) and Wire-and-Arc Additive Manufacturing (WAAM), that were used to process four different metal alloys: AlSi7Mg0.6 and Co28Cr6Mo alloys in case of LPBF, AISI 304L and AlMg4.5Mn in case of WAAM. Bearing in mind the different fields of application, divergencies and affinities of processes and materials were highlighted and main metallurgical-related issues in the investigated processed metals were examined. Microstructural features and mechanical properties of the printed alloys were well correlated to the peculiar solidification microstructures induced by the AM process, resulting from the theoretical background summarized in the first Chapter of the present dissertation.

Based on the results of the experimental investigations and on the literature review that supported all the activities, the following overall conclusions can be drawn:

- Process parameters and feedstock material play a major role in determining the quality, particularly in terms of low porosity content, of final parts. However, if process optimization is carried out alongside a thorough

microstructural analysis aimed at studying type of defects, almost defect-free parts can be obtained. In case of Co28Cr6Mo LPBF alloy for biomedical application, process optimization was based on the laser energy density (LED) parameter. In fact, LED resulted to be a robust parameter to define the quality of final parts, in terms of microstructural defects, hardness and surface roughness. In case of reactive materials as aluminum alloys, specific precautions have to be taken in order to limit porosity content. Particularly, a careful control of moisture in the feedstock material and gas entrapment has to be considered, as evidenced by experimental analyses conducted on LPBF and WAAM processed aluminum alloys. Specifically, in case of AlSi7Mg0.6 LPBF alloy, two different batches of feedstock powder were examined during process optimization. It was found that the quality of powder feedstock, especially in terms of shape, and its pre-treatment play a major role in the fabrication of near-full-density samples, along with process parameters.

- AM metal parts are characterized by a hierarchical microstructure, observed in all the investigated materials, with a few distinctive differences. This peculiar microstructure consists of a layered structure due to the subsequent formation of melt pools, large epitaxial grains crossing-over layers and a fine sub-structure within grains. WAAM involves the deposition of 1-2 mm of molten material, while in LPBF the typical layer thickness is in the range 20-30 μm. Moreover, scanning strategy of LPBF is considerably more complicated than WAAM and melt pool tracks are more evident in LPBF. As a consequence, the dimensions of melt pools formed in LPBF and WAAM are quite different. However, epitaxial grains crossing-over layers were found in all AM alloys, both LPBF and WAAM produced, due to epitaxial growth that develops during the solidification of liquid metal on the solid substrate made of its same chemical composition, thus the previously deposited layer. The sub-structure formed within columnar grains was cellular in case of both Co28Cr6Mo and AlSi7Mg0.6 LPBF alloys, and columnar-dendritic in case of AISI 304L and AlMg4.5Mn. Due to the high cooling rates, sub-structure was always very fine. As evidenced in the literature, morphology of the sub-structure is related to the solidification parameters (G and R) but it

is also driven by kinetics aspects and surface tension gradient formed in the melt pool.

- Rapid solidification conditions extend solid solubility of alloy elements, leading to a supersaturated solid solution. By exploiting solute trapping, innovative heat treatments can be developed and tailored on the peculiar AM microstructure. Heat treatments can be aimed at homogenizing the microstructure or inducing strengthening of the alloy. In case of heat-treatable Co28Cr6Mo and AlSi7Mg0.6 LPBF alloys it has been demonstrated that homogenization and/or strengthening can be obtained with shortened heat treatment with regard to the conventional alloy, thus also promoting the overall productivity. In case of Co28Cr6Mo alloy, the optimized heat treatment induced both strengthening and homogenization. Such treatment did not affect the wear behavior at contact pressures comparable to the in-service conditions and preliminary results on corrosion behavior showed that it increased corrosion resistance. This is a remarkable result since wear and corrosion resistance are main properties required for final applications of this alloys, being orthopedic implants. In case of AlSi7Mg0.6 LPBF alloy, a modified T6 and direct aging treatments were investigated and effect on residual stress, hardness and microstructure was assessed. T6 resulted in the complete homogenization of microstructure and in the complete release of residual stress and, with respect to the as-built alloy, it almost doubled the ductility and increased the yield stress. Direct aging, instead, preserved the as-built microstructure and resulted in the highest strengthening with a moderate release of internal stress.
- The hierarchical AM microstructure can result in the anisotropy in the mechanical response. In fact, in case of WAAM alloys anisotropy induced by the layer-wise process and epitaxial growth was evidenced by mechanical and microstructural characterization carried out along different directions, being parallel (L), perpendicular (T) and diagonal (D) to the deposited layer. For the almost defect-free AISI 304L, strong anisotropy in the mechanical behavior, in terms of yield and ultimate tensile strength, was positively correlated to the different orientation of epitaxial grains with respect to the tensile load direction among L, T and D specimens. The marked anisotropy

in the elastic modulus was instead correlated to the crystallographic texture induced by AM technology, thus to the elastic anisotropy of the fcc crystal structure of austenitic stainless steels. The tensile characterization of the AlMg4.5Mn alloy still evidenced a moderate anisotropy in the tensile strength, but the same was not found in the elastic properties. In this case, the difference in the mechanical response could be mainly ascribed to the marked presence of solidification defects affecting the cross-sectional area, as evidenced by microstructural analyses.